

# **Bandgap engineering in phase selective TiO<sub>2</sub> microflowers for photonic applications**

By

**Subhashree Sahoo**

**PHYS11201804013**

**National Institute of Science Education and Research, Bhubaneswar**

*A thesis submitted to the*

*Board of Studies in Physical Sciences*

*In partial fulfillment of requirements*

*for the Degree of*

**DOCTOR OF PHILOSOPHY**

*of*

**HOMI BHABHA NATIONAL INSTITUTE**

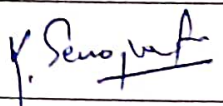
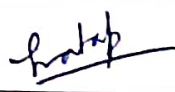
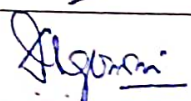
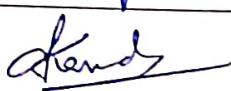
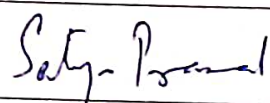



December, 2023



**Homi Bhaba National Institute**  
**Recommendations of the Viva Voce Committee**

As members of the Viva Voce Committee, we certify that we have read the dissertation prepared by **Subhashree Sahoo** entitled **Bandgap engineering in phase selective TiO<sub>2</sub> microflowers for photonic applications** and recommend that it may be accepted as fulfilling the thesis requirement for the award of Degree of Doctor of Philosophy.

Chairman - Dr. Kartikeswar Senapati		Date: 20/05/2024
Guide / Convener - Dr. Pratap Kumar Sahoo		Date: 20/05/2024
Examiner - Prof. Dipak K. Goswami		Date: 20/5/24
Member 1 - Dr. Ashis Kumar Nandi		Date: 20/05/24
Member 2 - Dr. Satyaprasad P Senanayak		Date: 20/5/24
Member 3 - Prof. Tapobrata Som		Date: 20/5/24

Final approval and acceptance of this thesis is contingent upon the candidate's submission of the final copies of the thesis to HBNI.

I/We hereby certify that I/we have read this thesis prepared under my/our direction and recommend that it may be accepted as fulfilling the thesis requirement.

Date : 20/05/2024  
Place : NISER, SGS



Signature

Guide

Dr. Pratap Kumar Sahoo





### STATEMENT BY AUTHOR

This dissertation has been submitted in partial fulfillment of requirements for an advanced degree at Homi Bhabha National Institute (HBNI) and is deposited in the library to be made available to borrowers under the rules of the HBNI.

Short quotations from this dissertation are acceptable without special permission as long as an exact source attribution is given. The Competent Authority of HBNI may grant requests for permission for an extensive quotation from or reproduction of this text in whole or in part if, in his or her opinion, the proposed use of the material is in the interests of research. Yet in every other circumstance, the author's consent is required.

*Subhashree Sahoo*  
Subhashree Sahoo



## DECLARATION

I, hereby declare that the investigation presented in the thesis has been carried out by me. The work is original and has not been submitted earlier as a whole or in part for a degree/diploma at any other Institute/University.

*Subhashree Sahoo*  
Subhashree Sahoo



## **List of Publications arising from the thesis**

### **Journal**

1. **Subhashree Sahoo**, Gurupada Ghorai, Kalyan Ghosh, Bidyadhar Das, Mrinal K Sikdar, Pratap K Sahoo. Anharmonicity of optical phonon modes in copper doped rutile TiO<sub>2</sub> nanorod composed microflowers. AIP Advances, 11, 105013, **2021**.
2. **Subhashree Sahoo** and Pratap K Sahoo. Weak-localization effect in Fano asymmetry of C implanted rutile TiO<sub>2</sub> nanostructure. Journal of Applied Physics, 133, 144301, **2023**.
3. **Subhashree Sahoo**, Binaya Kumar Sahu, Shivam Shukla, Sanjeev K. Srivastava, and Pratap K Sahoo. In-situ monitoring of plasmon induced Nanoscale photocatalytic activity from Au decorated TiO<sub>2</sub> Microflowers. Nano Futures, 7, 025002, **2023**.
4. **Subhashree Sahoo**, Km. Surbhi, Sourav Bhakta, Ritwick Das, and Pratap K Sahoo. Influence of defects on linear and nonlinear optical properties of Cu doped rutile TiO<sub>2</sub> microflowers. Phys. Chem. Chem. Phys., 26, 10191, **2024**.
5. **Subhashree Sahoo**, Soumendra Kumar Das, Bidyadhar Das, Prasanjit Samal, and Pratap K Sahoo. Defect selective optical tunability and ferromagnetic ordering in C ion intercalated TiO<sub>2</sub> nanorod composed microflowers. (Under preparation)
6. **Subhashree Sahoo**, Binaya Kumar Sahu and Pratap K Sahoo. Effect of plasmon-induced heat on Raman line shape of TiO<sub>2</sub> microflower decorated with Au nanoparticles. (Under preparation)
7. **Subhashree Sahoo** and Pratap K Sahoo. Nanoscale welding of TiO<sub>2</sub> nanorods by low energy ion beam. (Under preparation)

### **Conferences**

1. **Subhashree Sahoo** and Pratap K. sahoo. Tuning phonon coherent length of carbon ion implanted TiO<sub>2</sub> nanorod composed nanoflowers. 6th International Virtual Conference on Ion Beams in Materials Engineering and Characterizations (IBMEC -2020) December 08-11, 2020.

2. **Subhashree Sahoo** and Pratap K. sahuo. Bandgap engineering in TiO<sub>2</sub> micro-flowers through low energy Au ion irradiation. 6th International Virtual Conference on Nanos-structuring by Ion Beams (ICNIB 2021) October 05-08, 2021.
3. **Subhashree Sahoo**, Binaya Kumar Sahu, and Pratap K. sahuo. Photocatalytic activity of Au decorated TiO<sub>2</sub> microflower, Frontiers In Materials for Technological Applications (FIMTA-2022) August 03-05, 2022.
4. **Subhashree Sahoo** and Pratap K. sahuo. Phonon scattering in carbon ion implanted rutile TiO<sub>2</sub> micro-flowers. 7th International Conference on Ion Beams in Materials Engineering and Characterization (IBMEC 2022) November 16-19, 2022.
5. **Subhashree Sahoo**, Binaya Kumar Sahu, and Pratap K sahuo. Plasmon-Induced Nanoscale Photocatalytic Activity from Au-Decorated TiO<sub>2</sub> Microflowers by Raman spectroscopy. 11th International Conference on Materials for Advanced Technologies (ICMAT 2023) June 26-30, 2023.
6. **Subhashree Sahoo**, Binaya Kumar Sahu, and Pratap K sahuo. Plasmon-Induced Nanoscale Photocatalytic Activity from Au-Decorated TiO<sub>2</sub> Microflowers by Raman spectroscopy. Quantum condensed matter (QMAT 2023) November 27-30, 2023.
7. **Subhashree Sahoo**, Binaya Kumar Sahu, and Pratap K sahuo. Plasmon-Induced Nanoscale Photocatalytic Activity from Au-Decorated TiO<sub>2</sub> Microflowers by Raman spectroscopy. National Conference on Role of Indian Health and Allied Sciences for Sustainable Future February 15-16, 2024

#### **Workshop/Training**

1. Online training on “Fundamentals of Scanning Electron Microscope and its Applications”, organized by Carl Zeiss India Pvt. Ltd Research Microscopy Solutions Group, May 28, 2020.

#### **Others publications: Not included in the thesis**

1. Gurupada Ghorai, Kalyan Ghosh, Bidyadhar Das, **Subhashree Sahoo**, Bikash Patra, Prasanjit Samal, and Pratap Kumar Sahoo. Cathodoluminescence and Optical

Absorption Spectroscopy of Plasmonic Modes in Chromium Micro-rods. *Nanotechnology*, 34(7), 075707, 2022.

2. Laxmipriya Nanda, Bidyadhar Das, **Subhashree Sahoo**, Pratap K. Sahoo, and Kartik Senapati. Bismuth Phase Dependent Growth of Superconducting  $\text{NiBi}_3$  Nanorods. *Journal of Alloys and Compounds* 960, 170948, 2023.
3. Laxmipriya Nanda, **Subhashree Sahoo**, Pratap K. Sahoo, and Kartik Senapati. Fabrication of Ni- $\text{NiBi}_3$  ferromagnet-superconductor nanoparticles. *Journal of Nanoparticle Research*, 25, 251, 2023.
4. Utkalika P. Sahoo, Binaya Kumar Sahu, **Subhashree Sahoo**, Bidyadhar Das, and Pratap K. Sahoo. Plasmon mediated SERS and photocatalysis enhancement in Au nanoparticle decorated 2D- $\text{TiSe}_2$ , *Nanotechnology*, 2023.
5. Laxmipriya Nanda, Bidyadhar Das, **Subhashree Sahoo**, Pratap K Sahoo, and Kartik Senapati. Josephson coupling driven magnetoresistance in superconducting  $\text{NiBi}_3$  nanowires. (Under review)
6. Om Krishna Swarupa, **Subhashree Sahoo**, Pratap Kumar Sahoo, and Susanta Kumar Das. Structural and optical properties of two-step aqueous grown high-density ZnO nanoflowers. (Under review)

**Subhashree Sahoo**

*Dedicated to*

.....

***My beloved family***

.....





## ACKNOWLEDGEMENTS

First and foremost, I would like to sincerely thank Dr. Pratap Kumar Sahoo, my supervisor, for all of his help and advice during my doctoral study, including knowledge transfer, encouragement, and direction throughout my Ph.D. work. His trust and confidence in me served as the primary motivator for the Ph.D. path. The freedom, friendliness, and facilities he provided made my journey quite relaxing and stress-free. I feel very fortunate to be a part of his group.

I extend my thanks to the doctoral committee members, Dr. Kartik Senapati, Dr. Ritwick Das, Dr. Ashis Kumar Nandi, and Prof. Tapobrata Som, for their suggestions and comments during the annual evaluation meetings.

My heartfelt thanks to my lab seniors, Dr. Mrinal K Sidar, Mr. Bidyadhar Das, and Mr. Gurupada Ghorai for their help in handling instruments, guidance, and advice. I thank my lab friends Mr. Kalyan Ghosh, Mrs. Utkalika P. Sahoo, and Mr. Sourav Bhakta for their support, help, and scientific discussion throughout this Ph.D. journey. I thank my lab postdocs, Dr. Binaya K. Sahu, Dr. Soumendra K. Das, and Dr. Radheshyam for sharing their research experience and guidance. I also thank all my beloved friends Shaktiranjana Mohanty and Swati Das who have made my Ph.D. journey memorable.

This Ph.D. tenure will remain as some of the best days of my life, with a lot of parties and picnics with lab mates and my supervisor's family. I am really indebted to him for being such a nice supervisor. More importantly, the moral support, love, and joyful moments from him and his family, Seema Ma'am, Krrish, and Prince is unforgettable. I thank all the students who have done their semester and summer projects under my mentorship, through which I had learned a lot about how to handle the students. The company and working experience with Bhabesh Sarangi, Spanan Anupam, Anamika Jatheendran, Gautameshwar S, Pinky Anna Roy, and others will remain memorable. I am grateful to M.Sc. students Soumya Dasgupta, Mihir Chandra, Abhilash Rout, and Debabrata Barik for helping them with experimental works and sharing the joyful moments, which made our days more entertaining. I would like to thank all the members of the superconductivity lab, Laxmipriya Nanda, Tapas Ranjan Senapati, Debashree Nayak, and Dr. Bibekananda Das for their support during this journey.

I would like to thank the Department of Atomic Energy, Government of India, and NISER Bhubaneswar for their funding as well as fantastic infrastructure to carry out my Ph.D. research work. I thank the Institute of Physics (IOP, Bhubaneswar) and all the members of the IBL lab for their support during the use of the ion beam facility.

It would be like taking a drop of water from the ocean to thank my father. Whatever I am today is only because of his guidance, support, faith, and hard work. I am so grateful to my mother for her unwavering love and support. I would especially like to thank my brothers and sisters for supporting me and looking after my parents while I was away. I want to express my gratitude to my entire family for their love and emotional support. A special thank you to my lifelong wonderful supporter, for motivating me whenever I was suffering from depression. I am grateful that you have always been there for me. Thank you for being by my side whenever I needed it. I will always remain grateful to you for your mental support and guidance in every step of my life. My friends are no less than my family, motivated and helped me a lot in this journey. GANESHA, the strength of my life, thank you for removing all the obstacles and I need your blessings till my last breath. I would like to thank everything present in the universe for giving me positive energy.



## ABSTRACT

Titania ( $\text{TiO}_2$ ) is a wide bandgap semiconductor that has paid noticeable attention because of its potential applications in day-to-day life. It can also drive fundamental research along with applications in high-efficiency energy harvesting, integrated circuits in photonics, and optoelectronic devices for sensing. This thesis focused on the utilization of defects in various applications related to bandgap engineering of rutile  $\text{TiO}_2$  nanorod-composed microflower structures. A pure rutile phase of  $\text{TiO}_2$  microflowers was synthesized using a cost-effective hydrothermal method. Depending on the need, defects are desirable to tune the photonic, phononic, and magnetic properties of  $\text{TiO}_2$ . Therefore, we intentionally created defects in  $\text{TiO}_2$  by doping different elements through ion implantation technique and chemical method. Further, the noble metal (Au) is decorated over the  $\text{TiO}_2$  surface to create a metal-semiconductor junction. The selection of the dopant was on its atomic radii and metallicity so that it can create various kinds of defects. In the first part of the thesis, we doped  $\text{TiO}_2$  with C, which is a lighter ion and non-metallic. It is observed that the C ion implantation creates oxygen vacancy in the  $\text{TiO}_2$  matrix that increases the population of electrons in the conduction band enhancing the conductivity. We studied the physics of the Fano effect and the impact of dopant on the Fano asymmetry parameter which is related to electron-phonon interaction. In addition, the ferromagnetism observed in intrinsic defected  $\text{TiO}_2$  and C ion implanted  $\text{TiO}_2$  are studied experimentally with support from theoretical DFT calculations. In the second part,  $\text{TiO}_2$  is doped with Si, which is semiconducting. The low-energy Si ion affects the morphology of the sample. It has been observed that the tip of the nanorod is slightly changed at the highest fluence implanted sample, but at lower fluence, it remains unaffected. However, it does not affect the crystallinity property significantly. The defects created in this case also tune the bandgap with ion fluences. In the third part, we doped  $\text{TiO}_2$  with Cu, a medium-sized metallic ion, and studied the physics of the anharmonic effect. The linear and nonlinear optical properties are investigated with a noticeable saturable absorption, which is mainly attributed to the defect states. In the fourth part of the thesis, a metallic heavier ion, Au is doped by ion-implantation technique. It is observed that the surface morphology of the samples gets deformed at higher fluence due to strong electron-phonon coupling, which produces high temperatures up to 3500 K for a short

time scale of pico-second. This is a useful method to join two or more nanowires/ nanoscale materials and can be considered as a nano-welding technique. In the last part, we decorated  $\text{TiO}_2$  microflower surface with the noble metal Au. The charge transfer mechanisms and plasmonic enhancement effect have been investigated by studying the photocatalytic activity using Raman spectroscopy. The surface plasmonic resonance, photothermal effect, and carrier trapping by defect states enhance the photocatalytic property. The thermal activation modified the crystal structure at the interface of the Au nanoparticles and  $\text{TiO}_2$  that tune the Fano effect which is investigated through Raman spectra. It has been demonstrated that the charge carrier supplied from the Au nanoparticles to the conduction band of  $\text{TiO}_2$  enhances the Fano asymmetry parameter. In conclusion, the defects created in the  $\text{TiO}_2$  matrix by chemical or ion implantation introduce mid-gap states within the valence band maximum and conduction band minimum that narrow down the bandgap and tune the structural, optical, and magnetic properties of  $\text{TiO}_2$  microflowers, which can be suitable optoelectronic device applications.

# List of Abbreviations

FESEM	Field emission scanning electron microscope
TEM	Transmission electron microscope
HRTEM	High-resolution transmission electron microscopy
EDS	Energy dispersive spectroscopy
XRD	X-ray diffraction
UV	Ultraviolet
PL	Photoluminescence
DFT	Density functional theory
DOS	Density of states
RT	Room temperature
NP	Nanoparticle
VB	Valence band
CB	Conduction band
$E_g$	Bandgap
$E_F$	Fermi level/energy
SQUID	Superconducting Quantum Interference Devices

# Contents

<b>List of Figures</b>	1
<b>List of Tables</b>	8
<b>Chapter 1 Introduction</b>	9
1.1 TiO <sub>2</sub> : A promising wide bandgap semiconductor . . . . .	11
1.1.1 Crystal structure . . . . .	11
1.1.2 Electronic structure . . . . .	12
1.1.3 Linear optical properties . . . . .	13
1.1.4 Nonlinear optical properties . . . . .	14
1.1.5 Vibrational properties (Raman spectroscopy) . . . . .	14
1.1.6 Magnetic properties . . . . .	16
1.2 Defects in TiO <sub>2</sub> . . . . .	16
1.3 Doping in TiO <sub>2</sub> . . . . .	18
1.4 Defect induced Fano asymmetry . . . . .	20
1.5 Theme of the thesis . . . . .	22
<b>References</b>	27
<b>Chapter 2 Experimental methods and Characterization techniques</b>	34
2.1 Sample preparation . . . . .	34
2.1.1 Substrate cleaning . . . . .	34
2.1.2 Seed layer preparation . . . . .	35
2.1.3 Hydrothermal growth of TiO <sub>2</sub> microflowers . . . . .	35
2.2 Ion implantation . . . . .	36
2.3 Au deposition . . . . .	38
2.4 Charactrization techniques . . . . .	39
2.4.1 Field emission scanning electron microscopy (FESEM) . . . . .	39
2.4.2 Transmission electron microscopy (TEM) . . . . .	41



2.4.3	Energy-dispersive X-ray spectroscopy (EDS)	42
2.4.4	X-ray diffraction (XRD)	43
2.4.5	X-ray photoelectron spectroscopy (XPS)	45
2.4.6	Inductively Coupled Plasma Optical Emission Spectroscopy (ICP-OES)	46
2.4.7	Raman spectroscopy	46
2.4.8	Photoluminescence spectroscopy (PL)	49
2.4.9	Ultraviolet-Visible-Near infrared spectroscopy	50
2.4.10	Z-scan technique	53
2.4.11	Superconducting quantum interference device	54
<b>References</b>		<b>56</b>
 <b>Chapter 3 Defect assisted Fano effect and magnetism in C ion implanted rutile TiO<sub>2</sub></b>		
	<b>TiO<sub>2</sub></b>	<b>59</b>
3.1	Introduction	59
3.2	Experimental details	60
3.3	Ion beam simulations	61
3.4	Morphological, elemental, and structural studies	62
3.4.1	FESEM, TEM, and elemental mapping	62
3.4.2	XRD	63
3.5	Optical studies	65
3.5.1	UV-visible spectroscopy	65
3.6	Raman spectroscopy and Fano asymmetry	67
3.6.1	Conclusion on Fano asymmetry	72
3.7	Ferromagnetism (FM) in C ion implanted TiO <sub>2</sub>	73
3.8	Theoretical studies	75
3.8.1	Conclusions on ferromagnetism	79
<b>References</b>		<b>80</b>

---

<b>Chapter 4</b>	<b>Bandgap tuning in Si implanted TiO<sub>2</sub> microflowers</b>	<b>86</b>
4.1	Introduction . . . . .	86
4.2	Experimental details . . . . .	87
4.3	Ion beam simulations . . . . .	87
4.4	Characterizations and analysis . . . . .	88
4.4.1	FESEM . . . . .	88
4.4.2	XRD . . . . .	88
4.4.3	Raman spectroscopy . . . . .	90
4.4.4	UV-visible spectroscopy . . . . .	92
4.4.5	Photoluminescence (PL) spectroscopy . . . . .	94
4.5	Conclusions . . . . .	95
	<b>References</b>	<b>96</b>
<b>Chapter 5</b>	<b>Impact of Cu doping on linear, nonlinear properties, and anharmonicity of TiO<sub>2</sub> microflowers</b>	<b>98</b>
5.1	Introduction . . . . .	98
5.2	Experimental details . . . . .	99
5.3	Elemental, morphological, and structural studies . . . . .	100
5.3.1	ICP-OES . . . . .	100
5.3.2	FESEM . . . . .	101
5.3.3	EDS . . . . .	102
5.3.4	XRD . . . . .	102
5.3.5	TEM . . . . .	103
5.3.6	XPS . . . . .	104
5.4	Optical studies . . . . .	106
5.4.1	Photoluminescence . . . . .	106
5.4.2	UV-visible spectroscopy . . . . .	108
5.5	DFT calculations . . . . .	109
5.6	NLO studies . . . . .	112
5.7	Conclusion on nonlinear optical properties . . . . .	116

5.8	Anharmonicity and phonon lifetime from Raman spectroscopy . . . . .	117
5.9	Conclusions on phonon anharmonicity and lifetime . . . . .	123
<b>References</b>		125
 <b>Chapter 6    Nanoscale welding and melting of TiO<sub>2</sub> naorods by 30 keV Au ion beams</b>		
		131
6.1	Introduction . . . . .	131
6.2	Experimental details . . . . .	132
6.3	Ion beam simulations . . . . .	133
6.4	Morphological, elemental, and structural studies . . . . .	134
6.4.1	FESEM . . . . .	134
6.4.2	EDS . . . . .	135
6.4.3	XRD . . . . .	136
6.4.4	TEM . . . . .	137
6.5	Optical studies . . . . .	138
6.5.1	UV-visible and Raman spectroscopy . . . . .	138
6.6	The unified thermal spike model . . . . .	139
6.7	Effect of melting on TiO <sub>2</sub> junctions . . . . .	142
6.8	Conclusions . . . . .	144
<b>References</b>		145
 <b>Chapter 7    Photocatalytic activity of Au decorated TiO<sub>2</sub> microflowers</b>		
		148
7.1	Introduction . . . . .	148
7.2	Experimental details . . . . .	149
7.3	Morphological, elemental, and structural studies . . . . .	150
7.3.1	FESEM and EDS . . . . .	150
7.3.2	XRD and TEM . . . . .	151
7.4	Optical studies . . . . .	152
7.4.1	UV-visible spectroscopy and PL spectroscopy . . . . .	152
7.4.2	Raman spectroscopy . . . . .	154

7.5	XPS . . . . .	154
7.6	Photocatalytic performance analysis . . . . .	156
7.6.1	Proposed Mechanism . . . . .	160
7.7	Observation of Fano effect . . . . .	162
7.8	Conclusions . . . . .	164
<b>References</b>		<b>166</b>
<b>Chapter 8 Summary and future prospects</b>		<b>172</b>
8.1	Summary . . . . .	172
8.2	Future prospects . . . . .	179

# List of Figures

1.1	Schematic of energy level diagram for intrinsic and extrinsic semiconductor.	10
1.2	Crystal structure of unit cell of $\text{TiO}_2$ showing edge sharing and corner-sharing as observed from two different directions. . . . .	12
1.3	(a) Electronic band structure of pure $\text{TiO}_2$ . The density of states plot shows the bandgap of (a) pure $\text{TiO}_2$ and (b) defective $\text{TiO}_2$ . . . . .	13
1.4	Raman spectra of rutile $\text{TiO}_2$ with the schematic of different vibrational modes. . . . .	15
1.5	(a) Schematic showing origin of Fano asymmetry. (b) Asymmetry in Raman line shape. . . . .	21
1.6	Schematic representation of the theme of the thesis: Physics of Fano effect to photocatalytic application. . . . .	23
2.1	Schematic representation of $\text{TiO}_2$ microflower preparation method. . . . .	36
2.2	Schematic representation of ion beam implanter. . . . .	37
2.3	Schematic representation of ion implantation in $\text{TiO}_2$ microflowers. . . . .	38
2.4	Schematic of Au decoration over $\text{TiO}_2$ microflowers. . . . .	39
2.5	Schematic diagram of FESEM. . . . .	40
2.6	Schematic diagram of TEM. . . . .	41
2.7	(a) Schematic representation x-ray generation. (b) EDS spectra showing different elements. . . . .	43
2.8	Schematic of X-ray diffractometer with Bragg's diffraction. . . . .	44
2.9	Schematic representation of (a) XPS instrument (b) XPS photoemission process. . . . .	45
2.10	Schematic diagram of Raman spectrometer and vibrational energy level showing three types of scattering phenomena. . . . .	47
2.11	Schematic of PL emission for direct and indirect bandgap semiconductors. The dotted arrow represents non-radiative recombination and the solid arrow represents radiative recombination. . . . .	50

2.12	Ray diagram for UV-visible spectrometer for (a) transparent sample (b) opaque sample (Diffuse reflectance spectrometer). . . . .	51
2.13	Tauc plot for $\text{TiO}_2$ with the corresponding absorbance spectra in the inset. .	52
2.14	Schematic of Z-scan setup: ( $M_1, M_2$ ) mirrors; (HWP) half-wave plate; (PBS) polarizing beam splitter; ( $D_1$ ) reference detector; (L) lens; (S) sample; (A) aperture; ( $D_2$ ) signal photodetector. . . . .	53
3.1	(a) Depth profile of 1.5 MeV C ion in $\text{TiO}_2$ matrix with schematic in the inset. (b) Ti and O vacancy created due to 1.5 MeV C ion implantation. (c) Displacement per atom with depth for C ion implanted $\text{TiO}_2$ . . . . .	62
3.2	(a,b) FESEM image (c,d) HRTEM image with the corresponding low magnified image in the inset of pristine and $2 \times 10^{16}$ ions/cm <sup>2</sup> C implanted $\text{TiO}_2$ , respectively. (e-h) FESEM image and corresponding elemental mapping for $2 \times 10^{16}$ ions/cm <sup>2</sup> C implanted $\text{TiO}_2$ . . . . .	62
3.3	(a) XRD pattern pristine and C ion implanted $\text{TiO}_2$ . (b) Magnified view of (110) peak. (c) Variation crystallite size and FWHM with fluence. . . . .	64
3.4	(a) Kubelka-Munk function plotted against wavelength for pristine and C ion implanted $\text{TiO}_2$ . (b) Variation of bandgap (left panel) and Urbach energy (right panel) with C ion fluence. . . . .	66
3.5	Raman spectra of pristine and C ion implanted $\text{TiO}_2$ (a) in the range 150-850 cm <sup>-1</sup> (b) in the range 1200-1800 cm <sup>-1</sup> . (c) Raman spectra of $E_g$ mode showing the calculation of asymmetry ratio. (d) Variation of asymmetric ratio with C ion fluence for $E_g$ and $A_{1g}$ mode. . . . .	67
3.6	$E_g$ vibrational mode of (a) Pristine (b) $1 \times 10^{15}$ and (c) $5 \times 10^{15}$ ions/cm <sup>2</sup> C ion implanted $\text{TiO}_2$ fitted with equation (3.7). (d) Variation of $ 1/q $ with ion fluence for $E_g$ and $A_{1g}$ mode. (e) Theoretically plotted BWF function with varying asymmetry parameters for $E_g$ mode. . . . .	70
3.7	(a) Temperature dependent Raman spectra of pristine $\text{TiO}_2$ showing $E_g$ and $A_{1g}$ mode. (b) Variation of $ 1/q $ with temperature for $E_g$ and $A_{1g}$ mode of pristine $\text{TiO}_2$ . (c) Variation of $ 1/q $ with temperature for $1 \times 10^{15}$ and $2 \times 10^{16}$ ions/cm <sup>2</sup> C ion implanted $\text{TiO}_2$ . . . . .	72

3.8	(a) Room temperature magnetic moment vs magnetic field with the magnified view of the dotted rectangular area in the inset. (b) Variation of the coercive field with temperature. . . . .	74
3.9	Crystal structure of $\text{TiO}_2$ . (a) Pristine structure, with Ti, and with O vacancy. Blue balls represent Ti atom and red balls represent O atom. The spin-polarized total density of states of $\text{TiO}_2$ (b) Pristine structure (c) with Ti vacancy, (d) with O vacancy. (e) The corresponding partial density of states of $\text{TiO}_2$ with oxygen vacancy. . . . .	76
3.10	Crystal structure of $\text{TiO}_2$ with (a) oxygen vacancy and C at an interstitial site near the O vacancy, (b) oxygen vacancy and C at interstitial region far from oxygen vacancy, (c) C replacing the Ti atom, and (d) C replacing the O atom. (e) The spin-polarized total density of states for structure (a). The corresponding partial density of states of (f) Ti 3d, (g) O 2p, and (h) C 2p orbitals. . . . .	78
3.11	Crystal structure of C implanted rutile $\text{TiO}_2$ with oxygen vacancy (a) before (b) after structural relaxation. (c) Charge density difference of the relaxed $\text{TiO}_2$ . . . . .	79
4.1	(a) Depth profile (b) Vacancy plot for 30 keV Si ion in $\text{TiO}_2$ . . . . .	88
4.2	FESEM images of pristine and Si ion implanted $\text{TiO}_2$ . . . . .	89
4.3	(a) XRD pattern of pristine and Si implanted $\text{TiO}_2$ . (b) Variation of crystallite size and strain with Si ion fluence. . . . .	90
4.4	(a) Raman spectra of pristine and Si implanted $\text{TiO}_2$ . (b) Variation of peak position and FWHM with Si ion fluence. . . . .	91
4.5	Tauc plot for pristine and Si ion implanted $\text{TiO}_2$ . . . . .	92
4.6	Variation of phonon lifetime and bandgap with Si ion fluence. . . . .	93
4.7	(a) PL spectra of pristine and Si ion implanted $\text{TiO}_2$ . (b) Deconvoluted PL spectra of pristine $\text{TiO}_2$ . (c) Schematic diagram showing the origin of PL emissions and defect states. The dashed arrow mark represents nonradiative transition and the solid arrow mark represents radiative transition. . . . .	94

5.1	Top view FESEM image of TiO <sub>2</sub> microflower on (a) glass substrate (b) silicon substrate. . . . .	101
5.2	(a) FESEM image of 10% Cu doped TiO <sub>2</sub> microflower and the corresponding elemental mapping of (b) Ti, (c) O, and (d) Cu. . . . .	102
5.3	(a) XRD pattern of pristine and Cu doped TiO <sub>2</sub> microflowers. (b) Variation of 2 $\theta$ and crystallite size with Cu concentration. . . . .	103
5.4	(a) TEM images of pristine TiO <sub>2</sub> . (b) HRTEM image of pristine TiO <sub>2</sub> . (c) Schematic of the lattice diagram showing (110) plane for pristine TiO <sub>2</sub> . HRTEM images of (d) 6% Cu and (e) 8% Cu doped TiO <sub>2</sub> . (f) Schematic of the lattice diagram showing (110) Cu doped TiO <sub>2</sub> . . . . .	104
5.5	High resolution XPS spectra of (a) Ti 2p of undoped and 6% Cu: TiO <sub>2</sub> (b) O 1s of undoped TiO <sub>2</sub> (c) O 1s of 6% Cu:TiO <sub>2</sub> (d) Cu 2p of 6% Cu:TiO <sub>2</sub> . . . . .	105
5.6	(a) PL spectra of undoped and Cu doped TiO <sub>2</sub> . (b) Variation of integrated intensity with Cu concentration. (c) Deconvoluted PL spectra of undoped TiO <sub>2</sub> . (d) Schematic diagram showing the origin of PL emissions. . . . .	107
5.7	(a) Absorbance spectra of undoped and Cu doped TiO <sub>2</sub> . (b) Variation of bandgap with Cu concentration. . . . .	110
5.8	Band structure for (a) undoped (b) Cu doped TiO <sub>2</sub> . DOS plot for (c) undoped (d) Cu doped TiO <sub>2</sub> with their corresponding crystal structure in the inset. Dashed line at energy zero corresponds to the Fermi level. . . . .	111
5.9	Open-aperture (OA) Z-scan curves at 532 nm the excitation wavelength for the TiO <sub>2</sub> with different Cu concentrations (a) undoped (b) 2% Cu doped (c) 4% Cu doped (d) 6% Cu doped (e) 8% Cu doped (f) 10% Cu doped TiO <sub>2</sub> fitted with equation 5.2. . . . .	113
5.10	Close-aperture (CA) Z-scan curves at 532 nm the excitation wavelength for the TiO <sub>2</sub> with different Cu concentrations (a) undoped (b) 2% Cu doped (c) 4% Cu doped (d) 6% Cu doped (e) 8% Cu doped (f) 10% Cu doped TiO <sub>2</sub> fitted with equation 5.3. . . . .	115
5.11	Variation of FOM and n <sub>2</sub> with Cu concentration . . . . .	116



5.12	(a) Raman spectra of pristine and Cu doped TiO <sub>2</sub> . Temperature-dependent Raman spectra of (b) pristine (c) 8% Cu doped TiO <sub>2</sub> . (d) Variation FWHM with temperature fitted with equation 5.5. (e) Variation of Phonon lifetime with temperature for undoped and Cu doped TiO <sub>2</sub> . . . . .	118
5.13	(a) Magnified view of E <sub>g</sub> mode of undoped TiO <sub>2</sub> . (b) Variation of asymmetry parameter with temperature. . . . .	119
5.14	Experimental and theoretical fitted curve (solid lines) of Raman peak position of (a) E <sub>g</sub> mode (b) A <sub>1g</sub> mode of pristine and Cu TiO <sub>2</sub> . . . . .	121
5.15	Experimental and theoretical fitted curve (solid lines) of Raman peak position of (a) E <sub>g</sub> mode (b) A <sub>1g</sub> mode of R-TiO <sub>2</sub> . Phonon lifetime of pristine and Cu doped TiO <sub>2</sub> (c) E <sub>g</sub> mode (d) A <sub>1g</sub> mode. (e) Schematic representation of phonon scattering. . . . .	122
6.1	(a) Ti and O vacancy plot, (b) Atomic % of Au and (c) DPA for various fluence with depth for 30 keV Au ion implanted TiO <sub>2</sub> . . . . .	134
6.2	FESEM image of (a) pristine (inset shows FESEM image of pristine TiO <sub>2</sub> annealed at 800 <sup>0</sup> C) (b) 5 × 10 <sup>15</sup> (c) 1 × 10 <sup>16</sup> , and (d) 2 × 10 <sup>16</sup> ions/cm <sup>2</sup> Au implanted TiO <sub>2</sub> . . . . .	134
6.3	(a) FESEM image of 2 × 10 <sup>16</sup> ions/cm <sup>2</sup> Au implanted TiO <sub>2</sub> with the corresponding elemental mapping of Ti, O, and Au in (b-d) respectively. (e) EDS spectra for pristine and 2 × 10 <sup>16</sup> ions/cm <sup>2</sup> Au implanted TiO <sub>2</sub> . (f) Variation of atomic % of Au with ion fluence. . . . .	136
6.4	(a) XRD pattern of pristine and Au implanted TiO <sub>2</sub> . (b) Variation of crystallite size and microstrain with ion fluence. . . . .	136
6.5	(a) TEM image of 2 × 10 <sup>6</sup> ions/cm <sup>2</sup> Au implanted TiO <sub>2</sub> . (b) HRTEM image of the area bounded by red square in (a). (c) Au cluster size distribution. . . . .	138
6.6	(a) Variation of bandgap with Au ion fluence. (b) Raman spectra of pristine and Au ion implanted TiO <sub>2</sub> . (c) Variation of force constant with ion fluence. . . . .	139
6.7	Lattice temperatures at several radii from a 30 keV Au ion trajectory in TiO <sub>2</sub> . . . . .	141
6.8	FESEM image of pristine and Au ion implanted TiO <sub>2</sub> having different structures. . . . .	142

6.9	FESEM image of $2 \times 10^{16}$ ions/cm <sup>2</sup> Au implanted TiO <sub>2</sub> showing melting and welding of nanorods of two different flowers. . . . .	143
7.1	FESEM image of (a) TA-0 (b) TA-2 (c) TA-4 (d) TA-6. (e-h) FESEM image of TA-4 with the corresponding elemental mapping of Ti, O, and Au. (i) Variation of atomic % of Au with Au thickness. . . . .	150
7.2	XRD pattern of pristine and Au-decorated TiO <sub>2</sub> . . . . .	151
7.3	(a) TEM image of TA-4 sample. (b) Magnified view of the yellow encircled area of (a). Lattice fringes of (c) TiO <sub>2</sub> and (d) Au with corresponding FFT pattern in the inset. . . . .	152
7.4	(a) Absorption spectra (b) Magnified image of the dashed square area of figure 7(a). (c) Tauc plot, and (d) PL spectra of pristine and Au decorated TiO <sub>2</sub> samples. . . . .	153
7.5	(a) Raman spectra (b) Stoke anti-Stokes measurement (c) Raman peak shift (left panel) and laser-induced localized temperature (right panel) for pristine and Au decorated samples. . . . .	155
7.6	(a) XPS survey spectra of TA-0 and TA-4 .(b) Ti 2p region of TA-0 .(c) Ti 2p, (d) Au 4f region of TA-4. . . . .	155
7.7	Photocatalytic degradation of samples (a) Observed Raman peak intensity with exposure of 325 nm laser on TA-4. (b) Plot of $\ln \frac{C_0}{C_t}$ with time fitted with first order kinetics equation (1) and $\frac{C_t}{C_0}$ with time plot is presented in the inset for TA-2, TA-4, and TA-6 samples. . . . .	157
7.8	Photocatalytic degradation of samples (a) Observed Raman peak intensity with exposure of 532 nm laser source on TA-4. (b), (c), and (d) plot of $\ln \frac{C_0}{C_t}$ with time fitted with first order kinetics equation (1) and $\frac{C_t}{C_0}$ with time plot is presented in the inset for TA-2, TA-4, and TA-6 samples respectively for 532 nm laser source and white light . . . . .	159
7.9	Schematic of charge transfer under UV and visible light irradiation. . . . .	160
7.10	(a) FESEM image (b) HRTEM image of TA-4@800. (c) UV-visible absorbance spectra. (d) Raman spectra and (e) asymmetry parameter for TA-0, TA-0@800 and TA-4@800 samples. . . . .	163

8.1	(a) Variation of bandgap with dopant element of increasing atomic number.(b) Variation of bandgap with ion fluence for C, Si, Au ion implanted TiO <sub>2</sub> . (c) Variation of bandgap with Cu molar concentration. (d) Bandgap variation in Au decorated samples. . . . .	178
-----	--	-----

# List of Tables

3.1	$2\theta$ , dislocation density, and strain calculated from XRD . . . . .	64
4.1	Obtained values of FWHM ( $E_g$ mode), phonon lifetime, and bandgap for the pristine and Si implanted $\text{TiO}_2$ . . . . .	91
5.1	Initial and actual percentage of Cu in doped $\text{TiO}_2$ . . . . .	100
5.2	Obtained PL peak positions from literature and our measurements for Cu doped $\text{TiO}_2$ . . . . .	108
5.3	Obtained values of $\beta$ , $n_2$ and FOM for the pristine and Cu doped $\text{TiO}_2$ . . .	114
6.1	The parameters of $\text{TiO}_2$ used for the thermal spike calculation taken from ref [21] . . . . .	142
7.1	Value of $k$ ( $\text{min}^{-1}$ ) under 325 nm, 532 nm lase laser source and white light exposure . . . . .	158

# Chapter 1

## Introduction

Semiconductors are the foundation of modern electronics including transistors, solar cells, light-emitting diodes (LEDs), and digital and analog integrated circuits. As a crucial component for high-performance optoelectronic and electronic device applications, wide-band-gap semiconductors (WBS) have gained high demand[1]. WBS belongs to a class of semi-conducting materials whose bandgap is greater than conventional semiconductors such as Si (1.1 eV) and Ge (0.7 eV). Typically the WBS have bandgaps in the range above 2 eV and have electronic properties that fall in between those of conventional semiconductors and insulators. The larger bandgap, low intrinsic carrier concentration, and high breakdown voltage allow the WBS-based devices to be operated at much higher voltage, frequency, and temperature (over 300<sup>o</sup> C)[2]. Its large bandgap enables the fabrication of short-wavelength LEDs and lasers. Examples of some wide bandgap semiconductors are SiC, GaN, ZnO, AlN, ZnSe, and TiO<sub>2</sub> [3–5]. Among WBS, oxide WBS are of special interest due to their oxygen deficiency and interstitial defects that help in the formation of p or n-type semiconductors for better applications, without any other elemental doping. The oxide semiconductors such as TiO<sub>2</sub>, ZnO, and SnO<sub>2</sub> can be synthesized using cost-effective methods such as hydrothermal and sol-gel techniques. Each material offers certain advantages over the other. Again, the intrinsic semiconductors have low electrical conductivity due to fewer free charge carriers, which is a serious problem for their use in optoelectronic devices.

Doping is the process of adding impurities into intrinsic semiconductors intentionally to alter their electrical, optical, magnetic, and structural properties. The doped semiconductors

are known as extrinsic semiconductors. After doping, the semiconductor can be either n-type or p-type depending upon the nature of the dopants. The energy level diagram for intrinsic and extrinsic semiconductors (both n and p-type) is schematically presented in Figure 1.1. The dopant atoms introduce allowed energy states within the bandgap which is very close to the either valence band (VB) or conduction band (CB). The electron donor impurities create states near the CB while electron acceptor impurities create states near the VB. At a high level of n (p) type dopant concentration, the impurity band merges with the CB (VB), which is responsible for bandgap narrowing. In addition to this, the dopant ions create defects and enhance the electrical conductivity of the semiconductors.

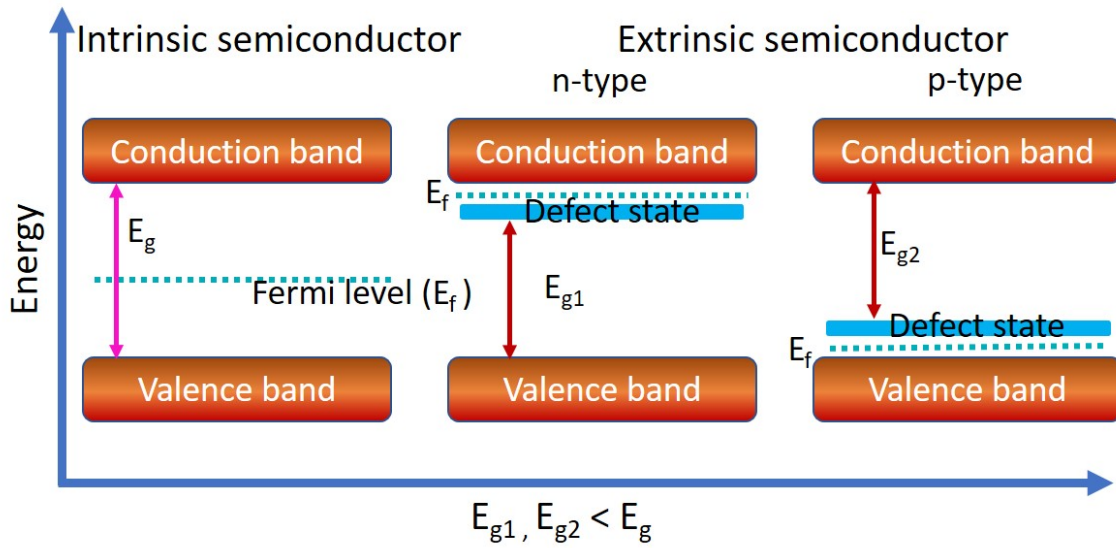


Figure 1.1: Schematic of energy level diagram for intrinsic and extrinsic semiconductor.

This thesis is dedicated to the rutile phase of  $\text{TiO}_2$ , which is a wide bandgap semiconductor. Here the effect of dopants on the structural, optical, and magnetic properties along with some basic concepts of physics for different applications are investigated.

## 1.1 TiO<sub>2</sub>: A promising wide bandgap semiconductor

Titanium oxide (TiO<sub>2</sub>) also known as titania is a wide bandgap semiconductor. It can exist in amorphous as well as crystalline forms. There are mainly three crystalline phases of TiO<sub>2</sub> named rutile, anatase, and brookite having optical bandgaps 3.02 eV, 3.2 eV, and 2.96 eV, respectively[6]. Among the three crystalline phases, the rutile phase is the stable phase, and the other two phases are metastable phases that can be converted to the rutile phase under thermal treatment. In addition, the rutile phase of TiO<sub>2</sub> has a high refractive index, higher photo-corrosion resistance, thermally stable, chemically inert, non-toxic, and cost-effective[7]. There exist several shapes and structures of TiO<sub>2</sub> nanostructures such as nanorods, nanoflowers, thin films, nanoparticles, nanotubes, nanosheets, nanowires, etc. In this thesis, we have focused on the rutile phase of TiO<sub>2</sub> microflowers, which are composed of individual nanorods. The flower-like structures enhance the performance of the photocatalytic effect, used as photoanode in dye-sensitized solar cells (DSSC) and supercapacitors to improve efficiency owing to its high surface area and light scattering property[8–10]. For dielectric and antireflective applications, rutile TiO<sub>2</sub> is a good material since it is thermodynamically more stable and has a higher refractive index than the other phases[11]. The properties of the TiO<sub>2</sub> can be varied by creating defects through doping and creating heterostructure and can be made suitable for its use in a wide range of applications such as pigments, photocatalysis, photovoltaics, sensors, optoelectronic and spintronic devices[7, 12, 13]. The general properties of rutile TiO<sub>2</sub> are discussed in the following subsections.

### 1.1.1 Crystal structure

The crystal structure of the rutile phase of TiO<sub>2</sub> is tetragonal with lattice parameters  $a=b=4.60$  Å,  $c=2.96$  Å, and  $\alpha=\beta=\gamma = 90^\circ$ . It belongs to space group P42/mnm. The unit cell of rutile TiO<sub>2</sub> contains 6 atoms (2 Ti and 4 O atoms). Each Ti<sup>4+</sup> ion is surrounded by six O<sup>2-</sup> ions

to form an octahedral structure and each O atom is coordinated to three Ti atoms. The octahedrons are linked with each other through edge-sharing and corner-sharing to form the  $\text{TiO}_2$  crystal. In a unit cell, an octahedron is in contact with ten neighbor octahedrons (two sharing edge oxygen pairs and eight sharing corner oxygen atoms). The crystal structure of rutile  $\text{TiO}_2$  as observed from two different directions is shown in Figure 1.2 designed using VESTA software[14]. The edge-sharing and corner-sharing of  $\text{TiO}_6$  octahedral is visible in the Figure.

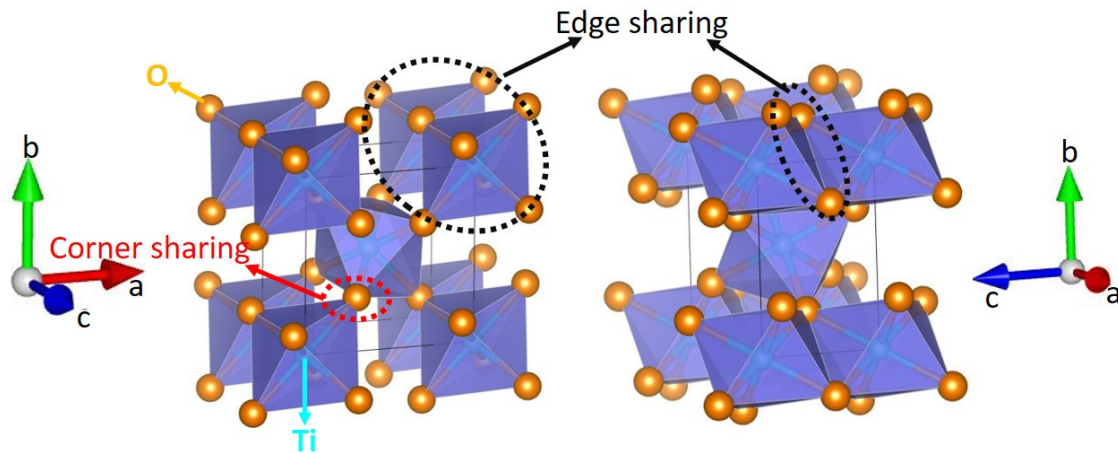


Figure 1.2: Crystal structure of unit cell of  $\text{TiO}_2$  showing edge sharing and corner-sharing as observed from two different directions.

### 1.1.2 Electronic structure

As in the earlier section, it is discussed that  $\text{TiO}_2$  is a wide bandgap semiconductor, the VB and CB are separated by 3.02 eV. The electronic band structure of rutile  $\text{TiO}_2$  is displayed in Figure 1.3(a). The VB describes a state of electrons that are tightly bound to the atomic nuclei whereas the CB reflects the electrons escaped from the materials to move entirely free in the crystal lattice. The contribution of orbitals of titanium and oxygen towards the formation of CB and VB can be observed from the density of states plot as shown in Figure



1.3(b). The CB is dominated by titanium 3d electron states and the VB is dominated by the oxygen 2p electron states. The energy difference between the top of the VB band and the bottom of CB is referred as the bandgap ( $E_g$ ). When a defect is introduced in the  $\text{TiO}_2$  lattice, the states associated with a defect are created in the bandgap region as shown in Figure 1.3(c).

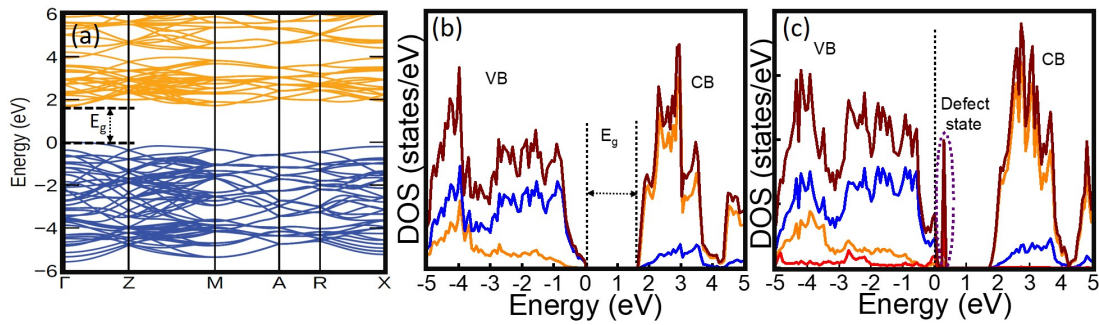


Figure 1.3: (a) Electronic band structure of pure  $\text{TiO}_2$ . The density of states plot shows the bandgap of (a) pure  $\text{TiO}_2$  and (b) defective  $\text{TiO}_2$ .

### 1.1.3 Linear optical properties

When broadband or monochromatic light is incident on  $\text{TiO}_2$ , the light may get absorbed, transmitted, or reflected. The electrons in the VB absorb the energy and get excited to the CB when the energy of the incident light is the same or greater than the bandgap of  $\text{TiO}_2$ . In this process, the electrons are populated in the CB and holes remain in the VB. These are called photogenerated carriers. The photogenerated electrons in the CB are not stable, so they deexcited to the VB and undergo recombination releasing energy in the form of photon. The energy of the emitted photon can be analyzed using photoluminescence spectroscopy.

When matter absorbs broadband light, the electrons get excited from the ground state to the excited state. The difference in the energies of the ground state and the excited state of the electron is always equal to the amount of UV or visible light absorbed by it. This

absorption can be witnessed using UV-visible spectroscopy.

When defect states are present in the sample, the electron excitation and recombination through the defect states can be noticed in both UV-visible and PL spectroscopy, which is normally denoted as linear optical properties.

### 1.1.4 Nonlinear optical properties

Along with the linear optical properties, TiO<sub>2</sub> possesses nonlinear optical properties. It has been reported that the origin of nonlinearity in TiO<sub>2</sub> is due to the hyperpolarizability of Ti-O pairs[15]. When light incident on a dielectric material, the material gets polarized. If the intensity of light is high enough, then the polarization varies non-linearly with the electric field and can be written as[16]

$$P = \epsilon_0[\chi^{(1)}E + \chi^{(2)}E^2 + \chi^{(3)}E^3 + \dots] \quad (1.1)$$

where  $\epsilon_0$  is the permittivity,  $\chi^{(i)}$  is i-th order optical susceptibility, and E is the electric field of incident light.  $\chi^{(1)}$  represents the linear susceptibility,  $\chi^{(2)}$  is the second order susceptibility which is zero in the case of TiO<sub>2</sub> as it is centrosymmetric[17]. Thus the third-order nonlinear effect is investigated in this thesis. The defects, impurities, and structural modifications can introduce new electronic state within the band structure of materials. These additional states lead to enhanced nonlinear responses compared to the perfect, defect-free crystal.

### 1.1.5 Vibrational properties (Raman spectroscopy)

The unit cell of rutile TiO<sub>2</sub> contains 6 atoms (2 Ti and 4 O) in the unit cell. It is associated with 18 vibrational modes, 15 optical, and 3 acoustical modes. The vibrational modes at  $\Gamma$  point can be described by the following irreducible representations[18]:

$$\Gamma_{opt} = A_{1g} + A_{2g} + A_{2u} + 2B_{1u} + B_{1g} + B_{2g} + E_g + 3E_u \quad (1.2)$$

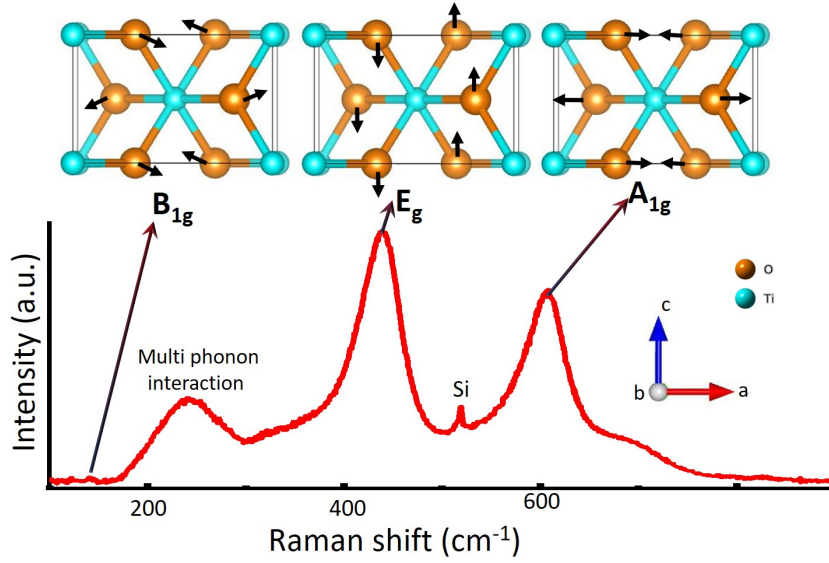


Figure 1.4: Raman spectra of rutile  $\text{TiO}_2$  with the schematic of different vibrational modes.

where the symbol g represents Raman active, and u represents infrared active mode. The modes represented with E are degenerate. For the Rutile  $\text{TiO}_2$  only  $B_{1g}$ ,  $E_g$ ,  $A_{1g}$ , and  $B_{2g}$  are the four Raman active modes[19]. The Raman peaks in rutile phase of  $\text{TiO}_2$  are positioned at  $143 \text{ cm}^{-1}$  ( $B_{1g}$ ),  $235 \text{ cm}^{-1}$  (multi phonon scattering),  $447 \text{ cm}^{-1}$  ( $E_g$ ),  $612 \text{ cm}^{-1}$  ( $A_{1g}$ ) and  $826 \text{ cm}^{-1}$  ( $B_{1g}$ )[20]. In the rutile phase, there is the only motion of anions (oxygen) with respect to the central cation (titanium). The intensity of  $B_{2g}$  is small and broad so it is not distinguished. However, the other peaks are distinguishable and the intensity of  $E_g$  and  $A_{1g}$  mode is high enough as compared to the intensity of  $B_{1g}$  mode.

In  $E_g$  mode, oxygen ions move along the C axis (out-of-plane mode) whereas, in  $B_{1g}$  and  $A_{1g}$ , the oxygen ions move perpendicular to the C axis (in-plane mode)[19]. Figure 1.4 shows the  $B_{1g}$ ,  $E_g$ , and  $A_{1g}$  vibrational modes observed using Raman spectroscopy with a schematic of their corresponding vibrations using the crystal structure.

### 1.1.6 Magnetic properties

Diluted magnetic semiconductors (DMS) have received a lot of attention because of their potential use in spintronic devices that use the charge and spin of electrons[21]. Magnetism in magnetic materials is directly related to unfilled orbitals of d or f subshells. The origin of magnetic moments in nonmagnetic materials is largely attributed to defects[22]. Generally, magnetic impurities are added to the semiconductors to study magnetic properties. When doped with magnetic materials like Fe, Co, and Ni,  $\text{TiO}_2$  exhibits room-temperature ferromagnetism[23]. The ferromagnetic nature of undoped  $\text{TiO}_2$  is studied both experimentally and theoretically in various kinds of literature[24, 25]. They reported that the origin of magnetism in undoped  $\text{TiO}_2$  is associated with defects and oxygen vacancies. Hence, the magnetic property in  $\text{TiO}_2$  can be controlled by controlling the defects in terms of oxygen vacancy. When one oxygen vacancy is created, two electrons occupy that place to maintain charge neutrality. The oxygen vacancy with two electrons is known as the F center ( $V_0 + 2e^- = F$ ). One of the two electrons tends to be captured by the  $\text{Ti}^{4+}$  ion and forms  $\text{Ti}^{3+}$  ( $\text{Ti}^{4+} + e^- = \text{Ti}^{3+}$ ) and the F center gets converted to  $F^+$ . The electronic configuration of  $\text{Ti}^{3+}$  is  $[\text{Ar}]3d^1$  and of  $F^+$  is  $1s^1$ . The exchange interaction between  $1s^1$  electron spin of  $F^+$  and  $3d^1$  of  $\text{Ti}^{3+}$  around the oxygen vacancy favors the ferromagnetism[8]. It is also reported that  $\text{Ti}^{3+}$  ions have one unpaired 3d electron that provides local moment in defective rutile  $\text{TiO}_2$  single crystal[26]. In this thesis, we have implanted low energy C ions in  $\text{TiO}_2$  to study the magnetic properties, which is originated from the ion-induced defects and oxygen vacancies.

## 1.2 Defects in $\text{TiO}_2$

Defects in  $\text{TiO}_2$  nanostructure have a great role in tuning the optical, electrical, structural, and magnetic properties. The defects can be point defects (vacancy, impurity), line defects

( dislocations), planar defects (grain boundaries ), and volume defects (lattice disorder and voids). In  $\text{TiO}_2$  some defects such as oxygen vacancy, Ti vacancy, Ti interstitials, and surface defects are created during the sample preparation procedure. However, some defects are created intentionally by introducing impurity elements. A brief description of the most common defects are as follows.

**Oxygen vacancy:** Oxygen vacancy is the most likely defect in  $\text{TiO}_2$  as the formation energy for this is less. The oxygen vacancy is responsible for n-type conductivity[27], bandgap narrowing, and occurrence of ferromagnetism in  $\text{TiO}_2$ . Oxygen vacancy is created by doping suitable elements and it also depends on the method of sample preparation.

**Interstitial defect:** This type of defect is created when an extra atom occupies the interstitial position. The extra atom may be Ti or an impurity atom. The presence of interstitial defects causes lattice distortion. In pristine  $\text{TiO}_2$  interstitial Ti defect is more common than O interstitial.

**Substitutional defect:** The substitutional defect in  $\text{TiO}_2$  arises due to the substitution of Ti or O by the dopant element. Depending upon the oxidation state and ionic radius of the dopant, it is decided whether it will replace Ti or O. The impact of these defects helps in narrowing the bandgap of  $\text{TiO}_2$ .

**Dislocations defect:** Dislocation defect in  $\text{TiO}_2$  refers to a structural irregularity in the arrangement of atoms. It occurs when the regular pattern of atoms in a crystal lattice is disrupted by the presence of an extra plane of atoms, a mismatch in the alignment of atoms, or the presence of one or more extra atoms within the lattice. Dislocations significantly affect the mechanical properties of materials. Understanding and controlling dislocations are crucial in materials engineering to tailor the mechanical properties of materials for various applications.

All the above defects can be incorporated in  $\text{TiO}_2$  by doping chemically or by ion implantation.

### 1.3 Doping in TiO<sub>2</sub>

Doping is an effective method for tuning the optoelectronic properties of semiconductors. All the properties of the material rely on the electronic structure, which depends on the chemical composition, atomic arrangement, and dimensions. Dopants can change the electronic structure of the host material by introducing defects and oxygen vacancies in the crystal lattice, which could form a forbidden band. Many investigations have been done to modify the electronic band structure of TiO<sub>2</sub> by doping with transition metals (Cu, Fe, Co, Nb, Ni, Mn, Cd, Sn, V, Mo, Au, Ag etc.), semiconductors (Si), and nonmetals (C, N, S, B, F etc.)[\[28–30\]](#). The dopant can occupy three possible positions, it may substitute Ti, O, or be placed in the interstitial position. It is desirable to maintain the integrity of the crystal structure of the photocatalytic host material and to produce favorable changes in electronic structure. The main motive of doping TiO<sub>2</sub> is to tune the bandgap and the electrical conductivity by creating defects. The dopants create energy levels below conduction band minima (CBM) or above valence band maxima (VBM) depending upon their nature and tune the bandgap. Doping rutile TiO<sub>2</sub> with elements having lower valence will create more oxygen vacancy and will enhance the electronic conductivity. As TiO<sub>2</sub> is a WBS, it absorbs only UV light, which is a very small part of the solar spectrum. In addition, electron-hole recombination is faster in TiO<sub>2</sub>. The above two issues can be resolved by doping. Dopants create intra-bandgap states leading to more absorption of visible light. This new intermediate energy level can act as an electron acceptor as well as an electron donor, which ultimately allows TiO<sub>2</sub> to absorb visible light and reduces electron-hole recombination through carrier trapping.

In the case of cationic doping, depending on the oxidation state of the dopant, two different situations can appear. When a cation of lower valence than Ti<sup>4+</sup> is introduced, it acts as an electron acceptor and is referred to as p-type doping. On the other hand, the intro-

duction of cation having higher valence than  $\text{Ti}^{4+}$  acts as an n-type dopant and are electron donor. Depending on the nature of the metal dopant (ionic radius and electronegativity), it may occupy the substitutional or interstitial position. Substitutional doping of  $\text{TiO}_2$  will tend to occur when the electronegativity and ionic radius of the doping metal cations match those of  $\text{Ti}^{4+}$ . In contrast, interstitial doping will be preferred if the electronegativity of the dopant metal ions approaches that of  $\text{Ti}^{4+}$  ion and the ionic radius is smaller. On the other hand, metal ions with larger ionic radii than  $\text{Ti}^{4+}$  present lower solubility in the  $\text{TiO}_2$  lattice, which hinders their substitutional incorporation, and will be more probably found as dispersed metal oxides[31]. In metal-doped  $\text{TiO}_2$ , the cations replace titanium atoms whereas, in the non-metal-doped  $\text{TiO}_2$ , the anionic dopants are expected to substitute the oxygen atoms[31].

### **Metal doping in $\text{TiO}_2$**

The most popular metals that are doped in  $\text{TiO}_2$  are transition metals. The transition metals have partially filled d-orbitals. The dopants with different d orbital energies relative to Ti atoms shift the CBM downwards[32]. Thus, the introduction of transition metals in  $\text{TiO}_2$  creates new energy levels near the CB that lead to a narrowing of the bandgap of  $\text{TiO}_2$ . In addition, metal doping reduces the recombination rate of photogenerated electron-hole pairs.

### **Non-metal doping in $\text{TiO}_2$**

Non-metal doping of  $\text{TiO}_2$  also leads to changes in the electronic band structure, resulting in a smaller bandgap energy value, and thus an improved response in the visible light. The most frequently used non-metals for doping in  $\text{TiO}_2$  are C, N, and S. These elements have p electrons. Generally, the introduction of dopants with different p orbital energies relative to the O atom shifts the VBM upwards.

Ion implantation is one of the versatile techniques for doping different ions in any solid materials. In this technique, the dopants can be inserted to the desired depth by playing with the ion energy. The depth of the dopant ions can be regulated by selecting the energy of the ions. A desired concentration of dopants can be inserted into the target material by using this technique. In the case of doping by chemical method, some residue of the chemicals may left in the material, however, this is not an issue with ion implantation. This technology plays a vital role in modern semiconductor fabrication, allowing for the creation of intricate and high-performing electronic components.

In this thesis,  $\text{TiO}_2$  is doped with noble metal (Au), transition metal (Cu), semiconductor (Si), and nonmetal (C) using chemical methods and ion implantation.

## 1.4 Defect induced Fano asymmetry

The electron-phonon interaction in semiconductors plays an important role in electronic and optoelectronic device applications[33]. The Fano effect, which can be understood through electron-phonon coupling, in semiconductors originates from the interference of the electronic continuum with discrete phonons[34, 35]. The Fano asymmetry is schematically presented in Figure 1.5(a) and the asymmetry observed in the Raman line shape is presented in Figure 1.5(b). The continuum state is achieved in semiconductors with heavy doping or photo-excitation, and the phonons provide the discrete state [34–37]. It can be observed in semiconductors only when the energy of a discrete state lies within the electronic continuum range. In general, the acoustic phonon interacts with intraband electronic transitions, while optical phonons interfere with interband electronic transitions[38]. Varying electronic continuum the electron-phonon interaction can be tuned. Many metamaterials, nanostructures, and semiconductors including CdTe,  $\text{SrTiO}_3$ , and  $\text{Ca}_x\text{Sr}_{1-x}\text{TiO}_3$ , Si, and boron-doped diamond exhibit the Fano effect[34, 36, 37, 39, 40]. Several methods, including Raman spec-



troscopy, scanning tunneling microscopy, UV-Vis absorption spectroscopy, and infrared spectroscopy can be used to observe the experimental Fano lineshape [34, 40–42]. In this thesis, the Fano effect is studied using Raman Spectroscopy.

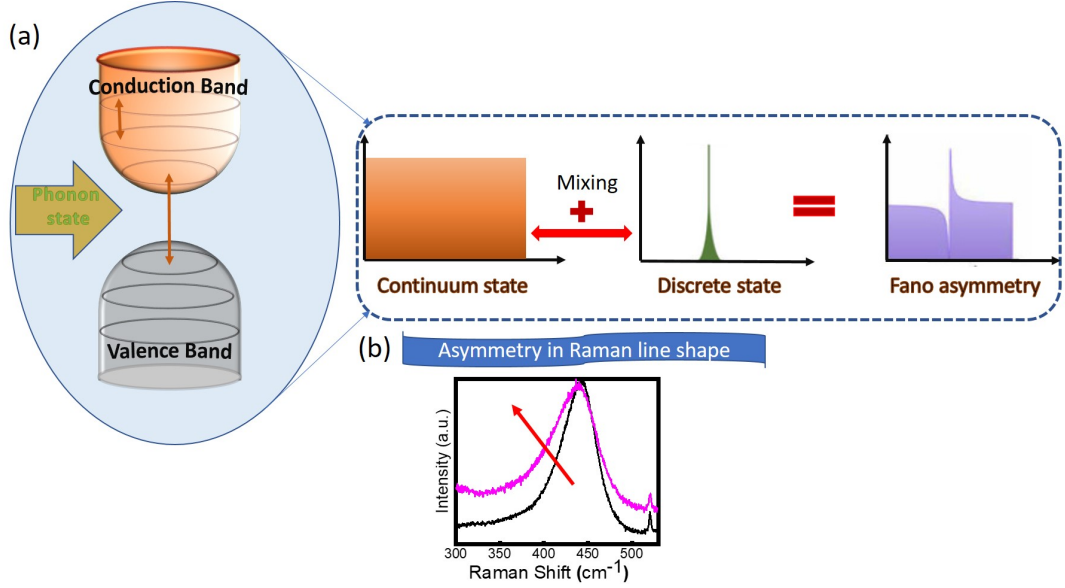


Figure 1.5: (a) Schematic showing origin of Fano asymmetry. (b) Asymmetry in Raman line shape.

The electron-phonon interaction causes the asymmetry in Raman spectra, which can be used as a measure of the electron-phonon coupling strength of a material[34]. In addition, the asymmetric lineshape can also give an idea about the n-type or p-type nature of the semiconductor. If the asymmetry is towards the lower wavenumber regime, it is n-type; otherwise, it is p-type[43]. In semiconductors, defects create a continuum of electronic states that interfere with the discrete states, resulting in asymmetry in the Raman line shape[40]. Defects like oxygen vacancies, titanium vacancies, and interstitials are produced when  $\text{TiO}_2$  is doped chemically or by ion implantation[44–47]. Several defect states increase with dopant concentration, enhancing the probability of electronic transition within the subbands[48, 49]. Oxygen vacancy increases the density of electrons in  $\text{TiO}_2$ . The ex-

periment with the oxygen vacancy can manipulate the electron concentration. As a result, the defect concentration can be used to tune the Fano resonance.

This thesis discusses the Fano effect in Chapters 3 and 7. In Chapter 3, the electronic continuum is provided by heavy doping, whereas in Chapter 7, it is discussed through photoexcitations. By doping, one can manipulate the electron-phonon coupling strength, which can be experimentally studied by analyzing the Fano asymmetry in Raman lineshape[39]. The asymmetric Raman lineshape is fitted with the Breit-Wigner-Fano formula, which is given as,

$$I(\omega) = I_0 \frac{(1 + \frac{\omega - \omega_0}{q\Gamma})^2}{1 + (\frac{\omega - \omega_0}{\Gamma})^2} \quad (1.3)$$

Where  $I(\omega)$  is the intensity of Raman lineshape as a function of  $\omega$ ,  $I_0$  is the maximum peak intensity,  $\omega_0$  is the peak position,  $\Gamma$  is the linewidth of the phonon mode, and  $1/q$  is the asymmetry parameter that measures the strength of the electron-phonon interaction[50]. The larger value of  $1/q$  suggests stronger electron-phonon interaction and causes the Raman peak to be more asymmetric. When  $1/q \rightarrow 0$ , the electron-phonon interaction becomes weak and the Raman lineshape will have a Lorentzian shape instead of a Fano lineshape [34, 35].

## 1.5 Theme of the thesis

This thesis is focused on bandgap engineering in phase-selective  $\text{TiO}_2$  microflowers for photonic applications. The defects produced in the  $\text{TiO}_2$  matrix by introducing elements of different atomic numbers such as C ( $Z=6$ ), Si ( $Z=14$ ), Cu ( $Z=29$ ), and Au (79). Further, the oxidation state of the dopants and atomic radii of the doped element decide whether the dopants will occupy the substitutional or interstitial position. The theme of the thesis is schematically presented in Figure 1.6. The innermost circle represents the rutile  $\text{TiO}_2$  into which dopants are incorporated. The next layer shows the names of dopants and de-

posited materials onto the  $\text{TiO}_2$ . The next two connected layers highlight the properties and applications studied in each case.

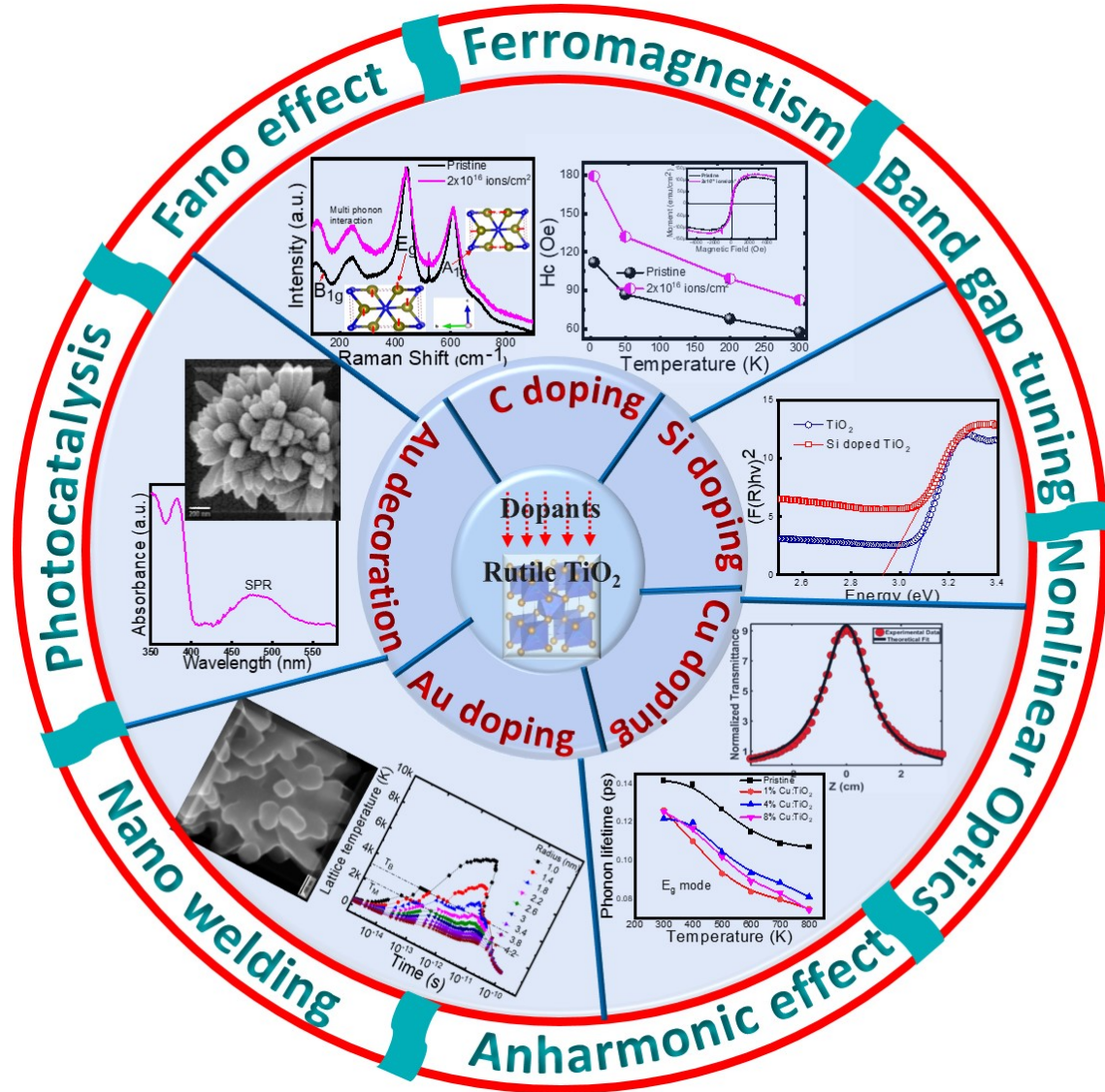


Figure 1.6: Schematic representation of the theme of the thesis: Physics of Fano effect to photocatalytic application.

In the first part,  $\text{TiO}_2$  is doped with a C ion, which is a lighter ion and non-metallic. The defect states created by C ion implantation narrow down the bandgap of the  $\text{TiO}_2$  matrix

from 3.04 to 2.98 eV. It is observed that the C ion implantation creates oxygen vacancy in the  $\text{TiO}_2$  matrix that increases the population of electrons in the CB enhancing the conductivity. This part contains two sections. In the first section, the Fano effect is studied by C ion implantations. The Fano effect arises due to the interaction of discrete phonon states with the continuum of electronic transition states. The continuum state is provided by heavy doping. Implantation of C ion into the  $\text{TiO}_2$  matrix creates a large number of oxygen vacancies. As each oxygen vacancy is associated with two electrons, the increased ion fluence increases the number of electrons in the CB of  $\text{TiO}_2$ . As the density of electrons in the CB increases, the probability of electron-phonon interaction increases giving rise to the higher value of the asymmetry in the Raman spectra, which is used to study the Fano effect.

In the second section, we studied the magnetic behavior of the samples. Intrinsic  $\text{TiO}_2$  is non-magnetic in nature and oxygen-deficient induced ferromagnetism. The oxygen vacancy created through C ion implantation motivated us to study the magnetic properties of the samples. From the magnetic measurement, all the samples including the pristine sample showed ferromagnetic behavior which indicated that along with the implanted samples, the pristine sample has some intrinsic oxygen vacancy. Theoretically, from DFT calculation, it has been observed that an ideal  $\text{TiO}_2$  is non-magnetic however, as the oxygen vacancy reduces the  $\text{Ti}^{4+}$  ion to  $\text{Ti}^{3+}$  ion that encompasses one unpaired d electron, induces a non-zero magnetic moment.

In the second part,  $\text{TiO}_2$  is doped with Si, which is semiconducting. The low-energy Si ion affects the morphology of the sample. It has been observed that the tip of the nanorod is slightly changed at the highest fluence implanted sample, but at lower fluence, it remains unaffected. However, it does not affect the crystallinity property significantly. The defects created in this case also tune the bandgap with ion fluences.

The third part focused on Cu doping in  $\text{TiO}_2$ , with medium-sized metallic ions. This

part also contains two sections. In the first section, the linear and nonlinear optical properties are studied. The sequential narrowing of the bandgap with Cu dopant concentration indicates the presence of midgap defect states in the forbidden region. The estimation of bandgap from density functional theory calculation follows the same trend of bandgap narrowing with Cu doping. These defect states slow down the recombination of electron-hole by trapping the charge carriers. The nonlinear optical property studied using open aperture z-scan technique revealed the SA behaviour and the nonlinear absorption coefficient gets improved with Cu concentration. Further, the close aperture z-scan technique showed the self-focusing behavior with doping percentage. We have demonstrated that the creation of defects plays an important role in tuning the linear and nonlinear optical properties of  $\text{TiO}_2$ . In the second section, we studied the anharmonic effect using high-temperature Raman spectroscopy. The peak broadening and peak softening with temperature are caused by an anharmonic effect that matches well with the Klemens model by combining three and four-phonon processes. The reduced phonon lifetime indicates the scattering of phonons by other phonons, impurities, electrons, and crystal boundaries.

In the fourth part, a heavier noble metal Au is doped in  $\text{TiO}_2$  using the ion implantation technique. In this case, it is observed that the surface morphology of the samples gets deformed at higher fluence. The nanorods of the microflowers are welded with each other. The localized temperature evolved during the ion implantation process, which is responsible for the above melting phenomena is studied through the unified thermal spike model (USTM). Both experimental and theoretical calculation demonstrates the nano-welding of two nanorods or nanoparticles by heavy ions. In addition, the Au dopant narrows down the bandgap indicating the presence of defect states in the mid-gap region.

In the last part of the thesis,  $\text{TiO}_2$  is decorated with Au of three different thicknesses 2, 4, and 6 nm to observe the extended surface-induced bandgap engineering for photocatalytic applications. The photocatalytic degradation of Rhodamine 6G ( $10^{-4}$  M) on Au-decorated

TiO<sub>2</sub> microflowers is studied. The photocatalytic study was carried out using Raman spectroscopy under exposure to both UV and visible light. It was concluded that the surface plasmonic resonance, photothermal effect, and carrier trapping by defect states enhance the photocatalytic activity. After annealing the sample, Au nanoparticles are formed on the surface of TiO<sub>2</sub> which influences the Fano effect. In this case, the excess charge carriers are pumped from the Au nanoparticles to the CB of TiO<sub>2</sub> which enhances the Fano asymmetry parameter observed from Raman spectroscopy.

In summary, the defects created by chemical doping and ion implantations in the TiO<sub>2</sub> matrix introduce mid-gap states within the VBM and CBM that engineer the bandgap for various optical and spintronic applications, which has been demonstrated by non-linear properties, Fano asymmetry, and photocatalytic properties. Also, it has been concluded that the production of defect states can be controlled by choosing the dopant ions based on their oxidation state and atomic radii that highly affect the bandgap tuning which is the basic constituent for the optoelectronic application in wide bandgap oxide semiconductors.

## References

- [1] Maciej Hebda, Grażyna Stochel, Konrad Szaciłowski, and Wojciech Macyk. Optoelectronic switches based on wide band gap semiconductors. *The Journal of Physical Chemistry B*, 110(31):15275, 2006.
- [2] Amit Kumar, Milad Moradpour, Michele Losito, Wulf-Toke Franke, Suganthi Ramasamy, Roberto Baccoli, and Gianluca Gatto. Wide band gap devices and their application in power electronics. *Energies*, 15(23):9172, 2022.
- [3] Vudentam Srikant and David R Clarke. On the optical band gap of zinc oxide. *Journal of Applied Physics*, 83(10):5447, 1998.
- [4] I Yonenaga. Thermo-mechanical stability of wide-bandgap semiconductors: high temperature hardness of SiC, AlN, GaN, ZnO and ZnSe. *Physica B: Condensed Matter*, 308:1150, 2001.
- [5] Ruhma Rashid, Iqrash Shafiq, Muhammad Rehan Hasan Shah Gilani, Muhammad Maaz, Parveen Akhter, Murid Hussain, Kwang-Eun Jeong, Eilhann E Kwon, Sungjun Bae, and Y-K Park. Advancements in TiO<sub>2</sub>-based photocatalysis for environmental remediation: Strategies for enhancing visible-light-driven activity. *Chemosphere*, page 140703, 2023.
- [6] Jamal Rzaïj and Amina M. Abass. Review on: TiO<sub>2</sub> thin film as a metal oxide gas sensor. *Journal of Chemical Reviews*, 2, 2020.
- [7] Subhashree Sahoo, Gurupada Ghorai, Kalyan Ghosh, Bidyadhar Das, Mrinal K Sikdar, and Pratap K Sahoo. Anharmonicity of optical phonon modes in copper doped rutile TiO<sub>2</sub> nanorod composed microflowers. *AIP Advances*, 11(10):105013, 2021.

- 
- [8] Jianjian Lin, Yoon-Uk Heo, Andrew Nattestad, Ziqi Sun, Lianzhou Wang, Jung Kim, Shi, and Xue Dou. 3d hierarchical rutile  $\text{TiO}_2$  and metal-free organic sensitizer producing dye-sensitized solar cells 8.6% conversion efficiency. *Scientific Reports*, 4, 2014.
- [9] Sawanta Mali, C.A. Betty, Popatrao Bhosale, P. Patil, and Chang Hong. From nanocorals to nanorods to nanoflowers nanoarchitecture for efficient dye-sensitized solar cells at relatively low film thickness: All hydrothermal process. *Scientific reports*, 4:5451, 2014.
- [10] Dinesh J. Ahirrao, Higgins M. Wilson, and Neetu Jha.  $\text{TiO}_2$ -nanoflowers as flexible electrode for high performance supercapacitor. *Applied Surface Science*, 491:765, 2019.
- [11] Prabitha B Nair, VB Justinictor, Georgi P Daniel, K Joy, KC James Raju, David Devraj Kumar, and PV Thomas. Optical parameters induced by phase transformation in rf magnetron sputtered  $\text{TiO}_2$  nanostructured thin films. *Progress in Natural Science: Materials International*, 24(3):218, 2014.
- [12] Edward JW Crossland, Nakita Noel, Varun Sivaram, Tomas Leijtens, Jack A Alexander-Webber, and Henry J Snaith. Mesoporous  $\text{TiO}_2$  single crystals delivering enhanced mobility and optoelectronic device performance. *Nature*, 495(7440):215–219, 2013.
- [13] Mohamed M Fadlallah and Ulrich Eckern. Electronic and optical properties of metal-doped  $\text{TiO}_2$  nanotubes: spintronic and photocatalytic applications. *New Journal of Physics*, 22(9):093028, 2020.
- [14] K. Momma and F. Izumi. Vesta 3 for three-dimensional visualization of crystal, volumetric and morphology data. *J. Appl. Crystallogr.*, 44:1272, 2011.



- 
- [15] Xinhua Zhu, Qi Li, Naiben Ming, and Zhongyan Meng. Origin of optical nonlinearity for PbO, TiO<sub>2</sub>, K<sub>2</sub>O, and SiO<sub>2</sub> optical glasses. *Applied physics letters*, 71(7):867, 1997.
- [16] R.W. Boyd. *Nonlinear Optics*. Electronics & Electrical. Academic Press, 2003.
- [17] TC Rossi, D Grolimund, O Cannelli, GF Mancini, C Bacellar, D Kinschel, JR Rouxel, N Ohannessian, D Pergolesi, and M Chergui. X-ray absorption linear dichroism at the ti k-edge of rutile (001) TiO<sub>2</sub> single crystal. *Journal of synchrotron radiation*, 27(2):425, 2020.
- [18] Estefania German, Ricardo Faccio, and Alvaro W Mombrú. A DFT+U study on structural, electronic, vibrational and thermodynamic properties of TiO<sub>2</sub> polymorphs and hydrogen titanate: tuning the hubbard ‘U-term’. *Journal of Physics Communications*, 1(5):055006, 2017.
- [19] Tian Lan, Xiaoli Tang, and Brent Fultz. Phonon anharmonicity of rutile TiO<sub>2</sub> studied by Raman spectrometry and molecular dynamics simulations. *Physical Review B*, 85(9):094305, 2012.
- [20] Ashis Manna, A Barman, Shalik R Joshi, B Satpati, P Dash, Ananya Chattaraj, SK Srivastava, PK Sahoo, A Kanjilal, D Kanjilal, et al. The effect of Ti<sup>+</sup> ion implantation on the anatase-rutile phase transformation and resistive switching properties of TiO<sub>2</sub> thin films. *Journal of Applied Physics*, 124(15), 2018.
- [21] Biswajit Choudhury and Amarjyoti Choudhury. Room temperature ferromagnetism in defective TiO<sub>2</sub> nanoparticles: Role of surface and grain boundary oxygen vacancies. *Journal of Applied Physics*, 114(20):203906, 2013.
- [22] Pablo David Esquinazi, Wolfram Hergert, Markus Stiller, Lukas Botsch, Hendrik

- Ohldag, Daniel Spemann, Martin Hoffmann, Waheed A Adeagbo, Angelika Chassé, Sanjeev K Nayak, et al. Defect-induced magnetism in nonmagnetic oxides: Basic principles, experimental evidence, and possible devices with ZnO and TiO<sub>2</sub>. *physica status solidi (b)*, 257(7):1900623, 2020.
- [23] Min Sik Park, SK Kwon, and BI Min. Electronic structures of doped anatase TiO<sub>2</sub>: Ti<sub>1-x</sub> M<sub>x</sub> O<sub>2</sub> (M = Co, Mn, Fe, Ni). *Physical Review B*, 65(16):161201, 2002.
- [24] Nguyen Hoa Hong, Joe Sakai, and Francois Gervais. Magnetism due to oxygen vacancies and/or defects in undoped semiconducting and insulating oxide thin films. *Journal of magnetism and magnetic materials*, 316(2):214, 2007.
- [25] Nguyen Hoa Hong, Joe Sakai, Nathalie Poirrot, and Virginie Brizé. Room-temperature ferromagnetism observed in undoped semiconducting and insulating oxide thin films. *Physical Review B*, 73(13):132404, 2006.
- [26] Shengqiang Zhou, E Čížmár, K Potzger, M Krause, G Talut, M Helm, J Fassbender, SA Zvyagin, J Wosnitza, H Schmidt, et al. Origin of magnetic moments in defective TiO<sub>2</sub> single crystals. *Physical Review B*, 79(11):113201, 2009.
- [27] A Janotti, JB Varley, P Rinke, N Umezawa, G Kresse, and CG Van de Walle. Hybrid functional studies of the oxygen vacancy in TiO<sub>2</sub>. *Physical Review B*, 81(8):085212, 2010.
- [28] Adriana Zaleska. Doped-TiO<sub>2</sub>: a review. *Recent patents on engineering*, 2(3):157, 2008.
- [29] Yan Su, Shuo Chen, Xie Quan, Huimin Zhao, and Yaobin Zhang. A silicon-doped TiO<sub>2</sub> nanotube arrays electrode with enhanced photoelectrocatalytic activity. *Applied Surface Science*, 255(5):2167, 2008.

- 
- [30] Aleksandra Piątkowska, Magdalena Janus, Kacper Szymański, and Sylwia Mozia. C-, N-and S-doped TiO<sub>2</sub> photocatalysts: a review. *Catalysts*, 11(1):144, 2021.
- [31] María Dolores Hernández-Alonso. Metal doping of semiconductors for improving photoactivity. In *Design of Advanced Photocatalytic Materials for Energy and Environmental Applications*, page 269. Springer, 2013.
- [32] Run Long and Niall J English. Band gap engineering of (N, Si)-codoped TiO<sub>2</sub> from hybrid density functional theory calculations. *New Journal of Physics*, 14(5):053007, 2012.
- [33] C Ciano, L Persichetti, M Montanari, L Di Gaspere, G Capellini, L Baldassarre, M Ortolani, A Pashkin, M Helm, S Winnerl, et al. Electron-phonon coupling in n-type ge two-dimensional systems. *Physical Review B*, 102(20):205302, 2020.
- [34] CI Medel-Ruiz, H Pérez Ladrón de Guevara, JR Molina-Contreras, and C Frausto-Reyes. Fano effect in resonant raman spectrum of cdte. *Solid State Communications*, 312:113895, 2020.
- [35] Shailendra K Saxena, Priyanka Yogi, Suryakant Mishra, Hari Mohan Rai, Vikash Mishra, M Kamal Warshi, Swarup Roy, Puspen Mondal, Pankaj R Sagdeo, and Rajesh Kumar. Amplification or cancellation of fano resonance and quantum confinement induced asymmetries in raman line-shapes. *Physical Chemistry Chemical Physics*, 19(47):31788, 2017.
- [36] Valentin Magidson and Robert Beserman. Fano-type interference in the raman spectrum of photoexcited si. *Physical Review B*, 66(19):195206, 2002.
- [37] Rajesh Kumar, HS Mavi, AK Shukla, and VD Vankar. Photoexcited fano interaction in laser-etched silicon nanostructures. *Journal of applied physics*, 101(6):064315, 2007.

- 
- [38] Souvik Bhattacharjee and Kalyan Kumar Chattopadhyay. Laser-induced fano asymmetry, electron-phonon coupling, and phase transition in lanthanide sesquioxide ( $\text{Ln}_2\text{O}_3$ ;  $\text{Ln} = \text{Eu, Gd, Dy}$ ) nanoparticles: A raman spectroscopic investigation. *Journal of Applied Physics*, 132(21):215107, 2022.
- [39] Sarbajit Banerjee, Dae-In Kim, Richard D Robinson, Irving P Herman, Yuanbing Mao, and Stanislaus S Wong. Observation of fano asymmetry in raman spectra of  $\text{SrTiO}_3$  and  $\text{Ca}_x\text{Sr}_{1-x}\text{TiO}_3$  perovskite nanocubes. *Applied physics letters*, 89(22):223130, 2006.
- [40] Joel W Ager III, W Walukiewicz, Matthew McCluskey, Mary Anne Plano, and Maurice I Landstrass. Fano interference of the raman phonon in heavily boron-doped diamond films grown by chemical vapor deposition. *Applied Physics Letters*, 66(5):616–618, 1995.
- [41] S Meierott, T Hotz, N Néel, and J Kröger. Asymmetry parameter of peaked Fano line shapes. *Review of Scientific Instruments*, 87(10):103901, 2016.
- [42] AB Kuzmenko, Iris Crassee, Dirk Van Der Marel, P Blake, and KS Novoselov. Determination of the gate-tunable band gap and tight-binding parameters in bilayer graphene using infrared spectroscopy. *Physical Review B*, 80(16):165406, 2009.
- [43] Subhashree Sahoo and Pratap K Sahoo. Weak-localization effect in Fano asymmetry of c implanted rutile  $\text{TiO}_2$  nanostructure. *Journal of Applied Physics*, 133(14), 2023.
- [44] Apostolos Kordatos, Nikolaos Kelaidis, and Alexander Chroneos. Defect pair formation in fluorine and nitrogen codoped  $\text{TiO}_2$ . *Journal of Applied Physics*, 123(16):161510, 2018.

- 
- [45] B Leedahl, DA Zatsepin, DW Boukhvalov, RJ Green, JA McLeod, SS Kim, EZ Kurmaev, IS Zhidkov, NV Gavrilov, SO Cholakh, et al. Structural defects induced by fe-ion implantation in TiO<sub>2</sub>. *Journal of Applied Physics*, 115(5):053711, 2014.
- [46] Zepeng Rao, Xiaofeng Xie, Xiao Wang, Asad Mahmood, Shengrui Tong, Maofa Ge, and Jing Sun. Defect chemistry of Er<sup>3+</sup>-doped TiO<sub>2</sub> and its photocatalytic activity for the degradation of flowing gas-phase vocs. *The Journal of Physical Chemistry C*, 123(19):12321, 2019.
- [47] AM Czoska, Stefano Livraghi, Mario Chiesa, Elio Giamello, S Agnoli, G Granozzi, E Finazzi, C Di Valentin, and G Pacchioni. The nature of defects in fluorine-doped TiO<sub>2</sub>. *The Journal of Physical Chemistry C*, 112(24):8951, 2008.
- [48] Nattakan Kanjana, Wasan Maiaugree, and Paveena Laokul. Photocatalytic activity of nanocrystalline Fe<sup>3+</sup>-doped anatase TiO<sub>2</sub> hollow spheres in a methylene blue solution under visible-light irradiation. *Journal of Materials Science: Materials in Electronics*, 33(7):4659, 2022.
- [49] Wenliang Zhu, Shoichiro Kitamura, Marco Boffelli, Elia Marin, Enrico Della Gaspera, Marco Sturaro, Alessandro Martucci, and Giuseppe Pezzotti. Analysis of defect luminescence in Ga-doped ZnO nanoparticles. *Physical Chemistry Chemical Physics*, 18(14):9586, 2016.
- [50] Eddwi H Hasdeo, Ahmad RT Nugraha, Mildred S Dresselhaus, and Riichiro Saito. Breit-Wigner-Fano line shapes in Raman spectra of graphene. *Physical Review B*, 90(24):245140, 2014.

## Chapter 2

# Experimental methods and Characterization techniques

This chapter contains a brief description of sample preparation processes and experimental techniques used in the thesis. Herein, the  $\text{TiO}_2$  microflowers are synthesized using the hydrothermal method. The defects are created in three different processes (i) doping by chemical method (ii) embedded defects by ion implantation, and (iii) surface defects by thermal deposition. The morphological and structural characterizations are performed using field emission scanning electron microscope (FESEM), transmission electron microscope (TEM), and X-ray diffraction (XRD) techniques. The elemental analysis were performed using energy-dispersive X-ray spectroscopy (EDS), X-ray photoelectron spectroscopy (XPS), and inductively coupled plasma optical emission spectroscopy (ICP-OES) techniques. The linear optical properties are analyzed using Raman, photoluminescence (PL), and UV-visible spectroscopy and the nonlinear optical properties are investigated using the Z-scan technique. The magnetic property was investigated using a superconducting quantum interference device (SQUID).

## 2.1 Sample preparation

### 2.1.1 Substrate cleaning

In this thesis,  $\text{TiO}_2$  microflowers are grown on  $\text{TiO}_2$  seeded Si and glass substrates. Before the growth of samples, the substrates are ultrasonically cleaned for 10 minutes in each of the following three mediums: acetone, isopropyl alcohol, and deionized water. Finally, the substrates are dried by purging nitrogen gas.

### **2.1.2 Seed layer preparation**

A seed layer is deposited on the Si substrate using a RF magnetron sputtering system. A commercially available TiO<sub>2</sub> target was used with purity 99.99%. The cleaned substrates are placed in a vacuum chamber and evacuated down to a base pressure of  $5 \times 10^{-6}$  mabr. The deposition is carried out at a working pressure of  $5 \times 10^{-3}$  mabr in an Ar ambient at a constant flow rate of 15 sccm. The substrate and the target are separated by 5 cm. A thin film of amorphous TiO<sub>2</sub> of thickness approximately 50 nm is deposited on the surface. The purpose of the seed layer is to avoid lattice mismatch to grow the TiO<sub>2</sub> nanostructure uniformly over the substrate.

### **2.1.3 Hydrothermal growth of TiO<sub>2</sub> microflowers**

The TiO<sub>2</sub> microflowers used in this study are synthesized by hydrothermal process on glass and TiO<sub>2</sub> seeded silicon substrate. Initially, 15 ml of HCl (37 wt %) is added to 25 ml of deionized water and mixed well. Subsequently, 0.2 ml of titanium butoxide is added to it and stirred until a clear solution is obtained. For Cu-doped samples, the required amount of copper nitrate trihydrate was added to the solution with molar concentration varying from 1 to 10%. The above solution is transferred into a Teflon-lined stainless steel autoclave. The substrates are dipped vertically in the solution inside the autoclave. The autoclave is then kept in the furnace at 150°C for 4 hours. After synthesis, the autoclave was naturally cooled to room temperature and the samples were rinsed with deionized water to remove the residuals from the surface and dried at room temperature. The use of HCl is essential in the hydrothermal synthesis of TiO<sub>2</sub> because titanium precursor is highly reactive in water and it also helps to control the nucleation rate of TiO<sub>2</sub>[1]. Titanium butoxide and copper nitrate trihydrate are used as sources of Ti and Cu, respectively. The schematic of the TiO<sub>2</sub> microflower preparation method is shown in Figure 2.1.

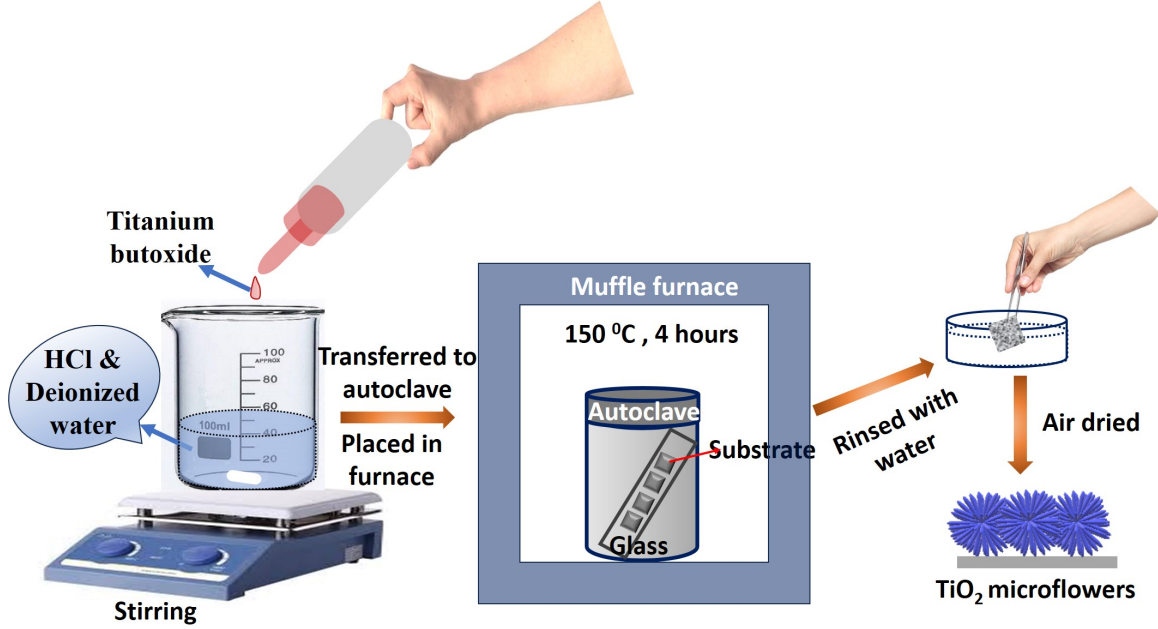


Figure 2.1: Schematic representation of TiO<sub>2</sub> microflower preparation method.

## 2.2 Ion implantation

Ion implantation is one of the versatile techniques for controllable doping of different ions in any solid materials. In the ion implantation process, the energetic ion beams are bombarded on a target material and implanted ions come to rest at the end of the range by losing energy. The energy loss or stopping power ( $S$ ) is defined as the energy ( $E$ ) lost per penetration depth ( $x$ ) and denoted as follows

$$S = \frac{dE}{dx} = \left(\frac{dE}{dx}\right)_n + \left(\frac{dE}{dx}\right)_e = S_n + S_e \quad (2.1)$$

where  $S_n$  and  $S_e$  are nuclear and electronic energy loss, respectively.  $S_n$  is dominant at low-energy ion implantation whereas, electronic energy loss is dominant at high-energy ion implantation. The bombarded ions before coming into rest create several defects in their path such as atomic displacement, sputtering, changing the overall composition of the



material, creating vacancies, and interstitial impurities. These defects affect the structural, optical, electrical, and magnetic properties of the material. The depth profile of the incident ion depends on the nuclear energy loss, electronic energy loss, and energy of the incident ion and follows a Gaussian distribution.

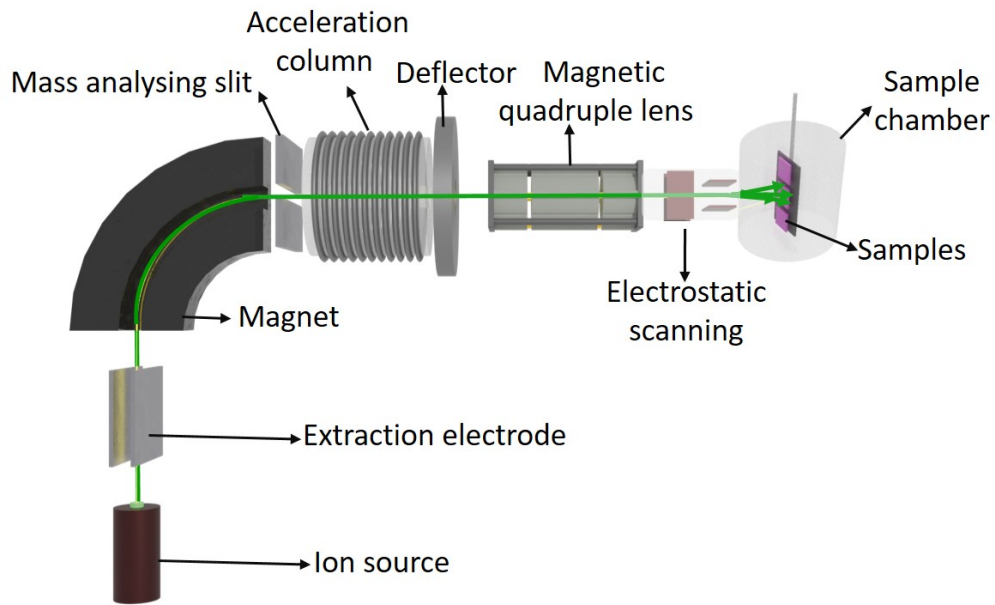


Figure 2.2: Schematic representation of ion beam implanter.

Figure 2.2 shows a typical schematic with different parts of a low-energy ion beam implanter. In general, the ion implanter consists of several parts as follows. The ion source generates specific charge particles for ion implantation either from solids using sputtering source or gaseous charge particles RF plasma source through ionization.

The ions are then extracted from the source by a high extractor potential and then passed through the bending magnet. In this part, selected ions are moved to the next part of the implanter through the mass-analyzing magnet and slit, and the other ions get blocked at the beam dumper. Further, the selected ions are accelerated to high velocities through the acceleration column, scanned by the scanning section, and finally scanned beams fall onto

the target surface.

A particular dose or fluence of ions are implanted into the target material by counting through a counter electronics using relation 2.2.

$$Counts(\eta) = \frac{fAeq}{s} \quad (2.2)$$

where  $f$  is fluence,  $A$  is the area of the beam,  $e$  is the charge of the electron ( $1.6 \times 10^{-19}$ ),  $q$  is the charge state of the ions and  $s$  is the scaling factor.

In this work,  $\text{TiO}_2$  microflowers are implanted with ions such as C, Si, and Au of energy 1.5 MeV, 30 keV, and 30 keV respectively. The energy of the ions is so chosen that the ions completely remain inside the  $\text{TiO}_2$  microflower. The C ions are implanted using a 3 MV Pelletron accelerator at the ion beam laboratory (IBL), Institute of Physics (IOP), Bhubaneswar. The negative ions were accelerated from a MC-SNICS source. The other two ions are implanted using low low-energy ion implanter at IOP. For implantation, the beamline is kept at a high vacuum of the order of  $10^{-6}$  mbar. The schematic of ion implantation on the  $\text{TiO}_2$  microflowers is shown in Figure 2.3.

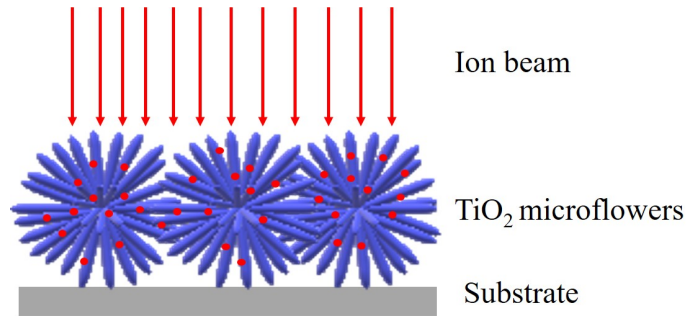


Figure 2.3: Schematic representation of ion implantation in  $\text{TiO}_2$  microflowers.

## 2.3 Au deposition

A thin layer of Au was deposited on the surface of as-prepared  $\text{TiO}_2$  microflowers using the thermal evaporation technique. The  $\text{TiO}_2$  microflowers were placed in a vacuum chamber

and evacuated down to a base pressure of  $2 \times 10^{-7}$  mabr. The thickness of the Au thin film was measured using a quartz crystal monitor placed inside the deposition chamber. The schematic of Au decoration over the  $\text{TiO}_2$  microflower surface is shown in Figure 2.4.

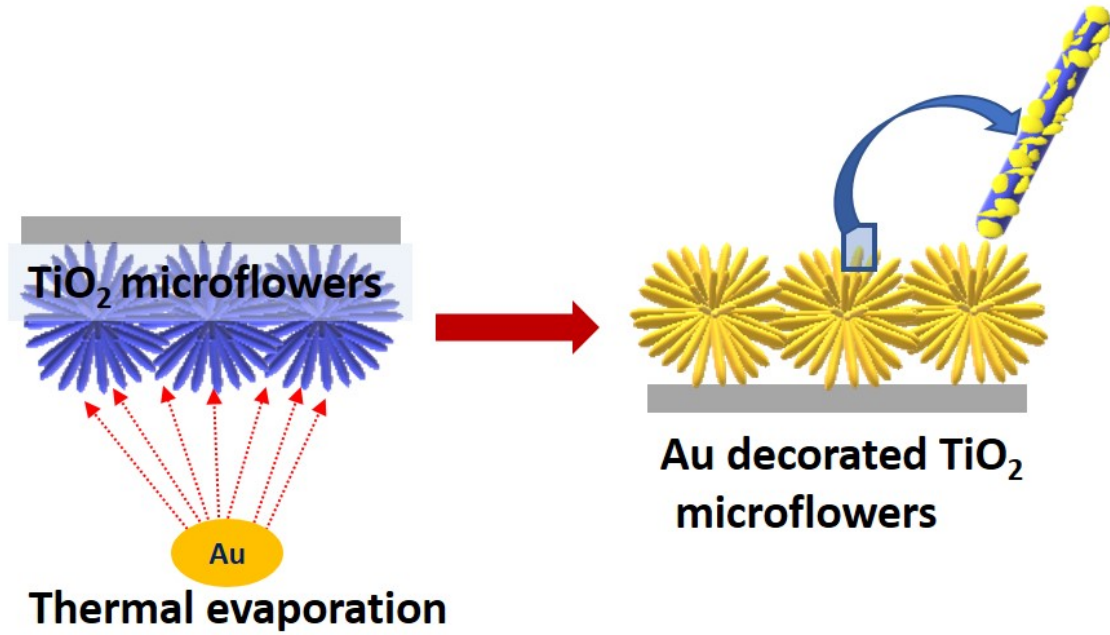


Figure 2.4: Schematic of Au decoration over  $\text{TiO}_2$  microflowers.

## 2.4 Characterization techniques

### 2.4.1 Field emission scanning electron microscopy (FESEM)

FESEM is extensively used to visualize the surface morphology of the samples. In this technique, an energetic beam of electrons is extracted from a field emission source (tungsten or lanthanum hexaboride) by thermionic emission technique. The electrons are accelerated in a high electric field gradient through an aperture of 20, 30, and 60  $\mu\text{m}$  depending on need. The highly energetic electrons are then focused and deflected by the electronic lenses and incident on the specimen forming secondary electrons, back-scattered electrons, Auger

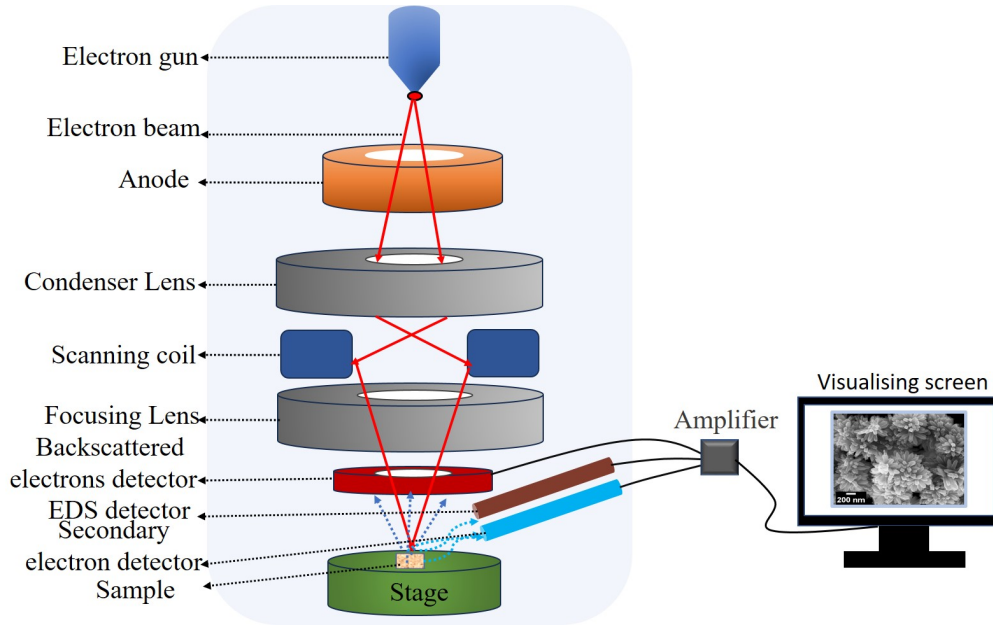


Figure 2.5: Schematic diagram of FESEM.

electrons, transmitted electrons, X-rays, etc. A specific detector inside the column chamber collects the secondary electrons, produces electronic signals, and converts the signal to an image. Secondary electrons produced close to the impact site of the primary beam are detected towards the in-lens detector. Since these electrons are produced near the upper portion of the sample, they offer surface morphology of the material. The in-lens detector is located in the beam path and is combined with an electrostatic/electromagnetic lens. The sample surface topography image with a depth of field is provided by the SE2 detector, which is positioned aside from the in-lens detector. The schematic diagram of FESEM is shown in Figure 2.5. The pressure of the vacuum chamber is kept at the range  $2 \times 10^{-5}$  mbar to  $\approx 10^{-6}$  mbar and the electron gun is maintained at  $\approx 3 \times 10^{-9}$  mbar pressure at the time of imaging.

In this thesis, the morphology of samples is studied using the FESEM of ZEISS, Sigma 350 model.

### 2.4.2 Transmission electron microscopy (TEM)

TEM is a useful technique for analyzing the microstructural properties of materials at the atomic resolution. In addition, it provides information on morphology, crystal structure, defects, and particle size. In this technique, a highly energetic beam of electrons (200 keV) extracted from the electron gun is transmitted through an ultra-thin sample of thickness approximately 80-120 nm. The highly energetic electrons having lower wavelength make it possible to get high-resolution images. The schematic of the TEM system is displayed in Figure 2.6. The condenser lens and aperture control the electron beam to incident on the specimen. After passing through the specimen, the electron beam is incident on the objective lens where the first image of the specimen is formed. Then this image is magnified by the intermediate and projector lens and the final magnified image is seen on the fluorescence screen. The energy of the electron used for capturing the TEM images is 200

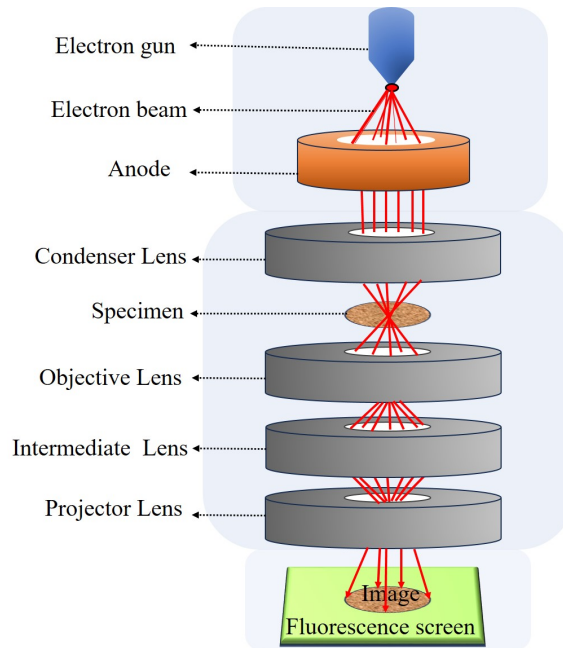


Figure 2.6: Schematic diagram of TEM.

keV. This causes the high resolution of TEM images. According to Rayleigh criterion, the

resolution (d) is given by[2]

$$d = \frac{0.61\lambda}{\mu \sin \beta} \quad (2.3)$$

where  $\lambda$  is the wavelength of electrons,  $\mu$  is the refractive index of the viewing medium, and  $\beta$  is the semi-angle of collection of the magnifying lens. In TEM, the speed of electrons is close to the speed of light in a vacuum,  $c$ , so the relativistic nature of electrons is to be considered. According to wave-particle duality, the electron has a wave nature with wavelength[3]

$$\lambda = \frac{h}{p} = \frac{h}{\sqrt{2meV(1 + \frac{eV}{2m_0c^2})}} \quad (2.4)$$

where  $p$  and  $m$  are the momentum, and rest mass of the electron, respectively.  $V$  is the voltage converted to energy in the form of eV. From equations 2.3 and 2.4, it can be concluded that if we increase the energy of the detecting electrons, its wavelength will decrease, and we can get a higher resolution. The wavelength of 200 keV electrons is calculated to be 2.51 pm.

In this thesis, microstructural analysis of samples is carried out using the Jeol JEM-F200 TEM system equipped with a Gatan Inc. imaging detector.

### 2.4.3 Energy-dispersive X-ray spectroscopy (EDS)

EDS is used for the elemental analysis of any kind of solid samples[4]. It is typically attached to FESEM or TEM. The basic principle involves the detection and analysis of X-rays emitted by a sample when it is bombarded with high-energy electrons from FESEM or TEM. The schematic of X-ray production from the sample is shown in Figure 2.7(a). The X-ray is produced when the energetic electron displaces the inner shell of the electron and is refilled by the outer shell and the energy released is the form of X-rays. At rest, the atoms of the samples have some discrete energy levels bound to the nucleus. When an electron beam of sufficient energy incident on the samples, the electrons in the inner shell of an atom get

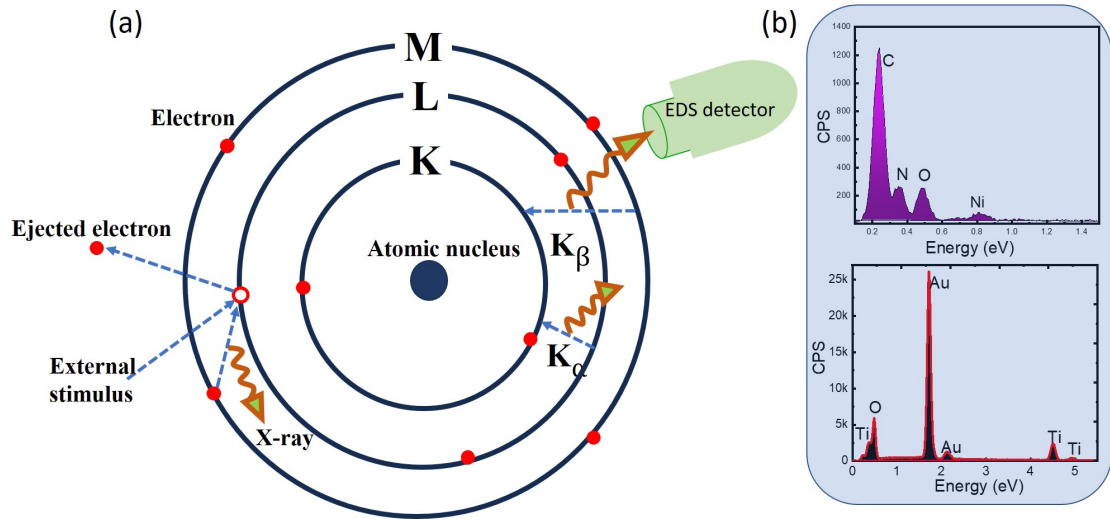


Figure 2.7: (a) Schematic representation x-ray generation. (b) EDS spectra showing different elements.

excited to the outer shell leaving a hole. An electron from the outer shell fills the hole by releasing energy as an X-ray. The energy of the X-ray is the energy difference between the inner and outer shell, which is unique to each element in the periodic table and can be detected by an energy-dispersive detector. The detector is capable of measuring the energy of each X-ray photon that strikes to collect the spectrum as well as mapping images. By analyzing the energy spectrum, it is possible to identify the elements present in the sample, the position of each peak corresponds to specific elements. The elements starting from lighter C atom to heavier Au can atom can be analyzed through this detector as shown in Figure 2.7(b).

#### 2.4.4 X-ray diffraction (XRD)

XRD is a non-destructive technique that provides information about the phase and crystal structure of samples. It is based on the principle of constructive interference of monochromatic X-ray [5]. When a beam of monochromatic X-ray incident on a crystalline sample,

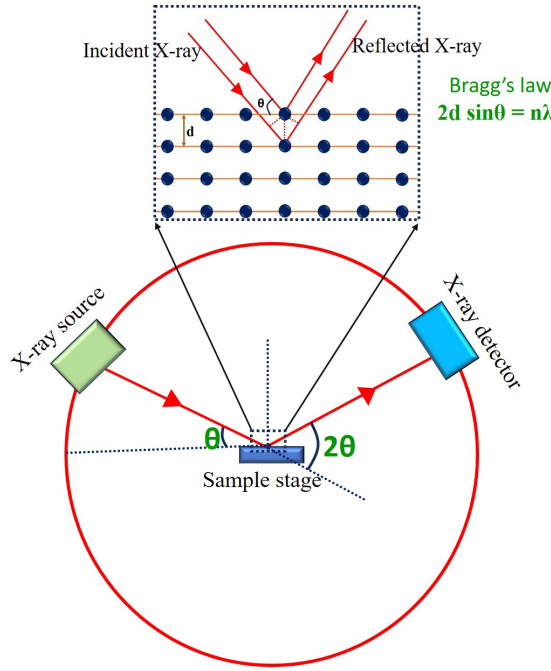


Figure 2.8: Schematic of X-ray diffractometer with Bragg's diffraction.

it gets scattered by the atoms and undergoes constructive and destructive interference depending upon the atomic arrangement. The condition for constructive interference given by Bragg's law

$$2d \sin\theta = n\lambda \quad (2.5)$$

Where  $d$ ,  $\theta$ , and  $\lambda$  are the inter-planar spacing, angle of incidence, and wavelength of the incident X-ray photon, respectively.  $n$  is an integer representing the order of diffraction. The diffraction pattern can be collected in different configurations such as  $\theta$ - $2\theta$  and grazing angle. The ray diagram and schematic of the X-ray diffractometer with Bragg diffraction configurations are shown in Figure 2.8.

In this thesis, the XRD data are collected using the Rigaku Smartlab X-ray diffractometer with monochromatic radiation Cu K $\alpha$  ( $\lambda = 1.5418 \text{ \AA}$ ). Almost in all cases, we have used grazing angle configuration for XRD measurements with an incident angle of  $1^\circ$ .



### 2.4.5 X-ray photoelectron spectroscopy (XPS)

XPS is an analytical technique used to study the electronic structure and its dynamics in atoms and molecules. It provides information about the chemical state and surface composition of materials[6]. In XPS, the primary beam is X-ray photons, which are irradiated on the sample surface and the ejected secondary beam (electrons) are collected and analyzed. The spectrum of XPS consists of a plot of the number of electrons or the power of electrons as a function of binding energy. When a monochromatic X-ray photon is incident on the sample surface, the inner shell electron abstracts energy from the X-ray photon and gets ejected. The kinetic energy of the ejected electron is recorded by the spectrometer and is given by

$$E_k = h\nu - E_b - \phi \quad (2.6)$$

Where,  $E_k$  is the kinetic energy of the ejected electron,  $h\nu$  is the energy associated with the incident photon,  $E_b$  is the binding energy of the ejected electron, and  $\phi$  is the work function of the material. The schematic of the XPS system and the photoemission process is shown in Figure 2.9(a) and (b), respectively.

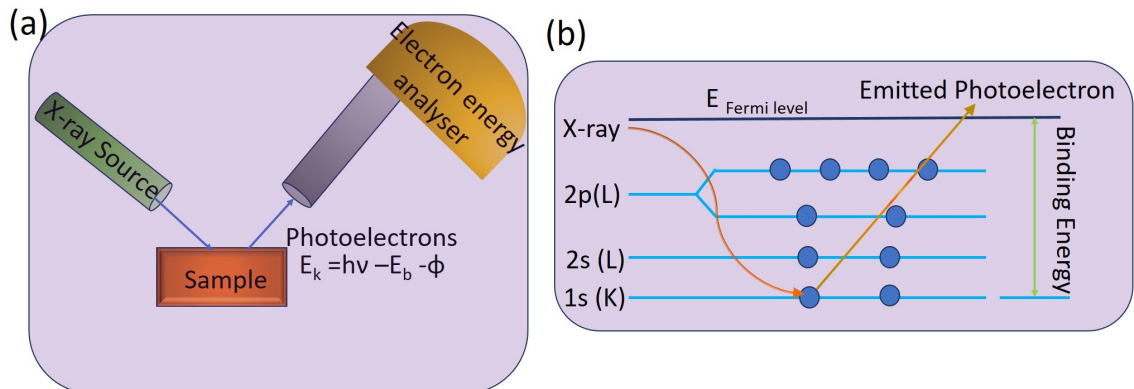


Figure 2.9: Schematic representation of (a) XPS instrument (b) XPS photoemission process.

In this thesis, XPS analysis is performed using a PHI 5000 Versa Probe-II (ULVAC, PHI, Inc.) spectrometer, which uses a monochromatic Al K $\alpha$  x-ray source of energy 1486.7 eV.

#### **2.4.6 Inductively Coupled Plasma Optical Emission Spectroscopy (ICP-OES)**

ICP-OES is a technique in which the composition of elements in a sample can be determined using plasma and spectrometer in ppm, bpm level[7]. It can be used with several kinds of samples, including organic and aqueous liquids and solids. Before measurement, a specific sample preparation method is used which may be different for different samples. In this technique, electrons are introduced into the argon gas when it passes through a plasma torch to create the plasma. Then, elements in the form of atoms, are introduced into the plasma. Within the plasma, a certain percentage of these atoms gets ionized. When an atom is excited within the plasma, the transition of an electron from a lower to a higher state takes place. The electron in the higher state relaxes to the ground state emitting energy in the form of photons. The wavelength of the emitted photons gives information about the elements present.

In this thesis, Thermo Scientific™ iCAP™ 7000 Series inductively coupled plasma optical emission spectroscopy is carried out in the elemental analysis of samples. We have used this technique to know the exact % of Cu doping in TiO<sub>2</sub> microflowers and compared it with the initial amount of Cu precursor taken during growth.

#### **2.4.7 Raman spectroscopy**

Raman spectroscopy is a contactless, nondestructive technique to study the vibrational properties of molecules and is based on scattering phenomena[8]. It acts as a fingerprint of molecules and is used for the identification of molecules[9]. In addition, it provides infor-

mation about the crystallinity, stress, strain, electron-phonon interaction, phonon lifetime, and bond strength in a molecule. Raman spectroscopy is based on the phenomena of scattering of light from molecules. When monochromatic light interacts with a molecule, the scattering of radiation from molecules takes place in two ways, (i) elastic and (ii) inelastic scattering. In elastic scattering, the energy of scattered light is same as the that of the incident light. This is called Rayleigh scattering. A very small part of incident light gets scattered with energy different from the incident light. This is the Raman scattering. The energy difference is associated with the Raman shift. The energy shift provides information about the phonon mode. The Raman scattering has two components, Stokes, and anti-Stokes scattering. In Stokes lines, the molecules after absorbing energy from the incident photon excited to a virtual state and then relax back to a higher vibrational state. In the anti-Stokes line, molecules are initially in the excited vibrational state and after absorbing energy excited to a virtual state, then relax back to a lower vibrational state. The schematic of energy levels and the Raman spectrometer is schematically presented in Figure 2.10.

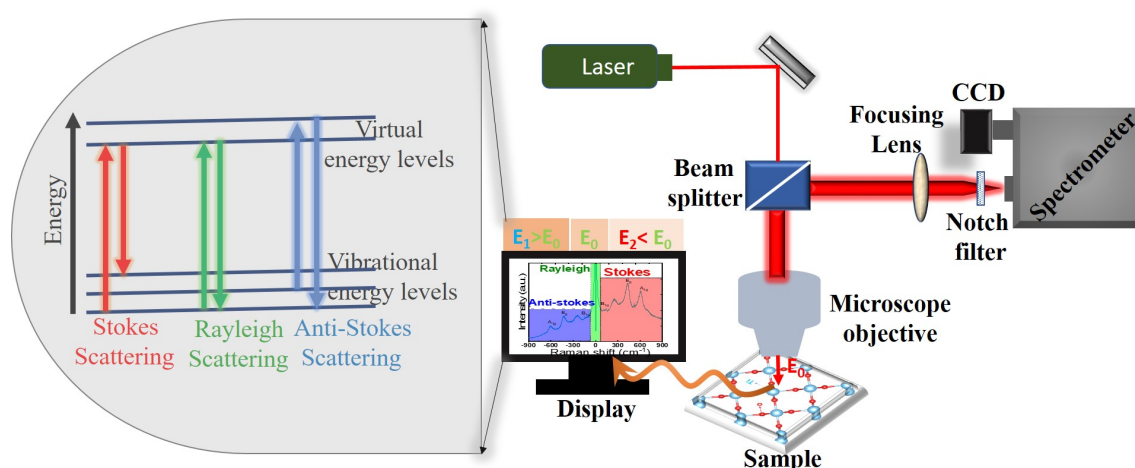


Figure 2.10: Schematic diagram of Raman spectrometer and vibrational energy level showing three types of scattering phenomena.

The origin of the Raman scattering process can be explained with the help of a classical

theory of scattering[10]. Let us consider a monochromatic light of frequency  $\nu$ , propagating in a particular direction. The amplitude of the oscillating electric field  $E$ , at any time  $t$ , can be expressed as

$$E = E_0 \cos 2\pi \nu t \quad (2.7)$$

where  $E_0$  is the maximum amplitude of the electric field. Let us consider a diatomic molecule with a natural frequency of vibration  $\nu_0$ , the nuclear displacement ( $q$ ) can be written as,

$$q = q_0 \cos 2\pi \nu_0 t \quad (2.8)$$

where  $q_0$  is the amplitude of the vibration. When the electromagnetic field of the incident photon interacts with this molecule, a dipole moment  $P$  is induced which is given by,

$$P = \alpha E = \alpha E_0 \cos 2\pi \nu t \quad (2.9)$$

where  $\alpha$  is polarizability. For small vibrations,  $\alpha$  can be expanded using Taylor's series as:

$$\alpha = \alpha_0 + \left(\frac{\partial \alpha}{\partial q}\right)_0 q + \dots \quad (2.10)$$

$\alpha_0$  demonstrates the polarizability at the equilibrium position and  $(\frac{\partial \alpha}{\partial q})_0$  is the rate of change of  $\alpha$  with respect  $q$ , calculated at the equilibrium position. Due to the small vibrations,  $\alpha$  can be considered as a linear function of  $q$  and the higher-order terms of  $q$  can be neglected.

Using equations 2.8 and 2.10 in 2.9 and after simplification, we can write

$$P = \alpha_0 E_0 \cos 2\pi \nu t + \frac{1}{2} \left(\frac{\partial \alpha}{\partial q}\right)_0 E_0 q_0 [\cos 2\pi(\nu - \nu_0)t + \cos 2\pi(\nu + \nu_0)t] \quad (2.11)$$

The first term in the expression represents Rayleigh scattering of frequency  $\nu$ . The second and third terms correspond to Stoke (frequency =  $\nu - \nu_0$ ) and anti-Stoke (frequency =  $\nu + \nu_0$ ) Raman scattering, respectively.

In addition, the laser-induced temperature can be calculated from Stokes anti-Stokes measurement using intensity ratio  $\frac{I_a}{I_s}$ . The intensity ratio in terms of Boltzmann distribution is given by

$$\frac{I_a}{I_s} = \left( \frac{\omega_0 + \omega_\nu}{\omega_0 - \omega_\nu} \right)^4 e^{-\frac{\hbar\omega_\nu}{kT}} \quad (2.12)$$

where,  $\omega_0$  is the wavenumber of exciting laser,  $\omega_\nu$  is the wave number of Raman mode,  $\hbar = h/2\pi$  with the Plank constant  $h$ ,  $k$  the Boltzmann constant, and  $T$  is the absolute temperature[11, 12].

In this thesis, we have used the Raman spectrometer (Horiba Jobin Yvon LabRam HR Evolution system) in back-scattering geometry. The laser of wavelength 532 nm and 633 nm are used as the source of excitation.

#### 2.4.8 Photoluminescence spectroscopy (PL)

PL is a useful method for exploring the emission properties of the materials, and to understand the charge carrier trapping and presence of intermediate defect states in between the valance band (VB) and conduction band (CB). The intensity of the PL spectra provides information about electron-hole recombination [13, 14]. Photoluminescence is the spontaneous emission of light from a material under photoexcitation. It occurs when a material emits light after absorbing a photon from an external monochromatic light source. In PL spectroscopy, the intensity of emitted light is measured as a function of wavelength by using an optical spectrometer. Photoexcitation causes electrons within the material to move into permissible excited states. When the light of energy is greater than or equal to the bandgap of the semiconductor is incident on it, the electrons in the VB are excited to the CB leaving holes in the VB. These excited electrons in the CB return to their equilibrium states through the non-radiative transition. The electrons jump from the CB minimum to VB maxima by releasing energy in the form of photons. The energy of the emitted photon

is related to the difference in energy between VB and CB. In semiconductor systems, the most common radiative transition is between VB and CB, with the energy difference being known as the bandgap. During a PL spectroscopy experiment, monochromatic laser light of a particular wavelength is used, with an energy much larger than the optical bandgap. In addition to band-to-band transition, the emissions related to defect states are also identified. The schematic of photoemission for both direct and indirect bandgap semiconductors are displayed in Figure 2.11.

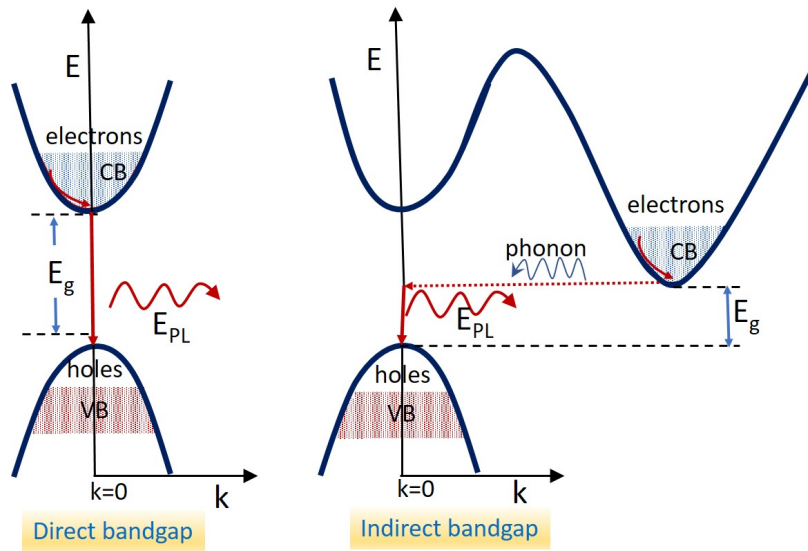


Figure 2.11: Schematic of PL emission for direct and indirect bandgap semiconductors. The dotted arrow represents non-radiative recombination and the solid arrow represents radiative recombination.

In this thesis, we used a He-Cd laser (325 nm) as the optical excitation source for PL measurement. The emitted light is collected and resolved using a monochromator and the signal output using a charge-coupled device (CCD) detector.

### 2.4.9 Ultraviolet-Visible-Near infrared spectroscopy

Ultraviolet-visible-near infrared (UV-Vis-NIR) spectroscopy is an important characterization technique that is widely used for investigating the optical bandgap of materials. When

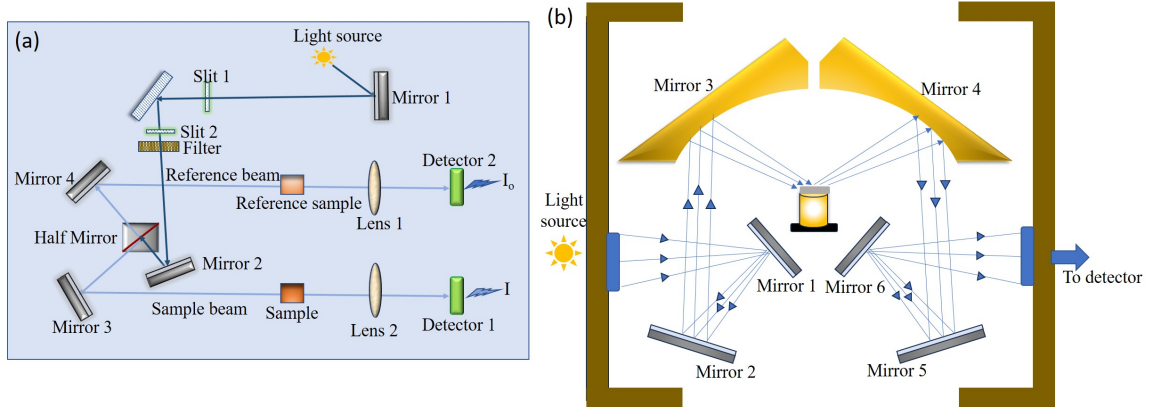


Figure 2.12: Ray diagram for UV-visible spectrometer for (a) translucent sample (b) opaque sample (Diffuse reflectance spectrometer).

electromagnetic radiation is incident on the surface of a material, three different processes occur; absorption, transmission, and reflection. For translucent samples absorbance and transmittance data are collected, whereas for opaque samples reflectance data are collected using different accessories provided in the UV-visible-NIR spectrometer.

For the measurement of absorbance, the ray diagram of the UV-Vis-NIR spectrometer is displayed in Figure 2.12(a). When light is incident on a material, electrons in the material receive energy and are promoted to a higher energy state. If  $I_0$  is the intensity of incident light and  $I$  is the intensity of transmitted light then absorbance  $A$  is defined as  $A = \log(I/I_0)$ . After collecting the absorbance data, the absorption coefficient ( $\alpha$ ) is obtained using the following relation[15],

$$\alpha = \frac{2.303A}{t} \quad (2.13)$$

where  $t$  is the thickness of the sample. The bandgap is determined using the Tauc relation given by

$$(\alpha h\nu)^{\frac{1}{n}} = A(h\nu - E_g) \quad (2.14)$$

where  $h$  Planck's constant,  $A$  is the proportional constant,  $E_g$  is the bandgap. The value of  $n$  indicates the type of electronic transition.  $n = \frac{1}{2}$  for direct allowed transition,  $n = 2$  for indirect

allowed transition[16]. As rutile  $\text{TiO}_2$  is a direct bandgap semiconductor,  $n=\frac{1}{2}$  is taken in this thesis for bandgap calculation. The bandgap is obtained by extrapolating the linear part of the  $(\alpha h\nu)^2$  versus  $h\nu$  plot to zero as shown in Figure 2.13.

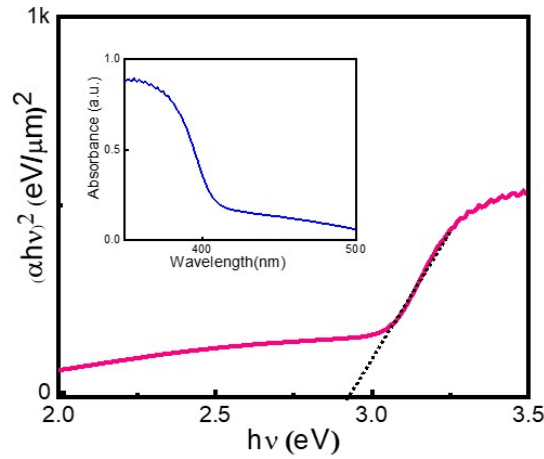


Figure 2.13: Tauc plot for  $\text{TiO}_2$  with the corresponding absorbance spectra in the inset.

For the opaque samples, the reflectance data were collected using diffuse reflectance spectroscopy (DRS) geometry. The ray diagram of the DRS is shown in Figure 2.12(b). Here, the light reflected from the sample is measured. One advantage of diffuse reflectance spectroscopy over other absorbance methods is to measure from the surfaces with rough or reflective. Here, the electromagnetic radiation reflected from the rough surface is collected and analyzed. The collected reflectance data are converted to the Kubelka-Munk function  $F(R)$  using equation 2.15.

$$F(R) = \frac{(1 - R)^2}{2R} \quad (2.15)$$

where  $R$  is the reflectance of the sample. The bandgap is calculated in the same process as done in the above case (equation 2.14). The only difference is that  $\alpha$  is replaced by  $F(R)$  in equation 2.14.



In this thesis, the absorbance spectra and reflectance of samples are analyzed using Agilent carry 5000 UV-Vis-NIR spectrometer in the UV and visible regions.

#### 2.4.10 Z-scan technique

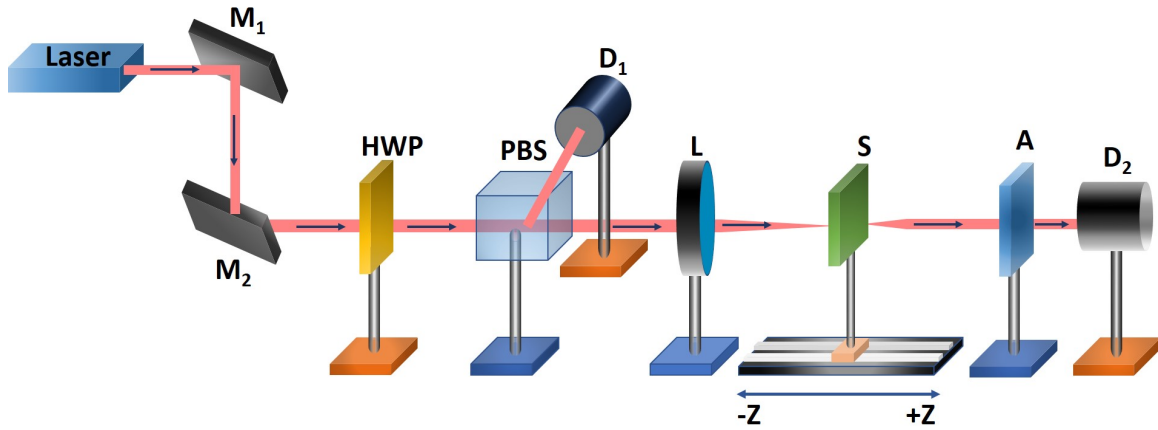


Figure 2.14: Schematic of Z-scan setup: ( $M_1, M_2$ ) mirrors; (HWP) half-wave plate; (PBS) polarizing beam splitter; ( $D_1$ ) reference detector; (L) lens; (S) sample; (A) aperture; ( $D_2$ ) signal photodetector.

Z-scan is a convenient technique to experimentally measure the nonlinear absorption coefficient and nonlinear refractive index of the samples using open aperture (OA) and closed aperture (CA) configurations, respectively. The NLO properties of the undoped and Cu-doped  $\text{TiO}_2$  nanoflowers were measured by the single beam Z-scan technique. The schematic of the Z-scan experimental setup is shown in Figure 2.14. The setup consists of a laser centered at wavelength 532 nm. The laser beam was aligned by mirrors  $M_1$  and  $M_2$  and the power was controlled by a combination of a half-wave plate (HWP) and a polarizing beam splitter (PBS). The reflected beam was captured by the reference detector ( $D_1$ ) and the transmitted beam was focused by the lens (L). The focused beam is passed through the sample and measured by the photo-detector ( $D_2$ ). In the case of OA, the aperture (A) was removed, and the detector ( $D_2$ ) detected all the transmitted power from the sample.

The normalized transmittance is fitted with equation (2.16) allows the determination of the nonlinear absorption coefficient[17].

$$\Delta T = 1 - \frac{\beta I_0 L_{eff}}{2^{3/2}(x^2 + 1)} \quad (2.16)$$

where  $I_0$  is the intensity of the laser beam at the focal plane (i.e.  $z=0$ ),  $L_{eff} = (1 - e^{-\alpha L})/\alpha$ ,  $L$  is the length of the sample,  $\alpha$  is linear absorption coefficient,  $x = z/z_0$ ,  $z$  is the sample position

In the CA measurement, the aperture was placed in front of the photo-detector ( $D_2$ ) to restrict the total optical power reaching the detector. The sample acts as a weak x-y dependent lens and a small distortion in the beam can be attributed to the nonlinear refractive index. The normalized transmittance is fitted with equation (2.17) allows the determination of the nonlinear refractive index[17].

$$\Delta T = 1 - \frac{4x\Delta\phi_0}{(x^2 + 9)(x^2 + 1)} - \frac{2(x^2 + 3)\Delta\Psi_0}{(x^2 + 1)(x^2 + 9)} \quad (2.17)$$

where  $\Delta\phi_0 = kn_2 I_0 L_{eff}$  and  $\Delta\Psi_0 = \beta I_0 L_{eff}/2$  is the phase change due to nonlinear refraction and absorption respectively,  $k=2\pi/\lambda$ ,  $\lambda$  is the laser wavelength.

The OA and CA measurements were carried out with a laser delivering linearly-polarized 500 ps pulses centered at a wavelength of 532 nm with a repetition rate of 1 kHz and a spot size ( $w_0$ ) 37.5  $\mu\text{m}$ . The Rayleigh length  $z_R = \frac{\pi w_0^2}{\lambda}$  was calculated to be 8.3 mm which is much greater than the thickness of the sample. The sample was placed on a translational stage, which moves along the z-axis through the focal plane.

#### 2.4.11 Superconducting quantum interference device

Superconducting quantum interference device (SQUID) is the most popular superconducting electronic device for measuring magnetic moment via the induction approach [18]. It is

a sensitive magnetometer that measures extremely weak magnetic fields as low as  $5 \times 10^{-14}$  T, based on superconducting loops containing Josephson junctions. The functioning of SQUID relies on two physical phenomena: flux quantization in a superconducting loop and Josephson tunneling[3].

In this thesis, the magnetic measurement is carried out using a Quantum Design MPMS3 SQUID-based magnetometer.

## References

- [1] Dinesh J. Ahirrao, Higgins M. Wilson, and Neetu Jha. TiO<sub>2</sub>-nanoflowers as flexible electrode for high performance supercapacitor. *Applied Surface Science*, 491:765, 2019.
- [2] Pavan M. V. Raja and Andrew R. Barron. Transmission Electron Microscopy, 2022.
- [3] MS Ramachandra Rao and Shubra Singh. *Nanoscience and nanotechnology: Fundamentals to Frontiers*. Wiley, 2017.
- [4] Amir Fayyaz, Haroon Asghar, and Tahani A Alrebdi. Laser-induced breakdown spectroscopy and energy-dispersive x-ray analyses for green mineral fluorite CaF<sub>2</sub>. *Results in Physics*, 52:106850, 2023.
- [5] Pandian Bothi Raja, Kabilashen Readdyi Munusamy, Veeradasan Perumal, and Mohamad Nasir Mohamad Ibrahim. Characterization of nanomaterial used in nanobioremediation. pages 57–83, 2022.
- [6] Kaihang Ye, Kunshan Li, Yirui Lu, Zhongjie Guo, Nan Ni, Hong Liu, Yongchao Huang, Hongbing Ji, and Pingshan Wang. An overview of advanced methods for the characterization of oxygen vacancies in materials. *TrAC Trends in Analytical Chemistry*, 116:102, 2019.
- [7] Layza Sá Rocha, Daniel Araújo Gonçalves, Daniela Granja Arakaki, Paula Fabiana Saldanha Tschinkel, Nayara Vieira de Lima, Lincoln Carlos Silva de Oliveira, Rita de Cássia Avellaneda Guimarães, and Valter Aragão do Nascimento. Data on elemental composition of the medicinal plant *hymenaea martiana hayne* (jatobá). *Data in brief*, 19:959, 2018.

- 
- [8] Haiying He and Zhaojun Zhang. Decay mechanism of optical phonons in  $\gamma$ -cui. *AIP Advances*, 9(5):055104, 2019.
- [9] Shuyan Zhang, Yi Qi, Sonia Peng Hwee Tan, Renzhe Bi, and Malini Olivo. Molecular fingerprint detection using raman and infrared spectroscopy technologies for cancer detection: A progress review. *Biosensors*, 13(5):557, 2023.
- [10] David W Hahn. Raman scattering theory. *Department of Mechanical and Aerospace Engineering, University of Florida*, 2007.
- [11] Ching-Lien Hsiao, Li-Wei Tu, Tung-Wei Chi, Min Chen, Tai-Fa Young, Chih-Ta Chia, and Yu-Ming Chang. Micro-raman spectroscopy of a single freestanding gan nanorod grown by molecular beam epitaxy. *Applied Physics Letters*, 90(4):043102, 2007.
- [12] Hirotaka Fujimori, Masato Kakihana, Koji Ioku, Seishi Goto, and Masahiro Yoshimura. Advantage of anti-stokes raman scattering for high-temperature measurements. *Applied physics letters*, 79(7):937, 2001.
- [13] Mitarani Sahoo, Sriram Mansingh, Satyabrata Subudhi, Priyabrat Mohapatra, and Kulamani Parida. A plasmonic aupd bimetallic nanoalloy decorated over a go/ldh hybrid nanocomposite via a green synthesis route for robust suzuki coupling reactions: a paradigm shift towards a sustainable future. *Catalysis Science & Technology*, 9(17):4678–4692, 2019.
- [14] Yongchao Huang, Wenjie Fan, Bei Long, Haibo Li, Fengyi Zhao, Zili Liu, Yexiang Tong, and Hongbing Ji. Visible light  $\text{Bi}_2\text{S}_3/\text{Bi}_2\text{O}_3/\text{Bi}_2\text{O}_2\text{CO}_3$  photocatalyst for effective degradation of organic pollutions. *Applied Catalysis B: Environmental*, 185:68, 2016.
- [15] RS Singh, S Bhushan, AK Singh, and SR Deo. Characterization and optical properties

- of CdSe nano-crystalline thin films. *Digest Journal of Nanomaterials and Biostructures*, 6(2):403, 2011.
- [16] Albert Zicko Johannes, Redi Kristian Pingak, and Minsyahril Bukit. Tauc plot software: Calculating energy gap values of organic materials based on ultraviolet-visible absorbance spectrum. In *IOP conference series: materials science and engineering*, volume 823, page 012030. IOP Publishing, 2020.
- [17] Mrinal K Sikdar, Nitul S Rajput, Ajanta Maity, and Pratap K Sahoo. Correlation between nonlinear optical properties and electronic band modification in cobalt-doped ZnO nanorods. *Physical Review Applied*, 14(1):014050, 2020.
- [18] Philippe Mangin, Rémi Kahn, Philippe Mangin, and Rémi Kahn. Superconducting quantum interference device “squid”. *Superconductivity: An introduction*, page 289, 2017.
- [19] A Kumari, A Kumar, R Dawn, J Roy, S Jena, R Vinjamuri, D Panda, SK Sahoo, VK Verma, S Mahapatra, et al. Effect of annealing temperature on the structural, electronic and magnetic properties of co doped TiO<sub>2</sub> nanoparticles: An investigation by synchrotron-based experimental techniques. *Journal of Alloys and Compounds*, 933:167739, 2023.

## Chapter 3

# Defect assisted Fano effect and magnetism in C ion implanted rutile $\text{TiO}_2$

### 3.1 Introduction

$\text{TiO}_2$  possesses intrinsic defects such as oxygen and titanium vacancies. The probability of oxygen vacancy is higher than the Ti vacancy. When a lighter and non-metallic atom like C is doped in  $\text{TiO}_2$ , it can take three possible positions; substitute O, substitute Ti, or occupy the interstitial position. From theoretical studies it is verified that the substitution of Ti by C is not favorable, so it can either substitute the O or occupy the interstitial position and create oxygen vacancy. The Stopping Range of Ions in Matter (SRIM) simulation indicates that both Ti and O vacancies are created upon C doping in  $\text{TiO}_2$  through ion implantation, and the number of O vacancies is higher than the Ti vacancy. In  $\text{TiO}_2$ , the presence of oxygen vacancy alters its electrical, optical, and magnetic properties. Based on the oxygen vacancy, two physical aspects are discussed in this chapter: (i) the Fano effect, (ii) defect-induced magnetism.

The electron-phonon interaction in semiconductors plays an important role in electronic and optoelectronic device applications[1]. Fano interaction is a special case of electron-phonon interaction arises due to interference of discrete states with the continuum of electronic state[2, 3]. In semiconductors, the discrete state is provided by phonons whereas the continuum state is achieved with heavy doping or photo-excitation[4]. This Fano interference is observed in semiconductors when the energy of a discrete state lies within the electronic continuum range. Unlike electron-phonon coupling the strength of Fano interaction

depends on the density of the electronic continuum state[5]. The oxygen vacancy is associated with two electrons. So increasing the number of oxygen vacancies, the population of the electrons in the conduction band can be enhanced and these electrons contribute to the Fano effect. Due to this Fano effect, the Raman spectra show asymmetry in the spectrum, and analysis of the Raman lineshape gives information on the strength of electron-phonon interaction [2].

The next part of this study explores magnetism in magnetic materials, which is directly related to unfilled orbitals of d- or f-subshells. The origin of magnetic moments in non-magnetic materials is largely attributed to defects[6]. The ideal TiO<sub>2</sub> is nonmagnetic, and it exhibits magnetism when vacancies (Ti vacancy and O vacancy) are created through doping in the TiO<sub>2</sub> matrix.

This chapter has two subsections: (a) the impact of the C ion on the Fano effect through Raman phonon modes asymmetry, (b) defect-induced ferromagnetic tuning through oxygen vacancies in rutile TiO<sub>2</sub> microflowers structures.

## 3.2 Experimental details

The TiO<sub>2</sub> microflowers were synthesized using the hydrothermal methods as discussed in Chapter 2. The prepared samples were implanted with 1.5 MeV C ions at different fluence of  $1 \times 10^{15}$ ,  $5 \times 10^{15}$ ,  $1 \times 10^{16}$ , and  $2 \times 10^{16}$  ions/cm<sup>2</sup>. The morphology of the samples were observed using FESEM and TEM. In addition to morphology, the local crystal structure was examined using TEM. The elemental composition of the sample was studied using EDS mapping. The crystal structure and crystal phase were analyzed using the XRD pattern. The optical property was studied using UV-visible spectroscopy with diffuse reflectance spectroscopy accessories. The vibrational modes were captured using Raman spectroscopy. The field-dependent magnetization (M-H) measurement was performed in the range of -



5000 to 5000 Oe in the temperature range of 5-300 K using SQUID magnetometry.

### 3.3 Ion beam simulations

When a target material is implanted with energetic ions, the projected range is decided by its kinetic energy, atomic mass, and density of target material. The distribution of ions in the samples and the vacancy created due to ion implantation were calculated from the SRIM simulations using 99,999 pseudo-particles[7]. As an input parameter for the simulation, the target density of rutile TiO<sub>2</sub> was taken 4.23 g/cm<sup>3</sup> and the energy of the implanted C was 1.5 MeV. The depth profile is obtained from the RANGE.txt file plotted in Figure 3.1(a). The schematic of ion implantation in TiO<sub>2</sub> flower is displayed in the inset of Figure 3.1(a). The mean projected range ( $R_p$ ) is found to be 1.36  $\mu$ m. In addition, the longitudinal straggling, lateral straggling, electronic energy loss, and nuclear energy loss are found to be 139 nm, 174 nm,  $1.812 \times 10^2$ , and 1.046 eV/Å, respectively. Further, the Ti and O vacancy created due to C ion implantation is obtained from the VACANCY.txt file as plotted in Figure 3.1(b). It has been observed that the number of oxygen vacancies is higher than the Ti vacancies. The defects (oxygen vacancy, C interstitials) created by C incorporation may displace the Ti and O atoms from their equilibrium positions. The defect density can be calculated using displacement per atom (DPA) as expressed in equation 3.1 for  $1 \times 10^{15}$ ,  $5 \times 10^{15}$ ,  $1 \times 10^{16}$ , and  $2 \times 10^{16}$  ions/cm<sup>2</sup> ion fluences. The value of  $\frac{vacancies}{ions \times A^o}$  was taken from the SRIM output file VACANCY.txt. The atomic density for rutile TiO<sub>2</sub> is  $9.56 \times 10^{22} \frac{atoms}{cm^3}$ . It has been observed that the number of DPA increases with ion fluence. So, with increasing ion fluence the defects in the TiO<sub>2</sub> system increases.

$$DPA = \left( \frac{vacancies}{ions \times A^o} \right) \times \frac{10^8 \left( \frac{A^o}{cm} \right) \times fluence \left( \frac{ions}{cm^2} \right)}{atom\ density \left( \frac{atoms}{cm^3} \right)} \quad (3.1)$$

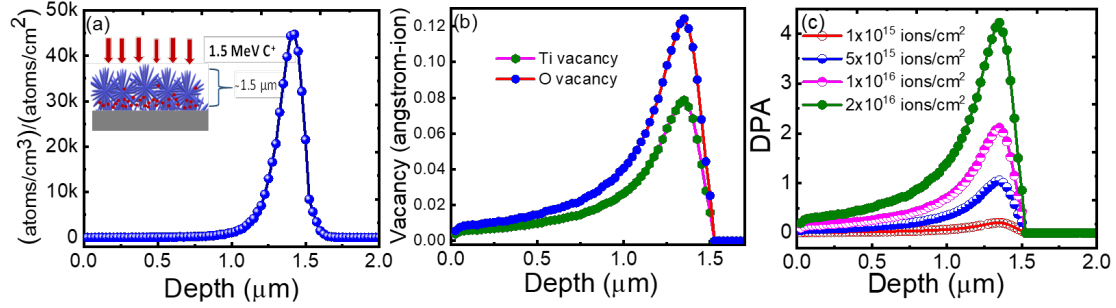


Figure 3.1: (a) Depth profile of 1.5 MeV C ion in  $\text{TiO}_2$  matrix with schematic in the inset. (b) Ti and O vacancy created due to 1.5 MeV C ion implantation. (c) Displacement per atom with depth for C ion implanted  $\text{TiO}_2$ .

### 3.4 Morphological, elemental, and structural studies

#### 3.4.1 FESEM, TEM, and elemental mapping

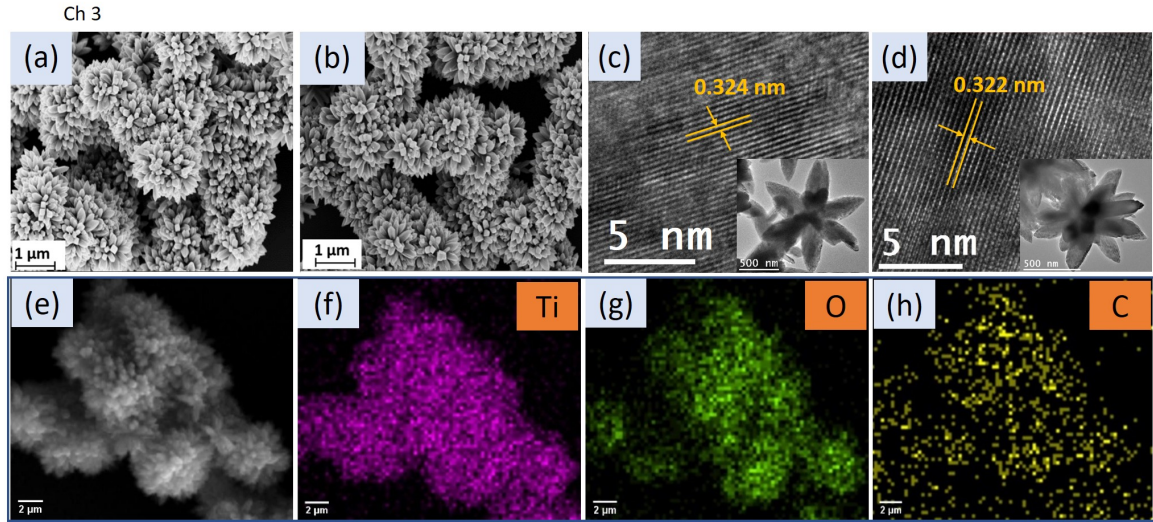


Figure 3.2: (a,b) FESEM image (c,d) HRTEM image with the corresponding low magnified image in the inset of pristine and  $2 \times 10^{16}$  ions/cm<sup>2</sup> C implanted  $\text{TiO}_2$ , respectively. (e-h) FESEM image and corresponding elemental mapping for  $2 \times 10^{16}$  ions/cm<sup>2</sup> C implanted  $\text{TiO}_2$ .

The FESEM images of all the samples are captured and it is observed that the morphol-

ogy of the samples remains unchanged after C ion implantation. Therefore the FESEM image of only two samples pristine and  $2 \times 10^{16}$  ions/cm<sup>2</sup> C ion implanted TiO<sub>2</sub> are shown in Figures 3.2 (a) and (b), respectively. The samples have a morphology similar to microflowers consisting of several nanorods. The length of nanorods is approximately 1.5-2  $\mu$ m, so the C ions will stay entirely inside the TiO<sub>2</sub> matrix. As a lighter element, C ions do not affect the sample surface morphology, however, the TiO<sub>2</sub> matrix becomes damaged due to defect formation. The affected crystallization is examined by XRD in the coming section.

The local microstructural characteristics of the samples are studied by taking the TEM images. The HRTEM images of pristine and  $2 \times 10^{16}$  ions/cm<sup>2</sup> C ion implanted TiO<sub>2</sub> are shown in Figures 3.2(c) and 3.2(d), respectively, with the corresponding low-magnified picture shown in the inset. The value of interplanar spacing is found to be 0.324 nm and 0.322 nm for pristine and  $2 \times 10^{16}$  ions/cm<sup>2</sup> C ion implanted sample, which is associated with the (110) plane of rutile TiO<sub>2</sub>.

Figure 3.2 (f-h) displays the elemental mapping of the  $2 \times 10^{16}$  ions/cm<sup>2</sup> C ion implanted TiO<sub>2</sub>, whereas Figure 3.2 (e) displays the corresponding FESEM image. This demonstrates that microflowers are composed of Ti and O atoms and the C atoms are distributed throughout the sample.

### 3.4.2 XRD

The X-ray diffraction pattern of pristine and C ion implanted TiO<sub>2</sub> for all fluences are shown in Figure 3.3(a). All the diffraction peaks correspond to the rutile phase of TiO<sub>2</sub> (JCPDS-870920). The crystallographic plane (110) is the highest intense peak, and the magnified view of this peak is displayed in Figure 3.3(b). From Figure 3.3(b), peak broadening and the peak shift towards a higher  $2\theta$  value are evident. The peak broadening with ion fluence indicates a decrease in crystallite size. The crystallite size of samples concerning the (110)

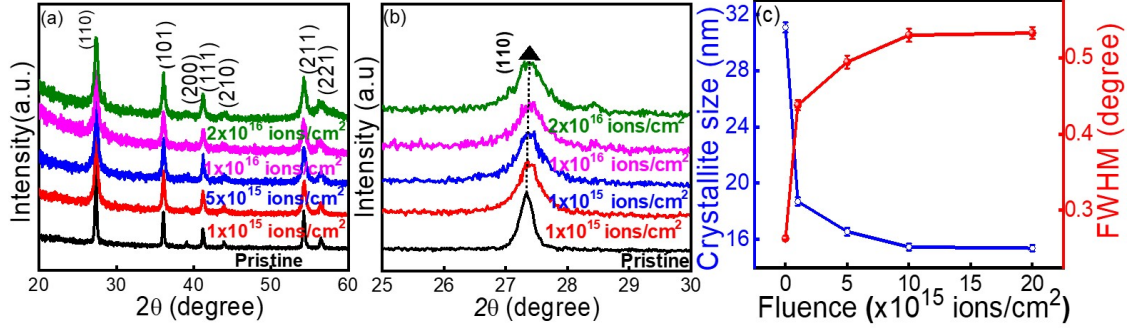


Figure 3.3: (a) XRD pattern pristine and C ion implanted TiO<sub>2</sub>. (b) Magnified view of (110) peak. (c) Variation crystallite size and FWHM with fluence.

peak is calculated using Sherrer's equation

$$D = \frac{0.9\lambda}{\beta \cos \theta} \quad (3.2)$$

where  $D$  is the crystallite size,  $\lambda$  is the wavelength of incident X-ray (1.5418 Å),  $\beta$  is the full-width at half maxima (FWHM) in radian and  $\theta$  is the angle of diffraction[8]. The variation of crystallite size and FWHM with C ion fluence is plotted in the left panel and right panel of Figure 3.3(c), respectively. The increased FWHM indicates degradation of crystalline quality due to structural defect[9, 10].

Table 3.1:  $2\theta$ , dislocation density, and strain calculated from XRD

Sample	$2\theta$ (degree)	$\delta$ ( $\times 10^{-3} nm^{-2}$ )	strain ( $\times 10^{-3}$ )
Pristine	27.334	1.035	4.723
$1 \times 10^{15}$	27.375	2.861	7.842
$5 \times 10^{15}$	27.382	3.648	8.853
$1 \times 10^{16}$	27.392	4.184	9.478
$2 \times 10^{16}$	27.384	4.230	9.533

The crystallite size is found to be decreased with increasing C ion fluence, which can be attributed to the interstitial doping of C in the TiO<sub>2</sub> matrix. The defects inside the matrix displace its crystallinity, which can be understood from the dislocation density ( $\delta$ ). This is

given by the relation [8]

$$\delta = \frac{1}{D^2} \quad (3.3)$$

It is defined as the number of dislocation lines per unit volume of crystal and illustrates the degree of crystallinity in a nanomaterial. The calculated value of  $\delta$  is displayed in Table 3.1. Additionally, the position of (110) peak shifts towards a higher  $2\theta$  value, which denotes the presence of compressive strain. The strain ( $\epsilon$ ) is calculated using equation 3.4[11].

$$\epsilon = \frac{\beta}{4\tan\theta} \quad (3.4)$$

The obtained value of  $2\theta$ , dislocation density, and strain are presented in Table 3.1. It has been observed that both the dislocation density and strain increase with ion fluence.

## 3.5 Optical studies

### 3.5.1 UV-visible spectroscopy

The optical bandgap calculation is performed using diffuse reflectance spectroscopy. The reflectance data were collected in the range 320 nm to 700 nm for pristine and C ion implanted TiO<sub>2</sub> and converted to Kubelka-Munk function ( $F(R)$ ) as shown in Figure 3.4(a). Then the bandgap is calculated using the Tauc relation defined as follows,

$$(F(R)h\nu)^n = A(h\nu - E_g) \quad (3.5)$$

where,  $E_g$  is the bandgap,  $h\nu$  incident energy, and A is constant. For direct and indirect bandgap semiconductors  $n=2$  and  $n=\frac{1}{2}$  respectively[12]. The bandgap is obtained by extrapolating the linear part of the  $(F(R)h\nu)^2$  versus  $h\nu$  plot to zero and plotted in the left panel of Figure 3.4(b). The value of the bandgap narrows down from pristine to the highest fluence of C implanted TiO<sub>2</sub>. This lowering in the bandgap may be attributed to the creation of different kinds of defects, such as oxygen vacancies and C-induced defect states. It has

been reported that the C ions create intermediate states above the valence band minimum, which leads to the red shifting of the absorption peaks[13].

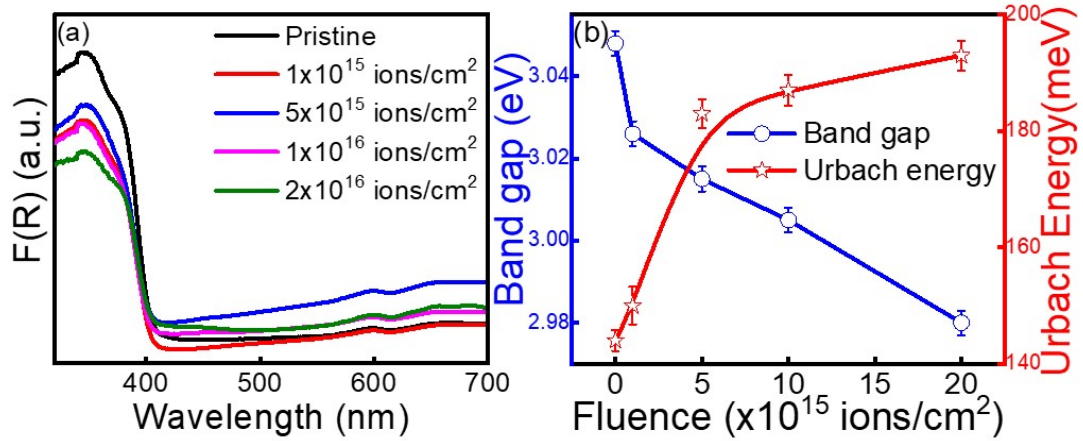


Figure 3.4: (a) Kubelka-Munk function plotted against wavelength for pristine and C ion implanted TiO<sub>2</sub>. (b) Variation of bandgap (left panel) and Urbach energy (right panel) with C ion fluence.

Additionally, the analysis of the Urbach energy is used to examine the crystal disorder in the material. The broadness of the density of states can be quantified through Urbach energy, which can be measured from the sharpness of the onset of absorption near the band edge. The value of Urbach energy increases with the number of defect states. The Urbach energy can be calculated using the relation

$$\alpha = \alpha_0 + \exp\left(\frac{E}{E_u}\right) \quad (3.6)$$

where  $\alpha$  is the absorption coefficient,  $E$  is the photon energy ( $h\nu$ ) and  $E_u$  is the Urbach energy[14]. By plotting  $\ln\alpha$  with energy ( $E$ ), we can determine the value of Urbach energy from the slope. The Kubelka Munk function  $F(R)$  is proportional to the absorption coefficient. So, we have plotted  $\ln F(R)$  with energy. The linear part of the curve is fitted with a linear equation, and a slope is obtained. The Urbach energy is the reciprocal of the slope. The value of Urbach energy increases from 144 meV to 198 meV while going from



pristine to the highest C implanted  $\text{TiO}_2$  as shown in the right panel of figure 3.4(b). This phenomenon is due to the disorder or defect introduced in the  $\text{TiO}_2$  matrix by incorporating carbon ions, which corroborates with the XRD data.

### 3.6 Raman spectroscopy and Fano asymmetry

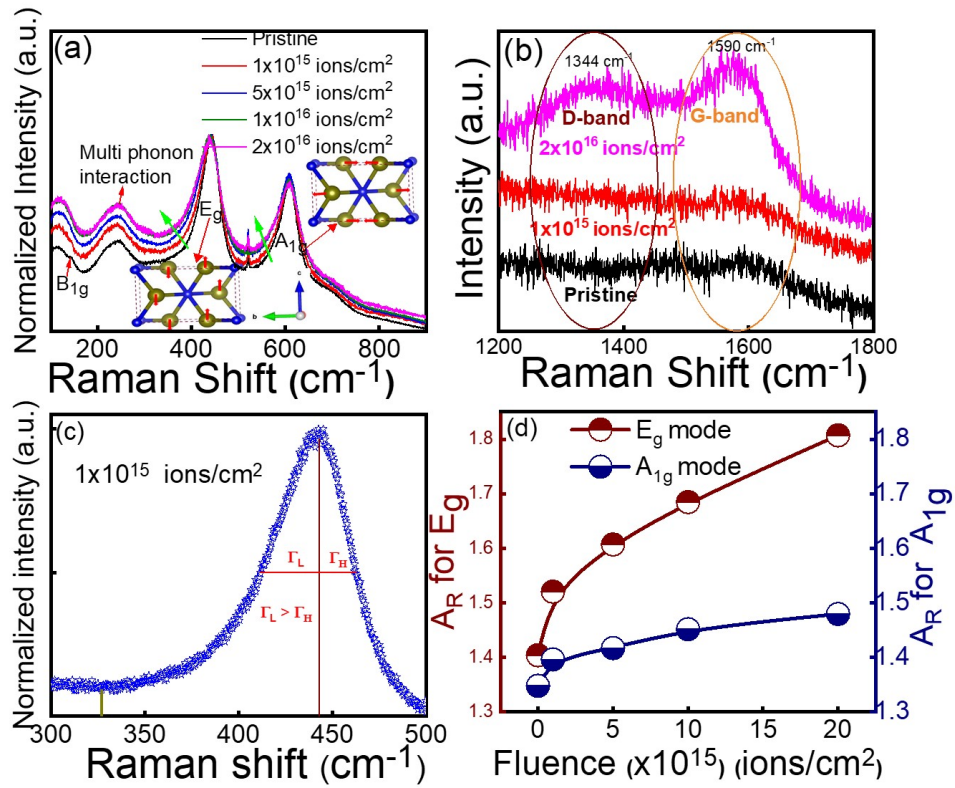


Figure 3.5: Raman spectra of pristine and C ion implanted  $\text{TiO}_2$  (a) in the range 150-850  $\text{cm}^{-1}$  (b) in the range 1200-1800  $\text{cm}^{-1}$ . (c) Raman spectra of  $E_g$  mode showing the calculation of asymmetry ratio. (d) Variation of asymmetric ratio with C ion fluence for  $E_g$  and  $A_{1g}$  mode.

The room temperature Raman spectra of pristine and C ion implanted  $\text{TiO}_2$  samples in the range 150-850  $\text{cm}^{-1}$  are displayed in Figure 3.5(a). The Raman peaks observed around 141, 245, 441, and 607  $\text{cm}^{-1}$  are attributed to  $B_{1g}$ , multi-phonon interaction,  $E_g$ , and  $A_{1g}$  mode of rutile  $\text{TiO}_2$ , respectively as discussed in Chapter 1(section 1.1.5). The small peak

at 521 cm<sup>-1</sup> originates from the silicon substrate. The vibrational modes E<sub>g</sub> and A<sub>1g</sub> are more noticeable, while B<sub>1g</sub> has a very low intensity. Here, we will concentrate on the E<sub>g</sub> and A<sub>1g</sub> modes. In Figure 3.5(a), it is observed that the asymmetry in the E<sub>g</sub> and A<sub>1g</sub> mode is increasing towards the lower wavenumber with increasing C fluence. The Raman peak associated with the E<sub>g</sub> mode of vibration is more asymmetric than the A<sub>1g</sub> mode of vibration. This demonstrates that ion implantation has a greater impact on the E<sub>g</sub> mode than the A<sub>1g</sub> mode. It is also reported in several literature that the E<sub>g</sub> mode gets more affected than the A<sub>1g</sub> mode in response to temperature and impurity[15, 16].

To look into the peaks that belong to C atoms, the Raman spectra of pristine, lowest (1 × 10<sup>15</sup> ions/cm<sup>2</sup>), and highest (2 × 10<sup>16</sup> ions/cm<sup>2</sup>) dose C ion implanted TiO<sub>2</sub> samples are displayed in Figure 3.5(b). Impellizzeri et al. reported the appearance of D and G bands of C located at 1450 and 1590 cm<sup>-1</sup> respectively in C ion implanted TiO<sub>2</sub> indicating the cluster of C present in TiO<sub>2</sub>[17]. In TiO<sub>2</sub> that has been chemically doped with C, the D and G bands of C have also been observed in the higher frequency range of Raman spectra[18, 19]. In this work, at the lowest fluence, there is no signature of C peak due to less amount of C. However, when the fluence rises, two broad peaks around 1344 cm<sup>-1</sup> and 1590 cm<sup>-1</sup>, which correspond to the D-band and G-band of C, respectively, arise[20]. This indicates the formation of C nanoclusters in TiO<sub>2</sub>. Similar results were observed when C ions of high fluence (6 × 10<sup>16</sup> ions/cm<sup>2</sup>) were inserted into SiO<sub>2</sub>[21].

Further, the Raman asymmetric broadening is characterized by the asymmetric ratio (A<sub>R</sub>) defined as  $A_R = \frac{\Gamma_L}{\Gamma_R}$ , where  $\Gamma_L$  and  $\Gamma_R$  are half widths on the low and high energy side of the peak, respectively[22]. Figure 3.5(c) depicts  $\Gamma_L$  and  $\Gamma_R$  of 1 × 10<sup>15</sup> C ion/cm<sup>2</sup> implanted sample of the E<sub>g</sub> mode, where  $\Gamma_L > \Gamma_R$ . Furthermore, the intensity at the left end of the peak is greater than the right end, indicating asymmetry in the lower wavenumber side. The value of A<sub>R</sub> for E<sub>g</sub> and A<sub>1g</sub> mode with ion fluences are plotted in Figure 3.5(d) and it is found to be greater than 1, indicating the asymmetry is pronounced in the lower



wavenumber region.

The quantum confinement effect and the Fano effect cause the asymmetry in the Raman line shape[2, 3]. The size of the crystal must be similar to the Bohr exciton radius to achieve the quantum confinement effect[23]. In our samples, quantum confinement is not feasible. So the asymmetry may be attributed to the Fano effect. To confirm this, the Raman line shape of E<sub>g</sub> and A<sub>1g</sub> mode was fitted with the Breit-Wigner-Fano (BWF) line shape which is given by the relation,

$$I(\omega) = I_0 \frac{(1 + \frac{\omega - \omega_0}{q\Gamma})^2}{1 + (\frac{\omega - \omega_0}{\Gamma})^2} \quad (3.7)$$

Where  $I(\omega)$  is the intensity of Raman line shape as a function of  $\omega$ ,  $I_0$  is the maximum peak intensity,  $\omega_0$  is the peak position,  $\Gamma$  is the linewidth of the phonon mode and  $1/q$  is the asymmetry parameter that measures the strength of the electron-phonon interaction[24]. The larger value of  $1/q$  suggests stronger electron-phonon interaction and causes the Raman peak to be more asymmetric. When  $1/q \rightarrow 0$ , the electron-phonon interaction becomes weak and the Raman line shape will have a Lorentzian shape instead of Fano line shape[2, 3].

As a function of ion fluences, the impact of defects on the asymmetry parameter is investigated for both the E<sub>g</sub> and A<sub>1g</sub> modes. Figure 3.6(a)-(c) shows the fitted curve of E<sub>g</sub> vibrational mode with equation (3.7) in the range 300-510 cm<sup>-1</sup>. The sign of the asymmetry parameter is found to be negative as the asymmetry is towards the lower wavenumber side. This indicates constructive interference between the discrete phonon and electronic continuum on the lower wavenumber side and destructive interference on the higher wavenumber side of the Raman line shape[22]. Figure 3.6(d) depicts the magnitude of the asymmetry parameter for E<sub>g</sub> and A<sub>1g</sub> modes with C ion fluence, which is found to increase with increasing C fluence. Further, Figure 3.6(e) shows the theoretical plot of the BWF function when the asymmetry parameter is varied. The shape of the curve is symmetric when  $1/q$  is zero,

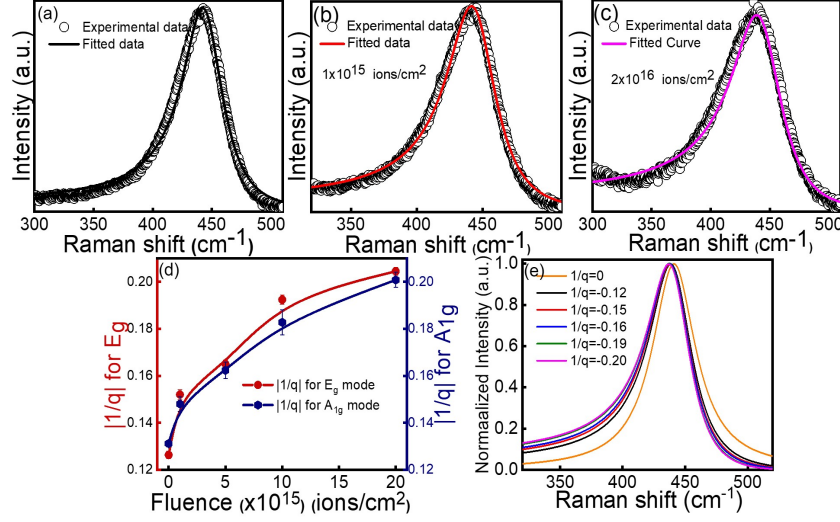


Figure 3.6:  $E_g$  vibrational mode of (a) Pristine (b)  $1 \times 10^{15}$  and (c)  $5 \times 10^{15}$  ions/ $\text{cm}^2$  C ion implanted  $\text{TiO}_2$  fitted with equation (3.7). (d) Variation of  $|1/q|$  with ion fluence for  $E_g$  and  $A_{1g}$  mode. (e) Theoretically plotted BWF function with varying asymmetry parameters for  $E_g$  mode.

and the asymmetry towards lower wavenumbers increases as the value of  $1/q$  increases.

In general,  $\text{TiO}_2$  is an n-type semiconductor due to the presence of oxygen vacancies[13]. In n-type semiconductors, the phonons interfere with the conduction band continuum and result in asymmetry in the lower energy side of the Raman peak[3]. The C ion implantation creates oxygen vacancies, as shown in Figure 3.1(b), and each oxygen vacancy is associated with two electrons. So with ion implantation, the number of electrons increases which enhances the probability of electron-phonon interaction. This results in the increasing value of asymmetric parameters with ion fluence. Magidson et al. reported that the increase in the asymmetry parameter with boron concentration in Si is due to an increase in the concentration of holes[25]. It can be expected that the asymmetry parameter is approximately proportional to the concentration of electrons.

The temperature-dependent Raman spectroscopy can provide an understanding of the effect of ion-induced defects on phonon modes. To study the effect of temperature on the

asymmetry parameter, temperature-dependent Raman spectroscopy was performed. The data were collected in the temperature range of 100-300 K. Figure 3.7(a) shows the Raman spectra as a function of temperature for E<sub>g</sub> and A<sub>1g</sub> modes. From the graph, it is clear that the rutile phase remains unchanged with temperature. Figure 3.7(b) is the plot of  $|\frac{1}{q}|$  with temperature for both E<sub>g</sub> (left side) and A<sub>1g</sub> (right side) mode of vibration. The asymmetry parameter remains almost constant up to 220 K, then it suddenly increases with an increase in temperature. This indicates that the electron-phonon interaction behavior is different below and above a critical temperature (T<sub>c</sub>) of 220 K. The flat region in the temperature range of 100 K to 220 K may be attributed to less mobility of free electrons. Above T<sub>c</sub>, the number of phonons increases with temperature and follows the Bose-Einstein distribution law, which contributes to an increase in the value of  $|\frac{1}{q}|$ . Magidson et al. reported the temperature-dependent (5-750 K) asymmetry parameter  $|\frac{1}{q}|$  for doped Si. They observed a flat region in the temperature range of 150–250 K for a low doped sample which is attributed to the reduction of the concentration of free holes at low temperatures [25]. As temperature increases, more phonons and free electrons are created. The phonon couples with the electronic system, enhancing the elastic and inelastic electron-phonon scattering and hence increasing the asymmetry parameter[26]. However, the BWF line shape looks different for the 1D geometry of TiO<sub>2</sub> nanorods in microflowers as compared to bulk-doped Si.

The variation in asymmetry parameter with temperature for the lowest and highest dose of C implanted samples are shown in Figure 3.7(c). In contrast to the pristine sample, as shown in Figure 3.7(c), the implanted samples exhibit sinusoidal behavior with a period of approximately 60 K. The amplitude is higher for the sample implanted with a dose of  $2 \times 10^{16}$  ions/cm<sup>2</sup>. After 240 K, the asymmetry parameter increases and starts falling at 280 K for  $2 \times 10^{16}$  ions/cm<sup>2</sup> and at 300 K for  $1 \times 10^{15}$  ions/cm<sup>2</sup> implanted sample. This behavior may be attributed to less number of defect concentration in  $1 \times 10^{15}$  ions/cm<sup>2</sup> implanted

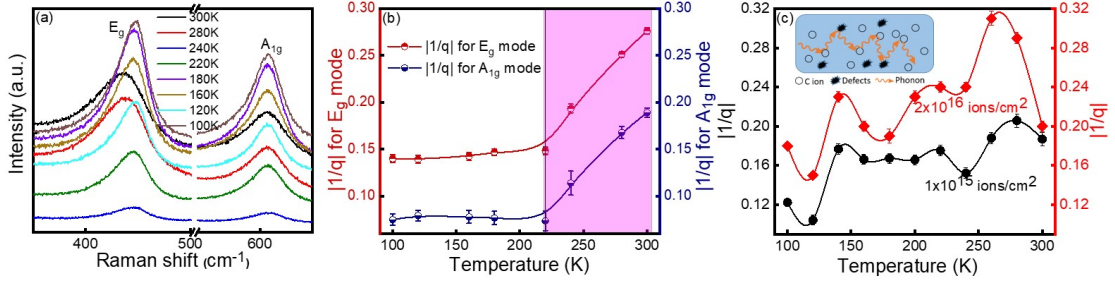


Figure 3.7: (a) Temperature dependent Raman spectra of pristine TiO<sub>2</sub> showing  $E_g$  and  $A_{1g}$  mode. (b) Variation of  $|\frac{1}{q}|$  with temperature for  $E_g$  and  $A_{1g}$  mode of pristine TiO<sub>2</sub>. (c) Variation of  $|\frac{1}{q}|$  with temperature for  $1 \times 10^{15}$  and  $2 \times 10^{16}$  ions/cm<sup>2</sup> C ion implanted TiO<sub>2</sub>.

samples than  $2 \times 10^{16}$  ions/cm<sup>2</sup> implanted sample. The sinusoidal behavior arises from the scattering of phonons by impurity ions and defects created by ion irradiation. At all temperatures, the value of the asymmetry parameter for the lowest implanted sample is less than the highest implanted sample, which supports the data presented in Figure 3.5(a). The inset shows a schematic diagram of the scattering mechanism inside TiO<sub>2</sub> nanorods. The projected range of 1.5 MeV C ions in TiO<sub>2</sub> is 1.36  $\mu\text{m}$ . From Figure 3.1(a), one can observe that the Ti and O vacancies are distributed in the range of 1000 to 1500 nm from the surface. Below 1500 nm depth, TiO<sub>2</sub> is crystalline. The interference between the defect states and discontinuous crystalline TiO<sub>2</sub> could be a possible reason for such sinusoidal oscillation of asymmetry parameters with temperature.

### 3.6.1 Conclusion on Fano asymmetry

The asymmetry parameter ( $|\frac{1}{q}|$ ) is a measure of electron-phonon interaction. At a particular temperature, the asymmetry parameter increases with increasing C ion implantation, indicating that the electron-phonon interaction increases with ion fluence. At lower temperatures, the number of phonons is less, so the probability of electron-phonon interaction is less, and the asymmetry parameter remains almost constant. As the temperature increases,

the asymmetry parameter increases as more phonons are generated. From the above discussion, we can conclude that the asymmetry parameter can be tuned locally by introducing defects and varying temperatures. When the defects have been introduced into a crystalline matrix, each defect center acts as a single scattering point for electrons and phonons. The scattered waves interfere and display a short-range phenomenon. The defects weaken the electron-phonon interaction, and a weak-localized Fano asymmetry can be observed. The study of the Fano effect helps to understand electronic transport and different phenomena occurring in the system at the microscopic level[27].

### 3.7 Ferromagnetism (FM) in C ion implanted TiO<sub>2</sub>

The field-dependent magnetic moment (M-H) of the pristine and C ion-implanted samples in the field range -5000 to 5000 Oe at four different temperatures, 300 K, 200 K, 50 K, and 5 K are collected to study the magnetic properties of samples. It is evident from the hysteresis loop that the samples are ferromagnetic at low temperatures as well as room temperature (RT). Therefore, only the M-H loop of pristine and C ion implanted samples collected at RT (300 K) is displayed in Figure 3.8(a). The S-shaped small hysteresis loop is the signature of weak ferromagnetism. It is well-known that the pure TiO<sub>2</sub> is non-magnetic. It shows ferromagnetism in the presence of O vacancy, Ti vacancy, and magnetic impurity[28–30]. Hence, in this work, the ferromagnetism observed in the pristine TiO<sub>2</sub> is attributed to the presence of defects such as oxygen vacancies and Ti vacancies which are intrinsic defects in TiO<sub>2</sub> and depend on the sample preparation method. However, the contribution of Ti vacancy towards magnetism is not clear. The non-magnetic property of TiO<sub>2</sub> upon Ti vacancy has been reported theoretically[31]. Additionally, it has been claimed in the literature that the emergence of ferromagnetism in undoped TiO<sub>2</sub> is caused by oxygen vacancies[29, 31, 32]. In contrast to Ti vacancy defects, Mansour *et al.* revealed that FM

is substantially related to oxygen vacancy[32].

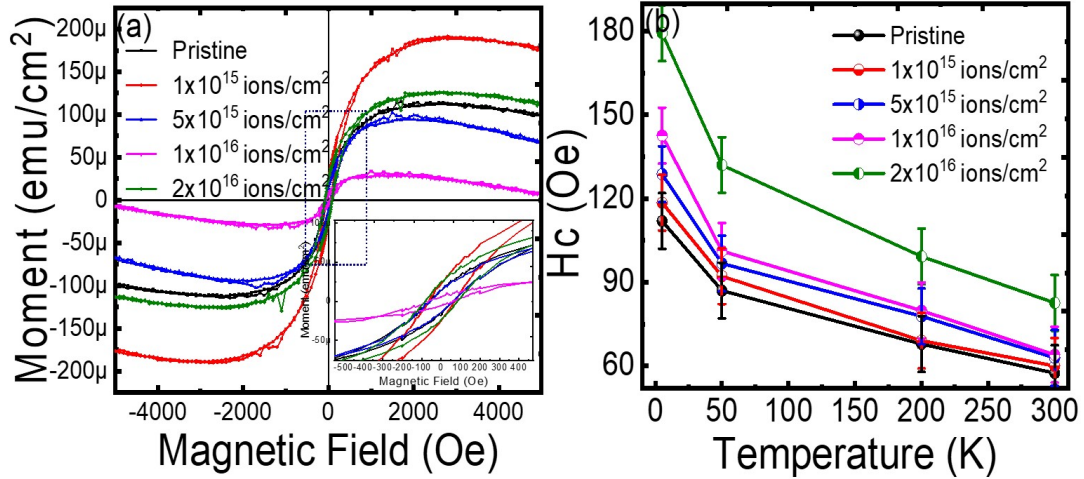


Figure 3.8: (a) Room temperature magnetic moment vs magnetic field with the magnified view of the dotted rectangular area in the inset. (b) Variation of the coercive field with temperature.

Furthermore, the C ion implantation produces both O and Ti vacancies however, the number of oxygen vacancies are higher than the number of Ti vacancies. Ion implantation modifies the defects and influences the magnetic property. It has been observed that the oxygen vacancy in TiO<sub>2</sub> is a major factor in the emergence of ferromagnetism. When one oxygen vacancy is created, two electrons occupy that place to preserve charge neutrality. The oxygen vacancy with two electrons is known as the F center ( $V_0 + 2e^- = F$ ). One of the two electrons tends to be captured by the Ti<sup>4+</sup> ion and forms Ti<sup>3+</sup> ( $Ti^{4+} + e^- = Ti^{3+}$ ) and the F center gets converted to F<sup>+</sup>. The electronic configuration of Ti<sup>3+</sup> is [Ar]3d<sup>1</sup> and of F<sup>+</sup> is 1s<sup>1</sup>. The exchange interaction between 1s<sup>1</sup> electron spin of F<sup>+</sup> and 3d<sup>1</sup> of Ti<sup>3+</sup> around the oxygen vacancy favors the ferromagnetism[33]. Zhou *et al.* also reported Ti<sup>3+</sup> ions having one unpaired 3d electron provide local magnetic moment in defective rutile TiO<sub>2</sub> single crystal[34].

Figure 3.8(b) displays the variation of the coercive field ( $H_c$ ) with temperature for pristine and C ion implanted TiO<sub>2</sub>. It is demonstrated that for all samples, the value of  $H_c$  increases exponentially when the temperature drops from 300 K to 5 K. This behavior is believed to be caused by less thermal agitation and strong magnetic moment due to net spin alignment in the direction of the external magnetic field at a lower temperature[35]. Furthermore, in C ion implanted TiO<sub>2</sub>, the coercive field is larger than in pristine TiO<sub>2</sub>. This may be attributed to the increase in crystal disorder of the TiO<sub>2</sub> matrix upon C ion implantation. Thus, by varying the C ion fluence, the coercive field can be altered.

### 3.8 Theoretical studies

The origin of ferromagnetic ordering in rutile TiO<sub>2</sub> was analyzed theoretically by performing first-principles density functional theory (DFT) calculations using VASP[36]. The Perdew-Burke-Ernzerhof (PBE) parametrization-based generalized gradient approximation (GGA) was chosen for the exchange-correlation functional[37]. The crystal structure of rutile TiO<sub>2</sub> was generated using VESTA [38] and a  $2 \times 2 \times 1$  supercell was considered for the calculation. The Ti or O vacancies were created by removing one Ti or O atom from the supercell. The plane wave expansion cut-off was chosen to be 520 eV. The Brillouin zone integration was performed using a  $\Gamma$ -centered ( $9 \times 9 \times 9$ ) k-mesh for the electronic structure calculation of TiO<sub>2</sub> nanocrystals. The geometry optimization used a  $\Gamma$  centered ( $7 \times 7 \times 7$ ) k-point samplings. All the structures are allowed for relaxation calculation to get the optimized atomic position until the total forces acting on each atom are less than 0.02 eV/Å. The magnetic property study was carried out using the spin-polarized density of states (DOS) calculation using the tetrahedron method with denser ( $18 \times 18 \times 18$ ) k-point samplings.

To study the defect-induced ferromagnetic properties in rutile TiO<sub>2</sub>, three different structures are taken into consideration namely pristine TiO<sub>2</sub>, TiO<sub>2</sub> with one Ti vacancy,



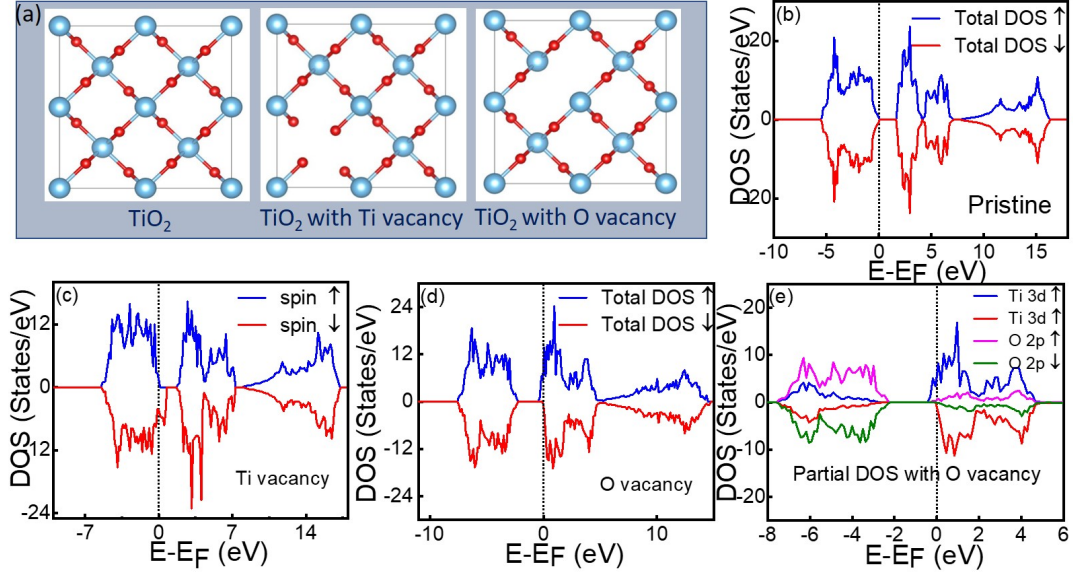


Figure 3.9: Crystal structure of  $\text{TiO}_2$ . (a) Pristine structure, with Ti, and with O vacancy. Blue balls represent Ti atom and red balls represent O atom. The spin-polarized total density of states of states of  $\text{TiO}_2$  (b) Pristine structure (c) with Ti vacancy, (d) with O vacancy. (e) The corresponding partial density of states of  $\text{TiO}_2$  with oxygen vacancy.

and  $\text{TiO}_2$  with one O vacancy, and are shown in Figure 3.9(a). The total energy calculated for each structure is -211.29, -188.94, and -201.88 eV respectively. Figure 3.9(b) illustrates the spin-polarized total density of states (DOS) for the pristine  $\text{TiO}_2$  which shows the equal population of up spin and down spin density of states with zero net magnetic moments. In the presence of either Ti or O vacancy, the density of states plot indicates a ferromagnetic character with unequal distribution of up spin and down spin states as shown in Figures 3.9(c-d). In the case of Ti vacancy, the down spin channel in the valence band region has a finite DOS at the Fermi level. Similarly, in the presence of oxygen vacancy, the up-spin states in the conduction band region have a finite population at the Fermi level. Since the total energy calculation indicates that the  $\text{TiO}_2$  with O vacancy is more favorable than  $\text{TiO}_2$  with Ti vacancy, we consider the  $\text{TiO}_2$  with oxygen vacancy as our initial undoped structure. The corresponding partial DOS as shown in Figure 3.9(d) illustrates the contribution



of the Ti-3d and O-2p states forming the ferromagnetic states. It is clear from the Figure that the valence band region is largely populated by O-2p states, whereas the conduction band region indicates a larger orbital occupancy of Ti-3d states.

The effect of C ion intercalation on the magnetic properties of TiO<sub>2</sub> is analyzed by inserting a carbon atom inside the TiO<sub>2</sub> unit cell at different possible sites such as (a) interstitial site near the O vacancy, (b) interstitial site far from oxygen vacancy, (c) replacing Ti atom, and (d) replacing O atom. The corresponding crystal structure designed using VESTA is shown in Figure 3.10(a-d). The total energy of the above-mentioned structures has values of -351.64 eV, -351.42 eV, -326.09 eV, and -339.63 eV respectively. It is found that when the C atom is in the interstitial region near the oxygen vacancy, the crystal structure has a minimum total energy thus indicating the stable ground state structure. Therefore it is concluded that the C atom after implantation prefers to stay near the interstitial region of the O vacancy. The lattice parameters of the undoped pristine TiO<sub>2</sub> supercell were  $a=b=9.206$  Å,  $c=2.966$  Å and  $\alpha = \beta = \gamma = 90^\circ$ . After structural relaxation, it was found that the unit cell of rutile TiO<sub>2</sub> in the presence of O vacancy, as well as C intercalation, undergoes a structural distortion along the three crystallographic axes. The lattice parameters of the optimized relaxed structure were  $a=9.147$  Å,  $b=9.657$  Å,  $c=3.015$  Å and  $\alpha = 95.20^\circ$ ,  $\beta = 89.72^\circ$ ,  $\gamma = 93.63^\circ$ .

Next, we performed spin-polarized total and partial DOS calculations to study the observed ferromagnetic nature of the C intercalated sample. However, calculations using GGA functionals alone exhibit the nonmagnetic behavior of the C implanted structure with a zero net magnetic moment. Therefore the calculations are performed again using GGA+U approximation, which indicates a highly ferromagnetic signature in the sample with the total magnetic moment was estimated to be around  $9 \mu_B$ . The spin-polarized total density of states calculations of the corresponding structure as shown in Figure 3.10(e), illustrate an unequal population of up-spin and down-spin states, thus indicating a finite nonzero

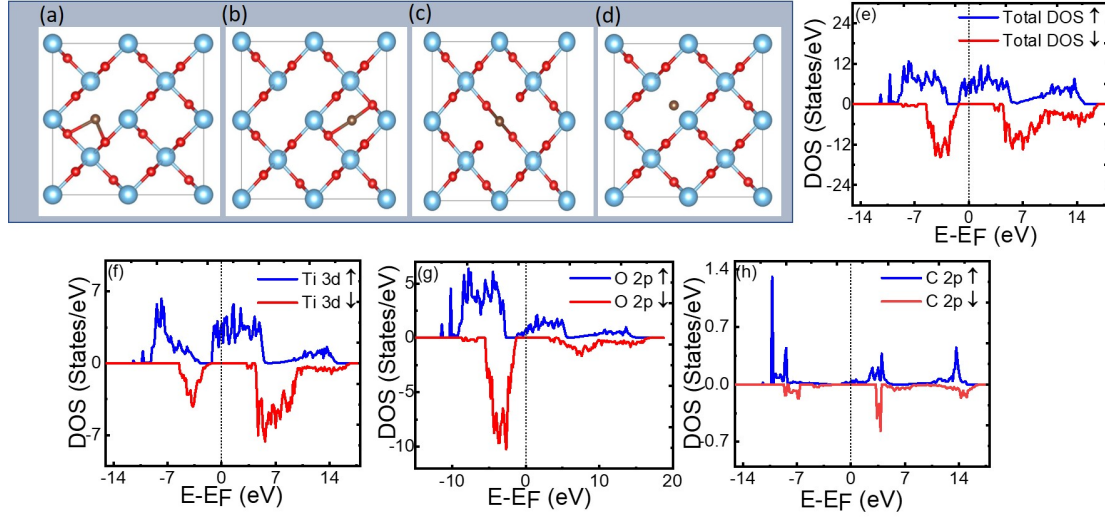


Figure 3.10: Crystal structure of  $\text{TiO}_2$  with (a) oxygen vacancy and C at an interstitial site near the O vacancy, (b) oxygen vacancy and C at interstitial region far from oxygen vacancy, (c) C replacing the Ti atom, and (d) C replacing the O atom. (e) The spin-polarized total density of states for structure (a). The corresponding partial density of states of (f) Ti 3d, (g) O 2p, and (h) C 2p orbitals.

magnetic moment. The spin-polarized partial DOS of the C intercalated  $\text{TiO}_2$  shows the contribution of different atomic orbitals responsible for the magnetic behavior of the sample. The 3d orbitals of Ti (Figure 10f) illustrate that the up spin states are nearly half-filled and the down spin states are mostly empty. Thus, the magnetic moment becomes larger due to the unequal population of Ti-3d orbitals. Interestingly, the nonmagnetic 2p states of O and C also exhibit spin polarization with a finite magnetic moment (Figure 3.10(g-h)). However, the O atoms exhibit a larger orbital occupancy in the valence band region and less occupancy in the conduction band region. On the other hand, the C atom indicates that the up spin electron is occupied, whereas the down spin orbital is vacant, indicating a finite magnetic moment. Thus, the increase in the magnetic moment in C implanted  $\text{TiO}_2$  is due to the interaction between Ti-3d and O-2p states.

The effect of C ion implantation on the charge density of  $\text{TiO}_2$  is evidenced by the

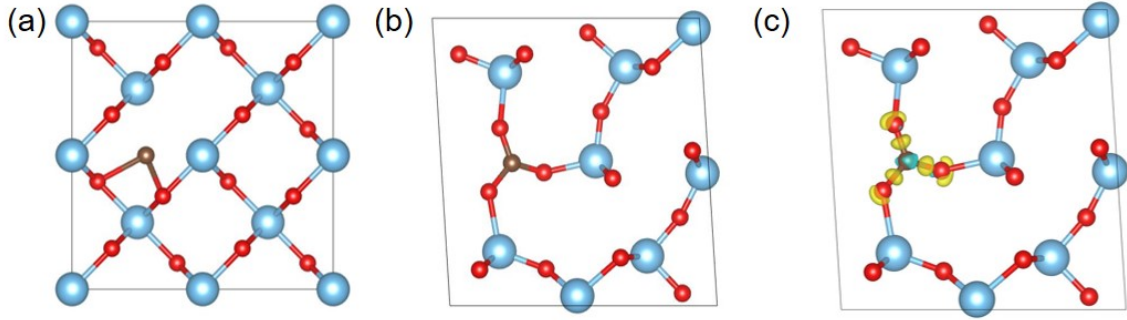


Figure 3.11: Crystal structure of C implanted rutile  $\text{TiO}_2$  with oxygen vacancy (a) before (b) after structural relaxation. (c) Charge density difference of the relaxed  $\text{TiO}_2$ .

calculated charge density difference calculations. This quantity is estimated by calculating the charge density of C implanted  $\text{TiO}_2$  and subtracting the charge density of isolated C atom and  $\text{TiO}_2$  without C atoms. From the charge density difference plot as shown in Figure 3.11, the cyan color represents a charge depletion that appears near the C atom. Similarly, the yellow color reveals a charge accumulation near the O atom. This indicates that there is a charge transfer from the C atom to the O atom.

### 3.8.1 Conclusions on ferromagnetism

As carbon ion is implanted in the  $\text{TiO}_2$ , more defects are created in  $\text{TiO}_2$  with fluence in terms of O and Ti vacancy. Again, the oxygen vacancy present in  $\text{TiO}_2$  is responsible for the ferromagnetic behavior. The coercivity of the samples is found to be increasing with C ion fluence indicating that higher defects produce better magnetism. The C ion implantation modifies both the optical and the ferromagnetic properties. Tuning the defect concentration these samples can be suitable for spintronic and magneto-optic applications.

# References

- [1] C Ciano, L Persichetti, M Montanari, L Di Gaspare, G Capellini, L Baldassarre, M Ortolani, A Pashkin, M Helm, S Winnerl, et al. Electron-phonon coupling in n-type Ge two-dimensional systems. *Physical Review B*, 102(20):205302, 2020.
- [2] CI Medel-Ruiz, H Pérez Ladrón de Guevara, JR Molina-Contreras, and C Frausto-Reyes. Fano effect in resonant Raman spectrum of CdTe. *Solid State Communications*, 312:113895, 2020.
- [3] Shailendra K Saxena, Priyanka Yogi, Suryakant Mishra, Hari Mohan Rai, Vikash Mishra, M Kamal Warshi, Swarup Roy, Puspen Mondal, Pankaj R Sagdeo, and Rajesh Kumar. Amplification or cancellation of Fano resonance and quantum confinement induced asymmetries in Raman line-shapes. *Physical Chemistry Chemical Physics*, 19(47):31788, 2017.
- [4] Subhashree Sahoo and Pratap K Sahoo. Weak-localization effect in Fano asymmetry of c implanted rutile TiO<sub>2</sub> nanostructure. *Journal of Applied Physics*, 133(14):144301, 2023.
- [5] Sarbajit Banerjee, Dae-In Kim, Richard D Robinson, Irving P Herman, Yuanbing Mao, and Stanislaus S Wong. Observation of Fano asymmetry in Raman spectra of SrTiO<sub>3</sub> and Ca<sub>x</sub>Sr<sub>1-x</sub>TiO<sub>3</sub> perovskite nanocubes. *Applied physics letters*, 89(22), 2006.
- [6] Pablo David Esquinazi, Wolfram Hergert, Markus Stiller, Lukas Botsch, Hendrik Ohldag, Daniel Spemann, Martin Hoffmann, Waheed A Adeagbo, Angelika Chassé, Sanjeev K Nayak, et al. Defect-induced magnetism in nonmagnetic oxides: Basic

- principles, experimental evidence, and possible devices with zno and  $\text{TiO}_2$ . *physica status solidi (b)*, 257(7):1900623, 2020.
- [7] JF Zeigler, JP Biersack, UNDU Littmark, et al. The stopping and range of ions in solids. *The Stopping and Range of Ions in Matter*, 1, 1985.
- [8] Mrinal K Sikdar, Avanendra Singh, Sourav Bhakta, Madhusmita Sahoo, SN Jha, DK Shukla, D Kanjilal, and Pratap K Sahoo. Modulation of intrinsic defects in vertically grown zno nanorods by ion implantation. *Physical Chemistry Chemical Physics*, 24(30):18255, 2022.
- [9] Ilhem Hadjoub, Tahar Touam, Chelouche Azeddine, Mohamed Atoui, Jeanne Solard, Mahmoud Chakaroun, A. Fischer, Boudrioua Azzedine, and Lung-Han Peng. Post-deposition annealing effect on rf-sputtered  $\text{TiO}_2$  thin-film properties for photonic applications. *Applied Physics A*, 122, 01 2016.
- [10] Biswajit Choudhury, Munmun Dey, and Amarjyoti Choudhury. Defect generation, d-d transition, and band gap reduction in cu-doped  $\text{TiO}_2$  nanoparticles. *International Nano Letters*, 3, 04 2013.
- [11] Yamerson Canchanya-Huaman, Angie F Mayta-Armas, Jemina Pomalaya-Velasco, Yéssica Bendejú-Roca, Jorge Andres Guerra, and Juan A Ramos-Guivar. Strain and grain size determination of  $\text{CeO}_2$  and  $\text{TiO}_2$  nanoparticles: Comparing integral breadth methods versus rietveld,  $\mu$ -Raman, and TEM. *Nanomaterials*, 11(9):2311, 2021.
- [12] Imen Ben Jemaa, F. Chaabouni, Lionel Presmanes, Yohann Thimont, M. Abaab, Antoine Barnabé, and Philippe Tailhades. Structural, optical and electrical investigations on nb doped  $\text{TiO}_2$  radio-frequency sputtered thin films from a powder target. *Journal of Materials Science: Materials in Electronics*, 27, 12 2016.

- 
- [13] Xiliang Nie, Shuping Zhuo, Gloria Maeng, and Karl Sohlberg. Doping of TiO<sub>2</sub> polymorphs for altered optical and photocatalytic properties. *International Journal of Photoenergy*, 2009, 2009.
- [14] Amarjyoti Paul, Susmita Choudhury. Investigation of the optical property and photocatalytic activity of mixed phase nanocrystalline titania. *Applied Nanoscience*, 4:839, 2014.
- [15] Qing-Yu Liu, Hao-Dong Wang, Rui Tang, Quan Cheng, and Yong-Jun Yuan. Rutile tio<sub>2</sub> nanoparticles with oxygen vacancy for photocatalytic nitrogen fixation. *ACS Applied Nano Materials*, 4(9):8674, 2021.
- [16] Tian Lan, Xiaoli Tang, and Brent Fultz. Phonon anharmonicity of rutile TiO<sub>2</sub> studied by Raman spectrometry and molecular dynamics simulations. *Physical Review B*, 85(9):094305, 2012.
- [17] G Impellizzeri, V Scuderi, L Romano, E Napolitani, R Sanz, Robert Carles, and V Privitera. C ion-implanted TiO<sub>2</sub> thin film for photocatalytic applications. *Journal of Applied Physics*, 117(10):105308, 2015.
- [18] Chengjiang Zhang, Amin Cao, Lianqing Chen, Kangle Lv, Tsunghsueh Wu, and Ke-jian Deng. One-step topological preparation of carbon doped and coated TiO<sub>2</sub> hollow nanocubes for synergistically enhanced visible photodegradation activity. *RSC advances*, 8(38):21431, 2018.
- [19] Lijun Ji, Yuheng Zhang, Shiyong Miao, Mindong Gong, and Xi Liu. In situ synthesis of carbon doped TiO<sub>2</sub> nanotubes with an enhanced photocatalytic performance under uv and visible light. *Carbon*, 125:544, 2017.
- [20] Xuan Pan, Yong Zhao, Shu Liu, Carol L Korzeniewski, Shu Wang, and Zhaoyang

- Fan. Comparing graphene-TiO<sub>2</sub> nanowire and graphene-TiO<sub>2</sub> nanoparticle composite photocatalysts. *ACS applied materials & interfaces*, 4(8):3944, 2012.
- [21] Prakash R Poudel, Bibhudutta Rout, KM Hossain, MS Dhoubhadel, Venkata C Kumari, Arup Neogi, and Floyd Del McDaniel. Formation and characterization of ion beam assisted nanosystems in silicon. *Revista mexicana de física*, 56(4):297, 2010.
- [22] Rajesh Kumar, HS Mavi, AK Shukla, and VD Vankar. Photoexcited Fano interaction in laser-etched silicon nanostructures. *Journal of applied physics*, 101(6):064315, 2007.
- [23] James Cassidy and Mikhail Zamkov. Nanoshell quantum dots: Quantum confinement beyond the exciton bohr radius. *The Journal of chemical physics*, 152(11):110902, 2020.
- [24] Eddwi H Hasdeo, Ahmad RT Nugraha, Mildred S Dresselhaus, and Riichiro Saito. Breit-wigner-Fano line shapes in Raman spectra of graphene. *Physical Review B*, 90(24):245140, 2014.
- [25] Valentin Magidson and Robert Beserman. Fano-type interference in the Raman spectrum of photoexcited si. *Physical Review B*, 66(19):195206, 2002.
- [26] Xin Zhou, Linqiu Li, Hao Dong, Ashutosh Giri, Patrick E Hopkins, and Oleg V Prezhdo. Temperature dependence of electron–phonon interactions in gold films rationalized by time-domain ab initio analysis. *The Journal of Physical Chemistry C*, 121(32):17488, 2017.
- [27] Rajesh Kumar. Asymmetry to symmetry transition of Fano line-shape: analytical description. *Indian Journal of Physics*, 87(1):49, 2013.

- 
- [28] Houmei Dai, Xin Li, Xiaolin Cai, and Ran Wei. The magnetism of titanium-defected undoped rutile  $\text{TiO}_2$ : first-principles calculations. *Physical Chemistry Chemical Physics*, 22(44):25930, 2020.
- [29] Guang-bing Han, Shu-jun Hu, Shi-shen Yan, and Liang-mo Mei. Oxygen vacancy induced ferromagnetism in rutile  $\text{TiO}_x$ . *physica status solidi (RRL)–Rapid Research Letters*, 3(5):148, 2009.
- [30] Min Sik Park, SK Kwon, and BI Min. Electronic structures of doped anatase  $\text{TiO}_2$ :  $\text{Ti}_{1-x}\text{M}_x\text{O}_2$  ( $\text{M} = \text{Co}, \text{Mn}, \text{Fe}, \text{Ni}$ ). *Physical Review B*, 65(16):161201, 2002.
- [31] Dongyoo Kim, Jisang Hong, Young Ran Park, and Kwang Joo Kim. The origin of oxygen vacancy induced ferromagnetism in undoped  $\text{TiO}_2$ . *Journal of Physics: Condensed Matter*, 21(19):195405, 2009.
- [32] Sh A Mansour, AH Farha, and MF Kotkata. Sol–gel synthesized co-doped anatase  $\text{TiO}_2$  nanoparticles: Structural, optical, and magnetic characterization. *Journal of Inorganic and Organometallic Polymers and Materials*, 29:1375, 2019.
- [33] Yiseul Park, Wooyul Kim, Hyunwoong Park, Takashi Tachikawa, Tetsuro Majima, and Wonyong Choi. Carbon-doped  $\text{TiO}_2$  photocatalyst synthesized without using an external carbon precursor and the visible light activity. *Applied Catalysis B: Environmental*, 91:355, 09 2009.
- [34] Shengqiang Zhou, E Čížmár, K Potzger, M Krause, G Talut, M Helm, J Fassbender, SA Zvyagin, J Wosnitza, H Schmidt, et al. Origin of magnetic moments in defective  $\text{TiO}_2$  single crystals. *Physical Review B*, 79(11):113201, 2009.
- [35] U Khan, N Adeela, K Javed, S Riaz, H Ali, M Iqbal, XF Han, and S Naseem. Influ-



- ence of cobalt doping on structural and magnetic properties of BiFeO<sub>3</sub> nanoparticles. *Journal of Nanoparticle Research*, 17:1, 2015.
- [36] Georg Kresse and Jürgen Furthmüller. Efficient iterative schemes for ab initio total-energy calculations using a plane-wave basis set. *Phys. Rev. B*, 54(16):11169, 1996.
- [37] John P Perdew, Kieron Burke, and Matthias Ernzerhof. Generalized gradient approximation made simple. *Phys. Rev. Lett.*, 77(18):3865, 1996.
- [38] Koichi Momma and Fujio Izumi. iVESTA 3/for three-dimensional visualization of crystal, volumetric and morphology data. *J. Appl. Crystallogr.*, 44(6):1272, 2011.
- [39] RP Wang, G Xu, and P Jin. Size dependence of electron-phonon coupling in ZnO nanowires. *Physical Review B*, 69(11):113303, 2004.
- [40] Subhashree Sahoo, Gurupada Ghorai, Kalyan Ghosh, Bidyadhar Das, Mrinal K Sikdar, and Pratap K Sahoo. Anharmonicity of optical phonon modes in copper doped rutile TiO<sub>2</sub> nanorod composed microflowers. *AIP Advances*, 11(10):105013, 2021.
- [41] Manushree Tanwar, Love Bansal, Chanchal Rani, Sonam Rani, Suchita Kandpal, Tanushree Ghosh, Devesh K Pathak, I Sameera, Ravi Bhatia, and Rajesh Kumar. Fano-type wavelength-dependent asymmetric Raman line shapes from MoS<sub>2</sub> nanoflakes. *ACS Physical Chemistry Au*, 2(5):417, 2022.
- [42] Peter E Blöchl. Projector augmented-wave method. *Phys. Rev. B*, 50(24):17953, 1994.

## Chapter 4

# Bandgap tuning in Si implanted TiO<sub>2</sub> microflowers

### 4.1 Introduction

TiO<sub>2</sub> has drawn significant interest from the photocatalysis and optoelectronics fields. Its wide range of optical applications is limited by the large bandgap. Thus, the bandgap narrowing by doping to improve photocatalytic activity and solar cell applications has been the subject of numerous theoretical and practical investigations[1, 2]. Bandgap narrowing of TiO<sub>2</sub> using metal and non-metal elements is extensively studied. However, the introduction of semiconducting dopants like Si is not much explored. The incorporation of Si into the TiO<sub>2</sub> matrix may lead to the creation of an intermediate defect state above the valence band maximum and subsequently narrow the bandgap[3]. According to a study, doping TiO<sub>2</sub> with Si alters its optical characteristics, electronic structure, and photocatalytic activity[4, 5]. Yang *et al.* conducted a theoretical analysis on the Si-doped TiO<sub>2</sub> and found that substituting Ti by Si is preferable to substituting O by Si [5]. Additionally, it has been observed that a wide range of optical absorption and photocatalytic activity are positively affected by substituting Ti with Si[6]. It is difficult to dope TiO<sub>2</sub> with Si using a chemical approach; however, doping with an ion implantation technique is simpler and can be done in a controlled way. This method modifies the chemical, optical, and electronic properties of TiO<sub>2</sub> along with the structural modifications.

This chapter explores the impact of Si ions on the morphological, optical, bandgap, and vibrational properties of TiO<sub>2</sub>. The correlation between phonon lifetime and the bandgap

narrowing caused by Si ion implantation is explored.

## **4.2 Experimental details**

Similar to the preceding chapter, the hydrothermal technique covered in Chapter 2 is employed in this work to synthesize the TiO<sub>2</sub> microflowers. The prepared samples are implanted with 30 keV Si ions at fluence ranges of  $1 \times 10^{15}$  to  $2 \times 10^{16}$  ions/cm<sup>2</sup>. The morphology of samples are observed using FESEM and the structural characterizations are performed by analyzing the XRD pattern. Raman spectroscopy is used to record the vibrational modes. The optical property is studied using UV-visible spectroscopy with diffuse reflectance spectroscopy accessories. The photoemission and defect states are characterized using photoluminescence spectroscopy.

## **4.3 Ion beam simulations**

Based on the SRIM simulations discussed in Chapter 2, the depth profile of the Si ion in the TiO<sub>2</sub> matrix is displayed in Figure 4.1(a). In contrast to 1.5 MeV C in the preceding chapter, 30 keV Si is implanted in this set of samples. The mean projected range ( $R_p$ ) is 272 Å. The values for nuclear energy loss, electronic energy loss, lateral straggling, and longitudinal straggling are 63.13 eV/Å, 23.50 eV/Å, 89 Å, and 124 Å, respectively. The Si ions create both O and Ti vacancies. The total number of vacancies created per incident ion with depth is presented in Figure 4.1(b). The area under the curve calculation gives a total displacement of 375/ions.

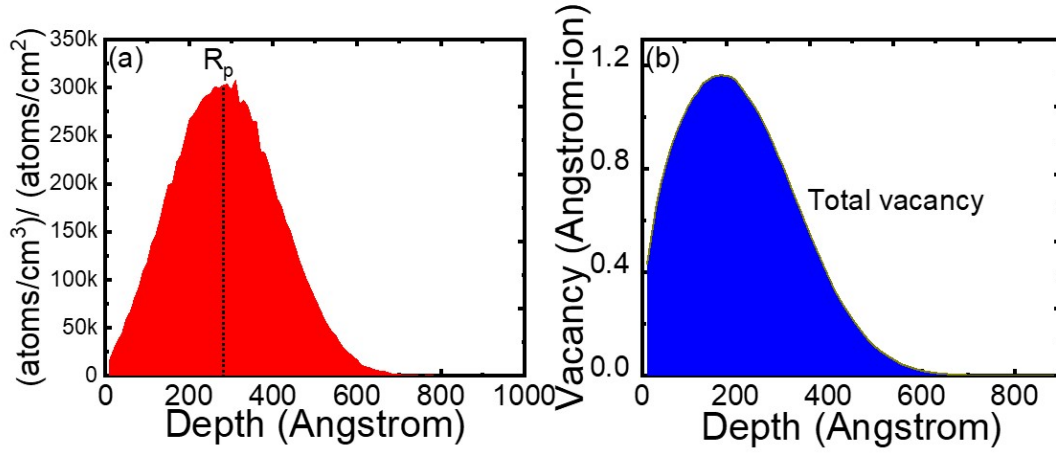


Figure 4.1: (a) Depth profile (b) Vacancy plot for 30 keV Si ion in TiO<sub>2</sub>.

## 4.4 Characterizations and analysis

### 4.4.1 FESEM

The FESEM micrographs of the pristine and 30 keV Si ion implanted TiO<sub>2</sub> with fluence range of  $5 \times 10^{14}$  to  $2 \times 10^{16}$  ions/cm<sup>2</sup> are presented in Figure 4.2. The flower-like structure is observed in all the samples. The surface of each nanorod in the microflower becomes smooth with ion fluence. At the highest fluence of  $2 \times 10^{16}$  ions/cm<sup>2</sup>, the surface looks like melting due to ion beams. It has been demonstrated that energy losses are dissipated in the form of heat, while the energy losses triggered by elastic processes generate atomic displacements and heat, simultaneously. So, along with the smooth surface of the nanorods, the shape of the tip also changed to blunt due to the heating effect of nuclear energy loss. The melting can be well understood by using the thermal spike model, and it is discussed in Chapter 6.

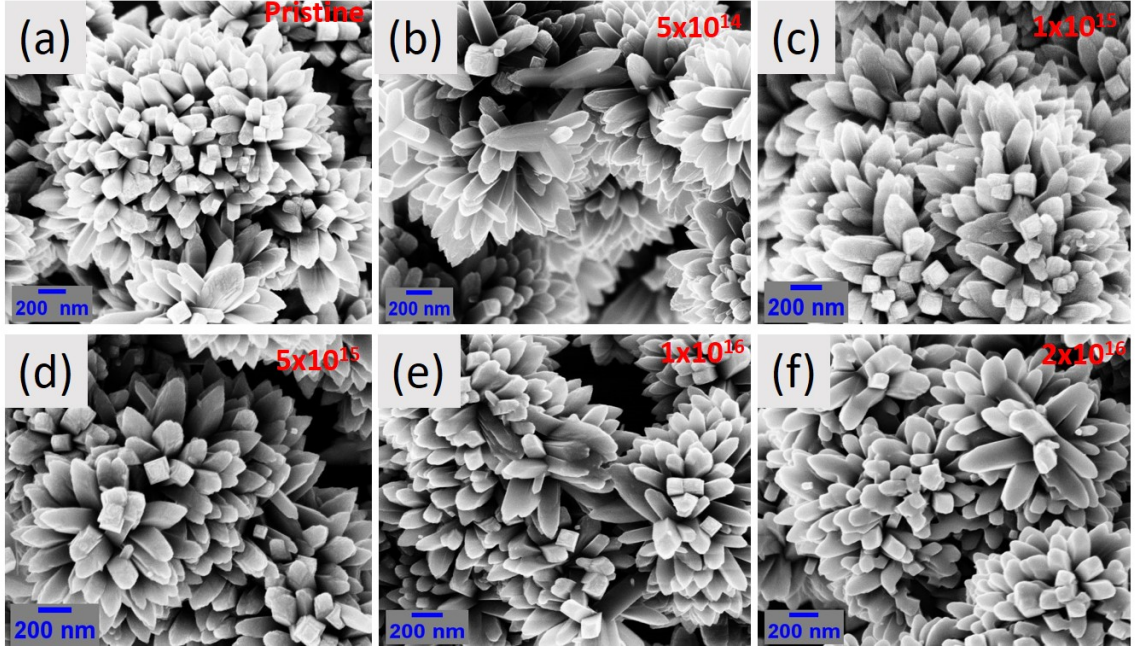


Figure 4.2: FESEM images of pristine and Si ion implanted TiO<sub>2</sub>.

#### 4.4.2 XRD

The XRD pattern of the pristine and Si ion implanted TiO<sub>2</sub> are presented in Figure 4.3(a). All the peaks observed are associated with the rutile phase of TiO<sub>2</sub>. The position of  $2\theta$  at 27.35, 36.06, 39.14, 41.20, 43.95, and 54.25 degrees corresponds to (110), (101), (200), (111), (210), and (211) lattice planes, respectively. There is almost negligible degradation of crystallinity after implantation. The crystallite size and strain developed due to Si ion irradiation are calculated using equations 3.2 and 3.4 presented in Chapter 3, respectively. The above values are calculated considering the highest intense (110) lattice plane, as shown in the shaded part of Figure 4.3 (a). The calculated values of crystallite size and strain are plotted in the left and right panels of Figure 4.3 (b), respectively. It is observed that the value of crystallite size decreases up to ion fluence of  $1 \times 10^{15}$  ions/cm<sup>2</sup>, and then it increases. The increase in crystallite size might be attributed to the melting of nanorods. Similarly, the

calculated value of strain increases up to ion fluence of  $1 \times 10^{15}$  ions/cm<sup>2</sup> then decreases. The strain developed is an indication of the incorporation of Si ions in TiO<sub>2</sub> matrix, and this affects the bond strength of Ti-O.

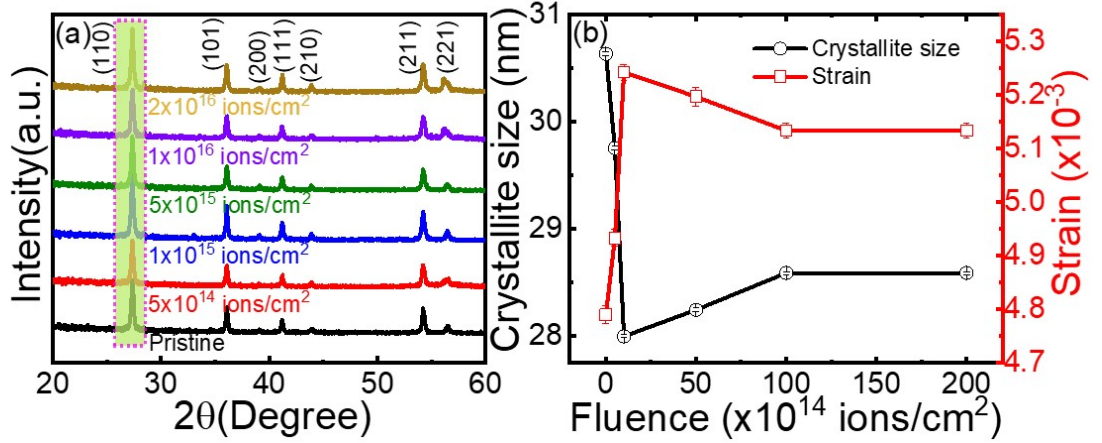


Figure 4.3: (a) XRD pattern of pristine and Si implanted TiO<sub>2</sub>. (b) Variation of crystallite size and strain with Si ion fluence.

#### 4.4.3 Raman spectroscopy

The Raman spectra of all the samples are displayed in Figure 4.4(a). All the peaks correspond to the rutile phase of TiO<sub>2</sub>. With Si ion implantation, the E<sub>g</sub> vibrational mode is shifting to the lower wave number side, suggesting the existence of strain. Strain in TiO<sub>2</sub> matrix increases upon Si ion implantation. The strain  $\epsilon_R$  is calculated using the relation[7]

$$\omega = \omega_0(1 - 3\epsilon_R) \quad (4.1)$$

where  $\omega$  is the vibrational frequency of the samples and  $\omega_0$  is the vibrational frequency of bulk samples. Further, the presence of Si ions affects the strength of the Ti-O bond, which can be determined from the force constant. The higher the value of the force constant, the higher the bond strength. The force constant ( $k$ ) is given by the relation,

$$k = (2\pi\omega)^2\mu \quad (4.2)$$

where  $\mu$  is the effective mass of Ti-O ( $1.98 \times 10^{-23}$  g),  $\omega$  is vibrational frequency. This relation shows that the force constant is proportional to the square of wavenumber[8]. As fluence increases the force constant decreases indicating that the Si ion weakens the Ti-O bond strength. In addition, the peak broadening seen after ion implantation suggested a reduction in phonon lifetime as a result of phonons being scattered by defects. Table 4.1 displays the calculated value of strain, force constant, and phonon lifetime for the most intense E<sub>g</sub> mode of vibration. The phonon lifetime ( $\tau$ ) is calculated using the energy-time uncertainty relation,

$$\frac{\Delta E}{\hbar} = 2\pi c\Gamma = \frac{1}{\tau} \quad (4.3)$$

where  $\Delta E$  is the uncertainty in the energy of phonon mode,  $\hbar$  is Planck's constant,  $c$  is the velocity of light, and  $\Gamma$  is the linewidth of phonon mode[9].

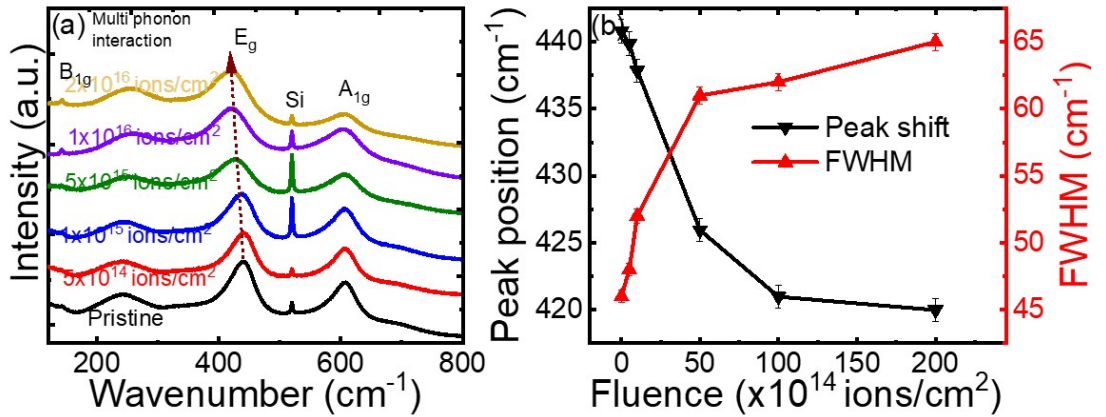


Figure 4.4: (a) Raman spectra of pristine and Si implanted TiO<sub>2</sub>. (b) Variation of peak position and FWHM with Si ion fluence.

From the table, it is observed that the strain develops and increases with Si ion fluence. Further, the Si ion weakens the Ti-O bond strength and the phonon scattering reduces the lifetime of phonons. The values of strain calculated from XRD and Raman spectroscopy

Table 4.1: Obtained values of FWHM ( $E_g$  mode), phonon lifetime, and bandgap for the pristine and Si implanted TiO<sub>2</sub>.

Si fluence (ions/cm <sup>2</sup> )	Strain( $\times 10^{-3}$ )	Force constant (N cm <sup>-1</sup> )	Phonon lifetime (ps)
0	4.68	1.36	0.115
$5 \times 10^{14}$	5.40	1.35	0.110
$1 \times 10^{15}$	6.90	1.34	0.101
$5 \times 10^{15}$	15.91	1.27	0.086
$1 \times 10^{16}$	19.66	1.24	0.085
$2 \times 10^{16}$	20.42	1.23	0.081

are approximately of the same order, however, the values are not the same. The value of strain calculated from Raman spectroscopy is larger than that calculated using XRD. A similar result is reported by Kibasomba et al.[7]. This is because the strain calculated using XRD is related to (110) plane and global effect, whereas in Raman spectroscopy, the strain calculation is associated with a particular mode of vibrations within a small area of the laser spot size.

#### 4.4.4 UV-visible spectroscopy

The bandgap of samples is calculated using the Tauc plot discussed in Chapter 3 (section 3.5.1). The corresponding Tauc plot for all the samples is shown in Figure 4.5. With an increase in Si fluence, a monotonic decrease in the bandgap is observed. There are two possible causes for the bandgap narrowing. First, the formation of midgap states, which is linked to oxygen vacancies; second, Si dopants are linked to the formation of midgap states. The implanted Si ion in the TiO<sub>2</sub> has the potential to replace the O and Ti ions or occupy the interstitial position. Defect states are formed at various places in the forbidden bandgap of TiO<sub>2</sub> matrix depending on where the Si is located. Theoretically, it is studied that when Si replaces O in a system, the Si 3p states lie near the edge of the conduction band, increasing the width of the band and slightly boosting the valence band maximum. On the other hand, there is no movement in the valence band maximum when Si replaces



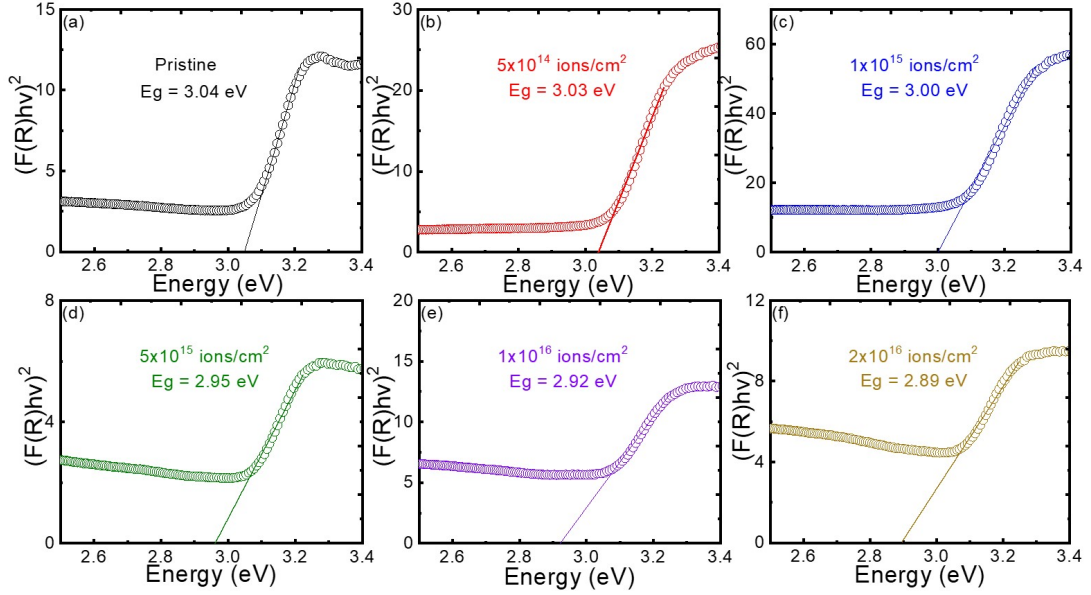


Figure 4.5: Tauc plot for pristine and Si ion implanted  $\text{TiO}_2$ .

Ti with a clear fall in the conduction band minima[5]. The substitution causes the bandgap to shrink. Furthermore, the formation of oxygen vacancy-related defect states beneath the conduction band aids to the reduction of bandgap [10]. More details of the defect states can be investigated by analyzing the photoluminescence spectrum as shown in the upcoming section.

The variation of phonon lifetime and bandgap is plotted against Si ion fluence in Figure 4.6. It is observed that the phonon lifetime decreases as the Si ion fluence increases. This indicates that at higher fluence the phonons get more scattered by the defects reducing their lifetime. This also confirms the presence and increasing number of defects with ion fluence. These defects create intermediate states in the bandgap region that help in narrowing the bandgap. Hence as the ion fluence increases, the number of defect states increases and the bandgap decreases sequentially.

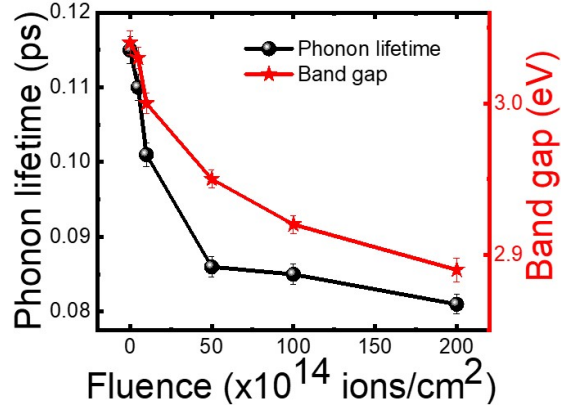


Figure 4.6: Variation of phonon lifetime and bandgap with Si ion fluence.

#### 4.4.5 Photoluminescence (PL) spectroscopy

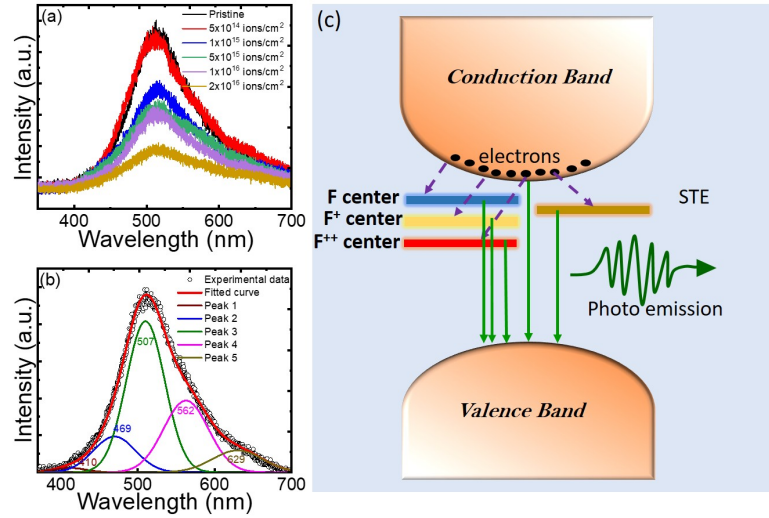


Figure 4.7: (a) PL spectra of pristine and Si ion implanted  $\text{TiO}_2$ . (b) Deconvoluted PL spectra of pristine  $\text{TiO}_2$ . (c) Schematic diagram showing the origin of PL emissions and defect states. The dashed arrow mark represents nonradiative transition and the solid arrow mark represents radiative transition.

The PL spectra of pristine and Si ion implanted  $\text{TiO}_2$  are presented in Figure 4.7 (a). From the figure it is observed that for the lowest fluence, the change of intensity is not significant, however, with increasing ion fluence, the intensity reduces monotonically. The

decrease in PL intensity arises due to the trapping of photogenerated electrons by the midgap defect states. Although there is a trend of decreasing PL intensity, the nature of the peaks remains invariant having similar peak positions. As the peaks are broad, the study of the origin of defect states is carried out by deconvoluting the peaks into five Gaussian peaks. The deconvoluted peak of the undoped sample is shown in Figure 4.7 (b). The fitted Gaussian peaks are centered at 410 nm, 469 nm, 507 nm, 562 nm, and 629 nm attributed to near band-edge transition, self-trapped excitons, radiative recombination of electrons from F, F<sup>+</sup>, and F<sup>++</sup> defect states, respectively[11–13]. The origin of PL emission from the midgap states is schematically shown in Figure 4.7(c). Details of the peaks are discussed in Chapter 5 (section 5.4.1).

## 4.5 Conclusions

In conclusion, we have investigated how the implantation of Si ions modifies the bandgap of TiO<sub>2</sub>. The SRIM simulation shows that Si ion implantation causes O and Ti vacancies in TiO<sub>2</sub>. The FESEM pictures make it clear that the tip of nanorod slightly changed at the maximum Si fluence due to melting. Ion implantation causes defects that alter the vibrational and optical characteristics of the host TiO<sub>2</sub> matrix, but it significantly does not affect the crystallinity of TiO<sub>2</sub>. The shift in the peak position of Raman spectra indicates the presence of stress and the increasing FWHM with ion fluence is affected to decreased phonon lifetime. The decreased phonon lifetime is due to the scattering of phonons by defects. The reduced bandgap with Si ion fluence is due to the creation of midgap defect states. The tuning of bandgap through defect engineering by semiconducting Si ion implantation can be considered for suitable applications in photocatalysis and optoelectronics devices.

## References

- [1] Mohammad Ehtisham Khan, Mohammad Mansoob Khan, Bong-Ki Min, and Moo Hwan Cho. Microbial fuel cell assisted band gap narrowed  $\text{TiO}_2$  for visible light-induced photocatalytic activities and power generation. *Scientific reports*, 8(1):1723, 2018.
- [2] T Umebayashi, T Yamaki, H Itoh, and K Asai. Band gap narrowing of titanium dioxide by sulfur doping. *Applied physics letters*, 81(3):454, 2002.
- [3] Run Long and Niall J English. Band gap engineering of (N, Si)-codoped  $\text{TiO}_2$  from hybrid density functional theory calculations. *New Journal of Physics*, 14(5):053007, 2012.
- [4] Ning Ma, Xie Quan, Yaobin Zhang, Shuo Chen, and Huimin Zhao. Integration of separation and photocatalysis using an inorganic membrane modified with Si-doped  $\text{TiO}_2$  for water purification. *Journal of Membrane Science*, 335(1):58, 2009.
- [5] Kesong Yang, Ying Dai, and Baibiao Huang. First-principles calculations for geometrical structures and electronic properties of Si-doped  $\text{TiO}_2$ . *Chemical Physics Letters*, 456(1-3):71, 2008.
- [6] Xiaoli Yan, Jing He, David G Evans, Xue Duan, and Yuexiang Zhu. Preparation, characterization and photocatalytic activity of Si-doped and rare earth-doped  $\text{TiO}_2$  from mesoporous precursors. *Applied Catalysis B: Environmental*, 55(4):243, 2005.
- [7] Pierre M Kibasomba, Simon Dhlamini, Malik Maaza, Chuan-Pu Liu, Mohamed M Rashad, Diaa A Rayan, and Bonex W Mwakikunga. Strain and grain size of

- TiO<sub>2</sub> nanoparticles from TEM, Raman spectroscopy and XRD: The revisiting of the williamson-hall plot method. *Results in Physics*, 9:628, 2018.
- [8] Yuliang Zhang, Cindel X. Harris, Petra Wallenmeyer, James Murowchick, and Xiaobo Chen. Asymmetric lattice vibrational characteristics of rutile TiO<sub>2</sub> as revealed by laser power dependent Raman spectroscopy. *The Journal of Physical Chemistry C*, 117(45):24015, 2013.
- [9] Thomas Beechem and Samuel Graham. *Journal of Applied Physics*, 103(9):093507, 2008.
- [10] Junpeng Wang, Zeyan Wang, Baibiao Huang, Yandong Ma, Yuanyuan Liu, Xiaoyan Qin, Xiaoyang Zhang, and Ying Dai. Oxygen vacancy induced band-gap narrowing and enhanced visible light photocatalytic activity of ZnO. *ACS applied materials & interfaces*, 4(8):4024, 2012.
- [11] Radhika V Nair, PK Gayathri, Venkata Siva Gummaluri, PMG Nambissan, and C Vijayan. Large bandgap narrowing in rutile TiO<sub>2</sub> aimed towards visible light applications and its correlation with vacancy-type defects history and transformation. *Journal of Physics D: Applied Physics*, 51(4):045107, 2018.
- [12] Amreetha Seetharaman, Dhanuskodi Sivasubramanian, Vinitha Gandhiraj, and Venugopal Rao Soma. Tunable nanosecond and femtosecond nonlinear optical properties of C–N–S-doped TiO<sub>2</sub> nanoparticles. *The Journal of Physical Chemistry C*, 121(43):24192, 2017.
- [13] Chetibi Loubna, Tetiana Busko, Nikolay Kulish, Djamel Hamana, Sahraoui Chaieb, and Slimane Achour. Photoluminescence properties of TiO<sub>2</sub> nanofibers. *Journal of Nanoparticle Research*, 19, 03 2017.

## Chapter 5

# Impact of Cu doping on linear, nonlinear properties, and anharmonicity of TiO<sub>2</sub> microflowers

### 5.1 Introduction

The wide bandgap of TiO<sub>2</sub> restricts its use to the UV spectrum. The bandgap can be narrowed down by doping appropriate dopants into the TiO<sub>2</sub> matrix. Numerous studies have been performed to narrow down the electronic band structure of TiO<sub>2</sub> by nonmetal and transition metal doping[1]. Doping TiO<sub>2</sub> with elements having a lower valence creates oxygen vacancies and improves the electronic conductivity. The dopant-induced defect states such as oxygen vacancies and impurity states created between the conduction band minima and valence band maxima help to alter the bandgap of TiO<sub>2</sub>. It is preferable to dope 3d transition metals in TiO<sub>2</sub> as the d state provides midgap states that reduce the bandgap[2]. The element Cu as a 3d transition metal is reasonable to use in TiO<sub>2</sub> as a dopant. In this chapter, Cu is doped in TiO<sub>2</sub> and it contains parts. The first part contains, the optical properties and the second part discusses the anharmonic effect.

The Cu dopant lowers the bandgap of TiO<sub>2</sub> creating defect states in the TiO<sub>2</sub> matrix. The nonlinear optical (NLO) properties of materials can be changed by modifying their bandgap. Nonlinear optical properties arise when polarization density  $P$  varies non-linearly to the electric field  $E$  of the light. The origin of nonlinearity in TiO<sub>2</sub> is due to the hyperpolarizability of Ti-O pairs[3].

The lattice distortion in any material that occurs by adding a dopant or increasing tem-

perature affects the harmonic potential terms, and it changes the vibrational properties of phonons, which can be probed by Raman spectroscopy. The frequency and linewidth change with the temperature and pressure of normal vibrational modes due to electron-phonon coupling or phonon-phonon interactions known as the anharmonic effect. The phono-phonon interaction and phonon decay with a short lifetime is the control knob to improve the efficiency of nanoscale semiconductor devices[4, 5].

This chapter contains two parts.

- (a) Impact of chemically doped Cu on the linear and third-order nonlinear optical properties of TiO<sub>2</sub> microflowers.
- (b) Effect of Cu dopant on phonon anharmonicity and lifetime through temperature-dependent Raman scattering in TiO<sub>2</sub> microflower structures.

## **5.2 Experimental details**

Microflowers of TiO<sub>2</sub> nanorods used in this study were synthesized by the hydrothermal process as discussed in Chapter 2 on TiO<sub>2</sub> seeded silicon substrate and glass substrate. For Cu doping, the required amount of copper nitrate trihydrate was added to the solution with a molar concentration varying from 1 to 10%. For quantifying Cu, inductively coupled plasma optical emission spectroscopy (ICP-OES) was carried out for the doped samples (Thermo Scientific™ iCAP™ 7000 Series). The samples were dispersed in aqua regia and mixed well using a sonicator for the measurement. The average value taken from three runs of the experiment is reported. The morphology of samples was carried out by field emission scanning electron microscopy (FESEM, ZEISS), and the elemental analysis was performed by energy dispersive X-ray spectroscopy (EDS) attached to FESEM. The local crystal structure and morphology of samples were studied using transmission electron microscopy (TEM, JEM-F200, JEOL). The samples were transferred to a copper grid for TEM

measurement. The crystal and phase structure of samples were carried out using an X-ray diffraction (XRD) pattern recorded by a Rigaku Smartlab X-ray diffractometer. The defect states of the samples were analyzed using photoluminescence spectroscopy (Jobin-Yvon LabRam HR Evolution, Horiba) with 40X objective. The bandgap was calculated from the absorption spectra collected from the UV-VIS-NIR spectrometer (Agilent, Carry 5000). A single-beam Z-scan technique with open and close aperture configuration using ultrashort pulses centered at 532 nm excitation wavelength was used to study NLO measurements. The OA and CA measurements were carried out with a laser delivering linearly-polarized 500 ps pulses centered at a wavelength of 532 nm with a repetition rate of 1 kHz and a spot size ( $w_0$ ) 37.5  $\mu\text{m}$ . The Rayleigh length  $z_R = \frac{\pi w_0^2}{\lambda}$  was calculated to be 8.3 mm which is much greater than the thickness of the sample. The sample was placed on a translational stage, which moves along the z-axis through the focal plane.

## 5.3 Elemental, morphological, and structural studies

### 5.3.1 ICP-OES

ICP-OES was used to quantify the amount of Cu present in the doped samples. Table 5.1 displays the computed value of Cu, which is determined to be roughly 50% of the initial value taken at the time of the experiment.

Table 5.1: Initial and actual percentage of Cu in doped TiO<sub>2</sub>

Initial % of Cu added	Actual % Cu doped
1	0.72
2	1.32
4	2.37
6	2.82
8	3.92
10	5.28



### 5.3.2 FESEM

The FESEM image of pristine and Cu doped samples grown on glass and  $\text{TiO}_2$  seeded silicon substrate are captured. The morphology of the samples are flower-like structure and the Cu dopant does not affect the morphology. So here we have displayed the FESEM image of  $\text{TiO}_2$  microflowers grown on glass substrate and seeded silicon substrate as shown in Figure 5.1(a) and (b), respectively. Although in both cases the morphology is similar, there is a change in the dimension of the microflowers. The average diameter of the microflowers grown on glass substrate is approximately  $2.11 \mu\text{m}$  whereas the flowers grown on seeded Si substrate have a diameter of  $2.92 \mu\text{m}$ .

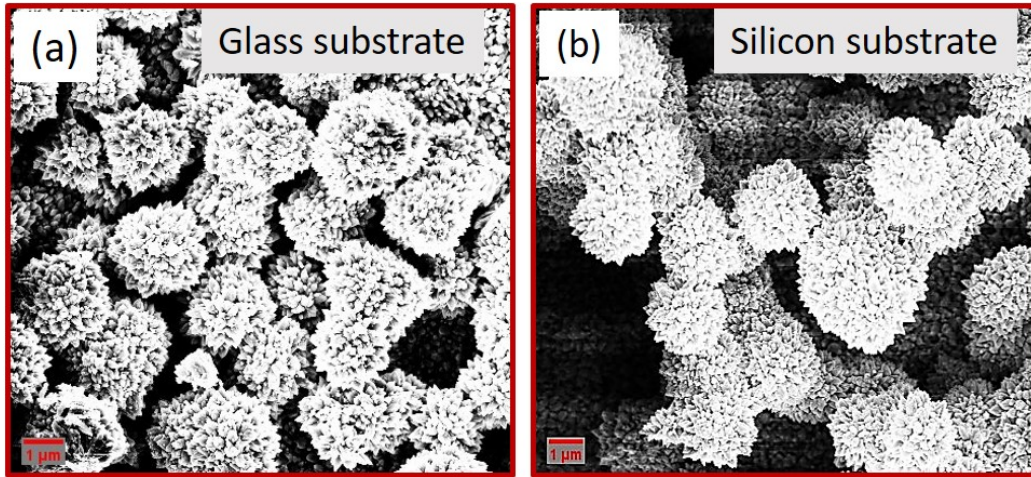


Figure 5.1: Top view FESEM image of  $\text{TiO}_2$  microflower on (a) glass substrate (b) silicon substrate.

Both the structures differ by the dimension of the flowers, so the basic characterizations such as elemental mapping, XRD, TEM, XPS, and photoluminescence properties of microflowers grown on seeded silicon substrate are discussed. The optical properties (both linear and nonlinear) are studied for the microflowers grown on the glass substrate as these measurements require a transparent sample. Further, the study of phonon anharmonicity is studied for the microflowers grown on seeded Si substrate as this requires measurement of

temperature-dependent Raman spectroscopy.

### 5.3.3 EDS

The elemental mapping of 10% Cu doped TiO<sub>2</sub> grown on the seeded silicon substrate with the corresponding FESEM image is shown in Figure 5.2(a). Figure 5.2(b), (c), and (d) show the equivalent elemental mapping for Ti, O, and Cu, respectively. The elemental mapping verifies the presence of Cu in the doped samples. Thus, the composition of the Cu doped TiO<sub>2</sub> microflower is confirmed to consist of Ti, O, and Cu, with each element being evenly distributed throughout the flower.

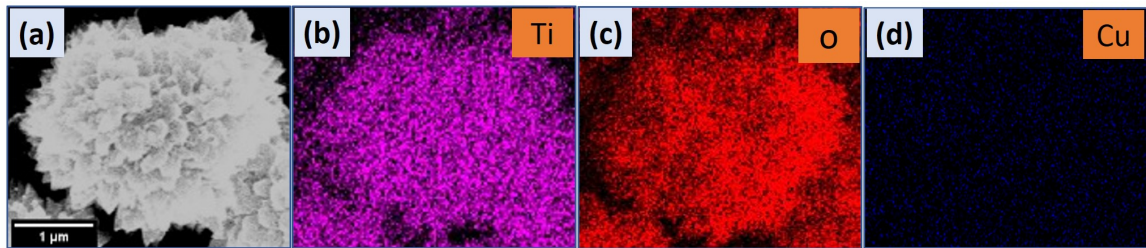


Figure 5.2: (a) FESEM image of 10% Cu doped TiO<sub>2</sub> microflower and the corresponding elemental mapping of (b) Ti, (c) O, and (d) Cu.

### 5.3.4 XRD

XRD pattern as shown in Figure 5.3(a) is used to examine the crystal structure and phases of TiO<sub>2</sub> microflowers. All the diffraction peak indexed is associated with the tetragonal rutile phase (JCPDS number 87-0920) of TiO<sub>2</sub>. The rutile phase of TiO<sub>2</sub> does not change upon doping, and even after 10% of doping, no Cu (CuO or CuO<sub>2</sub>) peaks are evident. The peak with the highest intensity, (110) appears to be shifting towards a lower  $2\theta$  value as the concentration of Cu increases. In the left panel of Figure 5.3(b), the peak position of (110) with Cu concentration is depicted. The crystallite size is calculated for all the samples concerning the (110) peak using the Debye-Scherrer formula (equation 3.2 ). The results

are presented in the right panel of Figure 5.3(b). The calculated crystallite size increases up to 4% of Cu concentration. The increase in crystallite size up to 4% Cu concentration is attributed to the substitution of Ti by Cu ion[6]. It should be noted that the smaller peak shift towards a lower  $2\theta$  is attributed to the ionic radii difference of Cu<sup>2+</sup> (0.72 Å) ion and Ti<sup>4+</sup> (0.68 Å) ion which is responsible for substitutional effect[7]. At higher doping concentrations, the Cu ions move to the interstitial position or are incorporated in the crystal boundary inhibiting crystallite growth[8].

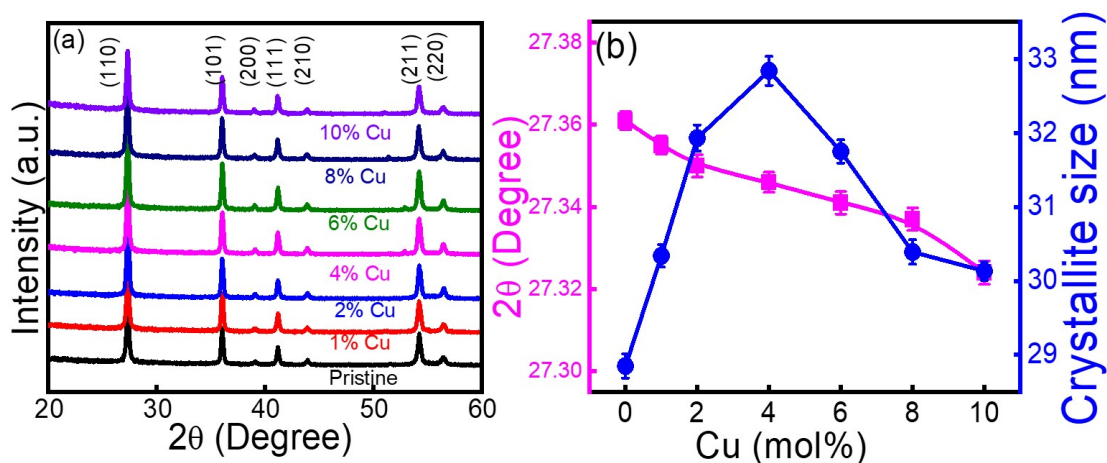


Figure 5.3: (a) XRD pattern of pristine and Cu doped TiO<sub>2</sub> microflowers. (b) Variation of  $2\theta$  and crystallite size with Cu concentration.

### 5.3.5 TEM

The microscopic structural analysis was obtained from HRTEM. A typical TEM image of a pristine TiO<sub>2</sub> microflower is shown in Figure 5.4(a), which clearly indicates the tip-shaped nanorods of TiO<sub>2</sub> matched with the FESEM image. The HRTEM image of pristine TiO<sub>2</sub> is shown in Figure 5.4(b). The interplanar spacing is 0.322 nm corresponding to (110) plane of rutile TiO<sub>2</sub>. The schematic representation of the (110) plane for pristine TiO<sub>2</sub> is displayed in Figure 5.4 (c).

To check the Cu doping, the HRTEM image of 6% Cu and 8% Cu doped  $\text{TiO}_2$  nanorods is shown in Figure 5.4 (d) and (e), respectively. The inter-planar spacing is found to be 0.324 nm and 0.329 nm for 6% Cu and 8% Cu doped  $\text{TiO}_2$ , respectively which corresponds to the (110) plane of rutile  $\text{TiO}_2$  and matches well with the XRD data of rutile  $\text{TiO}_2$ . This variation of inter-planar spacing value can be attributed to the strain developed after Cu doping in the  $\text{TiO}_2$  matrix. The schematic representation of the (110) plane for Cu doped  $\text{TiO}_2$  is displayed in Figure 5.4 (f).

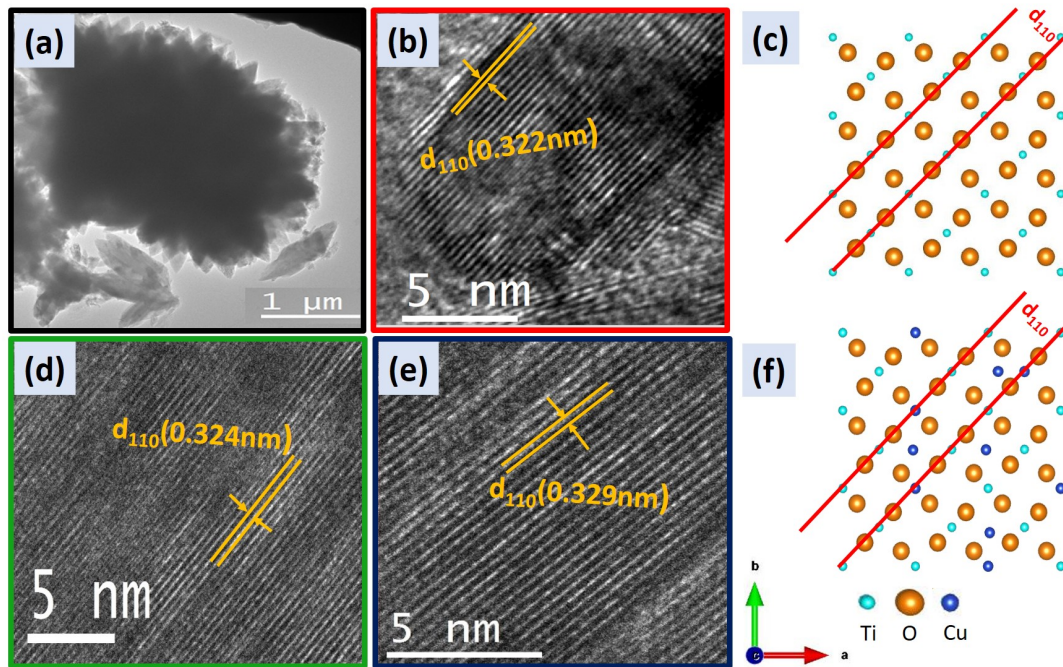


Figure 5.4: (a) TEM images of pristine  $\text{TiO}_2$ . (b) HRTEM image of pristine  $\text{TiO}_2$ . (c) Schematic of the lattice diagram showing (110) plane for pristine  $\text{TiO}_2$ . HRTEM images of (d) 6% Cu and (e) 8% Cu doped  $\text{TiO}_2$ . (f) Schematic of the lattice diagram showing (110) Cu doped  $\text{TiO}_2$ .

### 5.3.6 XPS

The change in the chemical states of the elements O and Ti with Cu dopant was examined using XPS to study the defects. The high-resolution Ti 2p spectra for undoped and 6% Cu



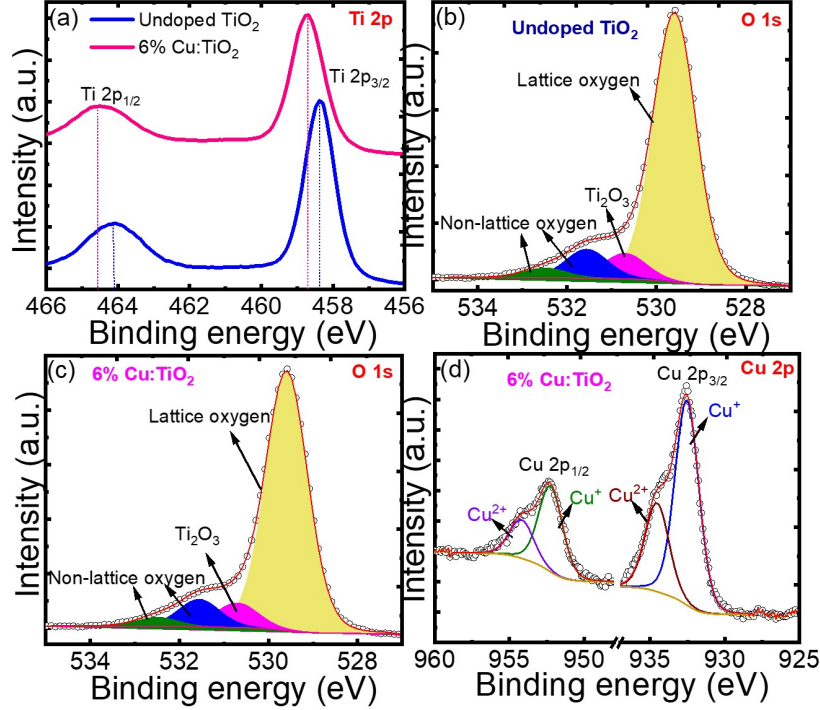


Figure 5.5: High resolution XPS spectra of (a) Ti 2p of undoped and 6% Cu: TiO<sub>2</sub> (b) O 1s of undoped TiO<sub>2</sub> (c) O 1s of 6% Cu:TiO<sub>2</sub> (d) Cu 2p of 6% Cu:TiO<sub>2</sub>.

doped TiO<sub>2</sub> are displayed in Figure 5.5(a). The peak at 458.41 eV and 464.08 eV corresponds to Ti 2P<sub>3/2</sub> and 2P<sub>1/2</sub>, respectively. The peak is slightly shifted towards a higher binding energy value in the case of 6% Cu doped TiO<sub>2</sub>. This shift reveals that Cu has been incorporated into the TiO<sub>2</sub> matrix [9]. The XPS spectra of O 1s for undoped and 6% Cu doped TiO<sub>2</sub> are shown in Figures 5.5(b) and (c), respectively. The spectra are deconvoluted into four peaks. The peaks centered at 529.59, and 530.71 eV are attributed to lattice oxygen (O<sub>L</sub>) and Ti<sub>2</sub>O<sub>3</sub> (oxygen vacancy, O<sub>V</sub>), respectively [10]. The 531.56 and 532.49 eV peaks are attributed to non-lattice or chemisorbed oxygen, (O<sub>C</sub>) [11]. The area of the peak corresponding to O<sub>L</sub> decreases from 80.84% to 68.65% after Cu doping. Conversely, after Cu doping, the area of peak linked to O<sub>V</sub> rises from 7.63% to 9.97%, indicating that an oxygen vacancy has been created in Cu doped TiO<sub>2</sub>. The high-resolution XPS spectra of Cu 2p

are deconvoluted into four peaks, as shown in Figure 5.5(d). The peaks centered at 932.58 and 952.28 correspond to Cu 2p<sub>3/2</sub> and 2p<sub>1/2</sub>, respectively, indicating Cu<sup>+</sup> oxidation state. Again the peaks for 2p<sub>3/2</sub> and 2p<sub>1/2</sub> at 934.58 and 954.28 eV, respectively are attributed to Cu<sup>2+</sup> oxidation state[12]. This result confirms that the Cu exists in the Cu<sup>+</sup> and Cu<sup>2+</sup> oxidation state.

## 5.4 Optical studies

The optical properties of semiconductor materials get modified after doping.

### 5.4.1 Photoluminescence

The photoluminescence (PL) spectrum is due to the radiative recombination of photo-generated electron-hole pairs. The analysis of PL spectra provides information about the distribution of mid-gap defect states. To study the defect states PL spectra of undoped and Cu doped TiO<sub>2</sub> were taken in the range 350 to 700 nm as shown in Figure 5.6(a). A laser of wavelength 325 nm (3.81 eV) was used to excite the electron from the valence band to the conduction band, which is greater than the bandgap (3.02 eV) of TiO<sub>2</sub>. All the spectra have a similar type of nature with approximately the same peak positions. The intensity of PL spectra determines the electron-hole recombination rate, the higher the intensity, the higher the recombination rate. The intensity of PL spectra decreases with Cu concentration as seen in Figure 5.6(a). The variation of integrated intensity with Cu concentration is plotted in Figure 5.6(b). The copper dopant creates oxygen vacancy. As the concentration of Cu increases, the oxygen vacancy increases which creates mid-states between the conduction band and valence band[13]. The photo-generated electrons get trapped by the midgap states reducing the electron-hole recombination and hence showing the decreasing trend of PL intensity.

The peaks are broad, so to study the origin of defects, the peaks are deconvoluted into five Gaussian peaks. As all the spectra have a similar trend, the deconvoluted peak of only

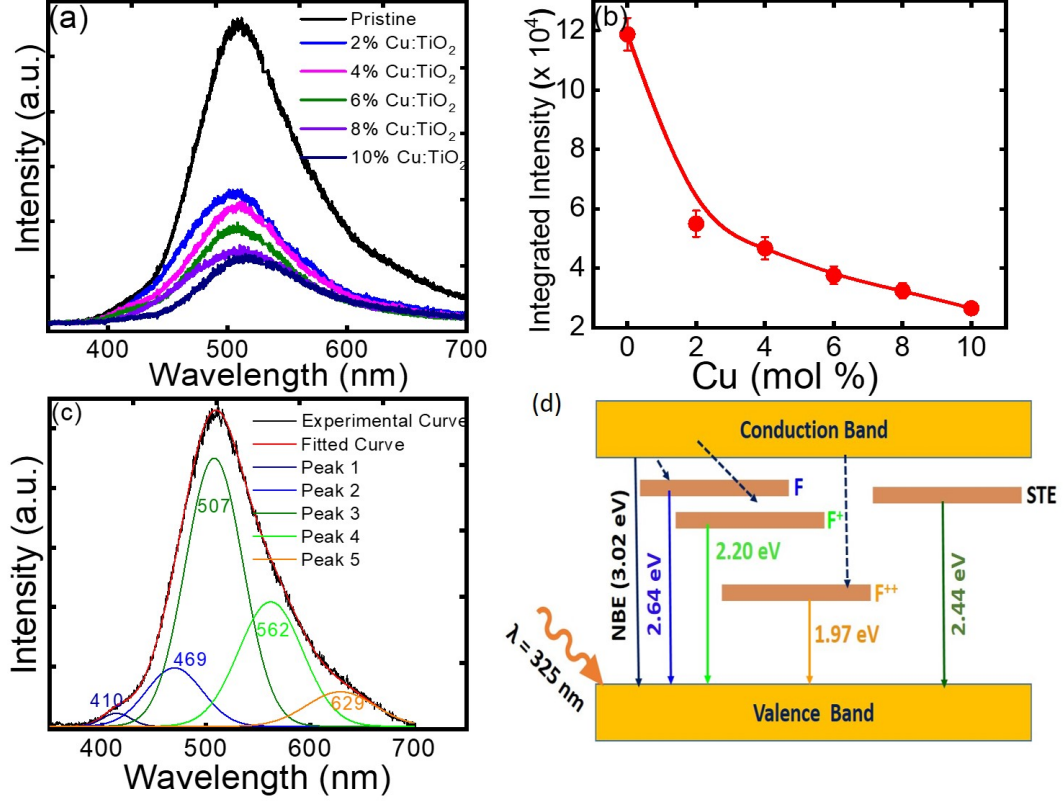


Figure 5.6: (a) PL spectra of undoped and Cu doped TiO<sub>2</sub>. (b) Variation of integrated intensity with Cu concentration. (c) Deconvoluted PL spectra of undoped TiO<sub>2</sub>. (d) Schematic diagram showing the origin of PL emissions.

the undoped sample is shown in Figure 5.6(c). The fitted Gaussian peaks are centered at 410 nm (3.02 eV, peak 1), 469 nm (2.64 eV, peak 2), 507 nm (2.44 eV, peak 3), 562 nm (2.20 eV, peak 4), 629 nm (1.97 eV, peak 5). When a photon of energy 3.81 eV falls on the TiO<sub>2</sub>, the electron from the valence band jumps to the conduction band leaving a hole behind. All the electrons do not recombine directly with the valence band holes, some of them get trapped by the defect states. The peak at 410 nm corresponds to the transition of electrons from the conduction band minimum to the valence band maximum (NBE). The other peaks are related to the defect state (oxygen vacancy) which is an intrinsic defect

in TiO<sub>2</sub> and it increases with the increasing concentration of Cu. The oxygen vacancy is associated with two electrons to maintain charge neutrality and forms the F center. The F center gets converted into F<sup>+</sup> and F<sup>++</sup> centers by losing electrons. The F and F<sup>+</sup> center form the shallow state below the conduction band and the energy of F<sup>++</sup> is lower than the above two states[14]. The transition of electrons from the conduction band to the shallow states occurs through the non-radiative transition. The emission spectra at 469 nm, 562 nm, and 629 nm correspond to the radiative recombination of electrons from F, F<sup>+</sup>, and F<sup>++</sup> defect states[15, 16]. The peak at 507 nm is due to self-trapped excitons confined in TiO<sub>6</sub> octahedra[17]. Table 1 lists the peak positions of the TiO<sub>2</sub> PL spectra examined by various researchers. The origin of PL emission observed in this work is schematically presented in Figure 5.6(d). It is well known that the defect states affect the optical bandgap of samples. So to analyze the effect of defects on the optical bandgap of materials, we performed UV-visible spectroscopy.

Table 5.2: Obtained PL peak positions from literature and our measurements for Cu doped TiO<sub>2</sub>

Peak positions (nm)	Excitation wavelength (nm)	Refference
410, 429, 464, 560, and 610	320	[16]
433,464,492, and 539	320	[18]
405, 420, 446, 470, 482, 492, and 508	270	[15]
530, 560, 569, 583,604, 619, 664, and 704	488	[15]
409, 432, 464, and 525	340	[19]
410, 469, 507, 562, and 629	325	This work

## 5.4.2 UV-visible spectroscopy

An important technique to measure the bandgap of a semiconductor is the absorption of incident photons. The absorbance spectra of pure and Cu doped TiO<sub>2</sub> microflowers are shown in Figure 5.7(a). The optical bandgap can be computed from the absorbance spectra



using the Tauc relation

$$\alpha h\nu = A(h\nu - E_g)^n \quad (5.1)$$

where  $\alpha$  is the coefficient of linear absorption,  $h\nu$  is the photon energy,  $A$  is a constant that depends on the transition probability,  $E_g$  is the optical bandgap energy of the material, and  $n$  is the index that characterizes the optical absorption process.  $n=1/2$  for direct and  $n=2$  for an indirect allowed transition[20]. The energy bandgap is obtained by extrapolating the linear region of the  $(\alpha h\nu)^2$  versus  $h\nu$  curve to the energy axis at  $\alpha=0$ . Figure 5.7(b) shows the changes in the bandgap with Cu concentration. It is seen that the bandgap decreases continuously with increasing Cu concentration and shifts the absorption tail towards the visible region of the electromagnetic spectrum. The narrowing of the bandgap indicates the presence of intermediate states in the forbidden gap of samples[21]. The valence band in TiO<sub>2</sub> is made up of the 3d orbitals of Ti and the 2p orbitals of O, while the conduction band is made up of the 3d orbitals of Ti, which are shown in the theoretical analysis of band structure that will be covered in the next part. Thus, electrons in pristine TiO<sub>2</sub> go from the valence band to the conduction band. The introduction of Cu into the TiO<sub>2</sub> matrix generates Cu 3d state in the mid-bandgap which enables the absorption in the visible region.[22] The optical bandgap is tunable and depends on Cu dopant concentration. This experimental result is well understood from the theoretical simulation of band structure and density of states (DOS) for pristine and Cu doped TiO<sub>2</sub>.

## 5.5 DFT calculations

To understand the role of Cu dopant on the electronic structure of rutile TiO<sub>2</sub> matrix, the band structure, and density of states (DOS) have been calculated for pristine and Cu doped TiO<sub>2</sub> based on the density functional theory (DFT) approach. In the Cu doped sample, one Ti is substituted by the Cu impurity. The DFT calculation is accomplished by im-

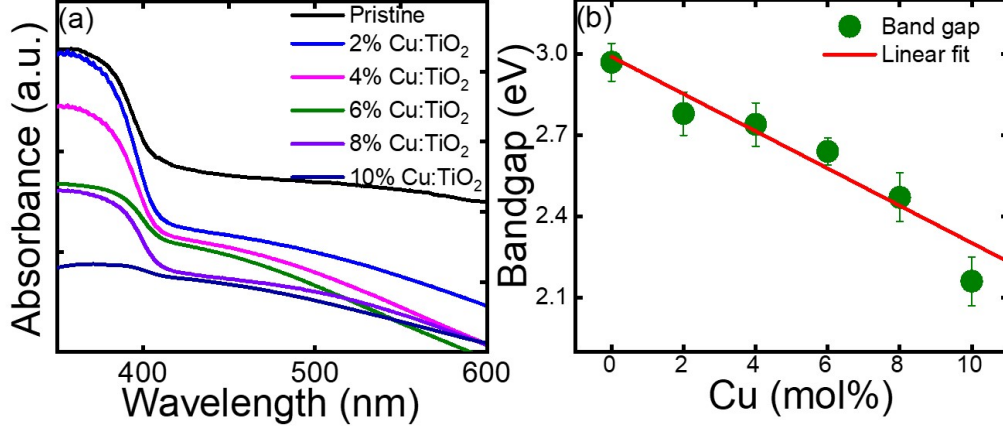


Figure 5.7: (a) Absorbance spectra of undoped and Cu doped TiO<sub>2</sub>. (b) Variation of bandgap with Cu concentration.

plementing the Vienna Ab initio Simulation Package (VASP) to relax the structure fully [23]. The complete relaxation happens when the forces surpass the value below 0.001 eV/Å for each atom using the generalized gradient approximation (GGA) scheme to account for the exchange-correlation interaction with the Perdew, Burke, and Ernzerhof (PBE) functional [24, 25]. The band structure and DOS are calculated using the most stable structure. The plane wave cut-off energy of 1000 eV was fixed for both calculations. The required convergence results within  $10^{-6}$  eV per atom are achieved by taking the suitable k points mesh of  $10 \times 10 \times 10$ . Figure 5.8(a) and (b) depict the simulated band structure for pristine and Cu doped TiO<sub>2</sub>, respectively. For pristine TiO<sub>2</sub>, the predicted bandgap is 1.65 eV. The values obtained from the UV-visible spectroscopy experiment sufficiently underestimate this theoretically calculated value. Previously, Mahmood et al. and Shao et al. reported the calculated bandgap to be 1.973 eV and 1.87 respectively using PBE-GGA which are closer to our calculated value [26, 27]. The bandgap of Cu doped TiO<sub>2</sub> is calculated to be 1.33 eV. This is because the introduction of Cu dopant states decreases the bandgap of TiO<sub>2</sub>. Though the theoretical and experimentally calculated values are different,

they follow the same trend upon Cu doping.

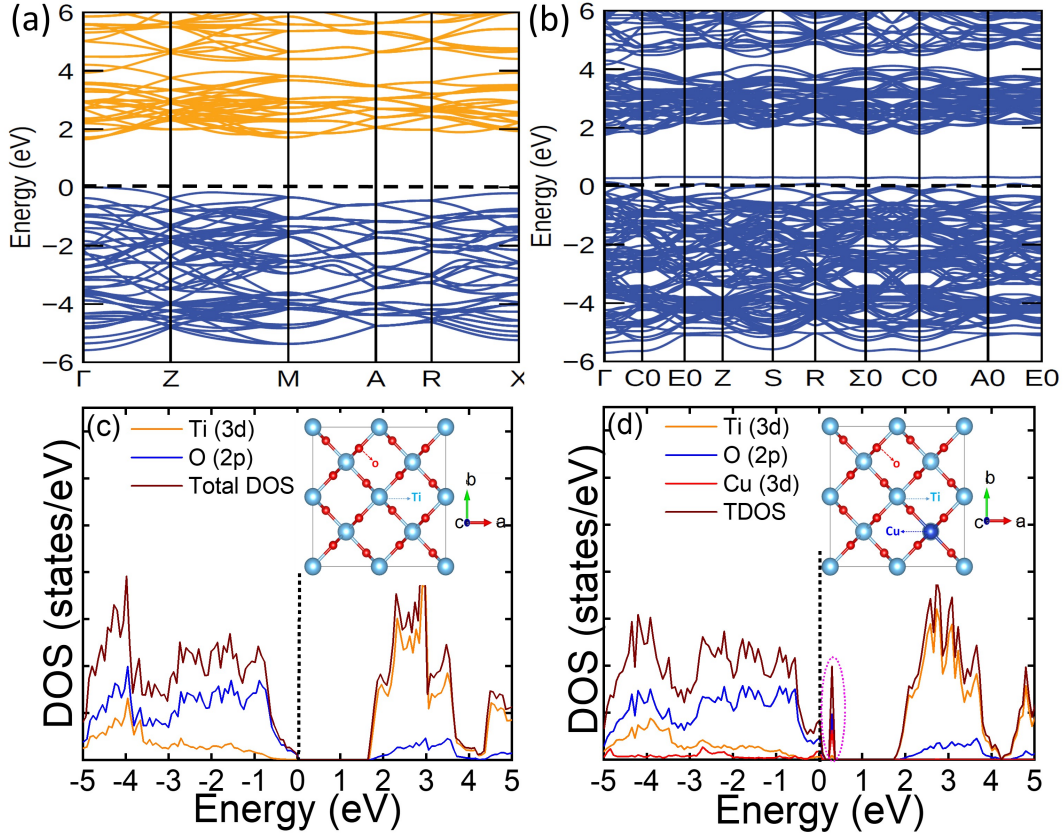


Figure 5.8: Band structure for (a) undoped (b) Cu doped TiO<sub>2</sub>. DOS plot for (c) undoped (d) Cu doped TiO<sub>2</sub> with their corresponding crystal structure in the inset. Dashed line at energy zero corresponds to the Fermi level.

In Cu doped sample, the Fermi level moves upward, reducing the bandgap as shown in Figure 5.8(b). To gain a better understanding of the bandgap lowering, we computed the DOS of pristine and Cu doped TiO<sub>2</sub> samples, which are displayed in Figure 5.8(c) and (d), respectively, and the corresponding crystal structures are shown in the inset. The crystal structures were created using VESTA software[28]. In Figure 5.8(c), we see that the valence band mainly consists of Ti-3d and O-2p states, and the conduction band is dominated by the Ti-3d state. In the Cu doped TiO<sub>2</sub> sample, the Cu 3d state which is the defect state is

generated above the Fermi level demonstrating the reduction of the bandgap. These findings verify that the substitution of the Ti atom by the Cu atom narrows down the bandgap.

## 5.6 NLO studies

The third-order NLO properties of pristine and Cu doped TiO<sub>2</sub> microflower are examined using the single beam Z-scan technique. The open aperture (OA) and closed aperture (CA) Z-scan measurements are used to obtain the nonlinear absorption coefficient ( $\beta$ ) and nonlinear refraction coefficient ( $n_2$ ) respectively. The values of  $\beta$  and  $n_2$  are obtained by fitting the normalized transmittance data with equations (5.2) and (5.3), respectively[29].

$$\Delta T = 1 - \frac{\beta I_0 L_{eff}}{2^{3/2}(x^2 + 1)} \quad (5.2)$$

$$\Delta T = 1 - \frac{4x\Delta\phi_0}{(x^2 + 9)(x^2 + 1)} - \frac{2(x^2 + 3)\Delta\Psi_0}{(x^2 + 1)(x^2 + 9)} \quad (5.3)$$

where  $I_0$  is the intensity of the laser beam at the focal plane (i.e.  $z=0$ ),  $L_{eff} = (1 - e^{-\alpha L})/\alpha$ ,  $L$  is the length of the sample,  $\alpha$  is linear absorption coefficient,  $x = z/z_0$ ,  $z$  is the sample position,  $\Delta\phi_0 = kn_2 I_0 L_{eff}$  and  $\Delta\Psi_0 = \beta I_0 L_{eff}/2$  is the phase change due to nonlinear refraction and absorption respectively,  $k=2\pi/\lambda$ ,  $\lambda$  is the laser wavelength.

The open aperture Z-scan measurements of TiO<sub>2</sub> samples at 532 nm excitation wavelength are shown in Figure 5.9. The measurements were taken at the on-axis peak intensity of  $1.51 \text{ GW/cm}^2$ . It is observed that for all the samples, the transmittance curve shows a peak at the focal plane, which establishes an indication of saturable absorption. When a material is exposed to highly intense laser light the electrons in the ground state of the material get excited to an appropriate higher state and get relax to the defect states. As a result, compared to the valence band, the stimulated band (conduction as well as a defect) has a higher occupation probability, which further prevents absorption. This causes the materials to be a saturable absorber with maximum transmission at the focal point. The

observed SA in the pristine and Cu doped TiO<sub>2</sub> is due to the presence of defect states in the forbidden gap. The presence of defect states has already been demonstrated from the XPS, PL, and UV visible spectroscopy. Both the intrinsic and impurity defects affect the NLO property of TiO<sub>2</sub>.

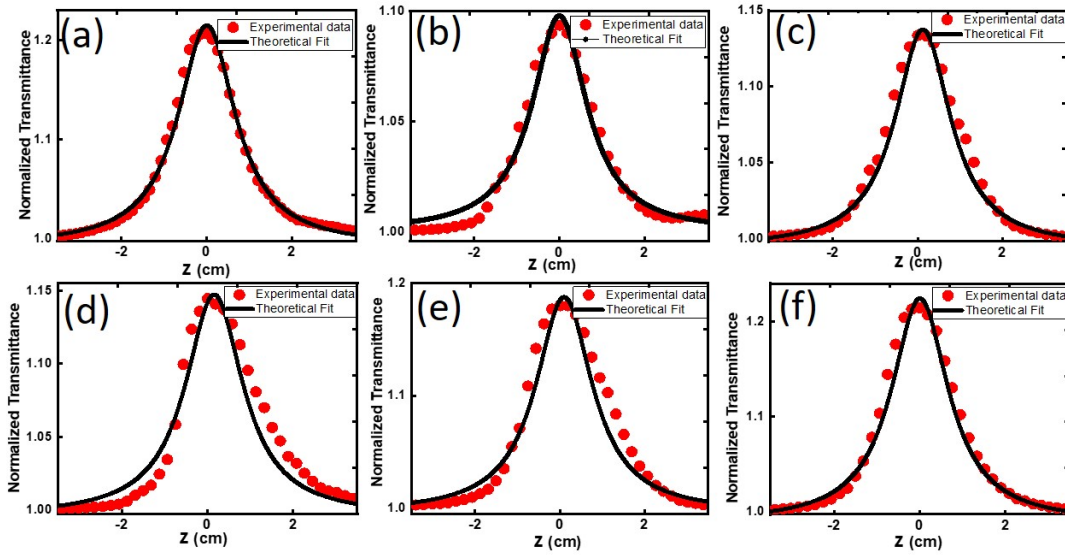


Figure 5.9: Open-aperture (OA) Z-scan curves at 532 nm the excitation wavelength for the TiO<sub>2</sub> with different Cu concentrations (a) undoped (b) 2% Cu doped (c) 4% Cu doped (d) 6% Cu doped (e) 8% Cu doped (f) 10% Cu doped TiO<sub>2</sub> fitted with equation 5.2.

Table 5.3: Obtained values of  $\beta$ ,  $n_2$  and FOM for the pristine and Cu doped TiO<sub>2</sub>

Sample	$\beta(cm/W) \times 10^{-5}$	$n_2(cm^2/W) \times 10^{-10}$	FOM (esu cm) $\times 10^{-13}$
TiO <sub>2</sub>	$-3.29 \pm 0.45$	$13.67 \pm 2.59$	$19.48 \pm 0.92$
2% Cu doped TiO <sub>2</sub>	$-5.68 \pm 0.87$	$8.92 \pm 2.45$	$26.95 \pm 0.93$
4% Cu doped TiO <sub>2</sub>	$-7.82 \pm 1.09$	$6.83 \pm 1.21$	$33.66 \pm 1.07$
6% Cu doped TiO <sub>2</sub>	$-9.69 \pm 1.3$	$1.20 \pm 0.36$	$41.05 \pm 1.12$
8% Cu doped TiO <sub>2</sub>	$-10.08 \pm 1.35$	$0.41 \pm 0.09$	$46.37 \pm 1.54$
10% Cu doped TiO <sub>2</sub>	$-9.24 \pm 1.27$	$-12.61 \pm 2.31$	$39.70 \pm 1.23$

As seen in Figure 5.9, the transmittance data were fitted using equation (5.2), and Table 5.2 contains a tabulation of the value of  $\beta$ . The black solid lines show the theoretically

fitted curve, and the red dots illustrate the experimental data. As the concentration of Cu rises, the value of  $\beta$  also rises. The additional defect states produced by doping, and the photothermal effect due to high laser excitation are primarily responsible for the rise in the value of  $\beta$  with Cu concentration[29].

The nonlinear refractive index ( $n_2$ ) of the samples is measured using close aperture Z-scan measurement. Figure 5.10 shows the normalized transmitted data of all the samples fitted with equation (5.3). The focal point is at  $z = 0$  and the positive and negative values of  $z$  represent the post-focal and prefocal positions, respectively. From pristine TiO<sub>2</sub> to 8% Cu TiO<sub>2</sub>, the samples exhibit valley-peak signatures indicating the positive value of  $n_2$  (self-focusing). On the other hand, the peak-valley signature of 10% Cu TiO<sub>2</sub> indicates a negative value of  $n_2$  (self-defocusing). The normalized transmittance curves were fitted with equation (5.3) to extract the value of  $n_2$  which is presented in Table 5.2. Additionally, it is noted that the difference in peak to valley position is higher in Cu doped TiO<sub>2</sub> samples as compared to pristine TiO<sub>2</sub>. Furthermore, the position of the valley is shifting away from the focal point in a negative Z direction from undoped TiO<sub>2</sub> to 8% Cu TiO<sub>2</sub> and establishes the occurrence of a sign reversal for 10% Cu TiO<sub>2</sub>. The increased number of defects at higher Cu concentrations may be absorbing more photons which causes the internal heating of the medium by the thermal agitation of the particles[30].

The absorption coefficient and nonlinear refractive index, respectively, are connected to the real and imaginary parts of third-order nonlinear susceptibility ( $\chi = \chi_r + i\chi_{im}$ ). The following relations establish the connection between  $\chi_{im}$  and  $\beta$

$$\chi_{im} = \left( \frac{10^{-7} c \lambda n^2}{96 \pi^2} \right) \beta \quad (5.4)$$

where  $c$  is the speed of light in vacuum,  $\lambda$  is the excitation wavelength, and  $n$  is the linear refractive index[31]. In this report, we defined the figure of merit (FOM) as  $FOM = \left| \frac{\chi_{im}}{\alpha} \right|$ ,



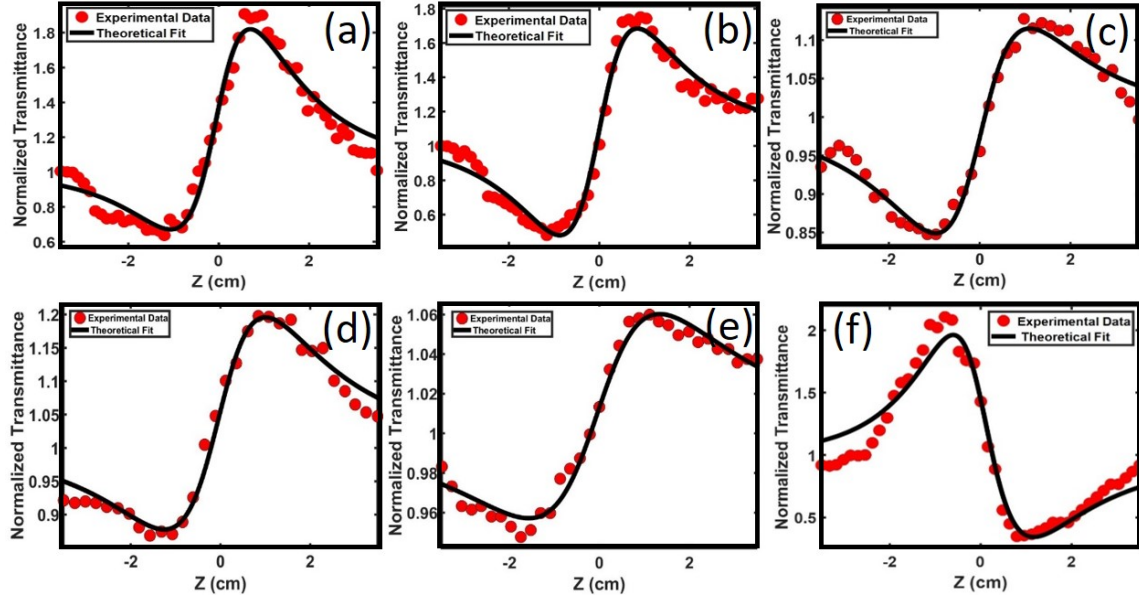


Figure 5.10: Close-aperture (CA) Z-scan curves at 532 nm the excitation wavelength for the TiO<sub>2</sub> with different Cu concentrations (a) undoped (b) 2% Cu doped (c) 4% Cu doped (d) 6% Cu doped (e) 8% Cu doped (f) 10% Cu doped TiO<sub>2</sub> fitted with equation 5.3.

which can give a correlation between the linear and nonlinear absorption coefficient[31].

The FOM is found to be increased and it has value  $19.48 \times 10^{-13}$ ,  $26.95 \times 10^{-13}$ ,  $33.66 \times 10^{-13}$ ,  $41.05 \times 10^{-13}$ ,  $46.37 \times 10^{-13}$ , and  $39.70 \times 10^{-13}$  esu cm for undoped TiO<sub>2</sub> to 10% Cu:TiO<sub>2</sub> sample, respectively. The FOM increases with increasing Cu concentration indicating that nonlinear absorption dominates over linear absorption. However, in the 10% Cu dope TiO<sub>2</sub>, the value of FOM deviates from the increasing order may be attributed to higher defect states. The variation of FOM and  $n_2$  with Cu concentration is presented in Figure 5.11. The value of FOM increases with higher concentration indicating stronger non-linear absorbance due larger number of defect states inside the TiO<sub>2</sub>. But the  $n_2$  decreases one order of magnitude up to 8% of Cu concentration and then becomes negative. This effect demonstrates the inverse behavior between  $\beta$  and  $n_2$  with defect concentration in Cu doping in TiO<sub>2</sub> nanostructures.

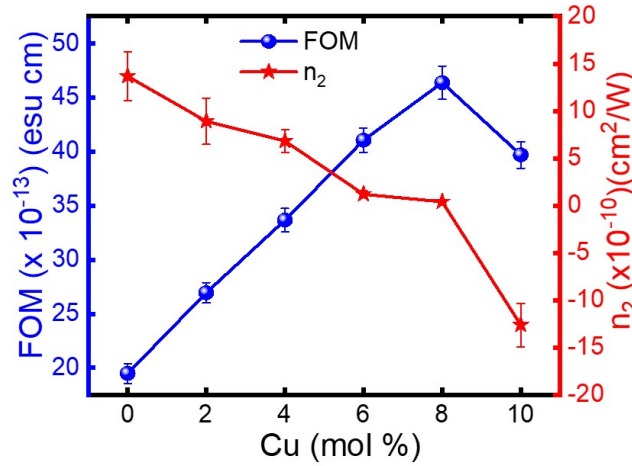


Figure 5.11: Variation of FOM and  $n_2$  with Cu concentration

## 5.7 Conclusion on nonlinear optical properties

In summary, Cu doped TiO<sub>2</sub> microflowers are prepared using the hydrothermal method. The ICP-OES, EDS, and XPS data reveal the elemental composition of the flowers to be Ti, O, and Cu. The XRD, HRTEM, and Raman spectroscopy confirm that the TiO<sub>2</sub> nanorod-composed microflower-like structures are purely in the rutile phase, and the phase remains unaltered after Cu doping. The Cu dopants improve the defect states, which help in electron trapping and slow down electron-hole recombination. In addition, the mid-bandgap states created by the Cu dopant shift the absorption band towards a higher wavelength region and reduce the bandgap of TiO<sub>2</sub> from 2.99 to 2.16 eV. The reduced bandgap is caused by the incorporation of defect states in the midgap region is analyzed from DFT calculations. In the OA measurement of NLO, all the samples show SA behavior and the nonlinear absorption coefficient gets improved with Cu concentration. Further, the CA measurement of NLO shows the self-focusing behavior of all the samples except 10 % Cu doped TiO<sub>2</sub> that shows self-defocusing behavior. The creation of defects plays a crucial role in tuning the linear and NLO properties of TiO<sub>2</sub>. The linear optical properties of the materials favor their usage



in photocatalysis and solar cells whereas, the NLO properties make it suitable for passive mode-locking, and Q-switching applications.

## 5.8 Anharmonicity and phonon lifetime from Raman spectroscopy

The room temperature Raman spectra of pristine TiO<sub>2</sub> and Cu doped TiO<sub>2</sub> are shown in Figure 5.12(a). Like in the previous chapters, the peak corresponding to different vibrational modes of rutile TiO<sub>2</sub> is identified in the Figure. Understanding the impact of dopant in the anharmonic effect of rutile TiO<sub>2</sub> will be helpful for high-temperature optoelectronic device applications. The anharmonic effect is dominant at high temperatures. So high-temperature Raman spectroscopy was carried out to extract the anharmonic effect of Cu doped TiO<sub>2</sub>. The temperature-dependent Raman spectra were collected for pristine, 1%, 4%, and 8% Cu doped TiO<sub>2</sub> samples in the temperature range of 300 – 800 K are shown in Figures 5.12 (b-d). From the Figures, it is observed that there is a systematic frequency shift and linewidth broadening of E<sub>g</sub> and A<sub>1g</sub> modes with temperature arising from the anharmonic effect[32]. The intensity of all the vibrational modes decreases with temperature and the intensity of the peak around 111 cm<sup>-1</sup> and 700 cm<sup>-1</sup> disappear at temp 800 K. With increasing the temperature, the E<sub>g</sub> mode is red shifted and the peak corresponding to multiphonon interaction (240 cm<sup>-1</sup>) is blue shifted. Now onwards, we will focus our study on the dominant peak of A<sub>1g</sub> and E<sub>g</sub> mode of vibration. The peak shift in Raman spectra can be interpreted as thermal expansion, cubic and quartic anharmonicities[33]. The shift of A<sub>1g</sub> is small as compared to E<sub>g</sub> mode attributed to the compensation of thermal expansion and higher-order anharmonicity[34].

From temperature-dependent Raman spectra, it is observed that the asymmetry of the Raman line shape is changing. So the most intense vibrational mode (E<sub>g</sub>) is fitted with the Breit-Wigner-Fano function as discussed in Chapter 1 (section 1.4). Figure 5.13(a) shows

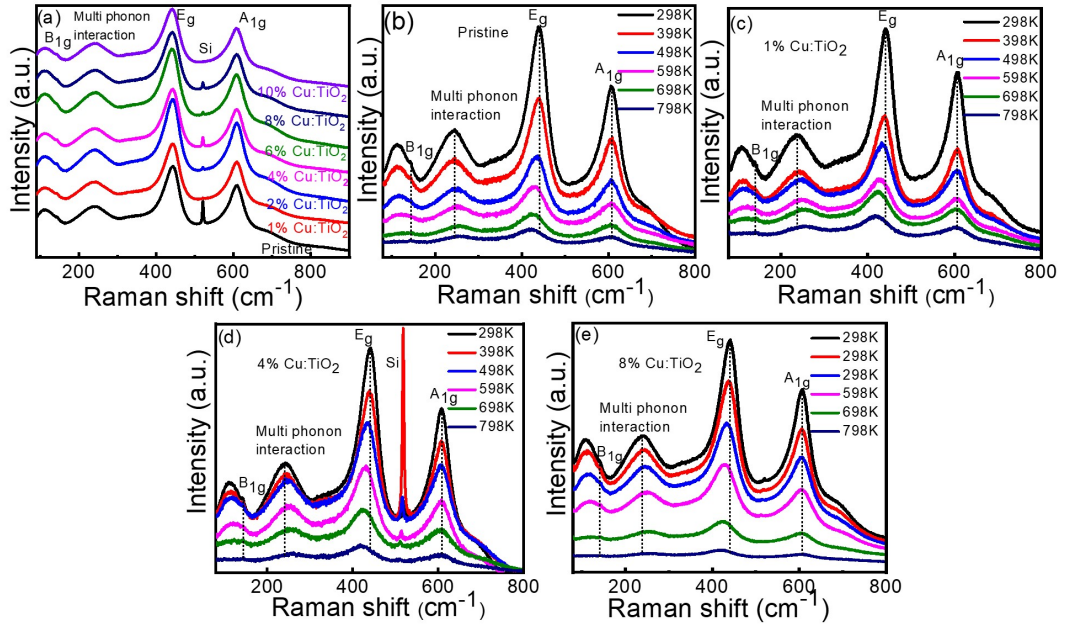


Figure 5.12: (a) Raman spectra of pristine and Cu doped  $\text{TiO}_2$ . Temperature-dependent Raman spectra of (b) pristine (c) 8% Cu doped  $\text{TiO}_2$ . (d) Variation FWHM with temperature fitted with equation 5.5. (e) Variation of Phonon lifetime with temperature for undoped and Cu doped  $\text{TiO}_2$ .

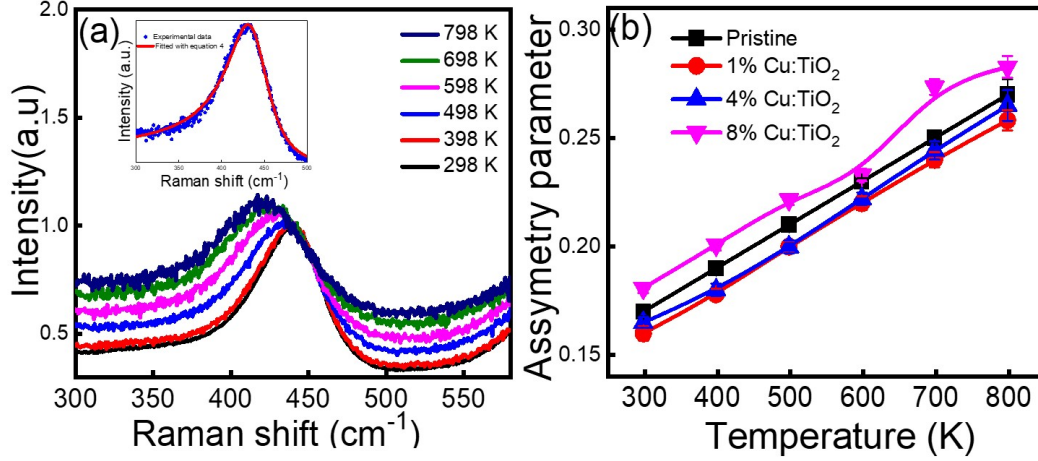


Figure 5.13: (a) Magnified view of  $E_g$  mode of undoped  $\text{TiO}_2$ . (b) Variation of asymmetry parameter with temperature.

the temperature-dependent Raman spectra of pristine  $\text{TiO}_2$  corresponding to  $E_g$  vibrational mode. As temperature increases, the  $E_g$  peak shifts towards the lower wavenumber, and asymmetry in the phonon curve is pronounced. At each temperature, the asymmetric parameter is calculated. The asymmetry parameter as a function of temperature is plotted in Figure 5.13(b) for pristine and Cu doped samples. The asymmetry parameter is negative as the asymmetry is in the lower wavenumber side of the peak[35]. The peak center shifted to a lower frequency is expected due to the combination of self-energy and stress in the lattice incorporation of substantial quantities of Cu. The asymmetry parameter initially decreases from pristine because of less stress and then increases monotonically with a higher concentration of Cu. Thus temperature-dependent Raman shift and linewidth fit well with the higher-order terms. Understanding the three and four-phonon interactions by doping with different concentrations will help to tune the thermal and electrical conductivity of the materials intriguing for better applications in miniaturizing the devices in industries and research.

The theoretical study predicts that asymmetry and anharmonicity are related to the deformed harmonic potential described by the interaction between atoms in the matrix[36]. So the more the asymmetry factor from the Raman peak, the higher anharmonicity can be observed. It is also known that the thermal expansion and the anharmonic coupling to phonons are the main two factors that affect the Raman shift with temperature. According to the Klemens model, the shift in Raman peak position as a function of temperature can be written as

$$\omega(T) = \omega_0 + \Delta\omega_1(T) + \Delta\omega_2(T) \quad (5.5)$$

where  $\omega_0$  is the harmonic frequency,  $\Delta\omega_1(T)$  is the contribution from thermal expansion and  $\Delta\omega_2(T)$  is the contribution from anharmonic interaction of phonons. The expression for  $\Delta\omega_1(T)$  is given by;

$$\Delta\omega_1(T) = \omega_0[\exp(-\gamma \int_0^T (2\alpha_{\perp}(T') + \alpha_{\parallel}(T'))dT') - 1] \quad (5.6)$$

where  $\gamma$  is Grüneisen parameter,  $\alpha_{\perp}$  and  $\alpha_{\parallel}$  are thermal expansion coefficients perpendicular and parallel to the c axis[37].  $\gamma$  is independent of temperature having value 2.43 for E<sub>g</sub> mode and 1.59 for A<sub>1g</sub> mode of vibration[34].

The anharmonic term  $\Delta\omega_2(T)$  can be written as

$$\Delta\omega_2(T) = A_{3-ph}(1 + \frac{2}{e^x - 1}) + B_{4-ph}(1 + \frac{3}{e^y - 1} + \frac{3}{(e^y - 1)^2}) \quad (5.7)$$

where,  $x = \frac{\hbar\omega(0)}{2K_B T}$ ,  $y = \frac{\hbar\omega(0)}{3K_B T}$ ,  $\omega(0)$  is Raman frequency at 0 K obtained by extrapolating the experimental data,  $A_{3-ph}$  and  $B_{4-ph}$  are fitting parameters for three-phonon and four-phonon processes respectively[37]. Depending on the phonon dispersion relation and single or diatomic material, the three or four-phonon interaction process dominates. However, both processes contribute to a good fitting in our case.

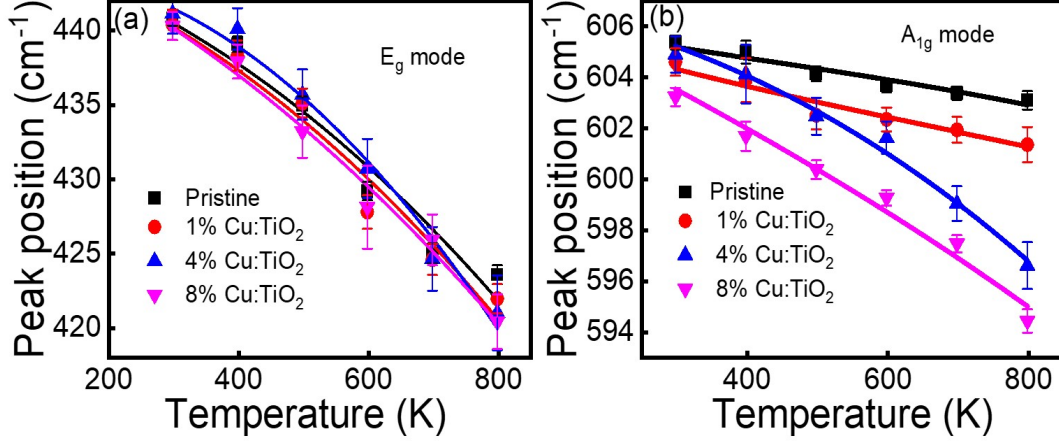


Figure 5.14: Experimental and theoretical fitted curve (solid lines) of Raman peak position of (a) E<sub>g</sub> mode (b) A<sub>1g</sub> mode of pristine and Cu TiO<sub>2</sub>.

Figures 5.14(a) and 5.14(b) show the Raman shift vs temperature for E<sub>g</sub> and A<sub>1g</sub> mode, respectively for pristine and Cu doped samples. Both the modes fitted using equation (5.5) with the least-square fittings parameters of the experimental data, continued the iteration fittings and obtained the best fitting. It is observed that E<sub>g</sub> mode becoming softened as compared to A<sub>1g</sub> mode. Initially, the Raman shift for E<sub>g</sub> mode reduced from the pristine value then reached a maximum at 4%, and then reduced again with temperature. However, the A<sub>1g</sub> is dominated by the thermal expansion part after 400°C and decreases monotonically with Cu%. The anharmonic effect also affects the linewidth of Raman spectra, which increases with temperature. Figures 5.15(a) and (b) show the variation of the linewidth of E<sub>g</sub> and A<sub>1g</sub> mode with temperature. The temperature-dependent linewidth is also fitted with the equation;

$$\Gamma(T) = \Gamma(0) + C_{3-ph} \left(1 + \frac{2}{e^x - 1}\right) + D_{4-ph} \left(1 + \frac{3}{e^y - 1} + \frac{3}{(e^y - 1)^2}\right) \quad (5.8)$$

where where,  $x = \frac{\hbar\omega(0)}{2K_B T}$ ,  $y = \frac{\hbar\omega(0)}{3K_B T}$ ,  $\omega(0)$  is Raman frequency at 0 K,  $C_{3-ph}$  and  $D_{4-ph}$  are fitting parameters for three-phonon and four-phonon processes respectively[34, 37].

$\omega(0)$  and  $\Gamma(0)$  obtained by extrapolating the experimental data to 0 K. The temperature-dependent linewidth for pristine and Cu doped samples was fitted using equation (5.8). The second term on the right side of equation (5.8) corresponds to the three-phonon process, and the third term is associated with the four-phonon process. The experimental linewidths are well fitted as shown in Figure 5.15(a,b) indicating that the three phonons and four phonon processes are also responsible for temperature-dependent variation of linewidth. This result is consistent with the result of Wang *et al.* in which they mentioned that the temperature-dependent linewidth rather depends on both the processes, not the individual three-phonon and four-phonon coupling[37].

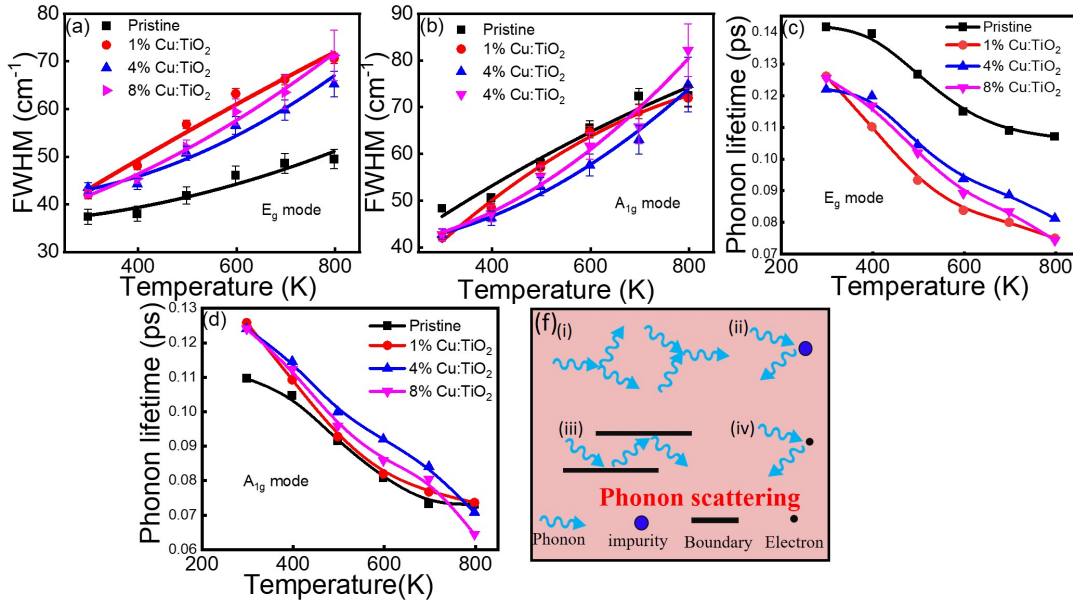


Figure 5.15: Experimental and theoretical fitted curve (solid lines) of Raman peak position of (a) E<sub>g</sub> mode (b) A<sub>1g</sub> mode of R-TiO<sub>2</sub>. Phonon lifetime of pristine and Cu doped TiO<sub>2</sub> (c) E<sub>g</sub> mode (d) A<sub>1g</sub> mode. (e) Schematic representation of phonon scattering.

The theory of Raman spectra line shape of a crystal lattice vibration in a dispersive medium predicts Lorentzian and the linewidth describes the damping effect, which is inversely proportional to the lifetime of the phonons. For an anharmonic potential, the linewidth

broadens due to crystal impurities (Cu in this case) and defects that provide the phonon decay channel and shorten the lifetime. The temperature-dependent Raman linewidth provides information about the phonon lifetime. The phonon lifetime was calculated using the energy-time uncertainty relation,

$$\frac{\Delta E}{\hbar} = 2\pi c\Gamma = \frac{1}{\tau} \quad (5.9)$$

where  $\Delta E$  is the uncertainty in the energy of phonon mode,  $\hbar$  is the Planck's constant,  $c$  is the velocity of light, and  $\Gamma$  is linewidth of phonon mode[38]. The calculated phonon lifetime for pristine and Cu doped samples with temperature is shown in Figure 5.15(c-d) for  $E_g$  and  $A_{1g}$  mode, respectively. In all the samples, the phonon lifetime decreases with an increase in temperature. Again the phonon lifetime falls faster in doped samples than in the pristine sample. The possible reason for the decay of phonon lifetime is the scattering of phonons. According to Matthiessen's rule, phonon lifetime has contribution from

$$\frac{1}{\tau} = \frac{1}{\tau_{phonon}} + \frac{1}{\tau_{defect}} + \frac{1}{\tau_{boundary}} + \frac{1}{\tau_{electron}} \quad (5.10)$$

The terms on the right side of equation (5.10) correspond to the scattering of phonons by phonons ( $\tau_{phonon}$ ), defects ( $\tau_{defect}$ ), boundary ( $\tau_{boundary}$ ), and electrons ( $\tau_{electron}$ ) respectively[39]. The phonon scattering is schematically presented in Figure 5.15(f). Phonon-phonon scattering is appreciable at high temperatures and causes a decrease in phonon lifetime with temperature. The second term in equation 5.10 is associated with defects which is contributed from Cu dopant atoms and oxygen vacancy. The phonon lifetime also depends on the crystallite size as indicated in the 3rd term of equation 5.10. It is observed that 4% Cu doped TiO<sub>2</sub> has a higher phonon lifetime. This could be due to the larger crystallite size and then the phonon lifetime decreases with a higher concentration of Cu dopant, which corroborated with the XRD shown in Figure 5.2(b). The number of free electrons associated with oxygen vacancy will increase upon Cu doping that scatters phonons reducing the phonon lifetime.

## **5.9 Conclusions on phonon anharmonicity and lifetime**

The temperature-dependent Raman spectroscopy illustrates the shift in peak position and linewidth of  $E_g$  and  $A_{1g}$  mode for pristine and Cu doped TiO<sub>2</sub>. The temperature-dependent Raman shift and linewidth fitted well with the non-linear parameters of the Klemens model and validated that the three and four-phonon processes are responsible for anharmonicity. The Cu dopant acts as an impurity that shortens the phonon lifetime and manifests the anharmonicity. In addition, the phonon lifetime decreases with an increase in temperature in all cases however, the trend of change in phonon lifetime and anharmonicity with Cu concentration is correlated with crystallite size. We have demonstrated that Cu dopant and oxygen vacancies act as a controlling knob to tune the parameters like crystallinity, bandgap, phonon lifetime, and asymmetry which tends to anharmonicity in TiO<sub>2</sub> matrix. Such tunable parameters can improve the thermal and photoconductivity in TiO<sub>2</sub> of nanoscale devices for various applications.



## References

- [1] Adriana Zaleska. Doped-TiO<sub>2</sub>: a review. *Recent patents on engineering*, 2(3):157, 2008.
- [2] B Leedahl, DA Zatsepin, DW Boukhvalov, RJ Green, JA McLeod, SS Kim, EZ Kurmaev, IS Zhidkov, NV Gavrilov, SO Cholakh, et al. Structural defects induced by Fe-ion implantation in TiO<sub>2</sub>. *Journal of Applied Physics*, 115(5), 2014.
- [3] Xinhua Zhu, Qi Li, Naiben Ming, and Zhongyan Meng. Origin of optical nonlinearity for PbO, TiO<sub>2</sub>, K<sub>2</sub>O, and SiO<sub>2</sub> optical glasses. *Applied physics letters*, 71(7):867, 1997.
- [4] Sugandha Dogra Pandey, Jasveer Singh, K Samanta, Nita Dilawar Sharma, and AK Bandyopadhyay. Temperature dependent variations of phonon interactions in nanocrystalline cerium oxide. *Journal of Nanomaterials*, 16(1):154, 2015.
- [5] Qi-C Sun, Dipanjan Mazumdar, Lena Yadgarov, Rita Rosentsveig, Reshef Tenne, and Janice L Musfeldt. Spectroscopic determination of phonon lifetimes in rhenium-doped MoS<sub>2</sub> nanoparticles. *Nano letters*, 13(6):2803, 2013.
- [6] Subhashree Sahoo, Gurupada Ghorai, Kalyan Ghosh, Bidyadhar Das, Mrinal K Sikdar, and Pratap K Sahoo. Anharmonicity of optical phonon modes in copper doped rutile TiO<sub>2</sub> nanorod composed microflowers. *AIP Advances*, 11(10):105013, 2021.
- [7] Javier Navas, Antonio Sánchez-Coronilla, Teresa Aguilar, Norge C Hernández, Desireé M de los Santos, Jesús Sánchez-Márquez, David Zorrilla, Concha Fernández-Lorenzo, Rodrigo Alcántara, and Joaquín Martín-Calleja. Experimental and theoret-

- ical study of the electronic properties of Cu-doped anatase TiO<sub>2</sub>. *Physical Chemistry Chemical Physics*, 16(8):3835, 2014.
- [8] Manoranjan Sahu and Pratim Biswas. Single-step processing of copper-doped titania nanomaterials in a flame aerosol reactor. *Nanoscale research letters*, 6:1, 2011.
- [9] Snehamol Mathew, Priyanka Ganguly, Stephen Rhatigan, Vignesh Kumaravel, Ciara Byrne, Steven J Hinder, John Bartlett, Michael Nolan, and Suresh C Pillai. Cu-doped TiO<sub>2</sub>: visible light assisted photocatalytic antimicrobial activity. *Applied Sciences*, 8(11):2067, 2018.
- [10] Bandna Bharti, Santosh Kumar, Heung-No Lee, and Rajesh Kumar. Formation of oxygen vacancies and Ti<sup>3+</sup> state in TiO<sub>2</sub> thin film and enhanced optical properties by air plasma treatment. *Scientific reports*, 6(1):32355, 2016.
- [11] Bing Wang, Xue Li, Shanshan Liang, Runxuan Chu, Dan Zhang, Hanqing Chen, Meng Wang, Shuang Zhou, Wei Chen, Xingzhong Cao, et al. Adsorption and oxidation of SO<sub>2</sub> on the surface of TiO<sub>2</sub> nanoparticles: the role of terminal hydroxyl and oxygen vacancy–Ti<sup>3+</sup> states. *Physical Chemistry Chemical Physics*, 22(18):9943, 2020.
- [12] Huizhi Sun, Osman Ahmed Zelekew, Xiaoyun Chen, Yuanbo Guo, Dong-Hau Kuo, Qingxin Lu, and Jinguo Lin. A noble bimetal oxysulfide Cu v OS catalyst for highly efficient catalytic reduction of 4-nitrophenol and organic dyes. *RSC advances*, 9(55):31828, 2019.
- [13] Javier Navas, Antonio Sánchez-Coronilla, Teresa Aguilar, Norge C. Hernández, Desireé M. de los Santos, Jesús Sánchez-Márquez, David Zorrilla, Concha Fernández-Lorenzo, Rodrigo Alcántara, and Joaquín Martín-Calleja. Experimental and theoretical study of the electronic properties of cu-doped anatase TiO<sub>2</sub>. *Phys. Chem. Chem. Phys.*, 16:3835, 014.

- 
- [14] A. Janotti, J. B. Varley, P. Rinke, N. Umezawa, G. Kresse, and C. G. Van de Walle. Hybrid functional studies of the oxygen vacancy in  $\text{TiO}_2$ . *Phys. Rev. B*, 81:085212, 2010.
- [15] Radhika V Nair, PK Gayathri, Venkata Siva Gummaluri, PMG Nambissan, and C Vijayan. Large bandgap narrowing in rutile  $\text{TiO}_2$  aimed towards visible light applications and its correlation with vacancy-type defects history and transformation. *Journal of Physics D: Applied Physics*, 51(4):045107, 2018.
- [16] Amreetha Seetharaman, Dhanuskodi Sivasubramanian, Vinitha Gandhiraj, and Venugopal Rao Soma. Tunable nanosecond and femtosecond nonlinear optical properties of C–N–S-doped  $\text{TiO}_2$  nanoparticles. *The Journal of Physical Chemistry C*, 121(43):24192, 2017.
- [17] Chetibi Loubna, Tetiana Busko, Nikolay Kulish, Djamel Hamana, Sahraoui Chaieb, and Slimane Achour. Photoluminescence properties of  $\text{TiO}_2$  nanofibers. *Journal of Nanoparticle Research*, 19, 2017.
- [18] Biswajit Choudhury and Amarjyoti Choudhury. Oxygen defect dependent variation of band gap, urbach energy and luminescence property of anatase, anatase–rutile mixed phase and of rutile phases of  $\text{TiO}_2$  nanoparticles. *Physica E: Low-Dimensional Systems and Nanostructures*, 56:364, 2014.
- [19] Fawad Tariq, Najeeb ur Rehman, Naureen Akhtar, Richard E George, Yaqoob Khan, and Shams ur Rahman. Room temperature photoluminescence in plasma treated rutile  $\text{TiO}_2$  (110) single crystals. *Vacuum*, 171:108999, 2020.
- [20] T Dhandayuthapani, R Sivakumar, and R Ilangoan. Growth of micro flower rutile  $\text{TiO}_2$  films by chemical bath deposition technique: Study on the properties of struc-

- tural, surface morphological, vibrational, optical and compositional. *Surfaces and Interfaces*, 4:59, 2016.
- [21] Radhika V Nair, P K Gayathri, Venkata Siva Gummaluri, P M G Nambissan, and C Vijayan. Large bandgap narrowing in rutile  $\text{TiO}_2$  aimed towards visible light applications and its correlation with vacancy-type defects history and transformation. *Journal of Physics D: Applied Physics*, 51(4):045107, jan 2018.
- [22] Ming-Chung Wu, Po-Yeh Wu, Ting-Han Lin, and Tz-Feng Lin. Photocatalytic performance of Cu-doped  $\text{TiO}_2$  nanofibers treated by the hydrothermal synthesis and air-thermal treatment. *Applied Surface Science*, 430:390, 2018.
- [23] Georg Kresse and Jürgen Furthmüller. Efficient iterative schemes for ab initio total-energy calculations using a plane-wave basis set. *Physical review B*, 54(16):11169, 1996.
- [24] Peter E Blöchl. Projector augmented-wave method. *Physical review B*, 50(24):17953, 1994.
- [25] John P Perdew, Kieron Burke, and Matthias Ernzerhof. Generalized gradient approximation made simple. *Physical review letters*, 77(18):3865, 1996.
- [26] Tariq Mahmood, Chuanbao Cao, R Ahmed, MA Saeed, Maqsood Ahmed, et al. Comparative study of structural and electronic properties of  $\text{TiO}_2$  at GGA and GGA+ U level. *Journal of Optoelectronics and Advanced Materials*, 16:117, 2014.
- [27] G Shao. Electronic structures of manganese-doped rutile  $\text{TiO}_2$  from first principles. *The Journal of Physical Chemistry C*, 112(47):18677, 2008.
- [28] K. Momma and F. Izumi. Vesta 3 for three-dimensional visualization of crystal, volumetric and morphology data. *J. Appl. Crystallogr.*, 44:1272, 2011.

- 
- [29] Mrinal K Sikdar, Nitul S Rajput, Ajanta Maity, and Pratap K Sahoo. Correlation between nonlinear optical properties and electronic band modification in cobalt-doped ZnO nanorods. *Physical Review Applied*, 14(1):014050, 2020.
- [30] Dhanuskodi Sivasubramanian, Rajeswari Ponnusamy, and Vinitha Gandhiraj. Low power optical limiting and thermal lensing in mn doped ZnO nanoparticles. *Materials Chemistry and Physics*, 159:93, 2015.
- [31] Km Surbhi, Sourav Bhakta, Pratap K Sahoo, and Ritwick Das. Impact of defects on the  $\chi$  (3) optical nonlinearity of sputtered WSe<sub>2</sub> thin films in the optical communication band. *Journal of Applied Physics*, 132(24), 2022.
- [32] Marko B Radović, ZD Dohcevic-Mitrovic, Aleksandar V Golubović, Branko Matović, Maja Šćepanović, and Zoran V Popović. Hydrothermal synthesis of CeO<sub>2</sub> and Ce<sub>0.9</sub>Fe<sub>0.1</sub>O<sub>2</sub> nanocrystals. *Acta Physica Polonica A*, 116(4):614, 2009.
- [33] Diptasikha Das, Subarna Das, P Singha, K Malik, AK Deb, A Bhattacharyya, VA Kulbachinskii, Raktima Basu, Sandip Dhara, S Bandyopadhyay, et al. Evolution of phonon anharmonicity in Se-doped Sb<sub>2</sub>Te<sub>3</sub> thermoelectrics. *Physical Review B*, 96(6):064116, 2017.
- [34] Tian Lan, Xiaoli Tang, and Brent Fultz. Phonon anharmonicity of rutile TiO<sub>2</sub> studied by Raman spectrometry and molecular dynamics simulations. *Physical Review B*, 85(9):094305, 2012.
- [35] Vitaly I Korepanov and Daria M Sedlovets. An asymmetric fitting function for condensed-phase Raman spectroscopy. *Analyst*, 143(11):2674, 2018.
- [36] Jenny Schneider, Masaya Matsuoka, Masato Takeuchi, Jinlong Zhang, Yu Horiuchi,

- Masakazu Anpo, and Detlef W Bahnemann. Understanding  $\text{TiO}_2$  photocatalysis: mechanisms and materials. *Chemical reviews*, 114(19):9919, 2014.
- [37] Deliang Wang, Bo Chen, and Jianhua Zhao. Lattice vibration fundamentals of nanocrystalline anatase: Temperature-dependent study using micro-Raman scattering spectroscopy. *Journal of applied physics*, 101(11), 2007.
- [38] Thomas Beechem and Samuel Graham. Temperature and doping dependence of phonon lifetimes and decay pathways in GaN. *Journal of Applied Physics*, 103(9):093507, 2008.
- [39] Qi-C Sun, Dipanjan Mazumdar, Lena Yadgarov, Rita Rosentsveig, Reshef Tenne, and Janice L Musfeldt. Spectroscopic determination of phonon lifetimes in rhenium-doped  $\text{MoS}_2$  nanoparticles. *Nano letters*, 13(6):2803, 2013.

## Chapter 6

# Nanoscale welding and melting of $\text{TiO}_2$ nanorods by 30 keV Au ion beams

## 6.1 Introduction

The manipulation of nanostructures for nanoscale devices is challenging and requires prompt attention. For a highly efficient device with optimal output, the morphology and defect in the nanostructures need to be controlled. Efforts are being made to interconnect the nanostructures using various techniques including scanning probe microscope [1], electron beam welding [2], ultrasonic welding [3], self-limited plasmonic welding [4] laser irradiation [5], thermal annealing [6] and ion beam irradiation [7, 8]. Among the above-mentioned techniques, nano welding by ion beam irradiation is a suitable approach for large-scale welding. In this case, the welding can be controlled by an ion beam fluence, beam current, and implanted ion. Welding of various one-dimensional metallic and semiconducting nanostructures has been done previously using ion beam irradiation. Shehla *et al.* used a 2.5 MeV proton beam with high beam current to fabricate different shapes of junctions such as X, Y, II, and T [7]. Hydrogen titanate nanowires are irradiated with  $\text{N}^+$  ions and state that the fluence plays a crucial role in forming junction [9]. A minimum fluence is required for the junction formation and is attributed to inhomogeneous defect generation, possible formation of chemical bonds between adjacent nanowires, and localized surface melting [9]. This is well known that for a very short time period, the target can go to a very high temperature or molten stage by ion irradiation, which depends on the thermal conductivity and  $S_n$ ,  $S_e$  value. The temperature evolution can be calculated using the elastic thermal spike model

(e-TSM) in the case of the low-energy ion beams and the inelastic thermal spike model (iTSM) for swift heavy ions (SHI). When the energy of the incident ion is relatively low one can use both the effect by the unified thermal spike model (UTSM) to calculate the temperature evolution. The ion beam-induced welding can be understood by the thermal spike model (TSM). When an ion is incident on a target material, it comes to rest by losing energy. This energy deposition creates a localized heat along the ion track taking the materials to a molten stage. When ion irradiation stops, the sudden quenching along the molten ion track can modify the materials and change the optical and structural properties of the material. In the case of nanomaterials, the melting can join two or more nanoparticles/rods/wires or melt the materials to make larger nanostructures.

In this work, we have explored the large area melting and welding of TiO<sub>2</sub> nanorods and microflowers by low energy (30 keV) Au<sup>+</sup> ion beam irradiation in a fluence ranges  $1 \times 10^{15} - 2 \times 10^{16}$  ions/cm<sup>2</sup>. The FESEM shows the melting of TiO<sub>2</sub> nanostructures after ion implantation. As the ion fluence increases, the surface morphology becomes smooth and shows a better melting effect. To understand the melting phenomena, the UTSM calculation was used considering the atomic subsystem heat transfer term due to nuclear energy loss, which provides the temperature raise in the system within a track radius of 1 to 10 nm range. In addition, the modification of structural and optical properties with low-energy heavy ion implantation is also discussed.

## **6.2 Experimental details**

The TiO<sub>2</sub> nanorods composed microflowers were synthesized using hydrothermal method as discussed in the experimental section and irradiated with by low energy (30 keV) Au<sup>+</sup> ion beam in a fluence ranges  $1 \times 10^{15} - 2 \times 10^{16}$  ions/cm<sup>2</sup>. The beam current of 60 nA was used to scan over an area of  $1 \times 1$  cm<sup>2</sup> for irradiation on all the samples. The surface morphology



and elemental composition of the samples were studied by field emission scanning electron microscopy (FESEM, ZEISS) attached with EDS. The X-ray diffraction (XRD) pattern was recorded by Rigaku Smartlab X-ray diffractometer using monochromatic radiation Cu K $\alpha$  ( $\lambda=1.5418$  Å) to analyze the crystal structure and phase of the sample. The local structural characterization of the sample was performed using a high-resolution transmission electron microscopy (HRTEM) system (JEM-F200, JEOL). The vibrational properties were examined using measurements done using the Raman spectrometer (Jobin-Yvon LabRam HR Evolution, Horiba) using a 532 nm laser. The absorbance spectra of samples were analyzed using a UV-VIS-NIR spectrometer (Agilent carry 5000 UV-Vis-NIR).

### **6.3 Ion beam simulations**

The projected range ( $R_p=12.6$  nm), vacancies, nuclear energy loss ( $S_n$ ), and electronic energy loss ( $S_e$ ) are simulated using the SRIM-2013 code.<sup>[10]</sup> The oxygen vacancy and Ti vacancy generated due to the Au ion implantation are plotted with depth in Figure 1(a), showing the number of oxygen vacancies is higher than that of Ti vacancy. During ion implantation, when the Au ion is implanted into the TiO<sub>2</sub> material, it undergoes collision with the nucleus and electrons of the Ti and O atoms and loses its energy through the nuclear stopping ( $S_n$ ) and electronic stopping ( $S_e$ ) power. The plot of  $S_e$  and  $S_n$  with energy of incident Au ion in the range 0-10 MeV is presented in Figure 1(b). It is observed that at lower energy below 3.75 MeV,  $S_n$  dominates over  $S_e$ , whereas at higher energy (above 3.75 MeV)  $S_e$  dominant, and the values of  $S_n$  and  $S_e$  are comparable when the energy of incident Au ion is 3.75 MeV. The simulated value of  $S_n$ , and  $S_e$  are 342 eV/Å and 32.8 eV/Å, respectively for 30 keV Au ions in TiO<sub>2</sub> matrix. The  $S_n$  dominates  $S_e$  at this low energy. Further, as the energy gets transferred from the Au ion to the TiO<sub>2</sub> matrix, it displaces the Ti and O atoms and creates Frenkel defects. The defect density can be calculated

using displacement per atom (DPA) as expressed in equation (6.1). The  $\frac{vacancies}{ions \times A^\circ}$  used in equation (1) was taken from the SRIM output file vacancy.txt file.

$$DPA = \left( \frac{vacancies}{ions \times A^\circ} \right) \times \frac{10^8 \left( \frac{A^\circ}{cm} \right) \times fluence \left( \frac{ions}{cm^2} \right)}{atom\ density \left( \frac{atoms}{cm^3} \right)} \quad (6.1)$$

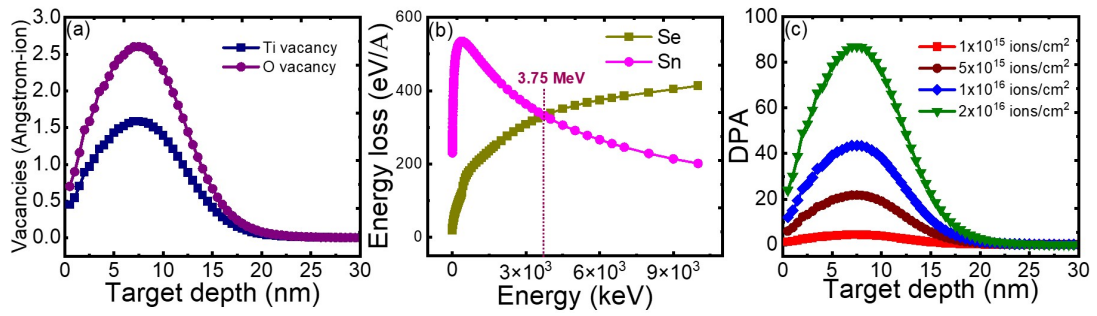


Figure 6.1: (a) Ti and O vacancy plot, (b) Atomic % of Au and (c) DPA for various fluence with depth for 30 keV Au ion implanted TiO<sub>2</sub>.

## 6.4 Morphological, elemental, and structural studies

### 6.4.1 FESEM

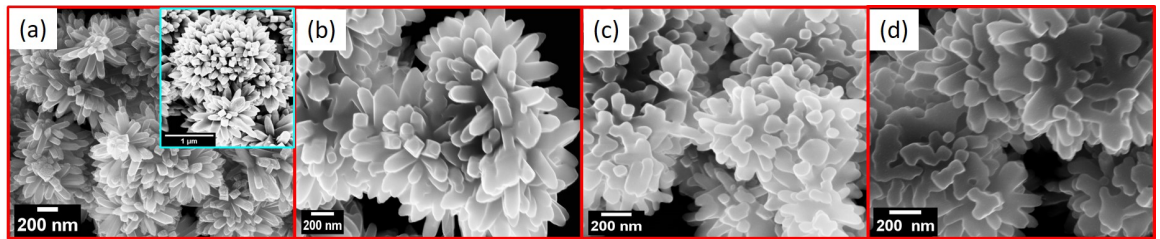


Figure 6.2: FESEM image of (a) pristine (inset shows FESEM image of pristine TiO<sub>2</sub> annealed at 800°C) (b) 5 × 10<sup>15</sup> (c) 1 × 10<sup>16</sup>, and (d) 2 × 10<sup>16</sup> ions/cm<sup>2</sup> Au implanted TiO<sub>2</sub>.

The surface morphology of the pristine and Au ion implanted TiO<sub>2</sub> microflowers are investigated using the FESEM images as shown in Figure 6.2. Figure 6.2(a) is the FESEM

image for the pristine sample. It is observed that the sample has flower structures that are formed by the interconnection of nanorods. Every single nanorod has a tetragonal shape and the tip has a pyramidal shape. At the lowest dose, there is no significant change in the morphology of the sample (not shown in the figure). At ion fluence  $5 \times 10^{15}$  ions/cm<sup>2</sup> a small change in the morphology is noticed, some nanorod tip gets flatted slightly as presented in Figure 6.2(b). At higher fluence ( $1 \times 10^{16}$  and  $2 \times 10^{16}$  ions/cm<sup>2</sup>) the morphology of the samples changes remarkably and the nanorods appear to be interconnected along with the flatted tip as shown in Figures 6.2(c) and 6.2(d). So we can conclude that surface deformation takes place sequentially with increasing the ion fluence. The diameter of flower structure in pristine TiO<sub>2</sub> is estimated to be nearly 1-2  $\mu$ m. The projected range of 30 keV Au ion in rutile TiO<sub>2</sub> is 12.6 nm, calculated from SRIM simulation. So the Au ions are completely embedded in the TiO<sub>2</sub> matrix in a Gaussian distribution within 5-15 nm below the surface. The structural deformation can be attributed to the generation of heat associated with ion irradiation. This phenomenon is discussed using the thermal spike model in the coming section. To compare the annealing effect due to ion beams, we have annealed the TiO<sub>2</sub> at 800<sup>o</sup>C and no change in the morphology of the sample is observed as seen in the inset of the FESEM image of the pristine sample (Figure 6.2(a)). The surface morphology confirms that ion irradiation can be used for the physical melting/welding of nanostructures.

#### **6.4.2 EDS**

The elemental composition of as-prepared samples is verified using EDS. Figure 6.3(b-d) shows the elemental mapping of  $2 \times 10^{16}$  ions/cm<sup>2</sup> Au implanted TiO<sub>2</sub> flower. The mapping shown in Figure 6.3(d) confirms the presence of Au in the flower. Again the EDS spectra for pristine and highest dose implanted samples are collected and depicted in Figure 6.3(e). Both the samples consist of Ti and O. A peak around 2.2 eV, corresponding to Au is observed in the implanted sample. The atomic percentage of Au increases from 0.05 % to 0.76 % in

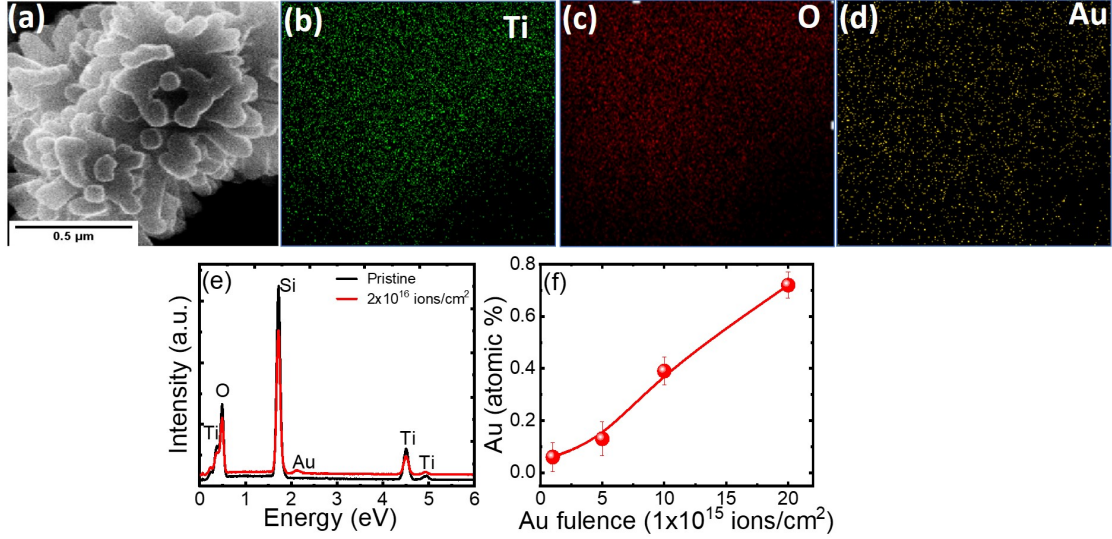


Figure 6.3: (a) FESEM image of  $2 \times 10^{16}$  ions/cm<sup>2</sup> Au implanted TiO<sub>2</sub> with the corresponding elemental mapping of Ti, O, and Au in (b-d) respectively. (e) EDS spectra for pristine and  $2 \times 10^{16}$  ions/cm<sup>2</sup> Au implanted TiO<sub>2</sub>. (f) Variation of atomic % of Au with ion fluence.

the implanted samples with ion fluence as shown in Figure 6.3(f).

### 6.4.3 XRD

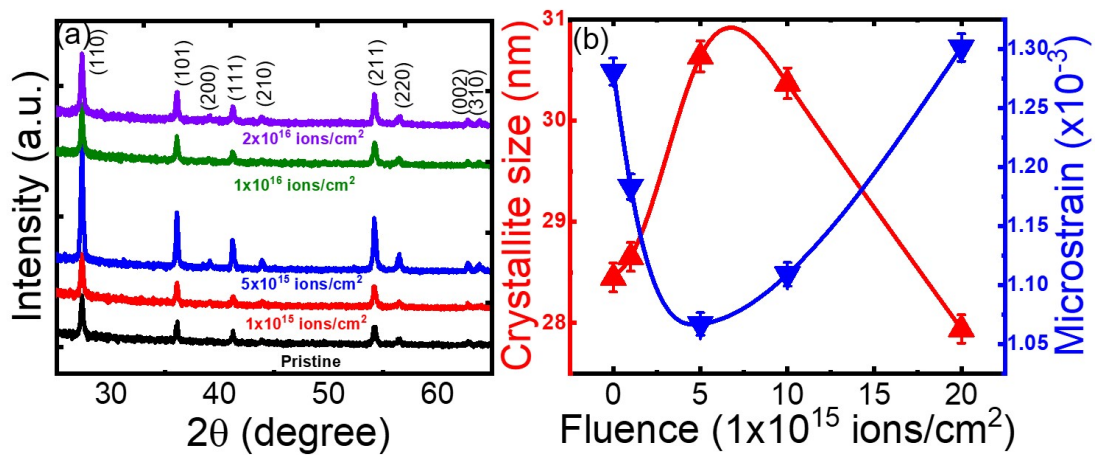


Figure 6.4: (a) XRD pattern of pristine and Au implanted TiO<sub>2</sub>. (b) Variation of crystallite size and microstrain with ion fluence.

The XRD pattern of pristine and Au ion implanted TiO<sub>2</sub> microflowers are shown in Figure 6.4(a). All the observed peaks correspond to the rutile phase of TiO<sub>2</sub>. Although a significant morphological change is noticed after Au ion implantation, the rutile phase of TiO<sub>2</sub> remains unaltered, and no other peaks are observed. The crystallite size of TiO<sub>2</sub> is calculated considering the highest intense diffraction peak (110) using the Debye-Scherrer formula as discussed in Chapter 3 (equation 3.2). The crystallite size is plotted against Au ion fluence in Figure 6.4(b). Initially, the crystallite size increases from pristine to  $5 \times 10^5$  Au ions/cm<sup>2</sup> implanted TiO<sub>2</sub> then decreases. The increase in crystallite size indicates substitutional doping of Au in TiO<sub>2</sub> [11]. At higher ion fluence, the interstitial doping of Au leads to a decrease in crystallite size. In addition, the microstrain is calculated using equation 3.4 and is plotted in the right panel of Figure 6.4(b). The Au ion may occupy the interstitial position due to its larger ionic radius as compared to both Ti and O atoms. So, the possible reason for increasing microstrain and decreasing crystallite size with ion fluence is attributed to the formation of new grain boundaries at higher fluence [12].

#### 6.4.4 TEM

The TEM micrograph of the  $2 \times 10^6$  ions/cm<sup>2</sup> Au implanted sample is presented in Figure 6.4. The dark contrast dots observed on the surface of the TiO<sub>2</sub> flowers in Figure 6.5(a) are Au clusters. The HRTEM image of the area bound by a red square is displayed in Figure 6.5(b). The black spots are crystalline Au nanoparticles with an interplanar spacing of 0.22 nm that matches with (111) planes of Au. The interplanar spacing of the region other than the black spots has an interplanar spacing of 0.33 nm matching with (110) plane of rutile TiO<sub>2</sub>. This data confirms that at the highest fluence, Au nanoparticles are formed in the TiO<sub>2</sub> matrix. Wang *et al.* also reported the formation of Au nanoclusters on the surface of TiO<sub>2</sub> nanostructure by implanting Au of energy 2 MeV with fluence  $6 \times 10^6$  ions/cm<sup>2</sup> [13]. They suggested that during the implantation, the Au ions are mobile, and segregate into Au

clusters. In our case, the average size of the cluster is found to be 2.2 nm calculated from the histogram of Figure 6.5(c).

Although the Au nanoparticles are observed from the FESEM and TEM data, the diffraction peak related to Au nanoparticles is missing. The reason can be attributed to (i) the detection limit of XRD is above the amount of Au and (ii) the smaller size of Au nanoparticles [14].

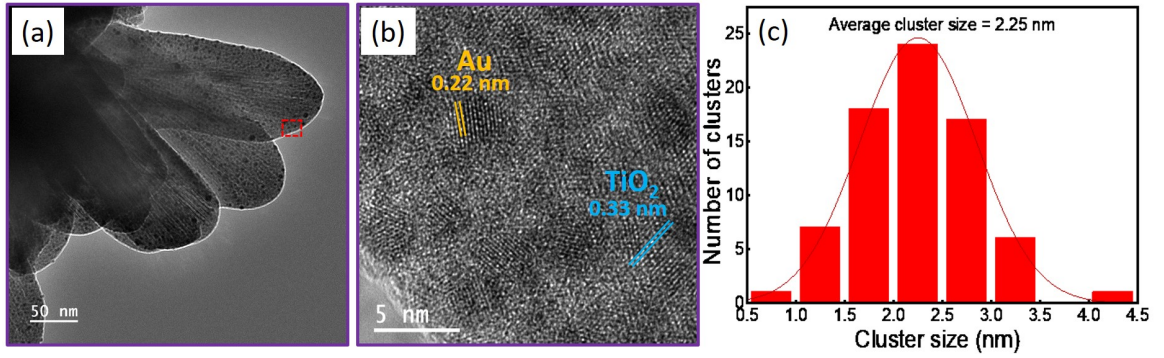


Figure 6.5: (a) TEM image of  $2 \times 10^6$  ions/cm<sup>2</sup> Au implanted TiO<sub>2</sub>. (b) HRTEM image of the area bounded by red square in (a). (c) Au cluster size distribution.

## 6.5 Optical studies

### 6.5.1 UV-visible and Raman spectroscopy

The UV-visible reflectance spectra of samples are collected using diffuse reflectance spectroscopy accessory. The collected reflectance data were converted to kubelka-Munk function  $F(R)$  and Tauc plot to calculate the bandgap, as discussed in Chapter 3 (subsection 3.5.1). The obtained bandgaps are plotted against the Au ion fluence depicted in Figure 6.6(a). The bandgap of pristine TiO<sub>2</sub> is 3.04 eV and it is decreasing sequentially down to 2.89 eV for the fluence of  $2 \times 10^6$  ions/cm<sup>2</sup>. The decrease in bandgap is attributed to the formation of midgap states in TiO<sub>2</sub>. Bhullar *et al.* theoretically reported that the introduction of impurity states caused by Au ion reduces the bandgap of TiO<sub>2</sub> [11].



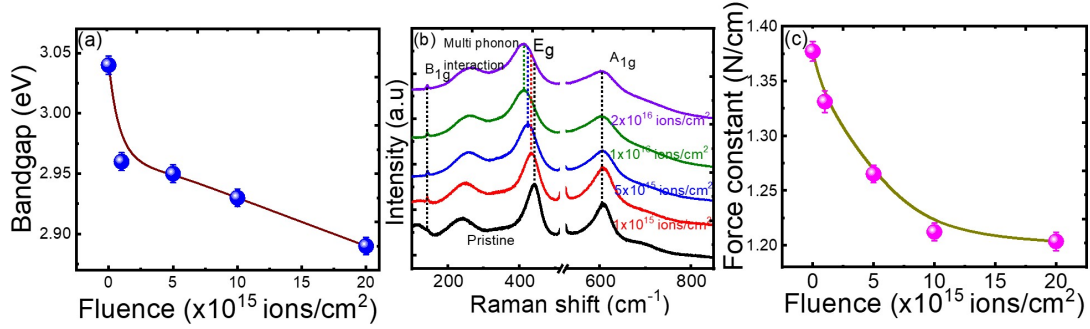


Figure 6.6: (a) Variation of bandgap with Au ion fluence. (b) Raman spectra of pristine and Au ion implanted TiO<sub>2</sub>. (c) Variation of force constant with ion fluence.

The Raman spectra of pristine and Au implanted samples are collected at room temperature in the range of 150-850 cm<sup>-1</sup>. The observed peaks are attributed to the rutile phase of TiO<sub>2</sub> (explained in detail in Chapter 2). The peak position of E<sub>g</sub> vibrational mode is shifting towards the lower wavenumber side with ion fluence. This peak shift indicates the presence of strain in the TiO<sub>2</sub> matrix upon ion implantation. The presence of Au ion affects the bond strength of the Ti-O bond, which can be determined from the force constant. The higher the value of the force constant, the higher the bond strength. The force constant ( $k$ ) is given by the relation,

$$k = (2\pi\omega_0)^2\mu \quad (6.2)$$

where  $\mu$  is the effective mass of Ti-O ( $1.98 \times 10^{-23}$  g),  $\omega_0$  is vibrational frequency. This relation shows that the force constant is proportional to the square of wavenumber[15]. As ion fluence increases the force constant decreases indicating that the incorporation of Au ions weakens the Ti-O bond strength. The value of  $k$  decreases from 1.37 to 1.20 N/cm while going from pristine to  $2 \times 10^6$  ions/cm<sup>2</sup> Au implanted TiO<sub>2</sub>.

## 6.6 The unified thermal spike model

For both basic research and material applications, the interaction of energetic ions with solids has drawn a lot of attention. Simulations have emerged as a powerful tool for studying the effect of incident ions on the host materials. The structural deformation of the TiO<sub>2</sub> microflowers can be explained based on the thermal spike model. It is reported that the thermal spike effect for low energy heavy ion is more dominant than other processes[16]. According to the thermal spike model, the target is comprised of two subsystems: atomic and electronic[17]. For swift heavy ions, the energy of the projectile ion is initially deposited in the electronic subsystem and the excited electrons release their energy to the lattice atoms by electron-phonon interaction causing the rise in temperature[18, 19].

For the low energy (30 keV) heavy ion beams, the nuclear energy deposition ( $S_n$ )=342 eV/Å is dominated as compared to the electronic energy deposition ( $S_e$ )=32.8 eV/Å. Thus, we have used a unified thermal spike model, where the nuclear contribution to the heating of the target was taken into consideration. The heat diffusion on both subsystems (electronic and atomic) are presented by a set of coupled differential equations in a cylindrical geometry as follows:

$$C_e \frac{\partial T_e}{\partial t} = \frac{1}{r} \frac{\partial}{\partial r} (r K_e(T_e) \frac{\partial T_e}{\partial r}) - g(T_e - T_a) + A(r, t) \quad (6.3)$$

$$C_a \frac{\partial T_a}{\partial t} = \frac{1}{r} \frac{\partial}{\partial r} (r K_a(T_a) \frac{\partial T_a}{\partial r}) + g(T_e - T_a) + B(r, t) \quad (6.4)$$

where  $r$  is the radial distance.  $C_{e,a}$ ,  $T_{e,a}$ , and  $K_{e,a}$  are the specific heat, temperature, and thermal conductivity of the electronic and atomic subsystem, respectively.  $g(T_e - T_a)$  is the coupling term with  $g$  being the phonon coupling coefficient[17]. The energy deposition on electrons through  $S_e$  at radial distance  $r$  and at time  $t$  is taken into account by the term  $A(r,t)$ , and the energy deposited to lattice through  $S_n$  is taken into account by the term  $B(r,t)$ .



). Here the electronic energy loss is neglected, and the nuclear energy loss is represented by the relation;

$$B(r, t) = b_n \times S_n \times e^{\frac{-t}{\tau}} \times e^{\frac{-r}{r_0}} / r \quad (6.5)$$

where  $b_n$  was chosen so that integration over time and space yields the total nuclear energy loss,  $\tau$  is the deposition time taken as  $1 \times 10^{-13}$ , and  $r_0$  is the radius of a cylinder in which the nuclear energy is deposited[20].

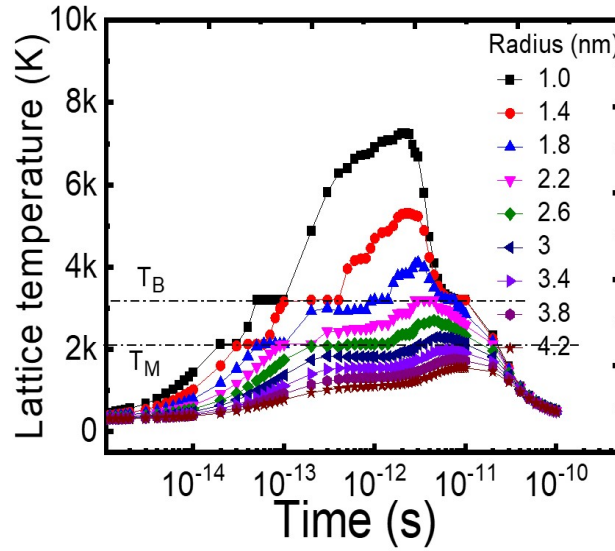


Figure 6.7: Lattice temperatures at several radii from a 30 keV Au ion trajectory in TiO<sub>2</sub>.

To calculate the value of  $r_0$  the mean energy transfer  $\langle T \rangle$  to Ti and O atoms was calculated from the screened elastic scattering cross-section. Then using SRIM, the corresponding mean range is calculated. The value of  $r_0$  was estimated to be 22 Å. In addition, the other parameters of TiO<sub>2</sub> used for the thermal spike calculation are listed in Table 6.1, and using these parameters the time-evolution curves of lattice temperatures for 30 keV Au in TiO<sub>2</sub> are simulated as shown in Figure 6.7. The melting point and boiling point of TiO<sub>2</sub> are shown as a horizontal line in Figure 6.7. As shown in the figure, 30 keV Au ion beams

melt the TiO<sub>2</sub> along a cylinder of radius 3.4 nm. As the number of ions increases (ion fluence increases), the TiO<sub>2</sub> nanorods melt by 30 keV ion beams and spread from its original diameter. When two nanorods are close to each other they join together and look like welding.

Table 6.1: The parameters of TiO<sub>2</sub> used for the thermal spike calculation taken from ref [21]

Parameter	Value
Latent heat of fusion (J/g)	838.07
Latent heat of vaporization (J/g)	838.07
Melting point (K)	2130
Boiling point (K)	3200
Density of solid (g/cm <sup>3</sup> )	4.25
Density of liquid (g/cm <sup>3</sup> )	3.21
Specific heat of electron (J/cm K sec)	1
Thermal conductivity of electron (J/cm K sec)	2
Specific heat of lattice (J/g K)	$C_a(T) = 0.96072 - 1.15732 \times e^{(-0.00482 \times T)}$
Thermal conductivity of lattice (J/cm K sec)	$K_a(T) = 0.03215 + 0.2836 \times e^{(-T/200)}$
Electron-phonon mean free path (nm)	5.8

## 6.7 Effect of melting on TiO<sub>2</sub> junctions

The surface deformation of TiO<sub>2</sub> flowers as observed in Figure 6.2 is the point of motivation to investigate the change in morphology of different kinds of nanostructures. Some selected shapes of joined nanorods having Y, X, and flower structures are displayed in Figure 6.8. We have selected some Y and X structures, in which the junction is damaged or not grown properly. With ion fluence, those damaged parts get recovered and the dimension of the structure also increases. This is caused by the melting of the nanorods. Due to the thermal spike, the nanostructures reach the molten stage, and the area as well as the diameter of the nanostructures increases. The width of the nanorod increased from approximately 48 nm (pristine TiO<sub>2</sub>) to 107 nm ( $2 \times 10^{16}$  ions/cm<sup>2</sup> Au implanted TiO<sub>2</sub>). In the flower structure, the nanorods are interlinked with each other at the center, which is visible in the pristine

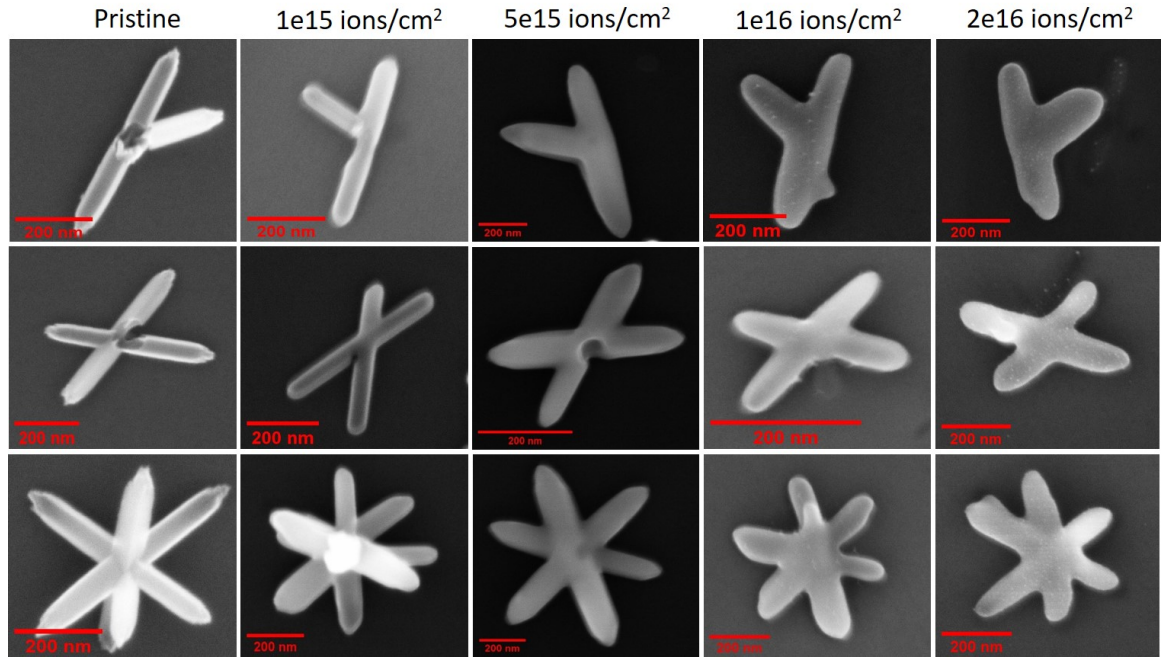


Figure 6.8: FESEM image of pristine and Au ion implanted  $\text{TiO}_2$  having different structures.

sample. As fluence increases the significant change at the junction is observed.

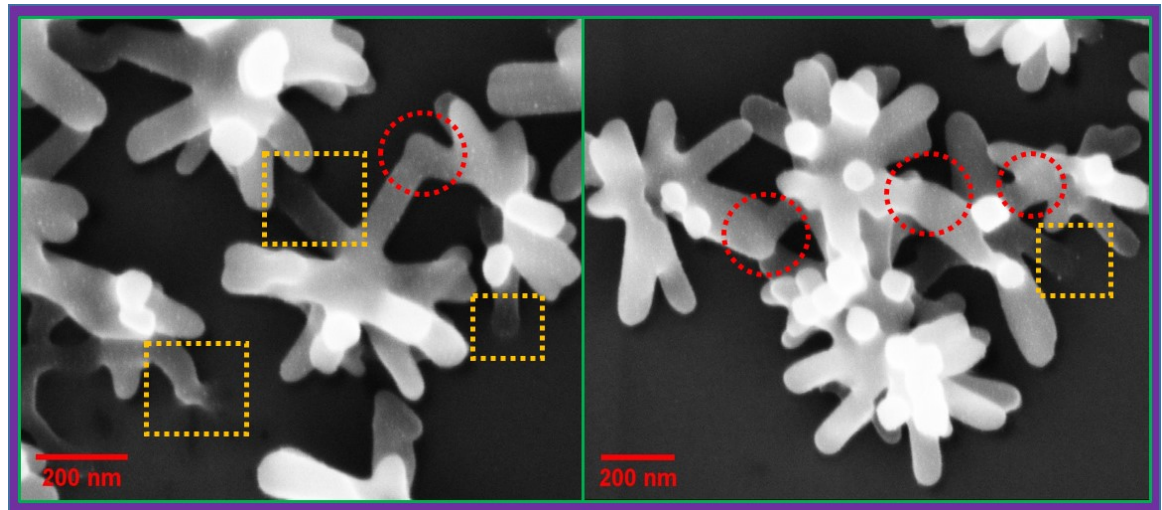


Figure 6.9: FESEM image of  $2 \times 10^{16}$  ions/cm<sup>2</sup> Au implanted  $\text{TiO}_2$  showing melting and welding of nanorods of two different flowers.

Further, the junction formed by two rods of different flowers is captured as shown in Figure 6.9. The regions with red dashed circles show the junction of two nanorods belonging to different flowers. The close nanorods look like welding at the junctions. The smoothness of the surface can be attributed to the improved crystallinity of the nanorods. The detail study of these junctions are in progress to understand the junction properties of the nanorods. It is also observed that some rods are melted and connected to the Si substrate as shown by area bounded by the yellow square. The observation can be extended to fabricate nano-junction of nanorods, nano-particles, or even thin films of different materials by ion irradiation of suitable ions, energy and fluences.

## **6.8 Conclusions**

In summary, TiO<sub>2</sub> microflowers are prepared using the hydrothermal method and then implanted with 30 keV Au ion at four different fluences. The SRIM simulation reveals that the displacements of atoms take place with Au ion irradiation that increases with ion fluence. FESEM images show remarkable structural modification of the microflowers and nanorods after ion implantation. The structural modification starts slowly from the lower fluence and becomes more noticeable as the fluence increases. The XRD data confirms the phase purity and crystalline nature of the TiO<sub>2</sub>, which remain intact after ion implantation. The EDS and TEM data confirm the presence of Au in the ion-implanted TiO<sub>2</sub> systems and at higher fluence nanoparticles of Au are observed. In addition to the structural properties, the optical properties of the TiO<sub>2</sub> get modified after ion implantation. The bandgap decreases monotonically with ion fluence indicating the incorporation of midgap states associated with Au ion implantation. It is demonstrated that irradiation of TiO<sub>2</sub> with 30 keV Au ions induces melting and junction formation of the nanorods. This melting is caused by the rise of temperature during ion implantation, which arises from the energy loss of the projected ion and

is theoretically simulated using the universal thermal spike model. This indicates that the welding can be manipulated by controlling the ion fluence. From the above discussions, it is clarified that the ion beam technique can be used for the fabrication of large-scale junctions which is essential in nano-electronic devices.

## References

- [1] Xiaojie Duan, Jin Zhang, Xing Ling, and Zhongfan Liu. Nano-welding by scanning probe microscope. *Journal of the American Chemical Society*, 127(23):8268, 2005.
- [2] Xiaomeng Liu, Quanlin Dong, Pengfei Wang, and He Chen. Review of electron beam welding technology in space environment. *Optik*, 225:165720, 2021.
- [3] Changxin Chen, Lijun Yan, Eric Siu-Wai Kong, and Yafei Zhang. Ultrasonic nanowelding of carbon nanotubes to metal electrodes. *Nanotechnology*, 17(9):2192, 2006.
- [4] Erik C Garnett, Wenshan Cai, Judy J Cha, Fakhruddin Mahmood, Stephen T Connor, M Greyson Christoforo, Yi Cui, Michael D McGehee, and Mark L Brongersma. Self-limited plasmonic welding of silver nanowire junctions. *Nature materials*, 11(3):241, 2012.
- [5] Seol Ji Kim and Du-Jeon Jang. Laser-induced nanowelding of gold nanoparticles. *Applied Physics Letters*, 86(3), 2005.
- [6] Jong Sik Oh, Ji Soo Oh, Jae Hee Shin, Geun Young Yeom, and Kyong Nam Kim. Nano-welding of Ag nanowires using rapid thermal annealing for transparent conductive films. *Journal of nanoscience and nanotechnology*, 15(11):8647, 2015.
- [7] Honey Shehla, Ahmad Ishaq, Yaqoob Khan, Iqbal Javed, Riaz Saira, Naseem Shahzad, and Malik Maaza. Ion beam irradiation-induced nano-welding of Ag nanowires. *Micro & Nano Letters*, 11(1):34, 2016.
- [8] Ahmad Ishaq, Zhichun Ni, Long Yan, Jinlong Gong, and Dezhang Zhu. Constructing carbon nanotube junctions by Ar ion beam irradiation. *Radiation Physics and Chemistry*, 79(6):687, 2010.

- 
- [9] Satyanarayan Dhal, Shyamal Chatterjee, Subhrangsu Sarkar, Lokesh C Tribedi, Rudheer Bapat, and Pushan Ayyub. Nano-welding and junction formation in hydrogen titanate nanowires by low-energy nitrogen ion irradiation. *Nanotechnology*, 26(23):235601, 2015.
- [10] JF Zeigler, JP Biersack, UND Littmark, et al. The stopping and range of ions in solids. *The Stopping and Range of Ions in Matter*, 1, 1985.
- [11] Viplove Bhullar, Devarani Devi, Fouran Singh, Sundeep Chopra, Anil Krishna Deb Nath, Dinesh Kumar Aswal, and Aman Mahajan. Ion implanted substitutionally dispersed au in TiO<sub>2</sub> nanostructures for efficient and stable dye sensitized solar cells. *Optical Materials*, 132:112800, 2022.
- [12] Jyotshana Gaur, Hitesh Kumar Sharma, Shrestha Tyagi, Chetna Tyagi, Pargam Vashishtha, Sanjeev K Sharma, and Beer Pal Singh. Enhancement of photosensitivity of thermally evaporated crystalline PbS thin films by low energy oxygen ions implantation. *Nano Express*, 1(2):020044, 2020.
- [13] Chong M Wang, Yanwen Zhang, V Shutthanandan, Suntharampillai Thevuthasan, and Gerd Duscher. Microstructure of precipitated au nanoclusters in TiO<sub>2</sub>. *Journal of applied physics*, 95(12):8185, 2004.
- [14] Gregor Žerjav, Matevž Roškarič, Janez Zavašnik, Janez Kovač, and Albin Pintar. Effect of au loading on schottky barrier height in TiO<sub>2</sub> + Au plasmonic photocatalysts. *Applied Surface Science*, 579:152196, 2022.
- [15] Yuliang Zhang, Cindel X. Harris, Petra Wallenmeyer, James Murowchick, and Xiaobo Chen. Asymmetric lattice vibrational characteristics of rutile TiO<sub>2</sub> as revealed by laser power dependent Raman spectroscopy. *The Journal of Physical Chemistry C*, 117(45):24015, 2013.

- [16] Q Yang, T Li, BV King, and RJ MacDonald. Thermal spike effects in low-energy single-ion impacts on graphite. *Physical Review B*, 53(6):3032, 1996.
- [17] DP Datta, A Chettah, V Siva, D Kanjilal, and PK Sahoo. Dewetting induced Au–Ge composite nanodot evolution in SiO<sub>2</sub>. *Applied Surface Science*, 428:676, 2018.
- [18] A Chettah, H Amekura, R Baeker, H Kucal, Y Takeda, M Matsuda, and A Iwase. The inelastic thermal spike model applied to metal/insulator interfaces. *physica status solidi (c)*, 12(1-2):102, 2015.
- [19] Paramita Patra, Sejal Shah, M Toulemonde, I Sulania, and F Singh. Investigation of radiation damage using thermal spike model for shi irradiation on Al<sub>2</sub>O<sub>3</sub>. *Radiation Effects and Defects in Solids*, 177:513, 2022.
- [20] Marcel Toulemonde, William J Weber, Guosheng Li, Vaithiyalingam Shutthanandan, Patrick Kluth, Tengfei Yang, Yuguang Wang, and Yanwen Zhang. Synergy of nuclear and electronic energy losses in ion-irradiation processes: The case of vitreous silicon dioxide. *Physical Review B*, 83(5):054106, 2011.
- [21] Sutapa Dey, Anusmita Chakravorty, Shashi Bhusan Mishra, Nasima Khatun, Arnab Hazra, Birabar Ranjit Kumar Nanda, Chandran Sudakar, Debdulal Kabiraj, and Somnath C Roy. Localized thermal spike driven morphology and electronic structure transformation in swift heavy ion irradiated TiO<sub>2</sub> nanorods. *Nanoscale Advances*, 4(1):241, 2022.



## Chapter 7

# Photocatalytic activity of Au decorated TiO<sub>2</sub> microflowers

### 7.1 Introduction

Photocatalysis is an effective method to remove toxic organic molecules coming out from different industries[1]. TiO<sub>2</sub> is a well-known wide bandgap semiconductor photocatalyst. The wide bandgap prohibits the usage of the visible range of the solar spectrum. In addition, the photogenerated electron-hole carriers face quick recombination to slow down the catalysis process. The two factors stated above have a substantial impact on photocatalytic activity and can be modified by creating suitable heterojunction of TiO<sub>2</sub> with noble metals[2]. The selection of proper plasmonic material is essential as it greatly influences the light-harvesting efficiency. The decoration of Au noble metal particles over the surface of TiO<sub>2</sub> has proved to have better photocatalytic efficiency by exploiting their plasmonic property from metal nanostructure[3]. These catalysts are commonly known as plasmonic photocatalysts. The plasmonic photocatalysts harvest electromagnetic energy in the visible region and create localized heating through the nonradiative decay of localized surface plasmon resonance (LSPR). Additionally, the Schottky junction formed at the interface of semiconductor and metals enhances charge transfer and charge separation[4]. The charge transfer from Au to conduction band (CB) of TiO<sub>2</sub> under light excitation owing to the SPR effect increases the density of electrons in the CB of TiO<sub>2</sub>. Again the localized heat generated due to the nonradiative decay of LSPR increases the population of phonons. So in an Au decorated TiO<sub>2</sub> system, the interaction of electron and phonon is most probable giving

rise to the higher value of Fano asymmetry parameter.

In this chapter Au is decorated over the surface of TiO<sub>2</sub> and the photocatalytic activity of the samples are studied under both UV and visible light excitations using Raman spectroscopy. Further, the physics of the Fano effect that causes asymmetry in the Raman line shape are explored.

## 7.2 Experimental details

The TiO<sub>2</sub> microflowers are prepared using the hydrothermal method as described in Chapter 2. The as-prepared TiO<sub>2</sub> microflowers are decorated with Au of thicknesses 2, 4, and 6 nm using the thermal evaporation technique as discussed in Chapter 2 (section 2.3). The prepared samples are named TA-2, TA-4, and TA-6 respectively. The morphology and elemental analysis of the samples are studied using FESEM equipped with EDS. The structural studies are performed using XRD, TEM and Raman spectroscopy. The optical properties are studied using UV-visible and PL spectroscopy. Photocatalytic degradation of Rhodamine 6G (R6G) dye of  $10^{-4}$  M is studied using Raman spectroscopy. For the photocatalytic study, an aqueous solution of R6G solution is drop casted on the Au decorated TiO<sub>2</sub> surface followed by air drying for 6 to 7 minutes. The intensity of the Raman spectra of R6G ( $1648\text{ cm}^{-1}$ ) under the irradiation of white light, 325 nm, and 532 nm laser sources are used to measure the degradation of R6G. After being exposed to light, the data were collected every three minutes after exposure to white light and 532 nm laser light, and for 325 nm, data were collected after each 0.5 min. In addition, Raman spectroscopy is also used to understand the interaction between electrons and phonons.

## 7.3 Morphological, elemental, and structural studies

### 7.3.1 FESEM and EDS

The top view FESEM micrograph of pristine and Au-decorated samples are shown in Figure 7.1 (a-d). The samples are nanorod composed flower-like structures. Each nanorod has a tetragonal shape and a nearly sharp tip. The nanorods grow radially outward from a single nucleation point to create a flower-like structure. In Au-decorated samples, discontinuous Au film is observed, as shown in Figure 7.1(b-d). These TiO<sub>2</sub> microflowers are believed to provide a higher surface area for dye adsorption and increased light harvesting capabilities in comparison to nanoparticles and one-dimensional nanostructures, which is suitable for enhanced photocatalytic activity[5].

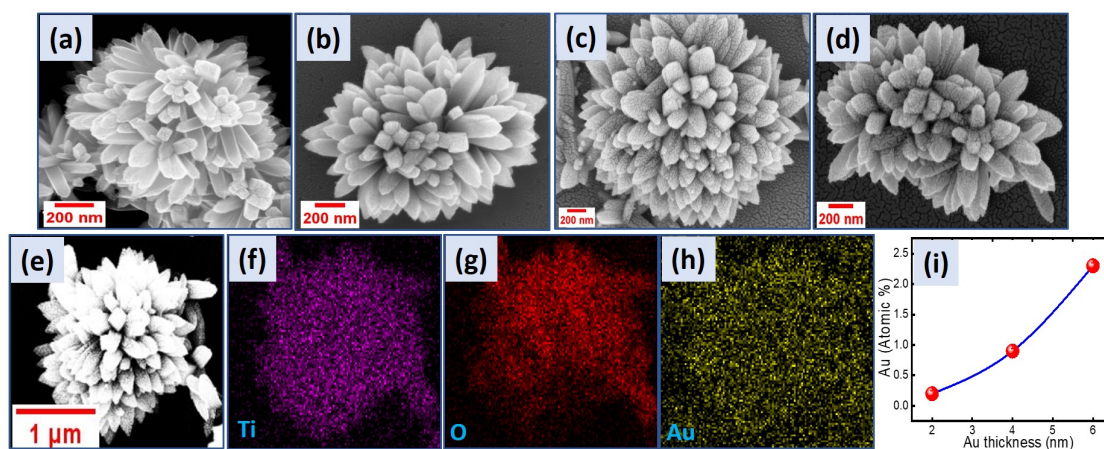


Figure 7.1: FESEM image of (a) TA-0 (b) TA-2 (c) TA-4 (d) TA-6. (e-h) FESEM image of TA-4 with the corresponding elemental mapping of Ti, O, and Au. (i) Variation of atomic % of Au with Au thickness.

Figure 7.1 (f-h) depicts the elemental mapping of Ti, O, and Au for the TA-4 sample. This information makes it very evident that the TiO<sub>2</sub> micro-flower are composed of Ti and O, with the Au distributed uniformly throughout. Figure 7.1 (i) depicts the atomic % of Au in various thicknesses of Au-decorated samples, which appears to rise with thickness. The

above analysis confirms that Ti, O, and Au are present in the sample.

### 7.3.2 XRD and TEM

XRD analysis was used to determine the phase and crystal structure of the as-prepared samples. The XRD pattern of pristine and Au-decorated TiO<sub>2</sub> samples are shown in Figure 7.2. In the pristine sample, all the peaks match entirely with the tetragonal rutile phase of TiO<sub>2</sub> (JCPDS No. 89-8304), indicating phase purity and poly-crystalline nature. In the TA-2 sample, the peak corresponding to Au is not observed, this could be due to the very low intensity of Au as compared to TiO<sub>2</sub>. However, in TA-4 and TA-6 samples, along with TiO<sub>2</sub> peaks, the peaks at 38.2°, 64.6°, and 77.6° correspond to the (111), (220), and (311) plane of face-centered cubic (FCC) Au (JCPDS No. 65-2870) are observed and they get more intense as the thickness of Au increases.

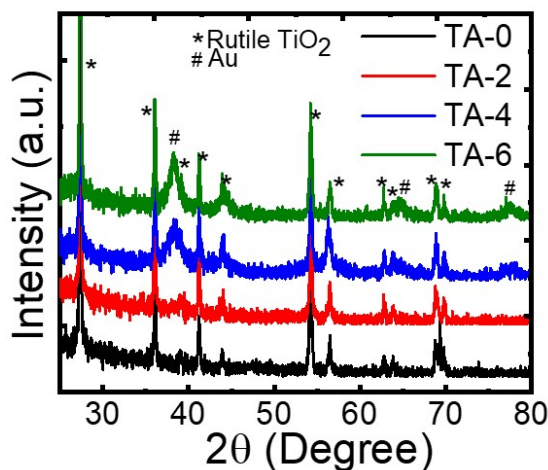


Figure 7.2: XRD pattern of pristine and Au-decorated TiO<sub>2</sub>.

The TEM micrograph of the TA-4 sample is shown in Figure 7.3. Figure 7.3(a) additionally reveals the flower structure of the sample. The yellow circled area in Figure 7.3(a) is magnified in Figure 7.3(b). In Figure 7.3(b), the discontinuous Au islands are visible over the TiO<sub>2</sub> surface having nanogap in between them, which is also found in the FESEM

image. Such nanogaps are vital for creating hotspots by concentrating the incident electromagnetic field[6]. Figure 7.3(c) is a HRTEM image of the nanogap region showing rutile TiO<sub>2</sub> lattice fringes with an interplanar spacing of 0.329 nm, matching the (110) plane of rutile TiO<sub>2</sub>, while Figure 7.3(d) shows the fringes of the dark region of Figure 7.3(b), with an interplanar spacing measured to be 0.236 nm, matching the (111) plane of Au. This TEM data agrees well with the XRD data.

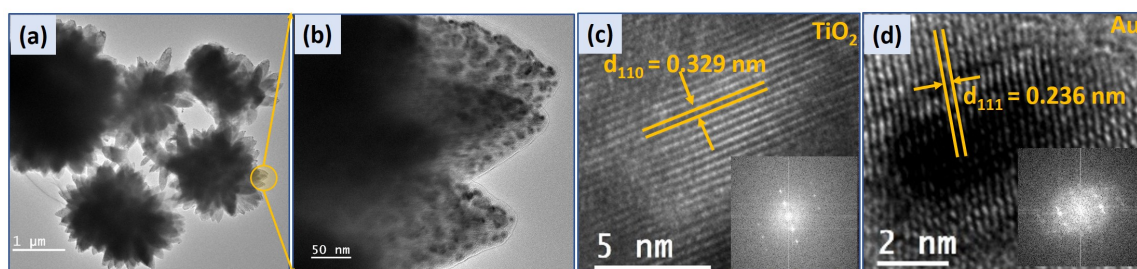


Figure 7.3: (a) TEM image of TA-4 sample. (b) Magnified view of the yellow encircled area of (a). Lattice fringes of (c) TiO<sub>2</sub> and (d) Au with corresponding FFT pattern in the inset.

## 7.4 Optical studies

### 7.4.1 UV-visible spectroscopy and PL spectroscopy

The UV-visible diffuse reflectance spectra for all the samples were collected in the range of 350-600 nm. The converted absorption spectra from reflectance spectra are shown in Figure 7.4(a). In all the samples, the absorption taking place around 400 nm corresponds to the transition of electrons from the valence band (VB) to the conduction band (CB) of TiO<sub>2</sub>[7]. In addition, there is a slight absorption in the visible region (bounded by the short dashed square in Figure 7.4 (a)) is replotted in Figure 7.4(b) after baseline correction. In the pristine sample, one peak is observed around 460 nm, which corresponds to the defect state of TiO<sub>2</sub> and is associated with oxygen vacancy[8, 9]. Apart from the defect peak, the

Au decorated TiO<sub>2</sub> samples have another peak in the visible region which corresponds to the LSPR of Au as shown in the shaded square of Figure 7.4(b)[10]. In the TA-2 sample, the LSPR peak is at a higher wavelength (498 nm) than the TA-4 (495 nm) and TA-6 (489 nm). The reduced spacing between Au with increasing the Au film thickness may be the cause of the blue shift in the SPR peak for the TA-4 and TA-6 samples[11]. To calculate the optical bandgap, the reflectance data were converted to Kubelka-Munk function  $F(R)$ , and the Tauc plot was plotted as shown in Figure 7.4(c). A systematic reduction in the bandgap of the samples was observed for TA-0, TA-2, TA-4, and TA-6, and the bandgaps are 3.06 eV, 3.01 eV, 2.88 eV, and 2.80 eV respectively. The emergence of midgap states in the TiO<sub>2</sub> energy gap, which was created by the interaction of Au and TiO<sub>2</sub> causes the bandgap narrowing[5, 12, 13].

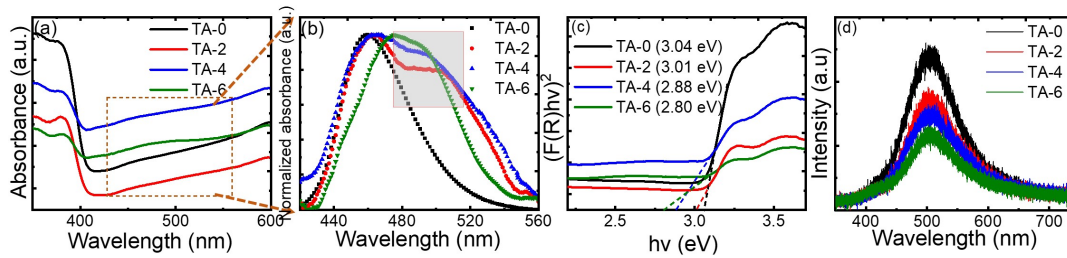


Figure 7.4: (a) Absorption spectra (b) Magnified image of the dashed square area of figure 7(a). (c) Tauc plot, and (d) PL spectra of pristine and Au decorated TiO<sub>2</sub> samples.

The PL spectra of pure and Au-decorated TiO<sub>2</sub> samples were collected with 325 nm laser excitation and are displayed in Figure 7.4(d). It is observed that as the thickness of Au on the surface of TiO<sub>2</sub> increases, the intensity of PL spectra, which is a measure of electron-hole recombination, decreases. The lowering of PL intensity indicates a lower recombination rate of the photogenerated electron-hole pairs and this helps to improve the photocatalytic activity[14]. The decoration of Au metal on the surface of TiO<sub>2</sub> creates a Schottky junction at their interface by transferring electrons from the TiO<sub>2</sub> to Au[15]. The

electron transfer is evident from the XPS spectra in the upcoming section. Upon UV light excitation (325 nm laser), electrons get transferred from CB of TiO<sub>2</sub> to Au reducing the amount of photo-generated electron-hole recombination.

### 7.4.2 Raman spectroscopy

To study the effect of Au decoration on the vibrational properties of TiO<sub>2</sub>, the Raman spectroscopy technique was used using a laser of excitation wavelength 532 nm. The laser power was set to be 8 mW with an acquisition time of 3 sec. Figure 7.5 (a) displays the Raman spectra of pristine and Au decorated TiO<sub>2</sub>. It is observed that as the thickness of Au increases on the surface of TiO<sub>2</sub>, the out-of-plane vibrational mode ( $E_g$ ) shifts towards the lower wavenumber and is plotted in the left panel of Figure 7.5(c). The peak shift may be due to the following reasons, firstly, the stress developed in TiO<sub>2</sub> after Au decoration suppresses the out-of-plane vibration of O atoms. Secondly, the localized heat generated due to the nonradiative decay of plasmons through electron-electron, electron-phonon, and phonon-phonon relaxation[16, 17]. Here, the redshift of  $E_g$  mode may be an indication of a localized heating effect that weakens the bond strength of Ti-O and results in a redshift of peak position. For further confirmation, stoke anti-stokes measurement was carried out as shown in Figure 7.5(b). The localized temperature generated for the 532 nm laser is calculated using equation 2.12 and is displayed in the right panel of Figure 7.5(c). It is found that the induced localized temperature for the Au decorated sample is higher than that of the pristine sample[18–20]. Localized heat is an important candidate that enhances the kinetics of photocatalysis[17].

## 7.5 XPS

Using the XPS technique, the chemical state and surface composition of materials were investigated. Figure 7.6 (a) depicts the survey spectra of the TA-0 and TA-4 samples and



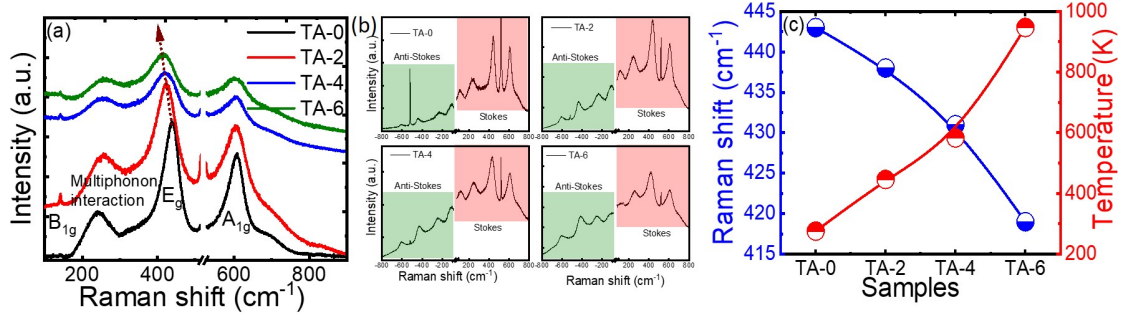


Figure 7.5: (a) Raman spectra (b) Stoke anti-Stokes measurement (c) Raman peak shift (left panel) and laser-induced localized temperature (right panel) for pristine and Au decorated samples.

identifies the corresponding C, Ti, O, and Au peaks. The peak signal found at 284.6 eV is associated with C 1s and is taken as a reference. The high-resolution Ti 2p peak of TA-0 is demonstrated in Figure 7.6 (b). The peaks at 458.47 and 464.24 eV are assigned to Ti 2p<sub>3/2</sub> and 2p<sub>1/2</sub>, respectively and both peaks belong to Ti<sup>4+</sup> oxidation state[21]. Further, the Ti 2p spectra of TA-4 are displayed in Figure 7.6 (c). The peak energies for the Ti 2p<sub>3/2</sub> and 2p<sub>1/2</sub> are 458.95 eV and 464.54 eV, respectively. The binding energy of TA-4 changes towards the higher energy side as compared to TA-0, showing the loss of electrons from the Ti in TA-4[22]. Figure 7.6 (d) shows the high-resolution XPS spectra of Au 4f. Two peaks at binding energies 83.94 and 87.61 eV are observed, and they stand for 4f<sub>7/2</sub> and 4f<sub>5/2</sub>, respectively, and confirm the presence of metallic Au on the surface of TiO<sub>2</sub>. The occurrence of a negative charge on Au may be responsible for the shift of Au 4f<sub>7/2</sub> relative to bulk Au with the binding energy of 84 eV[23]. As a result, we may say that when TiO<sub>2</sub> and Au interact, Ti of TiO<sub>2</sub> transfers its electrons to Au.

Under consideration of the above results, we have performed the in-situ photocatalytic behavior of Au decorated TiO<sub>2</sub> samples.



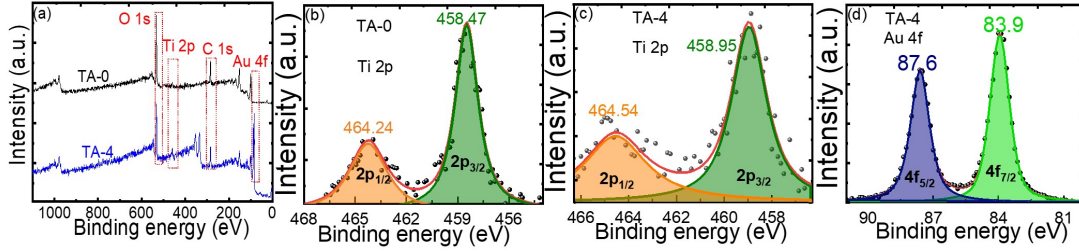


Figure 7.6: (a) XPS survey spectra of TA-0 and TA-4 .(b) Ti 2p region of TA-0 .(c) Ti 2p, (d) Au 4f region of TA-4.

## 7.6 Photocatalytic performance analysis

In-situ photocatalytic degradation of the R6G molecule is examined under Raman spectroscopy by observing the change in the Raman peak intensity of the dye molecule. The samples were exposed to white light and laser (325 and 532 nm) source. For 325 nm, the laser power was 3.1 mW with a time of exposure of 0.5 min whereas, for 532 nm, the laser power was 3.83 mW with a time of exposure of 3 minutes. The degradation of the dye was found to follow the first-order kinetics of the reaction as given in the following equation:

$$\ln \frac{C_0}{C_t} = kt \quad (7.1)$$

where  $C_0$  is the initial peak intensity,  $C_t$  peak intensity at time  $t$ , and  $k$  is the rate constant.[17]  $C_0$  and  $C_t$  can be directly correlated within the concentration of the dye at the beginning of the experiment and after time  $t$ , respectively. The experimental data of  $\ln \frac{C_0}{C_t}$  versus time is fitted with equation (7.1) and the value of  $k$  is the slope of the fitted line.

### Under UV light exposure:

The photocatalytic degradation of  $10^{-4}$  M R6G was studied for TA-2, TA-4, and TA-6 samples under UV laser exposure. Raman spectra of R6G, drop casted on samples under exposure of 325 nm laser for the different intervals of time collected. Figure 7.7(a) displays

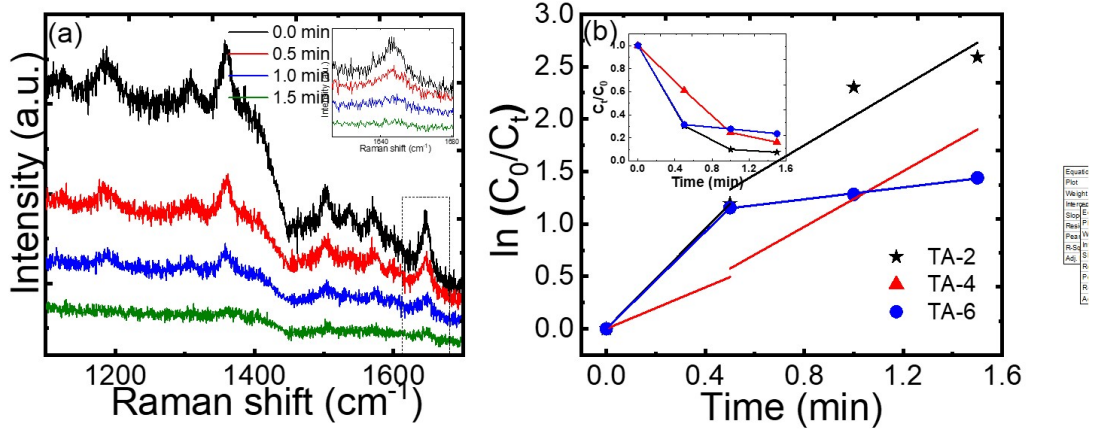


Figure 7.7: Photocatalytic degradation of samples (a) Observed Raman peak intensity with exposure of 325 nm laser on TA-4. (b) Plot of  $\ln \frac{C_0}{C_t}$  with time fitted with first order kinetics equation (1) and  $\frac{C_t}{C_0}$  with time plot is presented in the inset for TA-2, TA-4, and TA-6 samples.

the Raman spectra of an R6G drop cast on a TA-4 material exposed to a 325 nm laser for various time intervals. The photo-degradation study was carried out by considering the intensity of the Raman peak at 1648 cm<sup>-1</sup> [Figure 7.7(a) inset]. The kinetic plot for TA-2, TA-4, and TA-6 samples are shown in Figure 7.7(b). The variation in the ratio of the initial Raman peak intensity to the Raman peak intensity at time t is displayed in Figure 7.7(b) inset (top left corner). The R6G on TA-2, TA-4, and TA-6 degrades by 92 %, 83 %, and 76 % respectively, after 90 seconds of exposure to UV radiation. It has been observed that the catalytic activity for UV (325 nm) light exposure does not follow the linearity with time. For TA-2 and TA-6, the reaction rate is faster for the first 0.5 min and then decreases, whereas, in the TA-4 sample, the reaction rate is slow for the first 0.5 min and then increases. This behavior in TA-4 for the first 0.5 min can be attributed to the induction period for the reaction rate. This may be due to the optimal coverage of Au clusters on the surface of the TiO<sub>2</sub>, which inhibits the direct exposure of light. So, we fit the reaction into two regions. Between 0-0.5 min the reaction rate (k) is 0.98 min<sup>-1</sup> for TA-4 and 2.386 and 2.310 min<sup>-1</sup> for TA-2

and TA-6, respectively. However, between 0.5-1.5 min, the value of  $k$  decreases from  $1.398 \pm 0.475$  to  $0.284 \pm 0.017 \text{ min}^{-1}$ . It has been observed that the linear proportionality does not fit well for the lower Au layer (for TA-2) and becomes better with higher Au thickness. So, to consider the rate constant as a representative one, we have added the standard deviation in Table 1. The standard deviation represents uncertainty in the rate constant of the catalytic reaction, which may arise due to the distribution of Au decoration on the TiO<sub>2</sub> sample. The values of  $k$  for the exposure of all wavelengths are also given in Table 7.1.

Table 7.1: Value of  $k$  ( $\text{min}^{-1}$ ) under 325 nm, 532 nm laser source and white light exposure

Sample details	325 nm		532 nm	White light
	0-0.5 min	0.5-1.5 min		
TA-2	$2.386 \pm 0.000$	$1.398 \pm 0.475$	$0.099 \pm 0.007$	$0.065 \pm 0.008$
TA-4	$0.982 \pm 0.000$	$1.326 \pm 0.286$	$0.128 \pm 0.015$	$0.075 \pm 0.006$
TA-6	$2.310 \pm 0.000$	$0.284 \pm 0.017$	$0.069 \pm 0.006$	$0.053 \pm 0.006$

#### Under visible light exposure:

Under the exposure of a 532 nm laser and white light source, the photocatalytic degradation of  $10^{-4} \text{ M}$  R6G was investigated for TA-2, TA-4, and TA-6 materials. Figure 7.8(a) displays the Raman spectra of an R6G drop casted on a TA-4 material exposed to a 532 nm laser for various time intervals. It is observed that as exposure duration increases, the intensity of each Raman peak decreases. By tracking the peak intensity at  $1648 \text{ cm}^{-1}$  through time [Figure 7.8(a)inset], the photo-degradation rate constant was determined. For the TA-2, TA-4, and TA-6 samples under visible light, the inset of Figures 7.8(b),(c), and (d) shows the variation of the ratio of the intensity of the Raman peak at time  $t$  concerning the initial Raman peak intensity versus time. After 21 min, the TA-2 sample degrades R6G 100 % and 82 % under the exposure of white light and 532 nm laser, respectively. In the TA-4 sample, R6G gets degraded completely after 16 min in both white light and laser source. There is a 66 % and 79 % degradation after 21 min under white light and laser source, respectively,

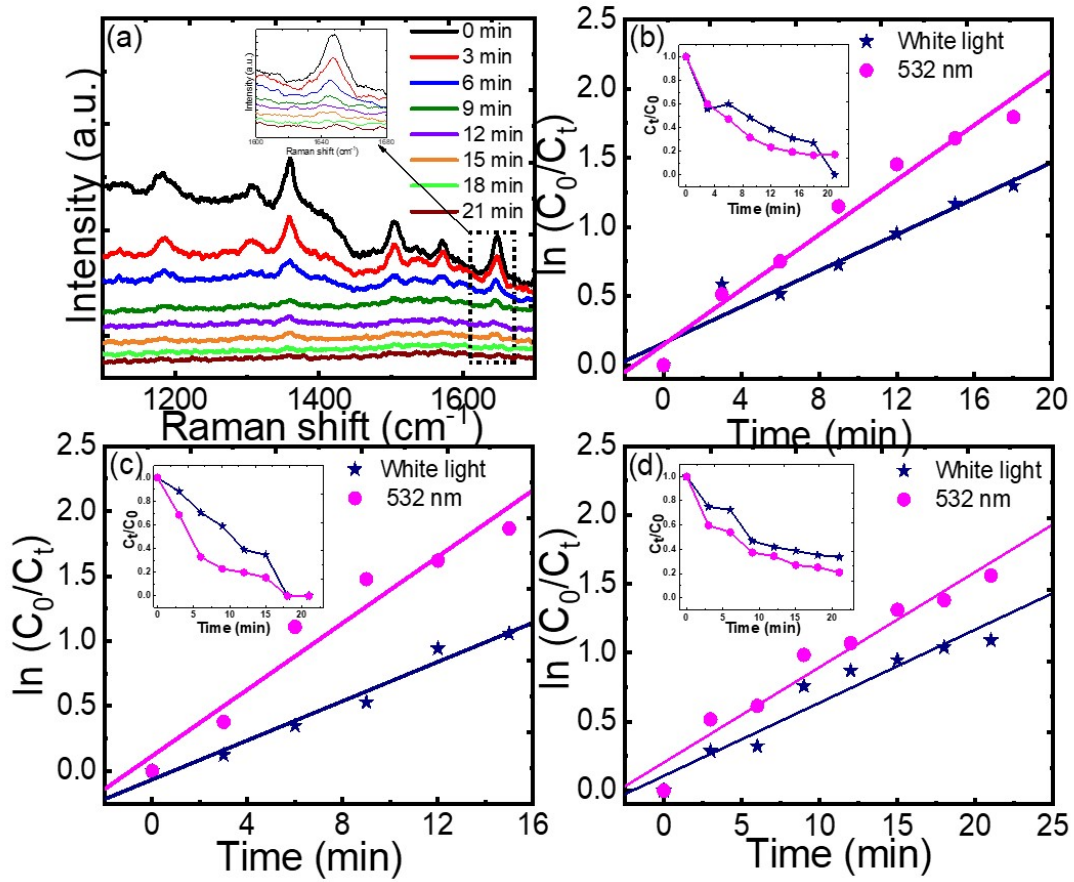


Figure 7.8: Photocatalytic degradation of samples (a) Observed Raman peak intensity with exposure of 532 nm laser source on TA-4. (b), (c), and (d) plot of  $\ln \frac{C_0}{C_t}$  with time fitted with first order kinetics equation (1) and  $\frac{C_t}{C_0}$  with time plot is presented in the inset for TA-2, TA-4, and TA-6 samples respectively for 532 nm laser source and white light

for the TA-6 sample. Figure 7.8(b),(c), and (d) represent the  $\ln \frac{C_0}{C_t}$  versus time plot for TA-2, TA-4, and TA-6, respectively, with exposure of white light and 532 nm laser source. The Au thickness dependant rate constant  $k$  for 532 nm laser and white light source are presented in Table 1. In both cases, the value of  $k$  increases from TA-2 to TA-4 and decreases for TA-6. So, we can conclude that the parameters for the TA-4 sample can be considered as an optimal condition.

### 7.6.1 Proposed Mechanism

1. The degradation mechanism in the Au decorated TiO<sub>2</sub> system can be explained using Figure 7.9. Figure 7.9(a) indicates the initial band structure before contact. After the deposition of Au on TiO<sub>2</sub>, a Schottky junction will be formed as shown in Figure 7.9 (b) and (c). This happens because the work function of Au and rutile TiO<sub>2</sub> is 5.2 eV and 4.4 eV respectively[24–27]. When they come in contact with each other, the Fermi levels line up to maintain equilibrium by transferring electrons from TiO<sub>2</sub> to Au[28]. As a result negative charge on Au and a positive charge on TiO<sub>2</sub> are developed near the interface and a depletion region is created by building an internal electric field that is directed toward Au. This forms a Schottky junction which is responsible for the separation of photo-generated charge carriers as it pushes electrons and holes in opposite directions.
2. Under the exposure of a UV light source, electrons in the valence band of TiO<sub>2</sub> get excited to the CB leaving behind a hole in the valence band[5]. Then the CB electron gets transferred to Au by suppressing the electron-hole recombination. The Schottky junction formed at the interface of Au and TiO<sub>2</sub> facilitates charge separation. The electrons in CB of TiO<sub>2</sub> react with atmospheric O<sub>2</sub> to produce super-oxide O<sub>2</sub><sup>-</sup> radical and the holes in Au react with H<sub>2</sub>O present in atmospheric humidity forming

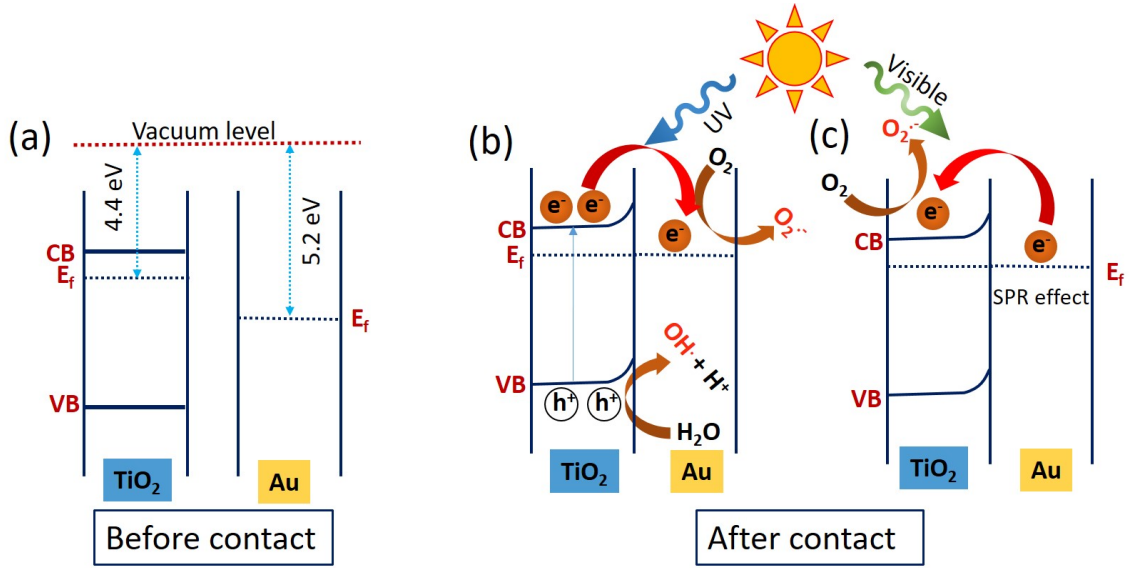


Figure 7.9: Schematic of charge transfer under UV and visible light irradiation.

OH $\cdot$  radicals as shown in figure 7.9(b)[29, 30]. O<sub>2</sub> $\cdot^-$  and OH $\cdot$  radicals help in the degradation of R6G dye.

3. Under visible light irradiation, a plasmonic resonance condition arises as confirmed from UV-visible spectroscopy. During this process, the electrons in Au get sufficient energy to cross the Schottky barrier height and transferred to the CB of TiO<sub>2</sub>, facilitating charge separation as shown in figure 7.9(c)[5, 31]. The electron in the conduction band of TiO<sub>2</sub> reacts with O<sub>2</sub> to produce superoxide O<sub>2</sub> $\cdot^-$  radical that helps in the degradation of dye. The defect states of TiO<sub>2</sub> are also responsible for a delay in the recombination rate to accelerate the photocatalytic reaction.
4. The decrease in the value of  $k$  for TA-6 than TA-4 is recorded as shown in Table 7.1. This may be due to a large coverage of Au on TiO<sub>2</sub> which prevents the direct exposure of light on the TiO<sub>2</sub> surface. In addition with the increasing thickness of Au, the Schottky barrier height decreases[2]. Hence decreases in the Schottky barrier

cause back flow of electrons from CB of TiO<sub>2</sub> and recombine with holes in the Au.

5. In all the samples, the value of  $k$  is higher for 325 nm laser excitation than other sources. Dai et al. reported that the lifetime of photo-electrons is higher in UV light than in visible light[32]. So the higher  $k$  value for UV light excitation is attributed to the higher lifetime of photo-generated charge carriers and the operational mechanism of charge transfer under both UV and visible sources. In the UV source, the SPR effect directly does not play the role to enhance the photocatalytic activity, but it helps in charge separation efficiently.

The photocatalytic degradation of R6G using Au decorated TiO<sub>2</sub> microflowers photocatalyst was investigated in both UV and visible light exposure. The efficiency of photocatalytic reaction can be enhanced by increasing the surface area, reducing charge recombination, facilitating charge transfer, extending the range of light absorption, and localized heating effect. The TiO<sub>2</sub> nanostructures are flowerlike structures consisting of nanorods has the advantage of a large surface area that provides larger surface area for the photocatalytic reaction to take place. Again the LSPR and the photothermal effect in visible light help in the degradation of the dye efficiently. The photogenerated charge carriers play an important role in photocatalytic performance.

## 7.7 Observation of Fano effect

In Chapter 3, it is stated that the continuum state is provided by photoexcited electrons which is experimentally studied in this section. In Figure 7.4 (a), it is observed that the intensity of the SPR peak is less intense. so the TA-4 sample is annealed at 800 °C using the muffle furnace in atmospheric conditions to form the Au nanoparticles. This sample is named as TA-4@800. For reference, the pristine sample is also annealed at the same temperature and named TA-0@800. The FESEM micrograph of the TA-4@800 is shown in Figure 7.10(a).



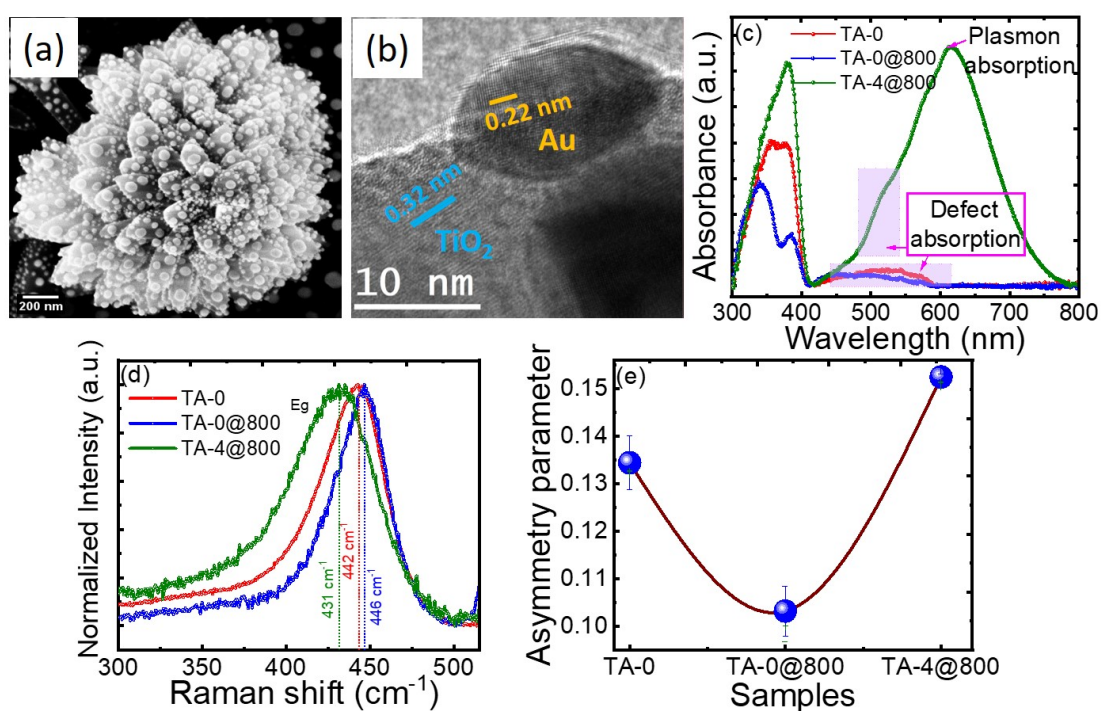


Figure 7.10: (a) FESEM image (b) HRTEM image of TA-4@800. (c) UV-visible absorbance spectra. (d) Raman spectra and (e) asymmetry parameter for TA-0, TA-0@800 and TA-4@800 samples.



It is observed that Au nanoparticles are formed over the TiO<sub>2</sub> surface and the average size of the particles is  $29 \pm 3.7$  nm. Figure 7.10(b) shows the high-resolution TEM image where both TiO<sub>2</sub> and Au are observed with their interplanar spacing  $d_{110}=0.32$  nm is associated with rutile TiO<sub>2</sub> whereas,  $d_{111}=0.22$  nm is associated with Au. The UV-visible spectra of the samples are shown in Figure 7.10(c). In the visible region, along with the defect peak, a strong absorption peak is observed in TA-4@800 which is caused by the SPR. Again the Raman spectra of the E<sub>g</sub> mode for three samples are presented in Figure 7.10(d). The peak position of TA-0 is red-shifted as compared to TA-0@800. This redshift is related to oxygen vacancy[33]. In general, intrinsic oxygen vacancy defect is present in TiO<sub>2</sub>. In TA-0@800, the oxygen vacancy gets filled up as it is annealed in the atmospheric environment and hence less oxygen vacancy and less number of electrons as compared to TA-0. The lowering of the oxygen vacancy in TA-0@800 is responsible for shifting the peak towards a higher wavenumber[34]. In the TA-0@800 sample, the peak position is red-shifted as compared to both TA-0 and TA-0@800 may be attributed to stress and localized heating effect. The Raman line shape is fitted with the Fano function as defined in the equation 1.3. and the value of the asymmetry parameter is plotted in Figure 7.10(e). In an Au-decorated TiO<sub>2</sub> system, the Fano asymmetry is influenced by both temperature and the presence of hot electrons. The transfer of hot electrons from Au to TiO<sub>2</sub> helps to improve the Fano asymmetry parameter.

## 7.8 Conclusions

The photocatalytic degradation of R6G using Au decorated TiO<sub>2</sub> microflowers photocatalyst was investigated in both UV and visible light exposure. The morphology of TiO<sub>2</sub> microflower and decoration of the Au helps to improve the photocatalytic efficiency. The TiO<sub>2</sub> nanostructures are flowerlike structures consisting of nanorods that have the advantage

of a large surface area that provides a larger surface area for the photocatalytic reaction to take place. The bandgap reduction and visible light absorption in the Au decorated samples confirmed from the UV-visible spectroscopy is another confirmation to improve the photocatalytic efficiency. The photogenerated charge carriers play an important role in photocatalytic performance. The Au decoration helps in reducing photo-generated charge carrier recombination confirmed by PL spectroscopy. The plasmon-induced heating effect which is proved by the Raman spectroscopy enhances the photocatalytic activity. Further, the Fano asymmetry studied using the annealed samples indicates the plasmon-induced charge transfer. The Fano asymmetry parameter and Raman peak position for the annealed pristine TiO<sub>2</sub> as compared to the pristine TiO<sub>2</sub> confirm the presence of oxygen vacancy in the pristine TiO<sub>2</sub>. Again the increased Fano asymmetry parameter in Au decorated annealed sample is attributed to plasmon-induced charge transfer. In short, the charge separation, Schottky junction, UV-visible light absorption, and photothermal effect together play a crucial role in greatly enhancing photocatalytic activity. Both the heating effect and charge transfer mechanism play a role in photocatalysis and the Fano effect.

## References

- [1] Yinghao Song, Li Ling, Paul Westerhoff, and Chii Shang. Evanescent waves modulate energy efficiency of photocatalysis within  $\text{TiO}_2$  coated optical fibers illuminated using leds. *Nature communications*, 12(1):1, 2021.
- [2] Gregor Žerjav, Matevž Roškarič, Janez Zavašnik, Janez Kovač, and Albin Pintar. Effect of au loading on schottky barrier height in  $\text{TiO}_2 + \text{Au}$  plasmonic photocatalysts. *Applied Surface Science*, 579:152196, 2022.
- [3] Shuang Shuang, Ruitao Lv, Zheng Xie, and Zhengjun Zhang. Surface plasmon enhanced photocatalysis of Au/Pt-decorated  $\text{TiO}_2$  nanopillar arrays. *Scientific reports*, 6(1):1, 2016.
- [4] Rachel C Elias and Suljo Linic. Elucidating the roles of local and nonlocal rate enhancement mechanisms in plasmonic catalysis. *Journal of the American Chemical Society*, 2022.
- [5] Yang Yu, Wei Wen, Xin-Yue Qian, Jia-Bin Liu, and Jin-Ming Wu. Uv and visible light photocatalytic activity of Au/ $\text{TiO}_2$  nanoforests with anatase/rutile phase junctions and controlled au locations. *Scientific reports*, 7(1):1, 2017.
- [6] Binaya Kumar Sahu, Anil Pal, Reshma TS, and A Das. Single-molecule detection-enabled plasmonic ag nanogap for unmasking vibrational properties in  $\text{0d snO}_2$ . *ACS Applied Nano Materials*, 5(9):12413–12422, 2022.
- [7] Ibram Ganesh, AK Gupta, PP Kumar, PSC Sekhar, K Radha, G Padmanabham, and G Sundararajan. Preparation and characterization of Ni-doped  $\text{TiO}_2$  materials for photocurrent and photocatalytic applications. *The Scientific World Journal*, 2012, 2012.

- 
- [8] Avishek Saha, Alicia Moya, Axel Kahnt, Daniel Iglesias, Silvia Marchesan, Reinhold Wannemacher, Maurizio Prato, Juan J Vilatela, and Dirk M Guldi. Interfacial charge transfer in functionalized multi-walled carbon nanotube  $\text{TiO}_2$  nanofibres. *Nanoscale*, 9(23):7911, 2017.
- [9] Biswajit Choudhury, Munmun Dey, and Amarjyoti Choudhury. Shallow and deep trap emission and luminescence quenching of  $\text{TiO}_2$  nanoparticles on Cu doping. *Applied Nanoscience*, 4(4):499, 2014.
- [10] Abhijit Biswas, Abhishek Swarnkar, Padmini Pandey, Prachi Kour, Swati Parmar, and Satishchandra Ogale. Dynamics of photo-generated carriers across the interface between  $\text{CsPbBr}_3$  nanocrystals and Au–Ag nanostructured film, and its control via ultrathin  $\text{MgO}$  interface layer. *ACS omega*, 5(21):11915, 2020.
- [11] Prashant K Jain, Susie Eustis, and Mostafa A El-Sayed. Plasmon coupling in nanorod assemblies: optical absorption, discrete dipole approximation simulation, and exciton-coupling model. *The Journal of Physical Chemistry B*, 110(37):18243, 2006.
- [12] Yan-Feng Zhu, Juan Zhang, Lu Xu, Ya Guo, Xiao-Ping Wang, Rong-Gui Du, and Chang-Jian Lin. Fabrication and photoelectrochemical properties of  $\text{ZnS}/\text{Au}/\text{TiO}_2$  nanotube array films. *Physical Chemistry Chemical Physics*, 15(11):4041, 2013.
- [13] Supriya K. Khore, Sunil R. Kadam, Sonali D. Naik, Bharat B. Kale, and Ravindra S. Sonawane. Solar light active plasmonic  $\text{Au}@ \text{TiO}_2$  nanocomposite with superior photocatalytic performance for  $\text{H}_2$  production and pollutant degradation. *New J. Chem.*, 42:10958, 2018.
- [14] Qiaoli Huang, Tong Gao, Feng Niu, Da Chen, Zhi Chen, Laishun Qin, Xingguo Sun, Yuexiang Huang, and Kangying Shu. Preparation and enhanced visible-light driven

- photocatalytic properties of Au-loaded TiO<sub>2</sub> nanotube arrays. *Superlattices and Microstructures*, 75:890, 2014.
- [15] Supriya K Khore, Sunil R Kadam, Sonali D Naik, Bharat B Kale, and Ravindra S Sonawane. Solar light active plasmonic Au@TiO<sub>2</sub> nanocomposite with superior photocatalytic performance for H<sub>2</sub> production and pollutant degradation. *New Journal of Chemistry*, 42(13):10958, 2018.
- [16] Subhashree Sahoo, Binaya Kumar Sahu, Shivam Shukla, Sanjeev K Srivastava, and Pratap K Sahoo. In-situ monitoring of plasmon-induced nanoscale photocatalytic activity from Au-decorated TiO<sub>2</sub> microflowers. *Nano Futures*, 7(2):025002, 2023.
- [17] Tanujjal Bora, David Zoepfl, and Joydeep Dutta. Importance of plasmonic heating on visible light driven photocatalysis of gold nanoparticle decorated zinc oxide nanorods. *Scientific reports*, 6(1):1, 2016.
- [18] Ching-Lien Hsiao, Li-Wei Tu, Tung-Wei Chi, Min Chen, Tai-Fa Young, Chih-Ta Chia, and Yu-Ming Chang. Micro-Raman spectroscopy of a single freestanding GaN nanorod grown by molecular beam epitaxy. *Applied Physics Letters*, 90(4):043102, 2007.
- [19] Mahak Dhiman, Ayan Maity, Anirban Das, Rajesh Belgamwar, Bhagyashree Chalke, Yeonhee Lee, Kyunjong Sim, Jwa-Min Nam, and Vivek Polshettiwar. Plasmonic colloidosomes of black gold for solar energy harvesting and hotspots directed catalysis for CO<sub>2</sub> to fuel conversion. *Chemical science*, 10(27):6594, 2019.
- [20] Arup Kumar Mandal, Aprajita Joshi, Surajit Saha, Binoy Krishna De, Sourav Chowdhury, VG Sathe, U Deshpande, D Shukla, Amandeep Kaur, DM Phase, et al. Raman mode softening in SrMnO<sub>3</sub> induced by optical excitation. *Physical Review B*, 106(10):104104, 2022.

- 
- [21] Fan Sun, Xueli Xing, Hui Hong, Bang Xu, and Yong Hao. Concentrated full-spectrum solar-driven CO<sub>2</sub> reduction with H<sub>2</sub>O to solar fuels by Au nanoparticle-decorated TiO<sub>2</sub>. *Energy & Fuels*, 36(12):6433, 2022.
- [22] Siti Khatijah Md Saad, Akrajas Ali Umar, Marjoni Imamora Ali Umar, Masahiko Tomitori, Mohd Yusri Abd. Rahman, Muhamad Mat Salleh, and Munetaka Oyama. Two-dimensional, hierarchical Ag-doped TiO<sub>2</sub> nanocatalysts: effect of the metal oxidation state on the photocatalytic properties. *ACS omega*, 3(3):2579, 2018.
- [23] Aalbert Zwijnenburg, Anton Goossens, Wim G Sloof, Menno WJ Craje, Adri M van der Kraan, L Jos de Jongh, Michiel Makkee, and Jacob A Moulijn. Xps and mössbauer characterization of Au/TiO<sub>2</sub> propene epoxidation catalysts. *The Journal of Physical Chemistry B*, 106(38):9853, 2002.
- [24] Ying-Chih Pu, Gongming Wang, Kao-Der Chang, Yichuan Ling, Yin-Kai Lin, Bob C Fitzmorris, Chia-Ming Liu, Xihong Lu, Yexiang Tong, Jin Z Zhang, et al. Au nanostructure-decorated TiO<sub>2</sub> nanowires exhibiting photoactivity across entire uv-visible region for photoelectrochemical water splitting. *Nano letters*, 13(8):3817, 2013.
- [25] Dimitar A Panayotov, Anatoly I Frenkel, and John R Morris. Catalysis and photocatalysis by nanoscale Au/TiO<sub>2</sub>: perspectives for renewable energy. *ACS Energy Letters*, 2(5):1223, 2017.
- [26] RM Dulanga S Somaratne and James E Whitten. Metallization of TiO<sub>2</sub> (110) with gold and lithium. *The Journal of Physical Chemistry C*, 125(48):26744, 2021.
- [27] Yongqing Cai, Zhaoqiang Bai, Sandhya Chintalapati, Qingfeng Zeng, and Yuan Ping Feng. Transition metal atoms pathways on rutile TiO<sub>2</sub> (110) surface: Distribution of

- Ti<sup>3+</sup> states and evidence of enhanced peripheral charge accumulation. *The Journal of chemical physics*, 138(15):154711, 2013.
- [28] An Wang, Shijie Wu, Jialu Dong, Ruoxin Wang, Jiawei Wang, Jiali Zhang, Shuxian Zhong, and Song Bai. Interfacial facet engineering on the schottky barrier between plasmonic Au and TiO<sub>2</sub> in boosting the photocatalytic CO<sub>2</sub> reduction under ultraviolet and visible light irradiation. *Chemical Engineering Journal*, 404:127145, 2021.
- [29] Samir Kumar, Devesh K Lodhi, and JP Singh. Highly sensitive multifunctional recyclable Ag–TiO<sub>2</sub> nanorod sers substrates for photocatalytic degradation and detection of dye molecules. *RSC advances*, 6(51):45120, 2016.
- [30] Ruizhen Li, Anhong Zhou, Qiang Lu, Changzhu Yang, and Jingdong Zhang. In situ monitoring and analysis of the photocatalytic degradation process and mechanism on recyclable Au nps-TiO<sub>2</sub> nts substrate using surface-enhanced raman scattering. *Colloids and Surfaces A: Physicochemical and Engineering Aspects*, 436:270, 2013.
- [31] Cláudia Gomes Silva, Raquel Juárez, Tiziana Marino, Raffaele Molinari, and Hermenegildo García. Influence of excitation wavelength (uv or visible light) on the photocatalytic activity of titania containing gold nanoparticles for the generation of hydrogen or oxygen from water. *Journal of the American Chemical Society*, 133(3):595, 2011.
- [32] Xiaojuan Dai, Zeqing Jiao, Zehan Ma, Kunhui Liu, Chen Wang, and Hongmei Su. Capturing the long-lived photogenerated electrons in Au/TiO<sub>2</sub> upon uv or visible irradiation by time-resolved infrared spectroscopy. *The Journal of Physical Chemistry C*, 123(33):20325, 2019.
- [33] Qing-Yu Liu, Hao-Dong Wang, Rui Tang, Quan Cheng, and Yong-Jun Yuan. Rutile

- TiO<sub>2</sub> nanoparticles with oxygen vacancy for photocatalytic nitrogen fixation. *ACS Applied Nano Materials*, 4(9):8674, 2021.
- [34] Biswajit Choudhury and Amarjyoti Choudhury. Room temperature ferromagnetism in defective TiO<sub>2</sub> nanoparticles: Role of surface and grain boundary oxygen vacancies. *Journal of Applied Physics*, 114(20):203906, 2013.
- [35] Binaya Kumar Sahu, Rabindra Nath Juine, Madhusmita Sahoo, Ravi Kumar, and A Das. Interface of GO with SnO<sub>2</sub> quantum dots as an efficient visible-light photocatalyst. *Chemosphere*, 276:130142, 2021.



# Chapter 8

## Summary and future prospects

### 8.1 Summary

This thesis explores the effect of different dopants, starting from lighter to heavier elements, on the structural, optical, magnetic, and morphological properties of pure rutile  $\text{TiO}_2$ . The defects produced in the  $\text{TiO}_2$  matrix by introducing elements of different atomic numbers such as C ( $Z=6$ ), Si ( $Z=14$ ), Cu ( $Z=29$ ), and Au (79). The C, Si, and Au ions are introduced by ion implantation techniques and Cu ions are introduced by chemical doping during  $\text{TiO}_2$  growth by hydrothermal method. The kind of defects produced and the placement of defects in  $\text{TiO}_2$  by doping depends on the oxidation state and atomic radii of the dopant. This also decides whether the dopants will occupy the substitutional or interstitial position. The dopant ions narrow down the bandgap of  $\text{TiO}_2$  by introducing new energy levels within the bandgap. The elements having p electrons create midgap states above the valence band maxima, however, the elements having d electrons create midgap states below the conduction band minima. In addition, the oxygen vacancy also creates midgap state in the bandgap region. The values of the bandgap after introducing dopant ions are discussed in the thesis. The surface defects or metal-semiconductor junction is created by decorating Au over the  $\text{TiO}_2$  surface to investigate plasmonic photocatalysis properties. A brief introduction of wide bandgap semiconductors along with the crystal structure, properties, and importance of  $\text{TiO}_2$  are discussed in Chapter 1. In addition, the physical concepts used in the thesis are explained. Chapter 2 discusses the sample preparation techniques as well as the characterization techniques.

This chapter explores the summary and the future prospects of the thesis as follows.

### **C doped TiO<sub>2</sub>**

In this part, the TiO<sub>2</sub> is doped with a lighter ion C, which is non-metallic. SRIM simulation confirms that with increasing C fluence, oxygen vacancy increases, which can affect the optical and magnetic properties. The FESEM images clarify that the morphology of samples remains unaffected after ion implantation, and the elemental mapping confirms the presence of C ions in the implanted sample. The C ion creates defect states in the TiO<sub>2</sub> matrix that help in reducing the bandgap and increasing the Urbach energy. This chapter investigated two different physics phenomena, the Fano asymmetry, and magnetism in C ion implanted TiO<sub>2</sub>. The Fano asymmetry arises due to the interaction of discrete phonon states with the continuum of electronic transition states. The continuum state is provided by heavy doping. Implantation of C ion into the TiO<sub>2</sub> matrix creates a large number of oxygen vacancies. As each oxygen vacancy is associated with two electrons, the increased ion fluence increases the number of electrons in the conduction band of TiO<sub>2</sub>. As the density of electrons in the conduction band increases, the probability of electron-phonon interaction increases giving rise to the higher value of the asymmetry in the Raman spectra. The Raman spectroscopy illustrates distinct asymmetry in the E<sub>g</sub> and A<sub>1g</sub> Raman lines towards the lower wavenumber. The asymmetric parameter is obtained by fitting the Raman line shape with the BWF function and is found to increase with increasing C ions fluence. In the second section, we studied the magnetic behavior of the samples. Intrinsic TiO<sub>2</sub> is non-magnetic in nature and oxygen-deficient induced ferromagnetism. The oxygen vacancy created through C ion implantation motivated us to study the magnetic properties of the samples. From the magnetic measurement, all the samples including the pristine sample showed ferromagnetic behavior which indicated that along with the implanted samples, the pristine sample has some intrinsic oxygen vacancy. Theoretically, from DFT calculation, it has been observed that an ideal TiO<sub>2</sub> is non-magnetic, however as the oxygen vacancy reduces the Ti<sup>4+</sup> ion to Ti<sup>3+</sup> ion that

encompasses one unpaired d electron, induces a non-zero magnetic moment. The coercivity of the samples is found to be increasing with C ion fluence, indicating that higher defects produce larger ferromagnetism. The C ion implantation modifies both the optical and the ferromagnetic properties. Tuning the defect concentration these samples can be suitable for sensing, magneto-optic applications.

### **Si doped TiO<sub>2</sub>**

In this part, TiO<sub>2</sub> is doped with 30 keV Si ion using ion implantation technique. The Si ion creates both oxygen and Ti vacancy as observed using SRIM simulations. The FESEM image revealed a change in the morphology of the nanorods with ion fluences. At the highest fluence the tip of the nanorod also modified. Ion implantation causes defects that alter the vibrational and optical characteristics of the host TiO<sub>2</sub> matrix, but it significantly does not affect the crystallinity of TiO<sub>2</sub>. The shift in the peak position of Raman spectra indicates the presence of stress and the increasing FWHM with ion fluence is attributed to decreased phonon lifetime. The decreased phonon lifetime is due to the scattering of phonons by defects. The reduced bandgap with Si ion fluence is due to the creation of midgap defect states. Its application in photocatalysis and optoelectronics might benefit from the reduced bandgap.

### **Cu doped TiO<sub>2</sub>**

In this part, Cu-doped TiO<sub>2</sub> microflowers are prepared using the hydrothermal method. The ICP-OES, EDS, and XPS data reveal the elemental composition of the flowers to be Ti, O, and Cu. The XRD, HRTEM, and Raman spectroscopy confirm that the TiO<sub>2</sub> nanorod-composed microflower-like structures are purely in the rutile phase, and the phase remains unaltered after Cu doping. The Cu dopants improve the defect states, which help in electron trapping and slow down electron-hole recombination. In addition, the mid-bandgap states

created by the Cu dopant shift the absorption band towards a higher wavelength region and reduce the bandgap of  $\text{TiO}_2$  from 2.99 to 2.16 eV. The reduced bandgap is caused by the incorporation of defect states in the midgap region is analyzed from DFT calculations. This chapter has two sections. In the first section, the nonlinear optical (NLO) properties are discussed and in the second part phonon anharmonicity is explained. In the OA measurement of NLO, all the samples show SA behavior, and the nonlinear absorption coefficient gets improved with Cu concentration. Further, the CA measurement of NLO shows the self-focusing behavior of all the samples except 10 % Cu-doped  $\text{TiO}_2$  that shows self-defocusing behavior. The creation of defects plays a crucial role in tuning the linear and NLO properties of  $\text{TiO}_2$ . The linear optical properties of the materials favor their usage in photocatalysis and solar cells whereas, the NLO properties make it suitable for passive mode-locking, and Q-switching applications. The phonon anharmonicity is studied using temperature-dependent Raman spectroscopy that illustrates the shift in peak position and increased linewidth of  $E_g$  and  $A_{1g}$  mode for pristine and doped samples. The temperature-dependent Raman shift and linewidth fitted well with the non-linear parameters of the Klemens model and validated that the three and four-phonon processes are responsible for anharmonicity. The Cu dopant acts as an impurity that shortens the phonon lifetime and manifests the anharmonicity. In addition, the phonon lifetime decreases with an increase in temperature in all cases however, the trend of change in phonon lifetime and anharmonicity with Cu concentration is correlated with crystallite size. We have demonstrated that Cu dopant and oxygen vacancies act as a controlling knob to tune the parameters like crystallinity, bandgap, phonon lifetime, and asymmetry which tends to anharmonicity in  $\text{TiO}_2$  matrix. Such tunable parameters can improve the thermal and photoconductivity in  $\text{TiO}_2$  of nanoscale devices for various applications.

### **Au doped TiO<sub>2</sub>**

In this part, TiO<sub>2</sub> microflowers are prepared using the hydrothermal method and then implanted with 30 keV Au ion of four different fluences. The SRIM simulation result reveals that the displacements of atoms take place with Au ion irradiation that increases with ion fluence. FESEM images show remarkable structural modification of the microflowers and nanorods after ion implantation. The structural modification starts slowly from the lower fluence and becomes more noticeable as the fluence increases. It is demonstrated that irradiation of TiO<sub>2</sub> with 30 keV Au ions induces melting and junction formation of the nanorods. This melting is caused by the rise of temperature during ion implantation which arises from the energy loss of the projected ion and is theoretically simulated using the thermal spike model. This indicates that the welding can be manipulated by controlling the ion fluence. The XRD data confirms the phase purity and crystalline nature of the TiO<sub>2</sub> which remain intact after ion implantation. The EDS and TEM data confirm the presence of Au in the ion-implanted TiO<sub>2</sub> systems and at higher fluence nanoparticles of Au are observed. In addition to the structural properties, the optical properties of the TiO<sub>2</sub> get modified after ion implantation. The bandgap decreases monotonically with ion fluence indicating the incorporation of midgap states associated with Au ion implantation. From the above discussions, it is clarified that the ion beam technique can be used for the fabrication of nano-scale junctions or welding nanoscale materials, which is essential in nano-electronic devices.

### **Au decorated TiO<sub>2</sub>**

In this part, two concepts are studied. In one part Au is decorated over the surface of TiO<sub>2</sub> to study the photocatalytic activity and in the second part, the Au decorated as well as the pristine TiO<sub>2</sub> is annealed to investigate the Fano asymmetry. The photocatalytic degradation of R6G using Au decorated TiO<sub>2</sub> microflowers photocatalyst was investigated in both UV and visible light exposure. The morphology of TiO<sub>2</sub> microflower and decoration of the Au helps

to improve the photocatalytic efficiency. The  $\text{TiO}_2$  nanostructures are flower like structures consisting of nanorods that have the advantage of a large surface area that provides a larger surface area for the photocatalytic reaction to take place. The bandgap reduction and visible light absorption in the Au decorated samples confirmed from the UV-visible spectroscopy is another confirmation to improve the photocatalytic efficiency. The photogenerated charge carriers play an important role in photocatalytic performance. The Au decoration helps in reducing photo-generated charge carrier recombination confirmed by PL spectroscopy. The plasmon-induced heating effect which is proved by the Raman spectroscopy enhances the photocatalytic activity. Further, the Fano asymmetry studied using the annealed samples indicates the plasmon-induced charge transfer. The Fano asymmetry parameter and Raman peak position for the annealed pristine  $\text{TiO}_2$  as compared to the pristine  $\text{TiO}_2$  confirm the presence of oxygen vacancy in the pristine  $\text{TiO}_2$ . Again the increased Fano asymmetry parameter in Au decorated annealed sample is attributed to plasmon-induced charge transfer. In short, the charge separation, Schottky junction, UV-visible light absorption, and photothermal effect together play a crucial role in greatly enhancing photocatalytic activity. Both the heating effect and charge transfer mechanism play a role in photocatalysis and the Fano effect.

### **Comparison of properties for different defects in $\text{TiO}_2$**

In this thesis, we have used ion implantation, chemical doping, and surface decoration methods for defect engineering in  $\text{TiO}_2$  microflowers for different properties. The defects created by chemical doping and ion implantations in the  $\text{TiO}_2$  matrix introduce midgap states within the valence band maximum and conduction band minimum that tune the bandgap for various optical, electronic, and spintronic applications, which has been demonstrated by non-linear properties, Fano asymmetry, and photocatalytic properties. Also, it has been concluded that the production of defect states can be controlled by choosing the doped ions

based on their oxidation state and atomic radii that highly affect the bandgap tuning which is the basic constituent for the optoelectronic application in wide bandgap oxide semiconductors.

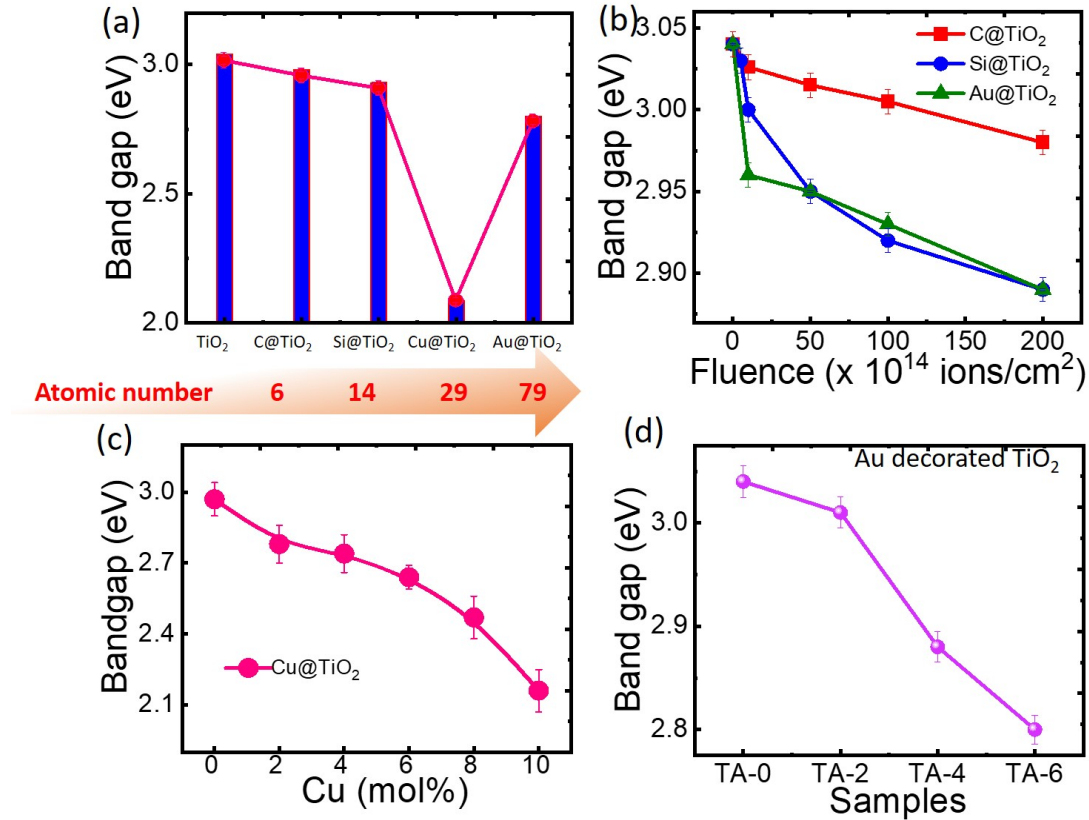


Figure 8.1: (a) Variation of bandgap with dopant element of increasing atomic number.(b) Variation of bandgap with ion fluence for C, Si, Au ion implanted  $\text{TiO}_2$ . (c) Variation of bandgap with Cu molar concentration. (d) Bandgap variation in Au decorated samples.

The bandgap narrowing due to the incorporation of dopants is summarised in Figure 8.1. From Figure 8.1 (a), it is observed that the dopant with a higher atomic number reduces the bandgap as compared to the pristine  $\text{TiO}_2$ . The lowest bandgap reduction is observed in the case of Cu doping, however, Cu is doped chemically not by ion implantation. For a better understanding, Figure 8.1 (b) shows the fluence-dependent bandgap reduction for

different ion doping. The bandgap narrowing in the case of C ion doping is lowest and highest in case of Au doping. At highest fluence ( $2 \times 10^{16}$  ions/cm<sup>2</sup>) the bandgap narrows down from 3.04 eV to 2.98 eV, 2.89 eV, and 2.89 eV for C, Si, and Au ions respectively. However, in the chemically Cu-doped TiO<sub>2</sub> the bandgap reduces to 2.16 eV at 10% Cu molar concentration as shown in Figure 8.1(c). Further, in the case of Au-decorated samples, the bandgap reduces to 2.80 eV for 6nm Au-decorated samples and is displayed in Figure 8.1(d). In addition, the variation of crystallite size gets modified depending on the atomic radii of the dopants. Further, the Fano asymmetry parameter can be tuned via doping different elements, which can be determined from the Raman lineshape analyses and BWF formalism.

In summary, Bandgap engineering is an art, which can be tuned through ion fluences as a controlling knob. The method of defect creation is also an important tuning parameter to understand the asymmetric nature through spectroscopic signature. The current thesis explored a few of such effects and demonstrates some applications through non-linear optical photocatalytic properties.

## **8.2 Future prospects**

1. We have chemically doped the Cu ions in TiO<sub>2</sub> and observed its effect on NLO properties and phonon asymmetry, however, the Cu ion implanted TiO<sub>2</sub> needs to be studied to compare with other ion implanted elements.
2. The Fano effect and phonon asymmetry parameters can be studied for Si, Au, and Cu ion implanted TiO<sub>2</sub>, which can provide an atomic mass-dependent comprehensive comparison of those phenomena.
3. It will be interesting to synthesize only the anatase phase and controllable mixed phase to observe the effect of bandgap tuning and the Fano effect via ion implantation.



